ANALYSIS OF LINEAR ELASTICITY AND NON-LINEARITY DUE TO PLASTICITY AND MATERIAL DAMAGE IN WOVEN AND BIAXIAL BRAIDED COMPOSITES

A Dissertation

by

DEEPAK GOYAL

Submitted to the Office of Graduate Studies of
Texas A&M University
in partial fulfillment of the requirements for the degree of

DOCTOR OF PHILOSOPHY

December 2007

Major Subject: Aerospace Engineering

ANALYSIS OF LINEAR ELASTICITY AND NON-LINEARITY DUE TO PLASTICITY AND MATERIAL DAMAGE IN WOVEN AND BIAXIAL BRAIDED COMPOSITES

A Dissertation

by

DEEPAK GOYAL

Submitted to the Office of Graduate Studies of
Texas A&M University
in partial fulfillment of the requirements for the degree of

DOCTOR OF PHILOSOPHY

Approved by:

Chair of Committee,	John D. Whitcomb
Committee Members,	Junuthula N. Reddy
	Ozden O. Ochoa
	Yongmei Jin
Head of Department,	Helen Reed

December 2007

Major Subject: Aerospace Engineering

ABSTRACT

Analysis of Linear Elasticity and Non-Linearity Due to Plasticity and Material Damage in Woven and Biaxial Braided Composites. (December 2007)

Deepak Goyal, B.E. (Hons.), Panjab University, Chandigarh, India;

M.S., Texas A&M University

Chair of Advisory Committee: Dr. John D. Whitcomb

Textile composites have a wide variety of applications in the aerospace, sports, automobile, marine and medical industries. Due to the availability of a variety of textile architectures and numerous parameters associated with each, optimal design through extensive experimental testing is not practical. Predictive tools are needed to perform virtual experiments of various options. The focus of this research is to develop a better understanding of linear elastic response, plasticity and material damage induced non-linear behavior and mechanics of load flow in textile composites.

Textile composites exhibit multiple scales of complexity. The various textile behaviors are analyzed using a two-scale finite element modeling. A framework to allow use of a wide variety of damage initiation and growth models is proposed. Plasticity induced non-linear behavior of 2x2 braided composites is investigated using a modeling approach based on Hill's yield function for orthotropic materials. The mechanics of load flow in textile composites is demonstrated using special non-standard postprocessing techniques that not only highlight the important details, but also transform the extensive amount of output data into comprehensible modes of behavior.

The investigations show that the damage models differ from each other in terms of amount of degradation as well as the properties to be degraded under a particular failure mode. When compared with experimental data, predictions of some models match well for glass/epoxy composite whereas other's match well for carbon/epoxy

composites. However, all the models predicted very similar response when damage factors were made similar, which shows that the magnitude of damage factors are very important.

Full 3D as well as equivalent tape laminate predictions lie within the range of the experimental data for a wide variety of braided composites with different material systems, which validated the plasticity analysis. Conclusions about the effect of fiber type on the degree of plasticity induced non-linearity in a ±25˚ braid depend on the measure of non-linearity.

Investigations about the mechanics of load flow in textile composites bring new insights about the textile behavior. For example, the reasons for existence of transverse shear stress under uni-axial loading and occurrence of stress concentrations at certain locations were explained.

To the good and bad times of Ketu Mahadasha

ACKNOWLEDGEMENTS

I am thankful to GOD for helping me stay sane in *those* times.

I will forever be indebted to the Texas A&M University, which blessed me with its love and rich traditions and provided me an opportunity to not only acquire academic knowledge but also helped me become a better person. I wish to express my deep sense of gratitude to my advisor, Dr. John D. Whitcomb for his constant academic guidance and financial support. His critical eye for detail, combined with my ceaseless pursuit of perfection, helped me learn what it takes to produce quality work.

I am thankful to Dr. Xiaodong Tang for being a great friend and mentor. I acknowledge his guidance early in my research and help concerning the use of several in-house computer codes. I express my gratitude to Dr. J. N. Reddy, Dr. Ozden O. Ochoa, Dr. Yongmei Jin and Dr. Xin-Lin Gao for serving on my advisory committee. I am especially thankful to Dr. Ochoa for her motivation, which helped me build a great deal of self-confidence. Dr. Reddy's excellent teaching abilities helped me get comfortable with mechanics fundamentals. I am also thankful to Dr. Whitcomb, Dr. Reddy and Dr. Walter Haisler for their support that helped me win AIAA's open topic graduate award.

I am thankful to Dr. Ajit Kelkar from North Carolina A&T University and Dr. Jitendra Tate from Texas State University, San Marcos, for helpful discussions and for providing me with the experimental data for braided composites.

My sincere thanks also go to the Aerospace Engineering Department staff, especially Ms. Karen Knabe who is a wonderful person and James Munnerlyn for their kind help during my graduate studies. I appreciate the International Student Services for their assistance concerning my study and stay in Aggieland. I acknowledge the computer support extended by the Texas A&M's Supercomputing Facility.

Current and past members of our research team especially Julian Varghese, Dr. Jiwoong Sue, Dr. Jongil Lim, Dr. Jae Noh, Woosick Choi, Bhavya Aggarwal, Kevin Maxwell, Brian Owens, Ross Mclendon have been awesome people to work with. I

extend my thanks to all of my friends, especially Bikram, Atul, Pallab, Shantanu, Chandraveer, Jatin, Chandan, Munish, Jitu and Nishu for always being there for me. I am thankful to all the people who have directly or indirectly encouraged and supported me to pursue a Ph.D. degree. I am thankful to Brain Owens and Chandraveer, also for proofreading this dissertation.

My sincere thanks go to Ameeta for being a great friend and for her unconditional support. Finally, I express my sincere appreciation to my mother, father and sister for their unlimited support, love and sacrifice for making it possible for me to pursue graduate studies in the US.

This work is based on research supported by the Federal Aviation Administration (FAA), the National Aeronautics and Space Administration's University Research, Engineering and Technology Institutes (NASA URETI), NASA Marshall Space Flight Center and the Air Force Office of Scientific Research (AFOSR). Any opinions, findings, recommendations or conclusions expressed herein are those of the author and do not necessarily reflect the views of the aforementioned funding agencies.

NOMENCLATURE

1 = Local fiber direction of the tow

$2,3$ = Local transverse directions of the tow

E_{11} = Longitudinal tensile modulus of the tow

E_{22} = Transverse tensile modulus of the tow in the 2 direction

E_{33} = Transverse tensile modulus of the tow in the 3 direction

G_{12} = Shear moduli of the tow in the 12 plane

G_{13} = Shear moduli of the tow in the 13 plane

G_{23} = Shear moduli of the tow in the 23 plane

$\upsilon_{12}, \upsilon_{13}, \upsilon_{23}$ = Poisson's ratios of the tow

S_{11} = uni-axial tensile strength in the 1 direction

S_{22} = uni-axial tensile strength in the 2 direction

S_{33} = uni-axial tensile strength in the 3 direction

S_{11}^{C} = uni-axial compressive strength in the 1 direction

S_{22}^{C} = uni-axial compressive strength in the 2 direction

S_{33}^{C} = uni-axial compressive strength in the 3 direction

S_{12} = uni-axial tensile strength in the 12 plane

S_{13} = uni-axial tensile strength in the 13 plane

S_{23} = uni-axial tensile strength in the 23 plane

Vfo = overall fiber volume fraction of the composite

Vft = Fiber volume fraction in the tow

$\langle \bullet \rangle$ = Volume averaged variable is defined as $\langle \bullet \rangle = \frac{1}{V}\int_{V} \bullet dV$, where $\bullet$ is the variable of interest

TABLE OF CONTENTS

Page

Page

Page

LIST OF FIGURES

Page

Page

Page

Page

Page

LIST OF TABLES

Page

1. INTRODUCTION

1.1. Introduction to Textile Composites

Composite materials have found a wide variety of applications in aerospace, automobile, sports, and marine industry for the past three decades because of their high specific strength and stiffness as compared to conventional metals/alloys [1]. The Air Force requirement for lightweight, high performance vehicles subjects materials to extreme service. Textile composites offer unique combinations of properties that cannot be obtained using conventional tape laminates. High speed textile preform manufacturing, and increased damage tolerance due to the tow interlacing are the primary advantages of textile composites [1]. Also, there is the potential for large reductions in part count due to the ability to create complex preforms. They can be mass produced and are cost-effective as compared to conventional tape laminates. Textile composites are being used in applications ranging from prostheses for amputees to shrouds to capture debris from a failed engine.

Figure 1.1. Aircraft horizontal stabilizer (www.braider.com).

This dissertation follows the style of Journal of Composites Part A.

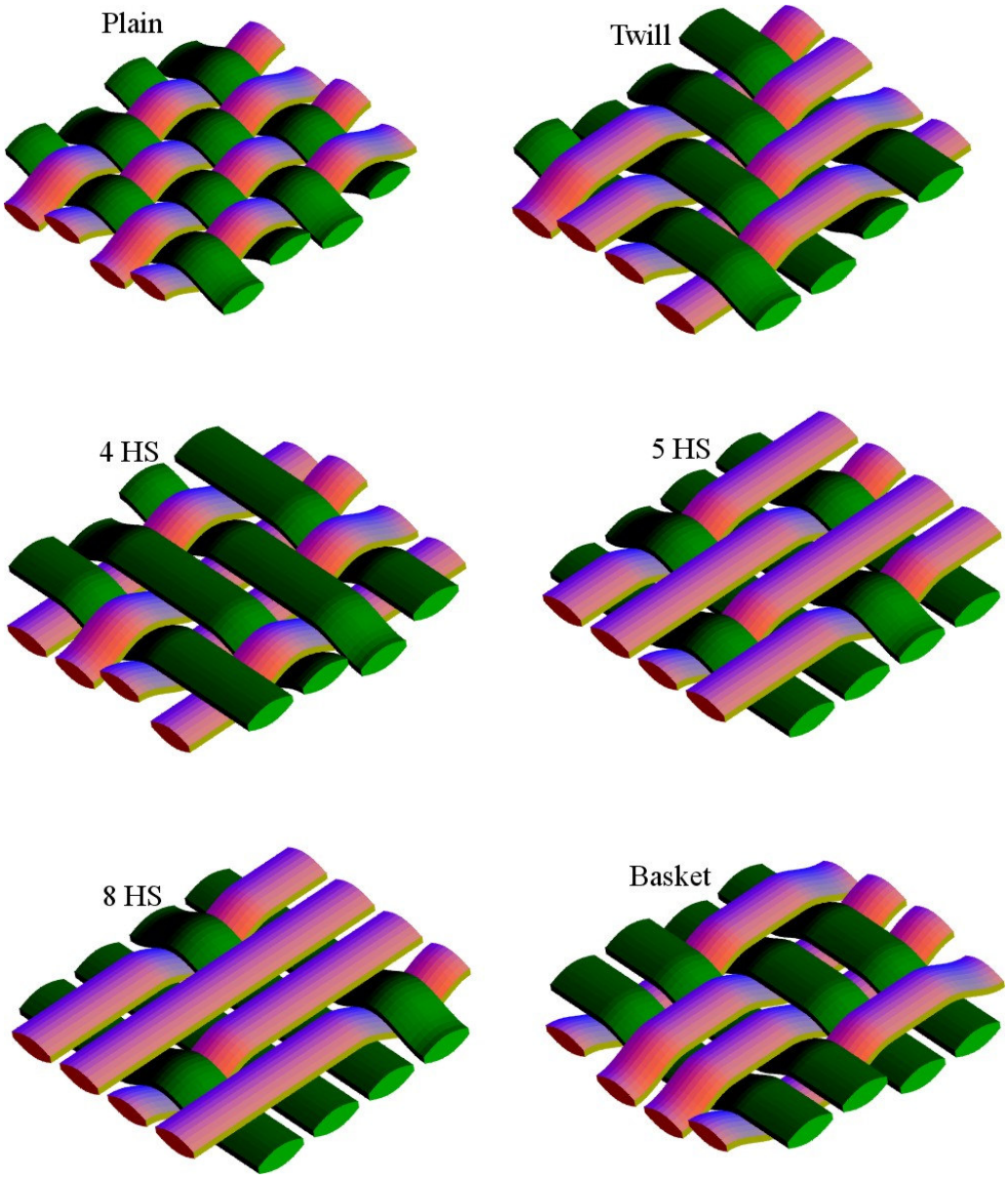

Figure 1.2. Idealized schematics of woven preforms without matrix pockets (HS means Harness Satin).

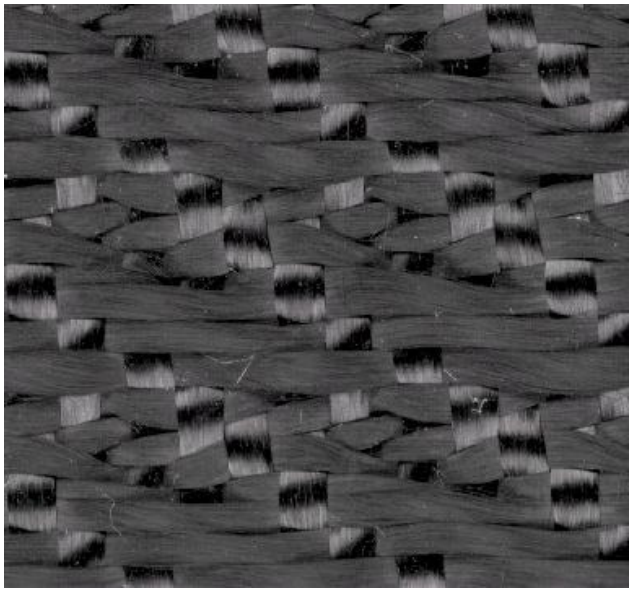

Figure 1.3. Architecture of a bumpy weave.

(a) a 2x2 biaxial braid

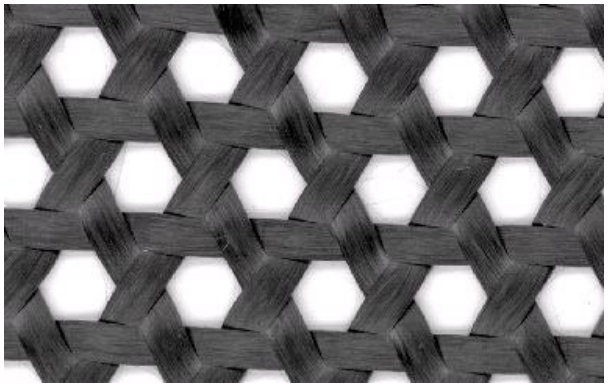

(b) a 2D triaxial braid

Figure 1.4. Architecture of braided composites.

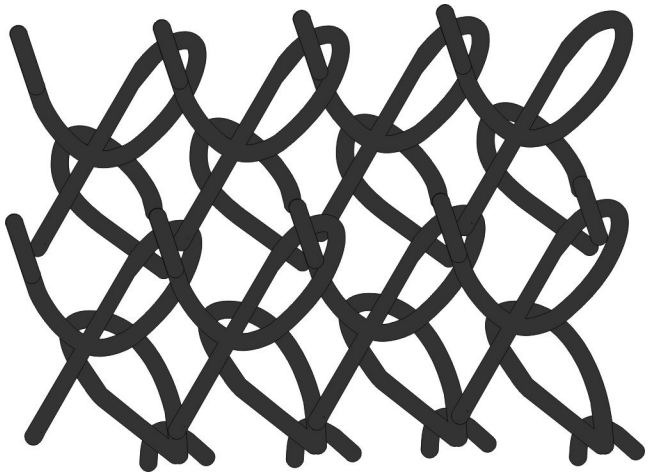

Figure 1.5. Schematic of knitted tows.

Figure 1.1 shows a successful application of braided composites (an aircraft horizontal stabilizer). There are a number of textile manufacturing techniques available to make fiber performs. The dominant forms of textile manufacturing techniques can be classified into braiding, weaving and knitting. They all share the characteristic that fiber tows are interlaced to create a preform that is impregnated with resin to make a composite. Figure 1.2 shows some of the possible idealized weave architectures and Fig. 1.3 shows an actual weave architecture. Figure 1.4 shows architectures of two types of braids: a 2x2 biaxial braid and a 2D triaxial braid. Figure 1.5 illustrates a knitted tow architecture. Both the weaves and the braids can exhibit high performance. The extreme amount of undulation in the knit makes for a very flexible preform, but the performance tends to be low. Hence, in terms of architecture, the focus of this research is on weaves and 2x2 biaxial braided composites. To facilitate discussion in the following chapters, the important geometric parameters and tow architecture of woven and braided composites are discussed below.

1.2. Definition of Geometric Parameters of Textiles

Textile composites have complex microstructure characterized by tow undulation and interlacing. The tow consists of thousands of fibers. The tows are interlaced with each other to obtain a mat and the mats are stacked on the top of each other in some kind of stacking sequence to obtain thickness. The mats are impregnated with the matrix to make the textile composite.

The woven structure is characterized by the orthogonal interlacing of two sets of tows called the warp and the fill tows. The fill tows run perpendicular to the direction of the warp tows. Plain weave, twill weave, 4-harness satin, 5-harness satin, 8-harness satin and basket weave are the dominant forms of woven architectures and are shown in Fig. 1.2. In all the cases, the tows have both the undulated and straight regions except for the case of the plain weave with lenticular cross-section in which the entire length of the tow of both fill and warp tows is undulated. But in the case of other weaves, the tows have some straight region before starting to undulate.

A 2x2 braid structure is formed by mutually intertwining or twisting two or more sets of tows (yarns) about each other (Fig. 1.7). The braid we are studying here can be specified as a "*2x2 biaxial ±θ braid"*. The numbers 2x2 mean that two +θ tows pass over and under two –θ tows and vice versa. Biaxial means that the tows run in two directions (if there are tows in axial direction also, then the resulting structure is called a triaxial braid), θ is the braid angle and it can vary from 15° to 75° [1]. Unlike woven composites, the +θ and –θ tows of a braid are not orthogonal to each other, except for a ±45° braid. A careful examination of the tow architecture of a twill weave and 2x2 biaxial braid (see Figs. 1.6-1.7) reveals that a ±45° 2x2 biaxial braid is geometrically indistinguishable from a 2x2 twill rotated by 45°. Both configurations have orthogonal tows.

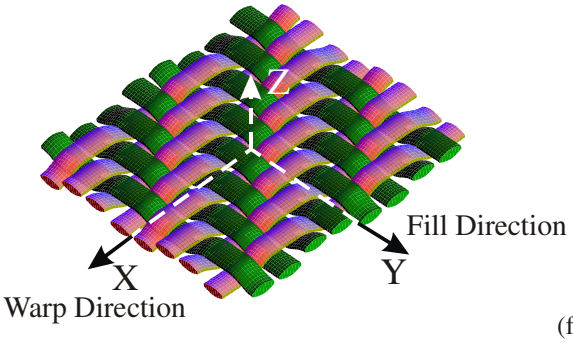

Figure 1.6. Twill weave.

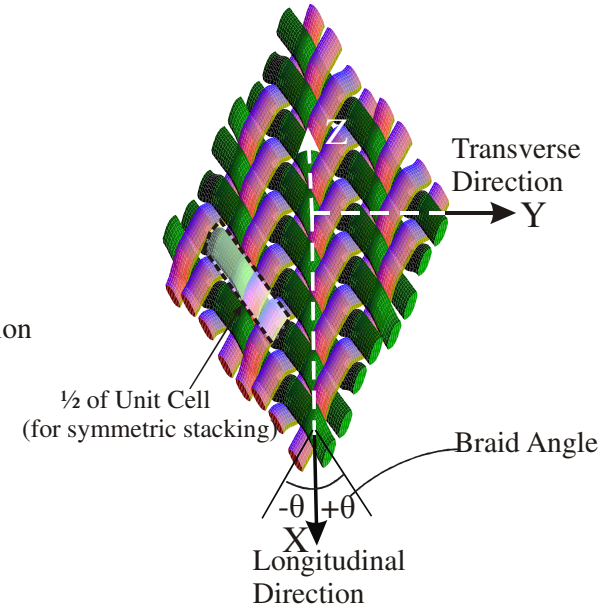

Figure 1.7. A 2x2 braid.

The idealized architectures of woven composites and 2x2 braids are shown in Figs. 1.2 and 1.7 respectively. The matrix pockets have been removed to show the architecture clearly. As is obvious from the figures, there is a repeated pattern of interlacing. In micromechanics this is referred to as "*periodicity*". The unit cell of a periodic microstructure is the smallest region that can produce the whole structure by spatially translating its copies without the use of rotation or reflection.

Figure 1.8 shows a typical tow taken out of the braid microstructure of Fig. 1.7. Note that *xyz* are the local directions for the braid tow in Fig. 1.8 and XYZ are the global directions for the braid in Fig. 1.7. The *x* is the direction along the +θ tow and X is the longitudinal direction. In Fig 1.8, *h* is the mat thickness and λ is the wavelength of the wavy region. The waviness ratio is defined herein as h/λ. This tow has straight as well as undulated regions. Here the straight and undulated regions cannot be separated by planes parallel to YZ plane except for the ±45° braid. This is due to the fact that the braid tows are not orthogonal to each other (except for the ±45º braid). Hence different fibers in a

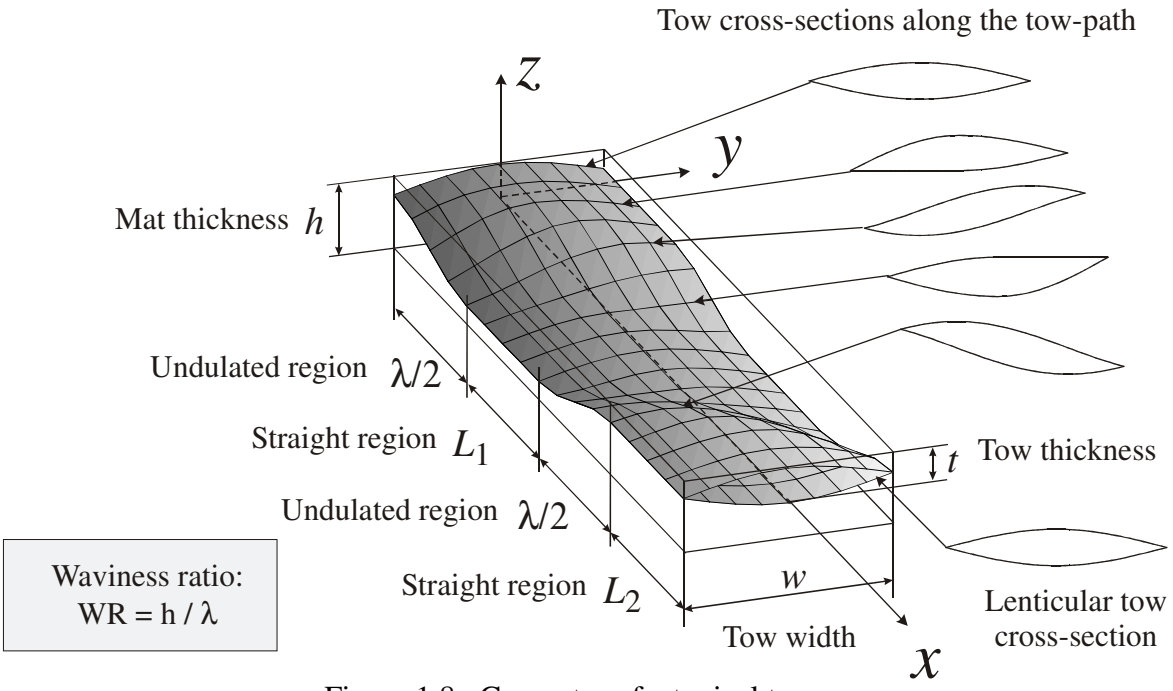

Figure 1.8. Geometry of a typical tow.

single tow do not have the same phase angle. This means that the different fibers of the tow do not uniformly undulate and straighten at the same x coordinate. The phase of a fiber running at the edge of the tow is not the same as that of a fiber running in the middle of the tow. This phase shift is $\phi = y * \tan(\theta)$, where θ is the braid angle. Since the tows are not orthogonal to each other for braids, this causes the tow cross-section to vary in an unusual fashion. This is illustrated in Fig. 1.8, which shows the cross-sections at different points along the towpath. Since the phase shift depends on the braid angle, θ, this causes the material architecture of braids with different braid angles to be different. It should be noted that unlike braids, since the interlaced tows of woven composites are always orthogonal to each other, the phase shift is zero and hence their cross-section shape does not change along the towpath. The shown braid tow in Fig 1.8 has an idealized lenticular cross-section in the straight region. In reality, the cross-section of the tow varies anywhere from lenticular to flattened to elliptical. Moreover, the cross-section

shape can be different at different places. The effect of heterogeneity was analyzed by Whitcomb et al. in ref. [2] and it was showed that the behavior can be reasonably predicted by average parameters. The curved portion of the cross-section can be defined by a simple sinusoidal function of the form

$$z = \frac{h}{4}\cos\left(\frac{2\pi(s+s_0)}{\lambda}\right) + z_0 \tag{1.1}$$

where s = x or y, s_0 and z_0 are offsets, h is the model thickness, and λ is the wavelength of the wavy region as shown in Fig. 1.8. Tows with flattened and lenticular cross-sections are shown in typical finite elements in Fig. 1.9.

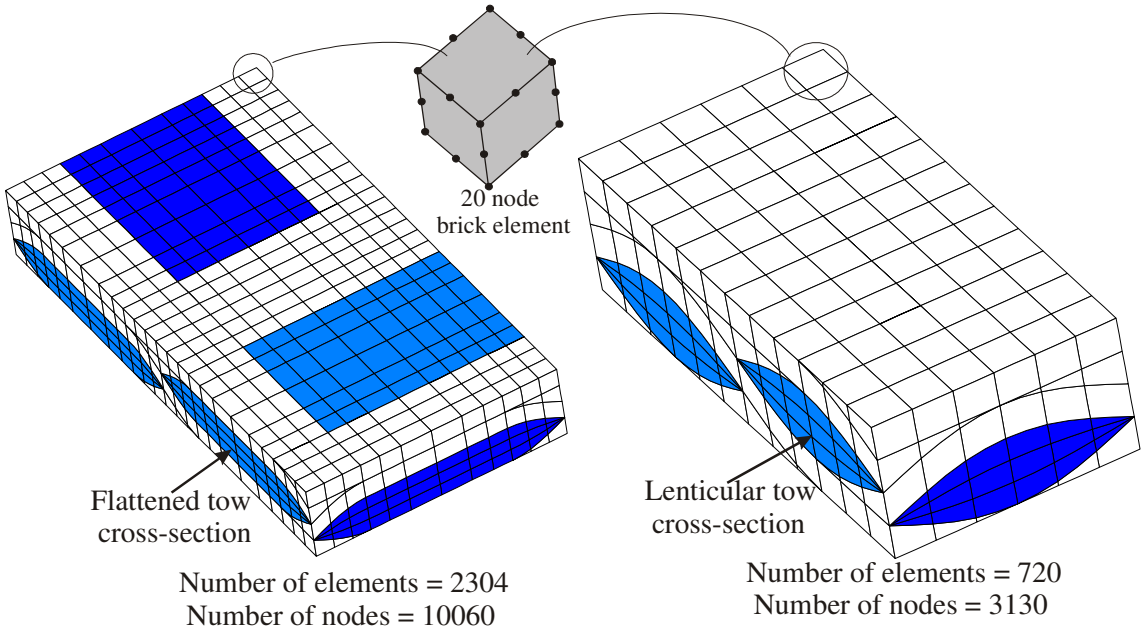

Figure 1.9. Flattened and lenticular cross-sections in typical finite elements of textiles.

The tow volume fraction (V_T) in the model and fiber volume fraction (V_{ft}) in the tow determine the overall fiber volume fraction (V_{fo}) as follows:

$$V_{fo} = V_T \times V_{fT} \tag{1.2}$$

Depending upon the requirement, any number of mats can be stacked on the top of each other. If braid mats are spatially translated in a direction perpendicular to the plane of the mat, and stacked on top of each other, we obtain a *simple stacking* of mats. In this case, the undulation of the tows is in phase for all the mats. If the mats are mirror images of each other at each mat interface, then the resulting sequence is called a *symmetric stacking*. Both simple and symmetric stacking of mats is shown in Fig. 1.10.

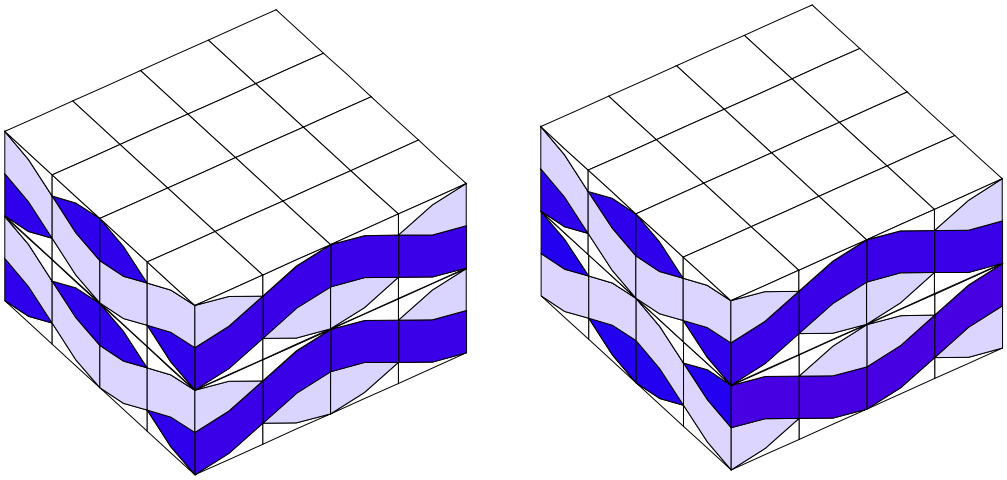

Simple Stacking Symmetric Stacking

Figure 1.10. Simple and symmetric stacking sequences.

1.3. Statement of Objectives

The goal of this work is to understand linear and non-linear behaviors of textile composites. To reach that goal, this work involves conducting linear elastic stress analysis, plasticity and material damage induced nonlinearity, and using special techniques for understanding the mechanics of load flow in woven and biaxial braided composites. There are four primary objectives:

1) Predict the stress distribution in braided composites, analyze the sensitivity of predicted stress concentrations to various design parameters (braid angle, waviness ratio) and compare the stress distribution with equivalent tape laminates.

2) Understand the non-linear behavior of textile composites due to damage initiation and progression. Present a framework to allow use of a variety of damage initiation and growth models. Use this framework to predict the damage initiation and growth in plain weave and twill weave composites using different damage models. Compare these predictions with available experimental data. Compare the salient features and predictions of different damage models with each other.

3) Understand the plasticity induced non-linear behavior of textile composites. Validate the plasticity analysis by comparing the finite element predictions with experimental data for a wide variety of braided composites with different material systems. Compare the predictions of equivalent tape laminates with full 3D finite element analysis and experimental data. Analyze the effect of fiber properties on plasticity induced non-linearity in braided composites using different measures of plasticity.

4) Understand mechanics of load flow using non-standard post-processing techniques. In particular, two techniques: stress resultants along the length of the tow and stress volume distribution in the tow, will be used to highlight the important details as well as to transform the massive amount of linear elastic, plasticity and damage analyses output data into comprehensible modes of behavior.

The following chapters will begin with a review of the literature that is relevant to this work. Then the scope of the research will be described. That will be followed by procedure, results and discussion.

2. REVIEW OF THE STATE OF THE KNOWLEDGE

The following subsections summarize the state of the art in analytical and experimental investigation of textile composites. First, the multiscale challenges inherent in predicting the behavior of textile composites will be described. Then, the analytical methods for describing the behavior of textile composites will be reviewed. Research efforts in developing simple as well as full 3D finite element models, and advantages and limitations of the various methods, will be discussed. Finally, progress in experimental characterization of textile composites will be reviewed.

2.1. Multiscale Analysis of Textile Composites

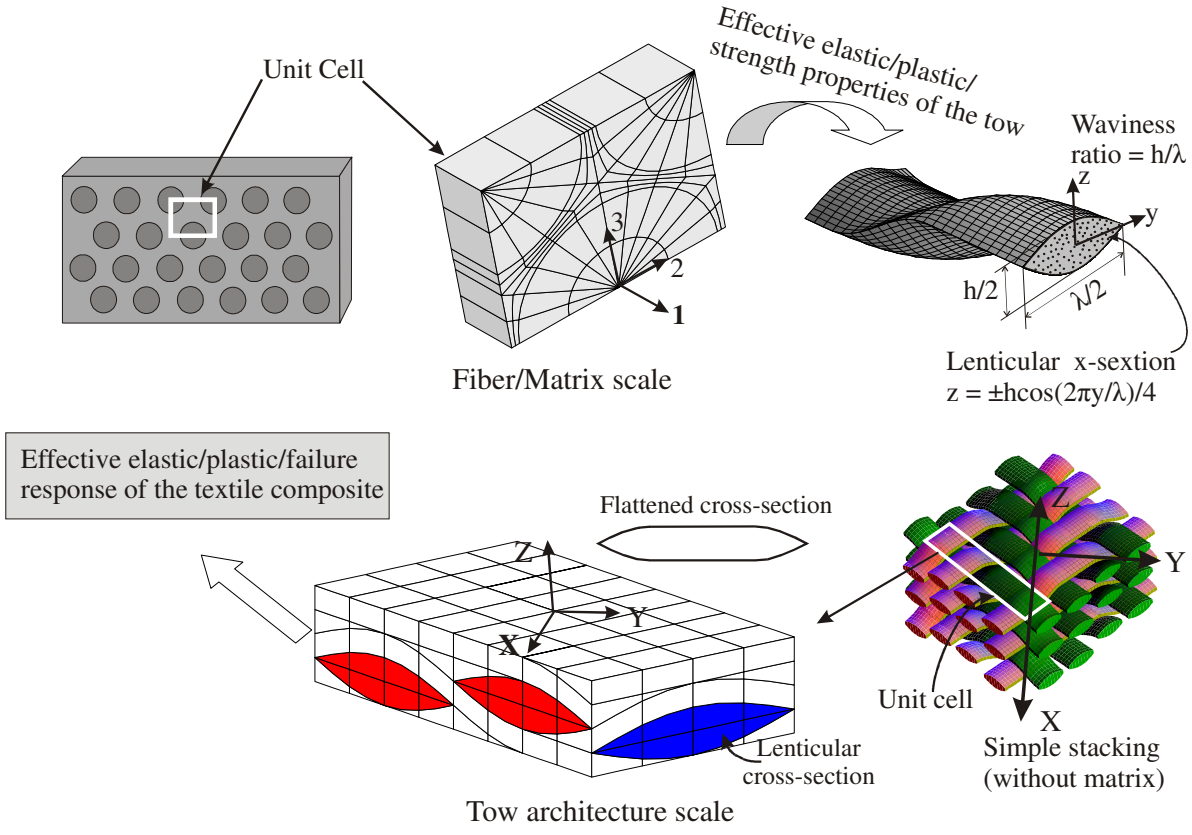

Figure 2.1. Multiscale Analysis.

Textile composites exhibit multiple scales of complexity. The major scales are the fiber/matrix scale, the tow architecture scale, the "laminate scale" (i.e. multi-layered textiles), and the structural scale [2]. Fiber/matrix and tow architecture scales are illustrated in Fig. 2.1. There is a very large literature on analysis at the fiber/matrix scale [3-5], but not much for plasticity and damage, which is the focus of this study. One of the main works left to be done is to tailor the techniques already present in the literature to account for plasticity and material damage induced non-linearity.

Accounting for the tow architecture scale presents severe challenges even for highly idealized cases. Compared to modeling of tape laminates [6-10], there has been relatively little effort for textile composites. For damage modeling of textiles, a common strategy for designers is to use laminated plate theory after knocking down the properties by certain factors. Obviously, this does not lead to fundamental understanding that could guide optimal design of the material. The following will review the wide range of analyses that have been developed.

2.2. Simple versus Full 3D Models

Most of the predictive models of textile composites can be categorized as either 1) very simple due to assuming isostrain or isostress or a combination of both, 2) a hybrid of strength of materials and piecewise isostrain or isostress assumptions or, 3) full three dimensional finite element modeling. The first two categories have close ties to laminated plate theory. There are also some hybrid approaches, such as the binary model developed by Cox et al. [11]. For certain engineering moduli, all of these approaches have been shown to give similar trends. For others, either the predictions of the engineering properties differ, or an estimate is not even provided by the simpler analyses. Whitcomb et al. [12] showed that the ability of the "enhanced laminate theory" models to predict in-plane extensional modulus for a plain weave was related to two simplifying assumptions that introduced canceling errors.

Simple models involve simplifying assumptions concerning geometric modeling of the tow path and boundary conditions. These models vary in terms of the accuracy of the assumed displacement or stress field. Nevertheless, simple models do offer some

significant insights into the behavior of textiles. However, one can not obtain detailed information like the microscopic stress distribution or the modes of failure. The insights obtained from full 3D models or the experiments can be utilized to refine and modify simpler models and make them more robust. The simpler models will be discussed first, and then the full 3D models will be reviewed.

2.3. Progress in Development of Simple Models

Ishikawa and Chou [13] pioneered the development of simple 1-D models based on lamination theory to predict thermo-elastic properties. The 1-D crimp model accounted for fiber undulation, but the mosaic model did not [13-15]. The basic strategy of the 1-D crimp model was extended to 2-D by Naik, Shembekar and Ganesh [16-17]. The translation to 2-D was accomplished by volume averaging in each subregion using isostrain or isostress assumptions and then combining the homogenized subregions… again using isostress or isostrain assumptions. They developed the so called *the parallel-series (PS) model and the series-parallel (SP) model* depending on assembling the elements first in parallel or in series respectively. Hahn and Pandey [18] extended the above 2-D models to a *3-D thermo-elastic model* that models the undulation of fibers in both directions along with a sinusoidal cross-section shape of the tows. The condition of isostrain was applied, whose accuracy still remains to be verified through experiments. It should be noted that if both the matrix and the tows are isotropic, a model based on isostrain conditions throughout the unit cell would predict no effect due to the undulation of the fiber, which is obviously incorrect. Verpoest [19] used the principle of minimum total complementary energy to develop a model for predicting the full set of 3D engineering moduli.

A few important observations can be made from the various efforts in using simple models. The first is that if the goal is to just predict engineering moduli of undamaged materials, the existing suite of simple models is probably sufficient. The reason is that in reality, comparatively flat weaves are used and their moduli are dominated by quite simple physics. Unfortunately, the accuracy of some of the simple models appears to be a result of fortuitous cancellation of errors rather than good

approximation of the physics [12]. Whitcomb and Tang [20] showed that all of the 3D engineering moduli can be predicted quite accurately even for very wavy weaves if the behavior of the undulated regions is described adequately. They also showed that some of the most popular approximations appear to have little physical basis.

2.4 Progress in Development of Full 3D Finite Element Models

Although moduli can be predicted fairly easily, prediction of the local stress state is not so easy. Figure 2.2 shows the predicted 3 dimensional stress state in the tows and matrix for a 5-harness satin when 1% uniaxial tensile strain was applied. The stress state is fully 3D even for the simplest loading. The interpretation of these stress states is a

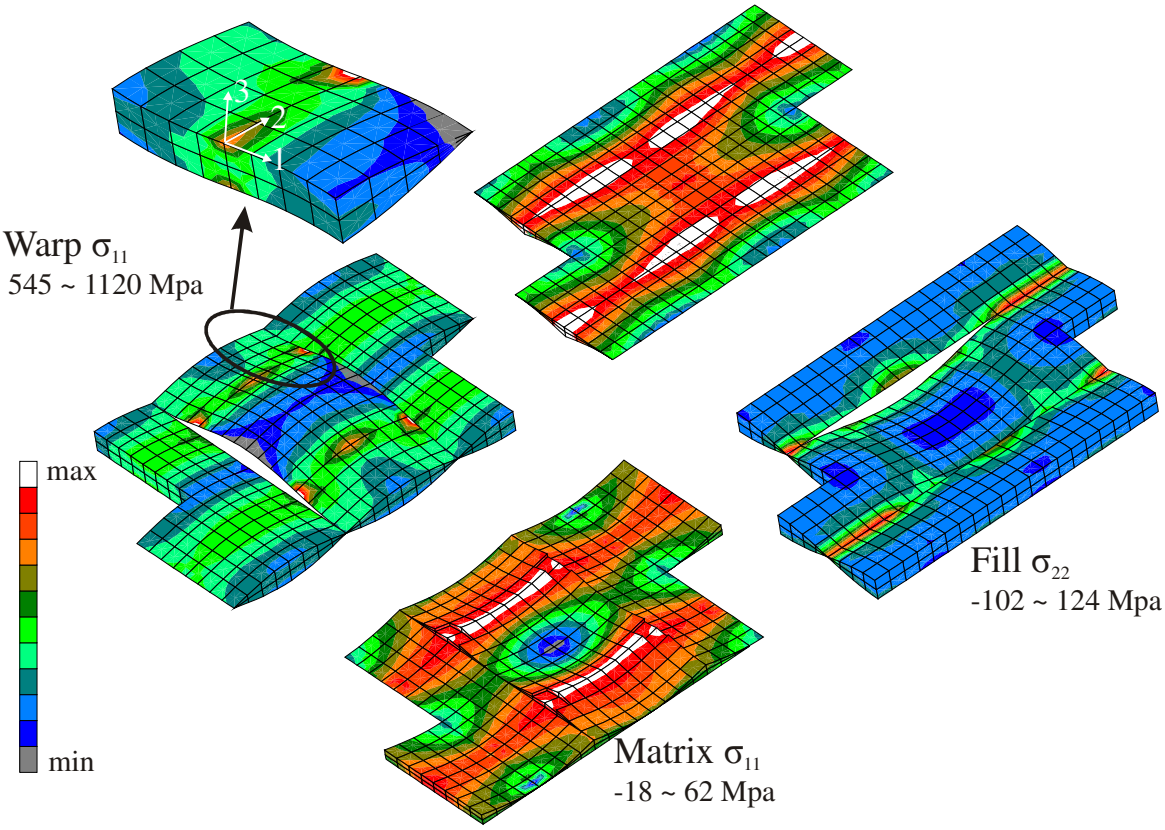

Figure 2.2. Three-dimensional stress state in the tows and matrix of 5 harness satin weave (Applied load is $<\varepsilon_{xx}> = 1\%$).

difficult job because the stresses can be so localized that the scale is small compared to the size of the fibers in the tow. The real tow architecture has more chaotic geometry than idealized textile geometry that will further increase the complexity of the stress state. Prediction of the three-dimensional stress state, effect of textile design on damage initiation and growth, non-linearity due to plasticity, and coupling of these phenomena requires a much more detailed description of the textile architecture than the simple models can possibly provide. Fortunately, the rapid increase in easily accessible computational power has made 3D analyses much more practical.

Some of the earliest 3D models of woven composites were developed by Paumelle et al. [21-22] and Whitcomb et al. [12, 23-24]. More recently Kuhn et al. [25-26], and Ji and Kim [27] have developed models for woven composites. These efforts predicted not only effective macroscopic moduli, but also local stress concentrations that could lead to premature failure. Geometric and material nonlinearities (including failure) were included in the work by Blackketter [28], Whitcomb [29], and Kollegal and Sridharan [30]**.** Gibson and Guan [31] examined the viscoelastic response of a woven composite. Most of the 3D models in the literature are for plain weave composites. The reason is that it is by far the simplest of the weaves, so mesh generation is relatively simple and the computational requirements are quite small, at least for linear analysis. However, there are exceptions. Whitcomb et al. [20, 23-24, 32] has also published results for 4, 5, and 8-harness satin weaves, twill weave and 2x2 braids. D'Amato [33] developed a model for triaxial braids. Naik [34] also developed models for braids.

Analysis of textile composites can require large finite element models. Fortunately, the periodicity can be exploited that reduces the analysis region to just a small unit cell of the microstructure. A unit cell is a region that can produce the whole microstructure by spatially translating its copies. The computational cost can be reduced further by exploiting symmetries within the textile unit cell. Unfortunately, the boundary conditions for partial unit cell models are much more complicated and not intuitive like they are for the full unit cell. For example, Fig. 2.3 shows the slave/master face pairs for

a 2x2 biaxial braid [32]. Refs. [35-36] describe systematic procedures for deriving these complex boundary conditions for partial unit cell models.

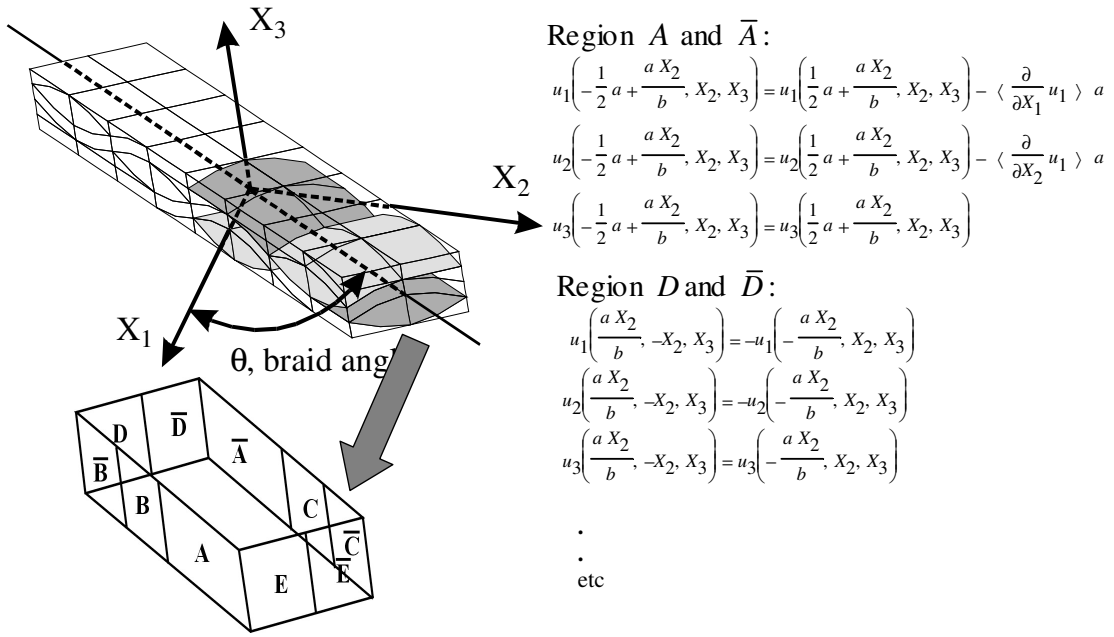

Figure 2.3. Multi-point constraint relations. A finite element mesh of the full unit cell is shown. The half unit cell model is the region in which the matrix packets are shown transparent. Multipoint constraints are imposed on the paired regions.

Mesh generation is one of the major challenges for the analyst. It is impractical to perform parametric study using 3D models unless the model itself is defined parametrically. That is, there must be a way to vary the characteristics of the tow architecture with the specification of only a few parameters. Tang used this technique very effectively in ref. [20], where results were generated for hundreds of different weave configurations.

2.5 Progressive Failure Analyses

One higher level challenge is the prediction of non-linearity caused by damage initiation and progression in textile composites. Using 3D finite element analyses, the failure can be predicted in two ways for textile composites. One involves a discrete modeling of damage and other involves accounting for damage in a homogenized way in which the modulus or strength properties are degraded whenever some damage is detected. An accurate modeling of geometry, implementation of a reasonable failure criteria and a property degradation model are prerequisites for this type of modeling approach.

There have been a few attempts in discrete modeling of damage [37]. Most of the efforts have been in homogenized modeling of damage. Various researchers have proposed different damage models. Most of these models are similar in the sense that they degrade the stiffness coefficient or increase the compliance coefficients of the tows and matrix after a failure criterion detects the occurrence of a damage mode. These models differ from each other in various ways. The models basically differ in what degradation factors [37] they use for degrading the properties under a particular failure mode. Secondly, some degrade only the diagonal entries in compliance or stiffness matrix and some affect the off-diagonal terms also [28, 37-43]. Another difference between damage models is whether the matrix, which is isotropic initially, is considered anisotropic or not after damage. Some of the models are based on the experimental observations while some have theoretical basis. A comparison of some of the damage models available in the literature will be provided here. The damage model given in ref. [28] has been widely used to predict initiation and growth of damage by many researchers [28, 38-40]. Whitcomb and Chapman [40] proposed a property degradation model based on the Blackketter et al.'s [28] model. This was a combination of the method used by Blackketter et al. [28], Stanton and Kipp [41] and Whitcomb and Srirengan [37]. The model involved increasing the compliance coefficients of the tows and matrix when a certain failure mode was detected. Also the matrix, if isotropic before failure, was treated as anisotropic after damage. Whitcomb and Chapman's [40] model is

similar to the model given by Blackketter el al. [28] except for a few differences like the degradation factors are different in the two models. Both models affect diagonal entries in the compliance matrix. Zako et al. [42] developed an anisotropic damage constitutive equation based on damage mechanics. Different damage modes were considered in the tows. The degradation factors were calculated from a damage tensor. This model inherently affects the off-diagonal terms also. An anisotropic damage model was considered for tows, and an isotropic damage model was considered for the matrix. Some questions arise about the selection of an isotropic damage model for the matrix because the matrix can behave anisotropically after damage has occurred. Tamma et al. [43] proposed a damage model in which they provided physical explanation of what properties should be degraded under a particular failure mode. They considered the degradation of off-diagonal terms also. Anisotropic damage models were proposed both for the tows and for the matrix. Recently Sankar et al. [44] developed a direct micromechanics method (DMM), which does not make any assumptions based upon homogenized properties. Failure envelopes for a plain-weave textile composite were developed and any arbitrary loading including the moments can be applied to their detailed 3D finite element model. The method employed was used to develop phenomenological failure criteria for textile composites. A drawback is that their method considers only damage initiation with no regard to damage progression.

2.6 Modeling Plasticity in Textiles

Figure 2.4 shows the experimental stress–strain data for ±45˚ and ±25˚ VARTM manufactured [45] carbon/epoxy braids subjected to uni-axial tension in the longitudinal direction. The figure shows that the response is highly non-linear. At 2% strain, the ±45˚ braid composite has lost 76% of its initial tangent tensile modulus and ±25˚ braid has lost 78% of its initial tangent modulus. Similarly, considerable plasticity induced non-linearity has been measured in S2-glass/SC-15 plain woven composites also [46]. The non-linear response shown by these textiles could be due to geometric (caused by tow interlacing and tow waviness) or material non-linearity (due to plasticity or progressive damage). The effect of geometric nonlinearity in woven composites has

been previously examined by the Whitcomb et al. [29]. It was found that the effect of geometric nonlinearity by itself is negligible, but becomes noticeable when coupled with material nonlinearity due to progressive damage, especially under compressive loading

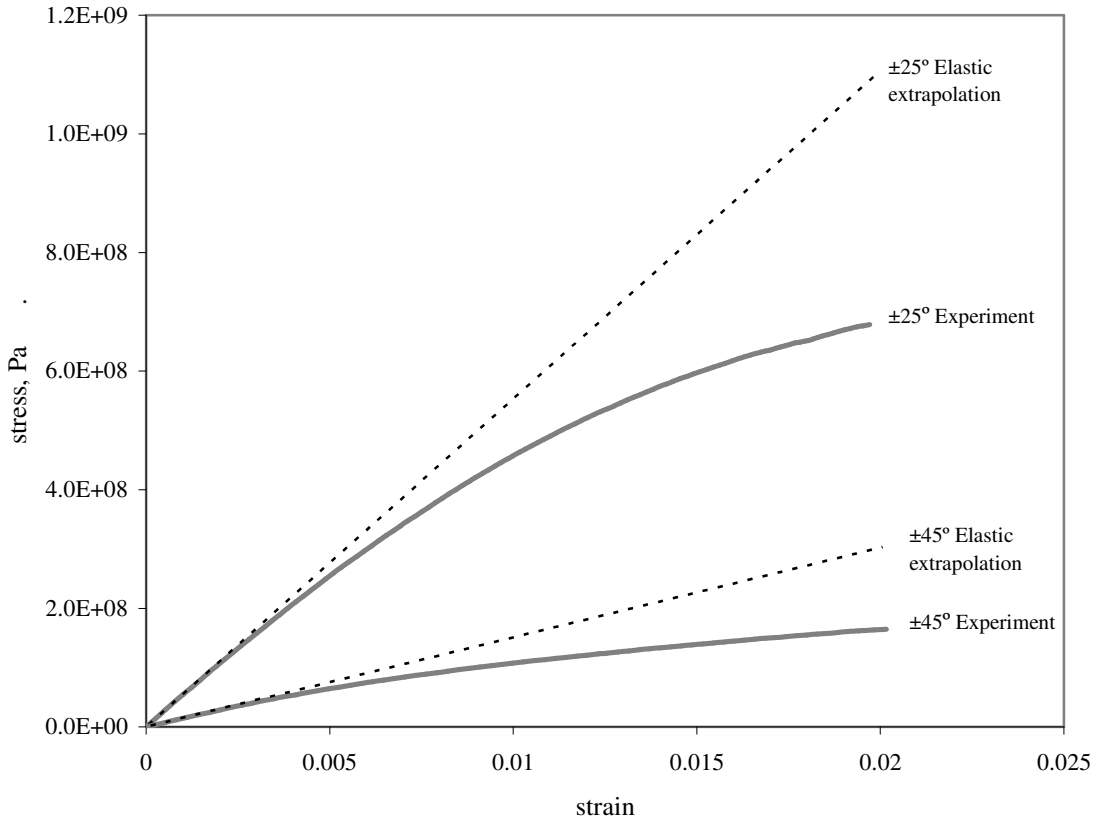

Figure 2.4. Deviation of the measured response from a linear elastic estimate for 2x2 biaxial braids subjected to uni-axial tension in longitudinal direction [45].

conditions. In this work, non-linearity in textiles due to material damage as well as due to plasticity will be considered. Plasticity induced non-linearity is considered because the resins systems typically used in textiles shows considerable plastic behavior. A few researchers have studied the nonlinear behavior of textile composites. Most of the efforts

were concerned very little with inelastic behavior due to plastic deformation, and none of them was devoted to understanding plasticity-induced nonlinearity in braided composites. Efforts in modeling the non-linear behavior due to material damage have been discussed earlier. Below, some efforts to model plasticity in textiles are reviewed.

The Hill's yield function [47-49] has been successfully used by many researchers for modeling fibrous composites [50-51]. Ishikawa et al. [52] studied the material and geometric nonlinear properties using simple crimp and bridging models. The nonlinear off-axis behavior induced by the pure shear was considered for both fill tows and matrix pockets by Hahn and Tsai [53]. Blackketter et al. [54] investigated the inelastic behavior of the fiber tows using an invariant-based plastic flow rule. Dasgupta et al. [55] examined the nonlinear behavior of a plain weave by considering the nonlinear behavior of the matrix surrounding the fiber tows and Tsai-Hill type failure in the transverse tows. Kollegal and Sridharan [30] conducted strength predictions of plain weave by including both geometric and material nonlinear analysis. A micro-model based on Aboudi's method of cells [56] was used to consider the plastic deformation of the tows.

2.7 Post Processing Techniques

Three-dimensional analysis produces a tremendous amount of information. Sometimes it is useful to post process the details to obtain a "bigger picture" interpretation. For example, Fig. 2.5 show stress contours and a stress vs. volume plot for a tapered plate under uni-axial tensile loading. The stress volume distribution plot reveals how much volume of the plate is subjected to the highest stresses, something that is hard to find just by looking at the stress contours that give only the surface information. Two non-conventional techniques will be utilized in this work to analyze the wealth of raw numerical information provided by non-linear finite element analysis of textile composites. The first technique is a stress versus volume distribution plot [57], which will be useful in assessing whether a local stress concentration is so localized that slight yielding will eliminate the high stress. The other technique is calculation of stress resultants as shown in Fig. 2.6. In approximate models the components of the textile are treated as simple structural elements like rods or beams and stress resultants are used to

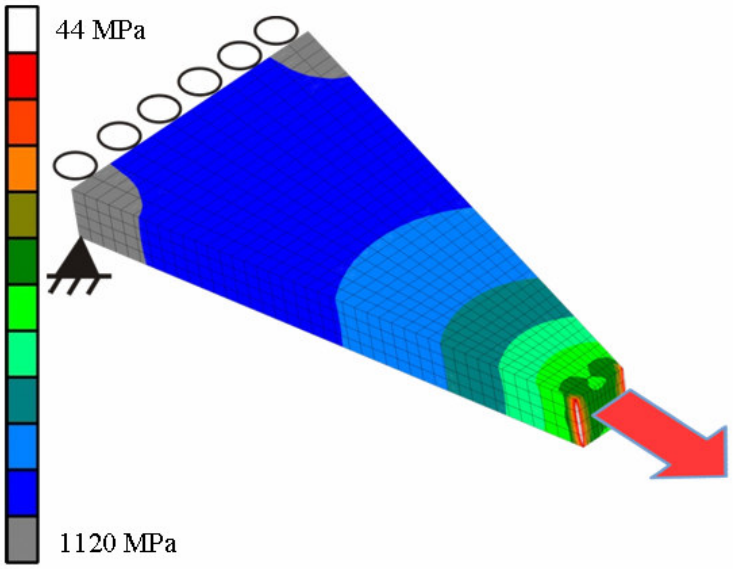

(a) Stress contours

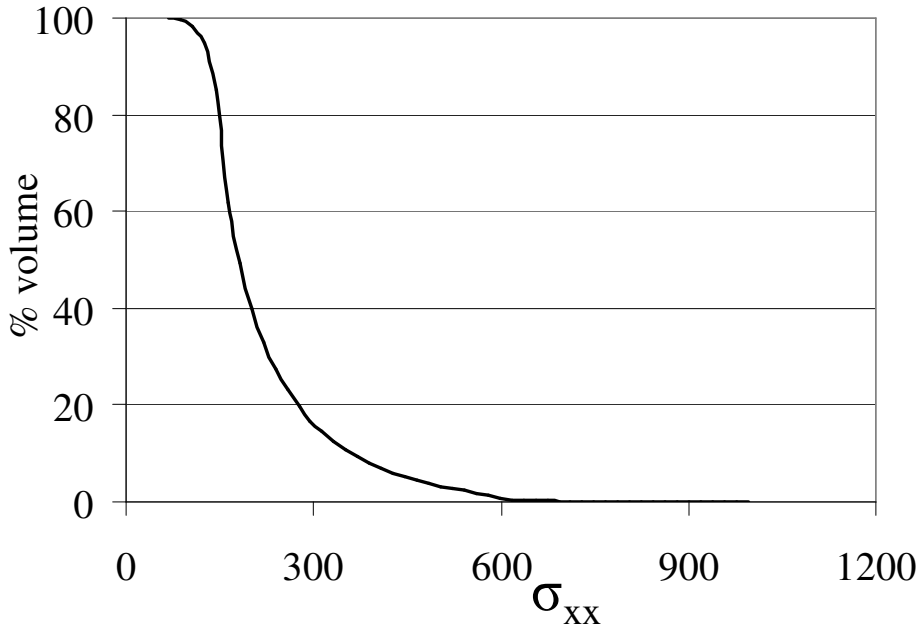

(b) Stress volume distribution

Figure 2.5. Stress contours and stress volume distribution for a tapered plate under uniaxial tensile loading.

describe the load flow. Stress resultants obtained from refined models are much more reliable than those obtained by using a simplified model. These kind of non-standard post processing techniques do not exist in literature.

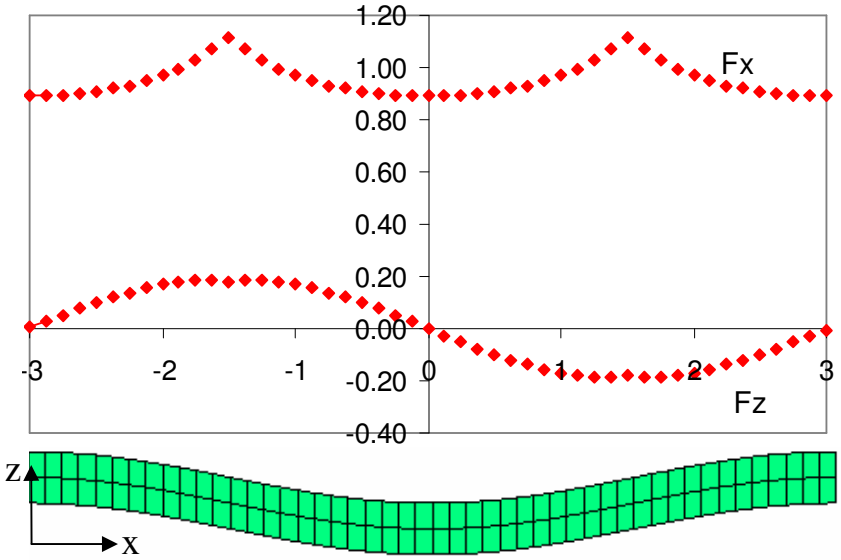

Figure 2.6. Tow stress resultants for plain weave in a linear elastic analysis $\left(Fx = \int \sigma_{xx} dA,\ Fz = \int \sigma_{xz} dA\right)$.

2.8 Modeling the Effect of Irregularity in Textile Architecture

Periodic analysis is generally used in the modeling of textile composites. This is obviously an approximation since in reality there are irregularities due to variations in tow geometric properties such as waviness, cross-section shape, and fiber volume fraction. A few researchers have considered variation of the tow architecture in a specimen. Aggarwal [58] predicted the effects of tow misalignment caused by the manufacturing process or forcing the fabrics to conform to molds. No detailed 3D

analysis was developed and only the effects on stiffness were predicted. Lee et al. [59] and Bednarcyk et al. [60] also investigated the effects of irregularity of the microstructure. However, there was no attempt to model the actual wavy shape of the tows. Whitcomb et al. [2] considered the effect of variation in braid parameters on the progressive failure behavior of a 2x2 braided composite laminate. A bottom-up multi-scale finite element modeling approach was employed that sequentially considered the fiber/matrix scale, the tow architecture scale and the laminate scale. Full 3D analysis was used to obtain effective 3D moduli for a variety of perturbations from a reference configuration. Then these effective properties were assigned to random locations in a macroscopic model of a uniaxial specimen. It was shown that various perturbations produced close response to the reference model [2] and response of the reference model can be predicted by using average parameters. Based on these observations average parameters will be considered in this work and no attempt will be made to model the irregularities that exist in the textile microstructures.

2.9 Experimental Characterization

Most of the experimental work has been focused on measuring the strength and the stiffness, particularly for the use of validating the analytical and the numerical models. For example, Dadkah et al. [61] and Falzon [62] measured the mechanical properties of two-dimensional braided composites under tensile, compressive and shear loading. The effect of fiber damage and tow waviness was also measured.

Due to their inherent weakness in the thickness direction, laminated fiber reinforced composites are susceptible to large delamination damage as well as splitting when subjected to transverse loading and microbuckling under in-plane compressive loading [63]. Various researchers have made efforts to compare the mechanical performance of two dimensional textile composites with those that have been reinforced in the third direction also. Due to very complex geometry, modeling of these three dimensional textile composites has been very limited and mainly experiments have dominated this area. Hosur et al. [63] attempted to improve the transverse strength by providing discrete 3D reinforcement in the form of pins and stitching the laminate in the

thickness direction. The effectiveness of the 3D reinforcement was compared with 2D-laminates, which did not have reinforcement in the thickness direction.

Takatoya and Susuki [64] characterized the fundamental properties of 3-D textile composites and compared them with those of two-dimensional laminated composites of the same resin system. Abot and Daniel [65] investigated the through-thickness deformation and failure of woven fabric composites. Elastic properties and strengths for moderately thick composites was measured and compared with equivalent tape laminates. Fedro and Willden [66] also compared experimentally the mechanical performance of the 2-D triaxially braided and the 3-D braided carbon/epoxy composites with those made from prepreg materials. In general, it has been seen that the third direction reinforcement improves the out of plane properties and impact damage tolerance but decreases the in-plane properties [66]. Baucom & Zikry [67] furthered the experimental research by investigating the effects of reinforcement geometry on damage tolerance in 2D and 3D woven fabric-reinforced composites. The enhanced damage tolerance of the 3D systems was attributed to unique energy absorption mechanisms, which involve the crimped portion of z-tows.

A very challenging area is the fatigue behavior of textile composites. Except for very little modeling [68], almost all of the work in this area has been experimental. Kelkar et al. [68] manufactured biaxial braided composites with different braid angles using vacuum assisted resin transfer modeling (VARTM). Static tension and tension-tension fatigue tests were performed to measure strength. It was concluded that the Sigmoidal function accurately represents the stress-fatigue life curve (S-N Diagram) of braided composites. Quaresimin et al. [69] studied the variation of crack density under fatigue loading of twill weave specimens.

In contrast to results from static testing, the effects of low energy impact damage in a fatigue environment were found to be the critical element leading to failure of woven fabric composites [70]. Other tests involved measuring the influence of temperature on fatigue resistance of plain weave woven CFRP [71] and investigating the

fracture behavior of woven composites containing various cracks geometries in terms of notched strengths [72].

All of the above work was mainly focused on characterizing macroscopic properties. There has been very little work in microscopic damage characterization that could give insights to researchers to develop and compare predictive models. Some work done by Quaresimin and Ricotta [69] involved identifying the main fatigue damage mechanisms like transverse matrix cracking, layer delamination and fiber failure by means of microscopic observation. Also, the crushing appearance and failure modes in the crushing zones for two-dimensional triaxially braided composite were examined by optical microscopy by Chiu et al. [73]. However, the microscopic damage initiation and progression observations, both under static and fatigue loading are far from sufficient to give confidence in modeling.

2.10 Summary

There has been very little detailed analysis of non-linearity induced by resin plasticity and material damage in textile composites. Non-standard techniques to obtain a bigger picture are almost non-existent in the literature. Based on these observations, the scope of this research is discussed in the next chapter.

3. SCOPE OF RESEARCH

Due to the availability of a variety of textile architectures and numerous parameters associated with each, optimal design through extensive experimental testing is not practical. Predictive tools are needed to perform virtual experiments of various options. Virtual experiments would include various linear and non-linear analyses. Fortunately, the increase in computational power that is readily available is making detailed three-dimensional finite element analyses practical. One of the weak links in developing these models has been the difficulty in creating a finite element model. For this reason, initial efforts focused on the plain weave composite. However, tools and techniques have improved and now 3D models have been developed for a variety of textiles. The goal of this work is to understand linear and non-linear behaviors of textile composites. To achieve that, different analyses like linear stress analysis, plasticity and material damage induced non-linearity are proposed for various woven and braided composites. Also, the mechanics of mechanics of load flow in textile composites will be understood using novel post processing.

Linear stress analysis is helpful in gaining some insights about the textile behavior. For example, the effect of various parameters on various in plane and out of plane moduli can be investigated, locations of potential damage spots can be found. But textile composites show considerable non-linear response. The non-linear response could be due to geometric (caused by tow interlacing and tow waviness) or material non-linearity (due to plasticity or progressive damage). This work investigates the linear elastic as well as non-linear behaviors of textile composites. A variety of textile composites like plain weave, twill weave, satin weaves and different braids are analyzed. Below, different proposed analyses for these textile configurations are discussed.

3.1. Linear Elastic Analysis of Stress Concentrations in 2x2 Braided Composites

The fact that tows are interlaced, have undulating and straight regions, and are not orthogonal to each other, causes a complex load path and complex three dimensional

stress distributions even for simple uni-axial loading. A significant concern is whether some stress concentrations appear only due to the peculiarities of a particular geometric approximation. Also, an intuitive understanding of why stress concentrations occur will allow one to attempt to design away or at least reduce the magnitudes.

Various parameters like type of loading, material properties, braid angle and waviness ratio affect the stress distributions in braids. The sensitivity of peaks to braid angle and waviness ratio will be studied. Detailed three dimensional (3D) finite element models will be analyzed to determine the effect of these parameters on stress distributions in braids. Tape laminates are widely used and their analysis can be easily performed and understood by engineers. Unlike tapes, much of the manufacturing can be

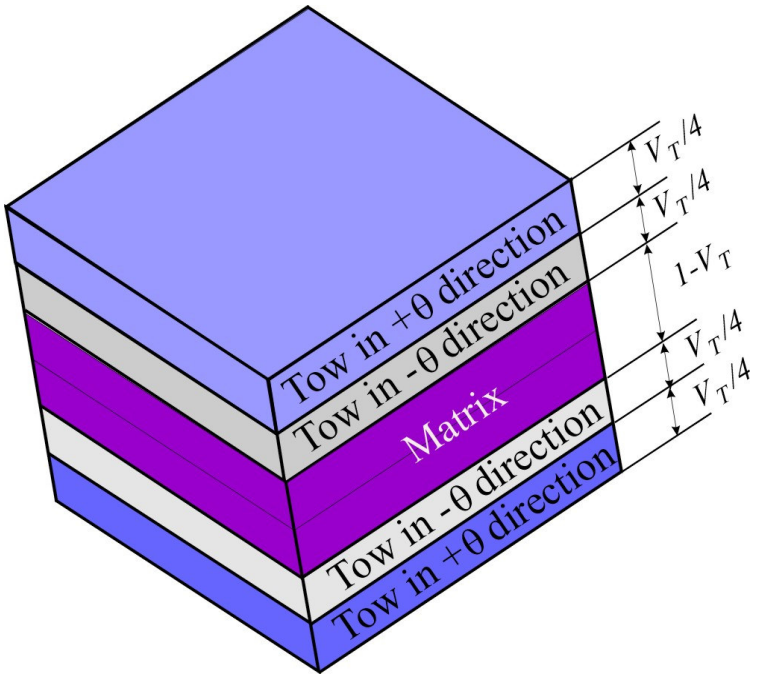

Figure 3.1. An equivalent tape laminate model
(V_T is the combined volume fraction of +θ and –θ tows in the braid model).

automated for braids, so braids have the potential for low cost as compared to tapes. The stress concentrations in braid will be compared with an equivalent tape laminate model. An equivalent tape laminate configuration, as shown in Fig. 3.1, consists of two unidirectional laminas (with properties of the tow) in the $+\theta$ and $-\theta$ directions and a third lamina of matrix to account for matrix pockets in the braid. The layer thicknesses in the laminate model are consistent with the tow and matrix volume fractions in the full 3D model. This will be useful to find out the severity of the peaks in braids as compared to those in an equivalent tape laminate.

Various techniques are used to process the stress distribution data. Stress contours give some surface information about stress distributions. Of course, much of the information is not seen in the contour plots. Stress volume distribution plots are used to characterize the extent of high stress regions. It will be shown that even for simple uni-axial loading, the stress state in braids is fully three-dimensional. The location and magnitude of peak stresses in the tow are predicted. The effect of braid angle on the magnitude of stress concentrations will be investigated. Effect of braid angle constitutes two parts: One is called *orientation effect* and the other is called *phase shift effect* herein. The orientation effect is due to the fact that the braid tows are oriented at angles of $\pm\theta$ to the longitudinal direction. This effect of orientation can easily be eliminated by normalizing with laminate theory results. The other effect is due to the fact that, the material architecture of braids with different braid angles is different, because the tow shape of different braids is different due to phase shift in the undulation (see section 1.2 for details). By matching the loading that a tow of different braids experiences, the orientation effect will be eliminated and the effect of phase shift on stress distribution will be investigated. Finally the variation of stress peaks with waviness ratio (a measure of crimp in tows) will be analyzed.

In summary, the goal of this part of the research will be to perform linear elastic stress analyses and to predict the stress distribution in the tow of a braid, analyze the sensitivity of predicted stress concentrations to various design parameters (braid angle, waviness ratio) and compare the stress distribution with an equivalent tape laminate.

3.2. Effect of Assumed Damage Model on Predicted Damage Evolution in Textile Composites

When excessive load or fatigue cycles are applied, damage initiates and grows in textile composites. To exploit the full potential of these materials, it is necessary to understand how damage initiates and progresses. The knowledge of the stress state that exists both in tows and matrix is required to be able to predict potential damage locations. Detailed 3D finite element models with refined meshes are required to determine the stress distribution and failure behavior.

Using the finite element models, the stress distribution can be predicted both in the tows and in the matrix. Although the moduli predictions are simple, prediction of the stress state is difficult as a full three dimensional stress state exists in the matrix as well as in the tows even for simple uni-axial loading. Hence the stress analysis tends to be complex. Prediction of accurate stress states is critical to predict damage initiation and progression.

Prediction of an accurate stress state is the first step of the challenge. The next one is utilizing this information to predict the damage evolution. Prediction of failure response is more challenging both in terms of computational time and modeling. As discussed earlier, various researchers have proposed different damage models. A damage model degrades the properties by a certain amount when a failure criterion detects occurrence of damage. Most of the models are similar in the sense that they either degrade the stiffness coefficients or increase the compliance coefficients of the tows and matrix after a failure criterion detects the occurrence of a damage mode. These models differ from each other in various ways. The models basically differ in terms of the degradation factors used for changing the stiffness or compliance coefficients. Secondly, some degrade only the diagonal entries in the compliance or stiffness matrix and some affect the off-diagonal terms also [28, 38-43]. Another difference between damage models is whether the matrix, which was isotropic initially, is considered anisotropic or not after damage. Some of the models are based on experimental observations while

some have only a theoretical basis. A comparison of some of the damage models available in the literature will be provided.

This work has two goals. One is to present a framework to allow use of a wide variety of damage initiation and growth models. Some of the damage models available in the literature and their salient feature will be compared. All the models will have a common implementation in terms of degradation of engineering properties to do a meaningful comparison of different models. The second goal is to predict the damage initiation and growth in woven composites using different damage models. The stress strain curves under uni-axial tensile loading will be predicted. Investigations will include analysis of a glass/epoxy and carbon/epoxy plain weave, and a carbon/epoxy twill weave. A comparison of predictions of stress-strain curves using different damage models will be shown. The finite element predictions for all these configurations will be compared with the experimental data. The reasons for differences or similarities between the predictions of different damage models will be explored.

3.3 Plasticity Induced Non-Linearity in 2x2 Braided Composites

Figure 2.4 shows the experimental stress–strain data for ±45˚ and ±25˚ VARTM manufactured [45] carbon/epoxy braids subjected to uni-axial tension in the longitudinal direction. The figure shows the response is highly non-linear. The non-linear response shown by these braids could be due to geometric (caused by tow interlacing and tow waviness) or material non-linearity (due to plasticity or progressive damage). In this work, non-linearity due to the material elastic damage and plasticity will be studied separately.

This part of the study investigates plasticity-induced nonlinearity in braided composites. There are several reasons for this effort. Firstly, conventional matrix materials, e.g. polymers and metals, used to make textile composites exhibit significant inelastic response. Secondly, due to fiber tow interlacing and undulation, the local stress concentrations are significant [74] and could cause matix/tow yielding at low overall stress level. Although such plastic deformation may be contained by the surrounding elastic material, it could be significant in cyclic loading situations.

In this analysis, the effect of plastic deformation on the stress-strain behavior of braided composites will be analyzed using finite element modeling. As illustrated in Fig. 2.1, a two scale modeling approach [47] will be used. The first scale, which is called the *fiber/matrix scale* herein, predicts the effective elastic and plastic properties of the tow from the properties of the constituent fiber and resin. The second scale, which is called the *tow architecture scale* herein, models the braided composite unit cell and utilizes the properties predicted by the first scale for the tow. Plastic deformation at both the scales will be modeled by using Hill's yield function [48] for an orthotropic material. A two-step procedure [47] will be used to determine the orthotropic parameters in the yield function for the tow. First, the effective stress/effective plastic strain relationships under various loading conditions will be obtained by micromechanics analysis of the fiber/matrix unit cell. Then the orthotropic parameters of the tow will be found such that all these effective stress versus effective plastic strain curves collapse into a narrow band around a single curve. A Matlab® [75] optimization utility will be used to determine the orthotropic parameters of the tow, which are material parameters in the Hill's yield function [48] for orthotropic materials. This will involve solving non linear least square problems using the *lsqnonlin* function. The narrow band will then be curve fitted to find parameters in an equation called the master curve [76] equation. The master curve equation is used to fit the yield stress versus effective plastic strain data. This master curve for the tow will then be used at the tow architecture scale to predict the plastic deformation of braided composites.

This modeling approach will be used to predict the behaviors of 2x2 braided composites consisting of AS4 carbon fiber [1] reinforced EPON 9504 epoxy [77] resin, E-glass fiber [1] reinforced EPON 9504 epoxy resin and S-glass fiber [1] reinforced EPON 9504 epoxy resin. The predicted stress-strain response for ±25˚, ±30˚ and ±45˚ carbon/EPON, ±25˚ E-glass/EPON and ±45˚ S-glass/EPON braids will be compared with the experimental data to validate the analysis.

If one is only interested in the macroscopic stress-strain response, it might be worthwhile to analyze an equivalent tape laminate (Fig. 3.1) also which requires only 3

elements and much less computational time. The predictions of equivalent tape laminates will be compared with the full 3D finite element models and experimental data as well. The tape analysis will also be helpful in comparing the performance of braided composites with tape laminates.

In this work, the effect of fiber properties on the plastic behavior of braided composites will also be analyzed. Plasticity induced non-linearity in 2x2 braids under the application of in-plane tensile loading will be analyzed. The two material systems, E-glass/EPON 9540 epoxy and AS4 carbon/EPON 9504 epoxy will be analyzed. Both have the same resin but different fibers so that the effect of fiber properties on the behavior of the braid could be examined. The effect of fiber material will be studied for a ±25˚ braid under uniaxial tensile load along the longitudinal direction.

The macroscopic stress-strain response only gives a quantitative measure of averaged behavior. To obtain insights about the potential damage spots, the effect of plastic deformation on local stress distributions will also be investigated. Development of the plastic zone at different load levels will be analyzed. The difference in stress distribution and plastic zone size due to change in fiber properties will also be discussed. In summary, this part of the research will focus on the following:

1. Validation of the elasto-plastic analysis by comparing the finite element predictions with experimental data.
2. Comparison of the predictions of equivalent tape laminates with full 3D finite element analysis and experimental data.
3. The effect of fiber type on plasticity induced non-linearity in ±25˚ braid. The effects are described in terms of
    - macroscopic stress-strain behavior
    - stress distribution plots
    - plastic zone plots

3.4. Mechanics of Load Flow in Textile Composites

The current 3D models of textile composites give much more information than the simple laminate theory models that were developed initially to understand the

behavior of textile composites. Simple models were based on intuition and provided behavior in terms of basic modes of deformation and load transfer. Simple models make many assumptions about the geometry and behavior and can not provide detailed information like the stress distribution in the tows and resin, effect of tow undulation or failure modes.

The full 3D models attempt to model the geometry as truly as possible and the results are also obtained with a similar lack of bias. Though, full 3D models provide a wealth of raw numerical information, it is difficult to utilize all this information to develop an intuitive understanding of the textile behavior. For example, the stress contours for the 3D stress state in a 5 harness satin weave shown in Fig. 2.2 give many details, but no framework for interpretation.

The focus of this part of the research is to massage the massive output data to understand mechanics of load flow in textile composites. Optimal use of rapidly improving 3D finite element models requires non-standard techniques to interpret the data. In particular, techniques must be developed that not only highlight the important details, but also transform the massive amount of output data into comprehensible modes of behavior. This work will discuss two techniques.

The first technique converts the 3D variation of a stress component into a stress versus volume distribution plot (e.g. Fig. 2.5). This plot reveals how much volume of the material has a stress magnitude larger than a particular value. The plot gives a measure of the non-uniformity of the stress distribution. This is especially useful for assessing whether a local stress concentration is so localized that slight yielding will eliminate the high stress. The other technique is calculation of stress resultants. In approximate models the components of the textile are treated as simple structural elements like rods or beams and stress resultants are used to describe the load flow. The fully three-dimensional finite element results can be postprocessed to obtain stress resultants, such as the axial force or moment in the tow. Fig. 2.6 illustrates typical results for an elastic analysis. It can be seen that both Fx and Fz have highest values where the tow undulation is maximum. Since these stress resultants are obtained from refined models, the results are

much more reliable than one could obtain by using a simplified model. It should be noted that these post processing techniques are not meant to eliminate the details. Instead a hierarchical strategy is proposed that allows interpretation of the predictions at different levels of detail. Also, by providing the "coarse level" interpretation of the results, a better basis is provided for evaluating and refining simpler models. These kind of post-processing are not available in commercial finite element programs.

These techniques can be applied in various ways to investigate textile behavior. First of all, various studies for understanding the mechanics of load flow in a plain weave composite will be conducted. Then the effect of textile architecture on the load flow in equivalent regions of the tow will be examined. Then, the focus will be on describing the effect of plasticity and damage on the volume distribution of stresses and stress resultants in a plain weave composite.

3.5. Summary

Textile composites have found a wide variety of applications in different areas. Due to the availability of a variety of textile architectures and numerous parameters associated with each, optimal design through extensive experimental testing is not practical. Enough predictive tools are not available to perform virtual experiments of various options. This work will focus on understanding various linear and non-linear behaviors and mechanics of load flow in textile composites.

4. THEORY AND EQUATIONS

In this work, the linear elastic as well as non-linear behaviors of textile composites were analyzed. The non-linear behavior can be caused by geometric non-linearity (tow undulation) or material non-linearity (due to plasticity or damage). Here non-linear behavior due to plasticity and damage initiation and progression were analyzed. The theory of the analysis and equations involved are discussed below. The finite element formulation is also discussed below.

For any boundary value problem, the following four sets of equations are necessary.

1. Equations of equilibrium
2. Kinematics (strain-displacement relations)
3. Constitutive relations
4. Boundary conditions

The equations of equilibrium, kinematics and boundary conditions are the same for all the analyses conducted in this work. But the constitutive relations are quite different. Below, first the equations of equilibrium, kinematics and boundary conditions for any 3D analysis are discussed. Then the constitutive relations for linear elastic analysis and the finite element formulation are discussed. Later, the constitutive equations for damage initiation and progression as well as for plasticity are discussed. In the equations below, a repeated index is a dummy index and denotes summation and a non-repeated index denotes a free index. A comma denotes a partial derivative with respect the coordinate *x*. For example, let ϕ, a_i and σ_{ij} be a scalar, vector and a tensor, respectively, then:

$$\phi_{,j} = \frac{\partial \phi}{\partial x_j}, \quad a_{i,j} = \frac{\partial a_i}{\partial x_j} \quad \text{and} \quad \sigma_{ij,j} = \frac{\partial \sigma_{ij}}{\partial x_j} \tag{4.1}$$

4.1. Equations of Equilibrium

Considering a general 3D body with volume V bounded by the surface S, the static equilibrium equation can be written as

$$\sigma_{ji,j} + f_i = 0 \tag{4.2}$$

where f_i are the body forces. In the absence of body moments, the conservation of angular momentum requires symmetry of the stress tensor, that is

$$\sigma_{ji} = \sigma_{ij} \tag{4.3}$$

4.2. Kinematics (Strain-Displacement Relations)

In this work, infinitesimal strains were used and for infinitesimal strain, the strain-displacement relation is

$$\varepsilon_{ij} = \frac{1}{2}(u_{i,j} + u_{j,i}) \tag{4.4}$$

4.3. Constitutive Relations

For a linear elastic material, the stress-strain relationships for the material are given by Hooke's Law:

$$\begin{aligned} &\sigma_{ij} = C_{ijkl}\varepsilon_{kl} \\ \text{or} \qquad &\varepsilon_{ij} = S_{ijkl}\sigma_{kl} \end{aligned} \tag{4.5}$$

where C is fourth order stiffness tensor and is inverse of fourth order compliance tensor S. If the components of 2nd order stress and strain tensors are written using Voight's notation as:

$$\varepsilon_i = \begin{Bmatrix} \varepsilon_{11} \\ \varepsilon_{22} \\ \varepsilon_{33} \\ \varepsilon_{12} \\ \varepsilon_{23} \\ \varepsilon_{13} \end{Bmatrix}, \qquad \sigma_i = \begin{Bmatrix} \sigma_{11} \\ \sigma_{22} \\ \sigma_{33} \\ \sigma_{12} \\ \sigma_{23} \\ \sigma_{13} \end{Bmatrix} \tag{4.6}$$

then the stress-strain relationships can be written as

$$\begin{aligned} \sigma_i &= C_{ij}\varepsilon_j \\ \text{or} \qquad \varepsilon_i &= S_{ij}\sigma_j \end{aligned} \tag{4.7}$$

where C_{ij} and S_{ij} are the second order stiffness and compliance tensors respectively and are given as:

$$S_{ij} = \begin{bmatrix} \frac{1}{E_{11}} & \frac{-\upsilon_{12}}{E_{11}} & \frac{-\upsilon_{13}}{E_{11}} & 0 & 0 & 0 \\ \frac{-\upsilon_{21}}{E_{22}} & \frac{1}{E_{22}} & \frac{-\upsilon_{23}}{E_{22}} & 0 & 0 & 0 \\ \frac{-\upsilon_{31}}{E_{33}} & \frac{-\upsilon_{32}}{E_{33}} & \frac{1}{E_{33}} & 0 & 0 & 0 \\ 0 & 0 & 0 & \frac{1}{G_{12}} & 0 & 0 \\ 0 & 0 & 0 & 0 & \frac{1}{G_{23}} & 0 \\ 0 & 0 & 0 & 0 & 0 & \frac{1}{G_{31}} \end{bmatrix} \tag{4.8}$$

and $$C_{ij} = S_{ij}^{-1}$$

4.4. Boundary Conditions

The traction boundary conditions are given as

$$T_i = \sigma_{ij} n_j \text{ on S} \tag{4.9}$$

and the displacement boundary conditions are given as

$$u_i = \hat{u} \text{ on } \hat{\text{S}} \tag{4.10}$$

where $\hat{u}$ is the specified displacement on the boundary $\hat{\text{S}}$.

As discussed earlier in the introduction chapter, textile composites have periodic microstructure. Later, we will see that for analyses involving periodic microstructures, the periodic boundary conditions involving multi point constraint relationships were used.

4.5. Statement of Virtual Work Principle

To obtain the statement of virtual work, equations of equilibrium are multiplied by an arbitrary virtual displacement, and are integrated over the volume to obtain the total virtual work for the body,

$$\int_V (\sigma_{ji,j} + f_i)\delta u_i dV = 0 \tag{4.11}$$

or

$$\int_V \sigma_{ji,j}\delta u_i dV + \int_V f_i \delta u_i dV = 0 \tag{4.12}$$

The first term can be written as

$$\int_V (\sigma_{ji}\delta u_i)_{,j}\, dV = \int_V \sigma_{ji,j}\delta u_i dV + \int_V \sigma_{ji}(\delta u_i)_{,j}\, dV \tag{4.13}$$

The first term on the right hand side will be written as

$$\int_V \sigma_{ji,j}\delta u_i dV = \int_V (\sigma_{ji}\delta u_i)_{,j}\, dV - \int_V \sigma_{ji}(\delta u_i)_{,j}\, dV \tag{4.14}$$

But,

$$\int_V (\sigma_{ji}\delta u_i)_{,j}\, dV = \int_S \sigma_{ji}\delta u_i n_j dS \tag{4.15}$$

Therefore Eqn. (4.12) can be written as

$$\int_V \sigma_{ji}(\delta u_i)_{,j}\, dV = \int_V f_i \delta u_i dV + \int_S \sigma_{ji}\delta u_i n_j dS \tag{4.16}$$

Using Eqn. (4.9)

$$\int_V \sigma_{ji}(\delta u_i)_{,j}\, dV = \int_V f_i \delta u_i dV + \int_S T_i \delta u_i dS \tag{4.17}$$

Now we will use infinitesimal strain-displacement relations to express $(\delta u_i)_{,j}$ as:

$$\frac{\partial \delta u_i}{\partial x_j} = \delta\left(\frac{\partial u_i}{\partial x_j}\right) = \delta\left(\frac{1}{2}\frac{\partial u_i}{\partial x_j} + \frac{1}{2}\frac{\partial u_j}{\partial x_j}\right) = \delta\varepsilon_{ij} \tag{4.18}$$

By inserting Eqn. (4.18) into Eqn. (4.17), the principle of virtual work statement is obtained as

$$\int_V \sigma_{ji}\delta\varepsilon_{ij} dV = \int_V f_i \delta u_i dV + \int_S T_i \delta u_i dS \tag{4.19}$$

That is, the statement of the virtual work principle is

$$\delta W = \delta W^{\text{int}} + \delta W^{ext} = 0 \tag{4.20}$$

where $\int_V \sigma_{ji}\delta\varepsilon_{ij}dV$ is the internal virtual work and $-\int_V f_i\delta u_i dV - \int_S T_i\delta u_i dS$ is the external virtual work.

If Voigt notation is used for stresses and strains, then the virtual work statement can be written as:

$$\int_V \sigma_k\delta\varepsilon_k dV - \int_V f_i\delta u_i dV - \int_S T_i\delta u_i dS = 0,\ \ i = 1..3,\ k = 1..6 \tag{4.21}$$

4.6. Virtual Work Statement: Discrete Form

One assumes a displacement field over the element in terms of nodal displacement u_i^{α}. The subscript *i* denotes the coordinate directions and the superscript α=1..n where n is the number of nodes per element.

The displacement can be expressed in terms of interpolation functions.

$$u_i = N^{\alpha}u_i^{\alpha} \tag{4.22}$$

where N^{α} are the interpolation functions. Equation (4.21) can be expressed in matrix form as

$$\int_V \{\delta\varepsilon\}^T\{\sigma\}dV = \int_V \{\delta q\}^T\{f\}dV + \int_S \{\delta q\}^T\{T\}dS \tag{4.23}$$

where $\{q\}$ is the vector of elemental nodal displacements and is given as:

$$\{q\} = \{u_1^1,\ u_2^1,\ u_3^1,\ .....u_1^{\alpha},\ u_2^{\alpha},\ u_3^{\alpha},\ .....\} \tag{4.24}$$

where the superscript α indicates the node number. In this work, 20 node hexahedral brick elements were used. Each node has three degrees of freedom, which are displacements u_1, u_2 and u_3 along three coordinate directions.

Substituting the stress-strain relation, $\{\sigma\} = [C]\{\varepsilon\}$, in Eqn. (4.23) gives

$$\int_V \{\delta\varepsilon\}^T[C]\{\varepsilon\}dV = \int_V \{\delta q\}^T\{f\}dV + \int_S \{\delta q\}^T\{T\}dS \tag{4.25}$$

The strain vector $\{\varepsilon\}$ can be written as

$$\{\varepsilon\} = [B]\{q\} \tag{4.26}$$

where [B] is defined by

$$[B] = \begin{bmatrix} \frac{\partial N_i}{\partial x} & 0 & 0 \\ 0 & \frac{\partial N_i}{\partial y} & 0 \\ 0 & 0 & \frac{\partial N_i}{\partial z} \\ \frac{\partial N_i}{\partial y} & \frac{\partial N_i}{\partial x} & 0 \\ 0 & \frac{\partial N_i}{\partial z} & \frac{\partial N_i}{\partial y} \\ \frac{\partial N_i}{\partial z} & 0 & \frac{\partial N_i}{\partial x} \end{bmatrix}$$

Using Eqn. (4.26), Eqn. (4.25) can be written as

$$\delta q^T (\int_V [B]^T [C][B] dV \{q\} - \int_V \{f\} dV + \int_S \{T\} dS \ ) = 0 \tag{4.27}$$

Since Eqn. (4.27) holds for any arbitrary nonzero selection of $\{\delta q\}$, this equation becomes

$$\int_V [B]^T [C][B] dV \{q\} = \int_V \{f\} dV + \int_S \{T\} dS \ ) \tag{4.28}$$

The finite element equations can be written as

$$[\mathrm{K}^e]\{\mathrm{q}^e\} = \{\mathrm{F}^e\} \tag{4.29}$$

where the element stiffness matrix is

$$[\mathrm{K}^e] = \int_V [B]^T [C][B] dV \tag{4.30}$$

and the element load vector is

$$\{F^e\} = \int_V \{f\} dV + \int_S \{T\} dS \tag{4.31}$$

Assembling the element stiffness matrices and the load vector yields

$$[\mathrm{K}]\{\mathrm{q}\} = \{\mathrm{F}\} \tag{4.32}$$

where [K] is the global stiffness matrix, $\{q\}$ is the global displacement vector, and $\{F\}$ is the global load vector.

This completes the theory and equations for the linear elastic analysis.

4.7. Boundary Conditions for Periodic Microstructures

For periodic structures, homogenized properties of the structure can be obtained by analyzing a representative volume element (RVE). The response of the RVE is volume averaged to obtain the effective properties. The periodic conditions state that the displacements of one unit cell differ from other unit cells only by a constant offset, which depends on the volume averaged displacement gradients [35-36]. Further, the strains and stresses are identical in all of the unit cells. This can be expressed as

$$u_i(x_\alpha + d_\alpha) = u_i(x_\alpha) + \left\langle \frac{\partial u_i}{\partial x_\beta} \right\rangle d_\beta \tag{4.33}$$

$$\varepsilon_{ij}(x_\alpha + d_\alpha) = \varepsilon_{ij}(x_\alpha) \tag{4.34}$$

$$\sigma_{ij}(x_\alpha + d_\alpha) = \sigma_{ij}(x_\alpha) \tag{4.35}$$

where d_β is a vector of periodicity [35-36]. The vector of periodicity is a vector from a point in one unit cell to an equivalent point in an adjacent unit cell.

If the RVE is a full unit cell, then boundary conditions can be obtained by exploiting periodicity. But, for textile composites, the number of degrees of freedom for a full unit cell model can be quite large. Tremendous savings can occur if we are able to reduce the size of the analysis region from a full unit cell to half or less. This is especially true for non-linear analyses like the problem at hand. Symmetry within the unit cell can be exploited to reduce the analysis region to part of the unit cell. The concept of *Equivalent Coordinate Systems* is useful in identifying the symmetries and constraint conditions [35-36]. Coordinate systems are equivalent if the geometry, spatial distribution of material, loading, and the various fields that describe the response (e.g., displacement, strains etc.) are identical in the two systems [35-36]. Some symmetries are destroyed by combined loading though. Periodicity and symmetry conditions were exploited to derive boundary conditions in this work. For the *fiber/matrix scale*, one-fourth of the unit cell was analyzed for obtaining linear elastic properties of the tow. For

plastic properties combined loading were imposed on the fiber/matrix scale and hence, symmetries could not be exploited and only periodicity was used to analyze the full unit cell. For the *tow architecture scale,* periodicity as well as symmetry was used and the analysis region was reduced to one half of the unit cell for simple stacking and one fourth of the unit cell for symmetric stacking of the mats for braids. Depending upon the weave type, the analysis region was reduced to one half or smaller region of the unit cell. For plain weave, sometimes the analysis region could be reduced to as small as 1/32nd part of the full unit cell.

4.8. Theory and Equations for Damage Initiation and Progression

A classical approach as shown in Fig. 4.1 was adopted for predicting damage initiation and progression. A particular load is applied initially. The stresses were computed at all 27 Gauss quadrature points for all elements. The initial load is scaled

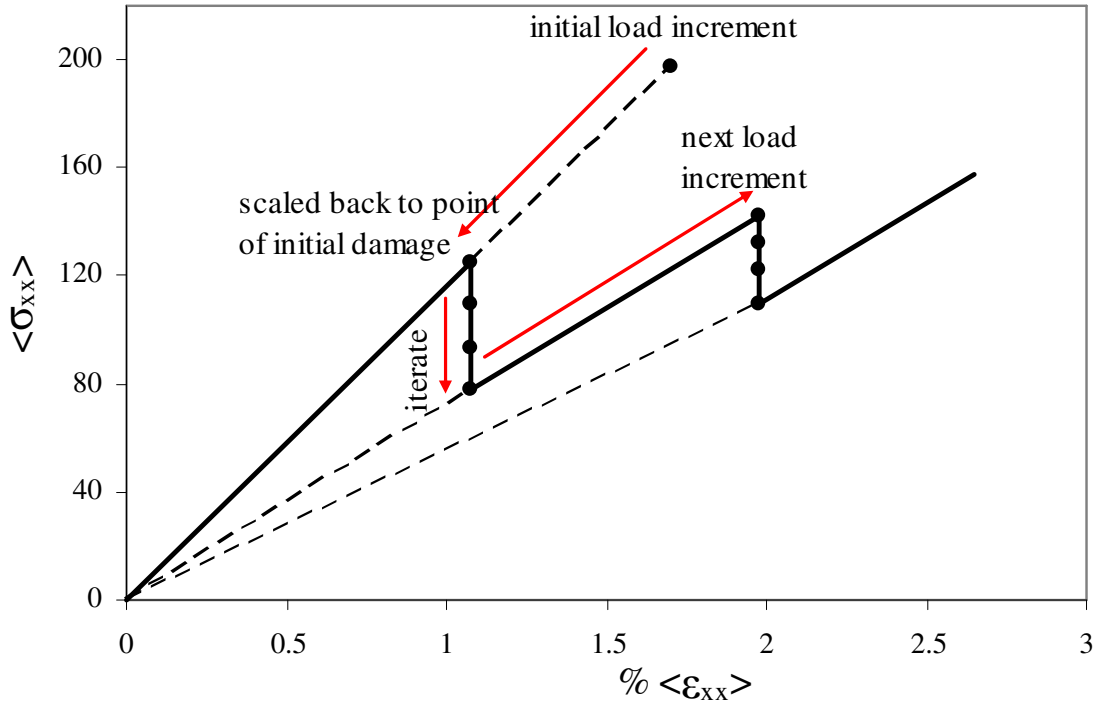

Figure 4.1. Procedure for predicting damage initiation and progression.

back or forth to the point of initial damage, which is defined by the load point when at least one Gauss quadrature point fails. The failure is determined by the evaluation of a damage criterion both for matrix and tows. When the stresses at any Gauss point exceeded the strength, the elastic properties at that Gauss point were degraded. After degrading the properties, the analysis was conducted again at the same load level to calculate redistributed stresses. This procedure was iterated until no further failure occurred and the model was in equilibrium. Then we go to the next load increment and repeat this procedure. This way, we are constantly moving in the load history and getting the stress-strain response of the composite as shown in Fig. 4.1. Note that a linear elastic analysis is conducted at each load step, and the properties at the Gauss quadrature points change during each iteration. The failure of any Gauss quadrature point is determined by pre-specified failure criteria. If any quadrature point fails, the constitutive matrix for that quadrature point is updated. The failure criteria and a typical property degradation model that were used are discussed below.

4.8.1. Failure criteria

Three dimensional heterogeneous FE models that consist of tows and matrix were employed. Tows and matrix were treated macroscopically as anisotropic and isotropic homogeneous bodies, respectively. The fibers are arranged uni directionally within lamina of the tape laminated composites, but they are in the form of fiber bundles in textile composites. The properties of the tow or fiber bundles were homogenized.

For the fibers, one or more damage modes, such as fiber breaking and transverse cracking, can take place. These modes strongly affect the mechanical behavior of the structure. The anisotropic damage model for fibers and the isotropic damage model for matrix were utilized to simulate the microscopic damage propagation and thus to characterize the damage modes.

Different failure criteria were used for transversely isotropic and isotropic materials. The maximum principal stress criterion is used for the matrix. The matrix is considered to be anisotropic after first failure is detected. For tows, the maximum stress criterion for anisotropic materials was used, which says that the failure occurs when any

of the stress components in the material coordinates exceeds its corresponding strength i.e. for tow, failure occurs when $\sigma_{ij} / S_{ij} > 1$ in the material coordinate system.

4.8.2. Property degradation scheme

Most of the property degradations models are common in the sense that they degrade the engineering properties whenever failure is detected at any quadrature point. If we relate the stresses and strains at any material point using the following compliance matrix,

$$\varepsilon_i = S_{ij}\sigma_j$$

$$S_{ij} = \begin{bmatrix} \frac{1}{E_{11}} & \frac{-\upsilon_{12}}{E_{11}} & \frac{-\upsilon_{13}}{E_{11}} & 0 & 0 & 0 \\ \frac{-\upsilon_{21}}{E_{22}} & \frac{1}{E_{22}} & \frac{-\upsilon_{23}}{E_{22}} & 0 & 0 & 0 \\ \frac{-\upsilon_{31}}{E_{33}} & \frac{-\upsilon_{32}}{E_{33}} & \frac{1}{E_{33}} & 0 & 0 & 0 \\ 0 & 0 & 0 & \frac{1}{G_{12}} & 0 & 0 \\ 0 & 0 & 0 & 0 & \frac{1}{G_{23}} & 0 \\ 0 & 0 & 0 & 0 & 0 & \frac{1}{G_{31}} \end{bmatrix} \tag{4.36}$$

Let E, G and ν be the original extensional moduli, shear moduli and Poisson's ratio respectively and $\overline{\mathrm{E}}, \overline{\mathrm{G}}$ and $\overline{\nu}$ are the degraded extensional moduli, shear moduli and Poisson's ratio respectively. Also let a_i (i = 1..9) are the damage factors, which specify the amount of degradation. Then a typical property degradation scheme will look like:

$$\begin{aligned} &\overline{E_{11}} = E_{11} / a_1, \quad \overline{E_{22}} = E_{22} / a_2, \quad \overline{E_{33}} = E_{33} / a_3 \\ &\overline{G_{12}} = G_{12} / a_4, \quad \overline{G_{23}} = G_{23} / a_5, \quad \overline{G_{13}} = G_{13} / a_6 \\ &\overline{\upsilon_{12}} = \upsilon_{12} / a_7, \quad \overline{\upsilon_{23}} = \upsilon_{23} / a_8, \quad \overline{\upsilon_{13}} = \upsilon_{13} / a_9 \end{aligned} \tag{4.37}$$

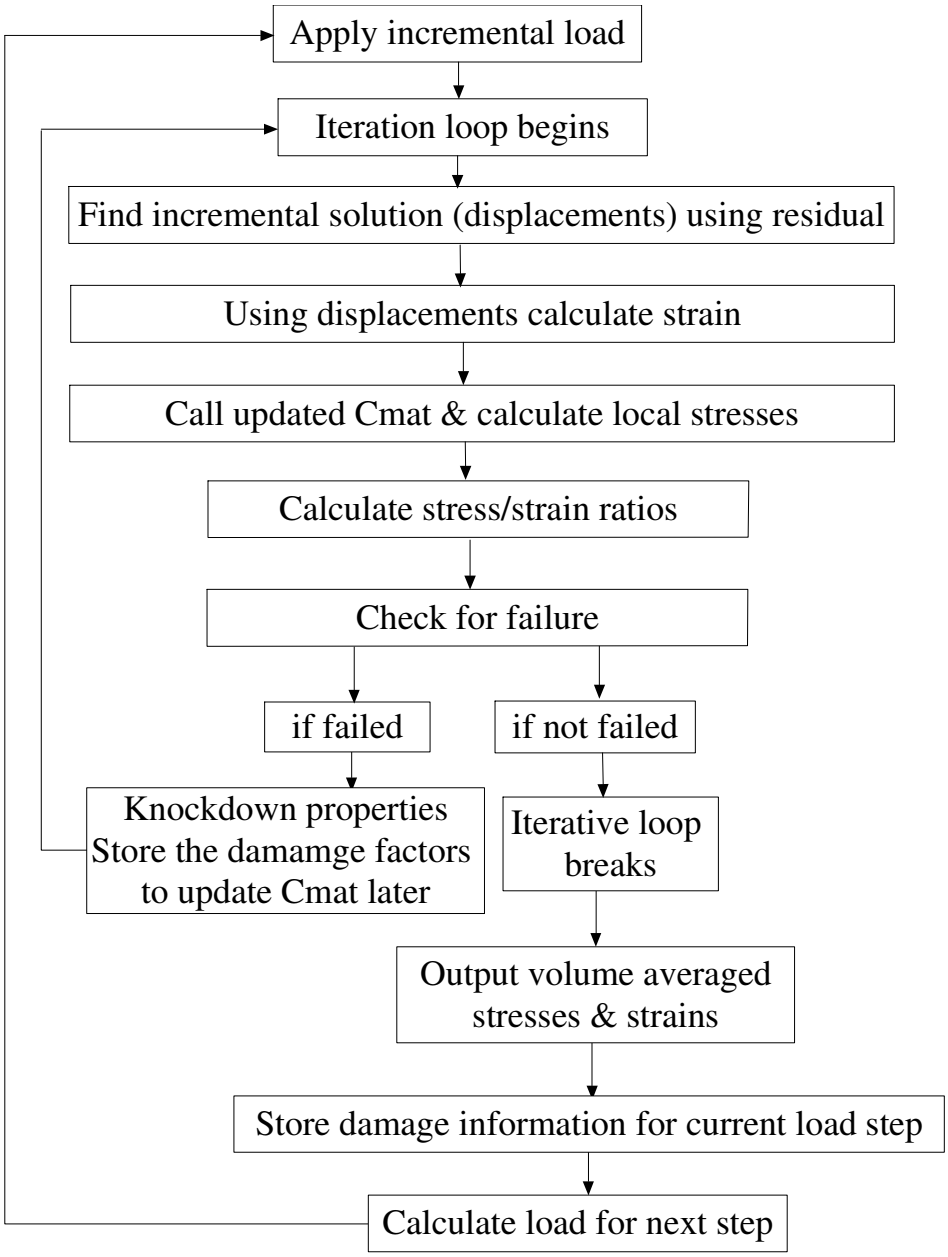

Figure 4.2. Flow chart for finite element implementation of damage analysis.

As an example, if a_1 =8, that implies that the E_{11} modulus is decreased by a factor of 8 from its current value if the material point fails. Note that in this general framework, diagonal as well as non-diagonal entries of the compliance matrix can be affected independently. In this work, various property degradation schemes were implemented and analyzed. The details of property degradation models will be given in chapter VI. A flow chart showing finite element implementation of damage analysis is shown in Fig. 4.2.

4.9. Theory and Equations for Plasticity Analysis

All the theory and equations involved in the plasticity analysis are discussed below.

4.9.1. Strain decomposition

Figure 4.3 shows a schematic of stress-strain curve which might be obtained from the uniaxial loading of a material. At a particular stress level σ_y at point A, the material yields and its modulus drops, the material starts to harden after this yielding. After the yield point, although the modulus of the material has decreased, the behavior is called hardening because the stress is increasing relative to perfectly plastic behavior [78].

The perfect plastic behavior is also shown in Fig. 4.3 and in that case, the strain in the material will keep on increasing at the yield point without any increase in stress. In case the material is hardening and we start unloading lets say at a point B, the material will stop deforming plastically (assuming no time dependent phenomenon), and will show a linearly decreasing stress, whose slope would be the same as the loading curve. The slope of the unloading curve is the Young's modulus E. When at point C, a state of zero stress is reached, we will have some permanent deformation in the material. The remaining strain is called plastic strain and the recovered strain is elastic strain [78].

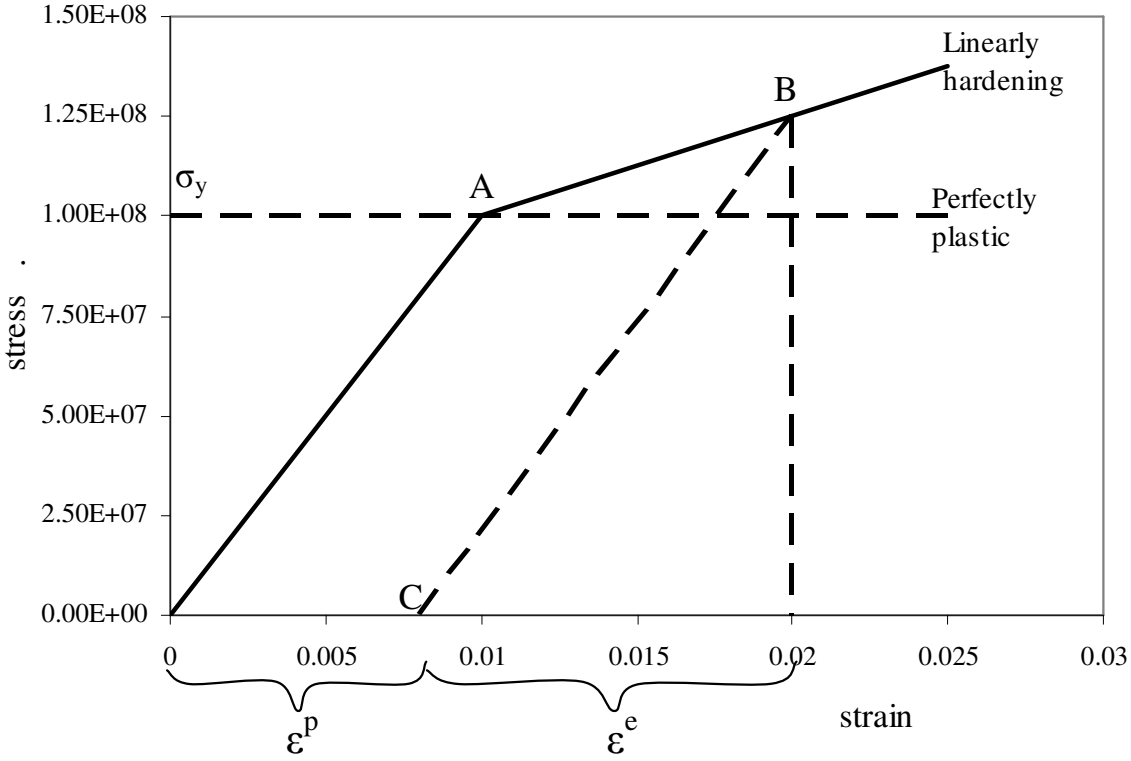

Figure 4.3. Schematic of stress-strain curve for a material with plastic yielding.

The total strain in the material, at any point of loading is sum of elastic and plastic components, i.e.

$$\varepsilon = \varepsilon^e + \varepsilon^p \tag{4.38}$$

This is called classical additive decomposition of plasticity [78]

4.9.2. Stress-strain relationship

It is obvious from Fig. 1 that the stress at any strain level ε is given by

$$\sigma = E\varepsilon^e = E(\varepsilon - \varepsilon^p) \tag{4.39}$$

and the incremental stress-strain relationship is given by:

$$d\sigma = Ed\varepsilon^e = E(d\varepsilon - d\varepsilon^p) \tag{4.40}$$

In the textile composite analysis, the state of stress in the tows and matrix is fully 3D, and the incremental stress strain relationship is written as:

$$d\sigma_{ij} = C_{ijkl}\left(d\varepsilon_{ij} - d\varepsilon_{ij}^{p}\right) \tag{4.41}$$

where C is the fourth order stiffness tensor.

4.9.3. Incompressibility condition

Experiments have shown that the plastic deformation in any material takes place without volume change. Due to this, the sum of the normal plastic strain components is zero.i.e.

$$d\varepsilon_{kk}^{p} = d\varepsilon_{11}^{p} + d\varepsilon_{22}^{p} + d\varepsilon_{33}^{p} = 0 \tag{4.42}$$

The deviatoric plastic tensor is defined as the plastic strain tensor minus the mean plastic strain or hydrostatic plastic strain tensor. Since the hydrostatic part is zero due to the incompressibility condition, the deviatoric plastic strain and plastic strain tensors are equal.

4.9.4. Effective stress and plastic strain rate

To identify at what stress level, the yielding will occur is straightforward in the case of monotonically increasing load in a uniaxial test.
For example,

$$\begin{aligned} &\text{If } \sigma < \sigma_y, \text{ the material is elastic} \\ &\text{and if } \sigma \geq \sigma_y, \text{ the material has yielded.} \end{aligned} \tag{4.43}$$

This relationship is not as simple for isotropic matrix that has a multi-axial stress state or for tows in textile composites, which are transversely isotropic and have a full 3D stress state. In the case of an isotropic matrix, a whole range of yield criteria exists. The Von-Mises yield criterion is quite common and is based on the calculation of an effective stress, which is defined as follow [78]:

$$\sigma_e = \sqrt{\frac{3}{2}(\sigma_{11}^2 + \sigma_{22}^2 + \sigma_{33}^2 + 2\sigma_{12}^2 + 2\sigma_{23}^2 + 2\sigma_{31}^2)} \tag{4.44}$$

Here σ_{ij} are the components of 3D stress state in the matrix. The effective stress σ_e is a scalar quantity and its origin lies in the postulate that yielding occurs when material reaches a critical shear energy [78].

Similarly, the state of plastic strain can be fully 3D and an effective plastic strain can be defined as [78]:

$$d\bar{\varepsilon}^p = \sqrt{\frac{2}{9}\left[(d\varepsilon_1^p - d\varepsilon_2^p) + (d\varepsilon_2^p - d\varepsilon_3^p) + (d\varepsilon_3^p - d\varepsilon_1^p)\right]} \tag{4.45}$$

If σ'_{ij} is the deviatoric stress tensor and is defined as

$$\begin{aligned} \sigma'_{ij} &= \sigma_{ij} - \frac{1}{3}\sigma_{kk}\delta_{ij} \\ d\varepsilon_{ij}^{p'} &= d\varepsilon_{ij}^p - \frac{1}{3}d\varepsilon_{kk}^p\delta_{ij} \\ &= d\varepsilon_{ij}^p \quad \text{(because } d\varepsilon_{kk}^p = 0 \text{ from incompressibility)} \end{aligned} \tag{4.46}$$

then the effective stress and effective plastic strain can be conveniently written as:

$$\bar{\sigma} = \sqrt{\frac{3}{2}\sigma'_{ij}.\sigma'_{ij}} \tag{4.47}$$

$$d\bar{\varepsilon}^p = \sqrt{\frac{2}{3}d\varepsilon_{ij}^{p'}d\varepsilon_{ij}^{p'}} = \sqrt{\frac{2}{3}d\varepsilon_{ij}^p d\varepsilon_{ij}^p} \tag{4.48}$$

It must be noted that, in the case of uniaxial loading, the effective stress can be shown to be equal to the uniaxial stress and the effective plastic strain to be equal to the uniaxial plastic strain.

When stress and strain are fully 3D, the effective plastic strain can be calculated from the definition of plastic work.

Based on increment of plastic work per unit volume, the effective stress, $\bar{\sigma}$ and effective plastic strain, $\bar{\varepsilon}^p$, are defined based on the increment of plastic work per unit volume [47-49]

$$dW^p = \sigma_{ij}d\varepsilon_{ij}^p = \bar{\sigma}d\bar{\varepsilon}^p \tag{4.49}$$

$$\Rightarrow d\bar{\varepsilon}^p = \frac{\sigma_{ij}d\varepsilon_{ij}^p}{\bar{\sigma}(\sigma)} \tag{4.50}$$

4.9.5. Yield criterion

The Hill's yield function [47-49] has been successfully used by many researchers for modeling fibrous composites [50-51, 54] and was used herein to describe the plastic behavior of fiber tow with matrix. Since matrix is elasto-plastic and a constituent in tow, the tow also behaves elasto-plastically.

The yield function f for orthotropic materials can be described as:

$$f(\sigma, \bar{\varepsilon}^p) = \bar{\sigma}(\sigma) - \sigma_y(\bar{\varepsilon}^p), \quad \text{where} \tag{4.51}$$

$$\bar{\sigma} = \sqrt{\frac{3}{2}\left[F(\sigma_{22}-\sigma_{33})^2 + G(\sigma_{33}-\sigma_{11})^2 + H(\sigma_{11}-\sigma_{22})^2 + 2L\sigma_{23}{}^2 + 2M\sigma_{31}{}^2 + 2N\sigma_{12}{}^2 \right]}$$

$$\bar{\sigma} = \sqrt{3 f_h}, \tag{4.52}$$

$$f_h(\sigma_{ij}) = \frac{1}{2}\left[F(\sigma_{22}-\sigma_{33})^2 + G(\sigma_{33}-\sigma_{11})^2 + H(\sigma_{11}-\sigma_{22})^2 + 2L\sigma_{23}{}^2 + 2M\sigma_{31}{}^2 + 2N\sigma_{12}{}^2 \right] \tag{4.53}$$

σ_y is the yield stress. If the material is hardening, the yield stress is a function of effective plastic strain, $\bar{\varepsilon}^p$.

The F, G, H, L, M and N are *orthotropic parameters*. For the resin, which is isotropic, F = G = H = 1 and L = M = N = 3 and it can be shown that $\bar{\sigma}$ reduces to

$\bar{\sigma} = \sqrt{\frac{3}{2}\sigma'_{ij}\sigma'_{ij}}$, which is the Von-Mises effective stress (see Eqn (4.47)).

For the transversely isotropic tow, it can be shown that G = H and M = N [47-49]. Without loss of generality, let L = 1. Therefore, only three orthotropic parameters, F, G and M, need to be determined by either experiment or micromechanics analysis.

4.9.6. Normality condition

The normality condition enables us to determine the direction in which the plastic flow occurs. The associated flow rule states that the increment in plastic strain tensor is in a direction that is normal to the tangent to the yield surface at the point of load (see Fig. 4.4).

$$d\varepsilon_{ij}^p = \frac{\partial f}{\partial \sigma_{ij}} d\lambda \tag{4.54}$$

Here $\frac{\partial f}{\partial \sigma_{ij}}$ gives the direction of the plastic strain increment and $d\lambda$ gives the magnitude of incremental plastic strain. $d\lambda$ is called the plastic multiplier or consistency parameter.

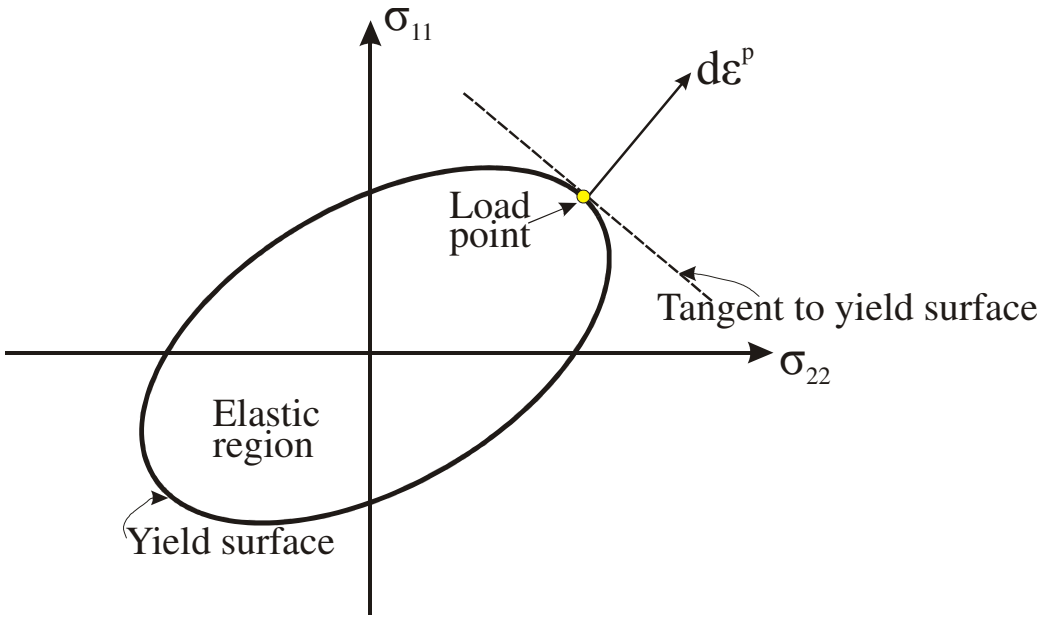

Figure 4.4. Direction of plastic flow is normal to the yield surface at the load point.

4.9.7. Consistency condition

The requirement that the load point (see Fig. 4.4) has to stay on the yield surface is called the consistency condition [78]. The condition enables us to calculate the plastic multiplier or the magnitude of incremental plastic strain.

The yield function has dependence on the current state of the stress and effective plastic strain (because the yield stress depends on plastic strain due to hardening). Equation 4.51 states that,

$$f(\sigma, \bar{\varepsilon}^p) = \bar{\sigma}(\sigma) - \sigma_y(\bar{\varepsilon}^p)$$

The consistency condition is written for incremental changes in stress and effective plastic strain as:

$$f(\sigma_{ij} + d\sigma_{ij}, \bar{\varepsilon}^p + d\bar{\varepsilon}^p) = 0 \tag{4.55}$$

$$df = \frac{\partial f}{\partial \sigma_{ij}} d\sigma_{ij} + \frac{\partial f}{\partial \bar{\varepsilon}^p} d\bar{\varepsilon}^p = 0 \tag{4.56}$$

$$\Rightarrow \frac{\partial f}{\partial \sigma_{ij}} d\sigma_{ij} + \frac{\partial f}{\partial \sigma_y} \frac{\partial \sigma_y}{\partial \bar{\varepsilon}_p} d\bar{\varepsilon}_p = 0 \tag{4.57}$$

Substituting incremental stress-strain relationships $d\sigma_{ij} = C_{ijkl}\left(d\varepsilon_{ij} - d\varepsilon_{ij}^p\right)$ from Eqn. (4.41) into the above equation, we obtain:

$$\frac{\partial f}{\partial \sigma_{ij}} C_{ijkl}\left(d\varepsilon_{ij} - d\varepsilon_{ij}^p\right) + \frac{\partial f}{\partial \sigma_y} \frac{\partial \sigma_y}{\partial \bar{\varepsilon}_p} d\bar{\varepsilon}_p = 0 \tag{4.58}$$

This equation can be expanded as:

$$\left\{\frac{\partial f}{\partial \sigma_{ij}}\right\}^T \left([C]\{d\varepsilon_{ij}\} - [C]\{d\varepsilon_{ij}^p\}\right) + \frac{\partial f}{\partial \sigma_y} \frac{\partial \sigma_y}{\partial \bar{\varepsilon}_p} d\bar{\varepsilon}_p = 0 \tag{4.59}$$

Using associated flow rule $d\varepsilon_{ij}^p = \frac{\partial f}{\partial \sigma_{ij}} d\lambda$, from Eqn. (4.54), the above equation becomes:

$$\left\{\frac{\partial f}{\partial \sigma_{ij}}\right\}^T \left([C]\{d\varepsilon_{ij}\} - [C]\left\{\frac{\partial f}{\partial \sigma_{ij}}\right\} d\lambda\right) + \frac{\partial f}{\partial \sigma_y} \frac{\partial \sigma_y}{\partial \bar{\varepsilon}_p} d\bar{\varepsilon}_p = 0 \tag{4.60}$$

Substituting the associated flow rule $d\varepsilon_{ij}^p = \frac{\partial f}{\partial \sigma_{ij}} d\lambda$ from Eqn. (4.54), into Eqn. (4.50) for incremental plastic strain and effective stress $d\bar{\varepsilon}^p = \frac{\sigma_{ij}}{\bar{\sigma}(\sigma)} d\varepsilon_{ij}^p$, we obtain:

$$d\bar{\varepsilon}^p = \frac{\sigma_{ij}}{\bar{\sigma}(\sigma)} \frac{\partial f}{\partial \sigma_{ij}} d\lambda \tag{4.61}$$

It can easily be shown that the expression $\sigma_{ij} \frac{\partial f}{\partial \sigma_{ij}}$ is equal to the the following:

$$\sigma_{ij}\frac{\partial f}{\partial \sigma_{ij}} = 2f = 2\frac{\bar{\sigma}^2}{3} \tag{4.62}$$

Substituting the above expression in to Eqn. (4.61), we obtain

$$d\bar{\varepsilon}^p = \frac{2\bar{\sigma}}{3}d\lambda \tag{4.63}$$

Substituing this expression in Eqn. (4.60), the consistency condition becomes,

$$\left\{\frac{\partial f}{\partial \sigma_{ij}}\right\}^T \left([C]\{d\varepsilon_{ij}\} - [C]\left\{\frac{\partial f}{\partial \sigma_{ij}}\right\} d\lambda \right) + \frac{\partial f}{\partial \sigma_y}\frac{\partial \sigma_y}{\partial \bar{\varepsilon}_p}\frac{2\bar{\sigma}}{3}d\lambda = 0 \tag{4.64}$$

This gives,

$$d\lambda = \frac{\left\{\frac{\partial f}{\partial \sigma_{ij}}\right\}^T [C]\{d\varepsilon_{ij}\}}{-\frac{2}{3}\bar{\sigma}\frac{\partial f}{\partial \sigma_y}\frac{\partial \sigma_y}{\partial \bar{\varepsilon}_p} + \left\{\frac{\partial f}{\partial \sigma_{ij}}\right\}^T [C]\left\{\frac{\partial f}{\partial \sigma_{ij}}\right\}} \tag{4.65}$$

The expression

$$\text{H} = -\frac{2}{3}\bar{\sigma}\frac{\partial f}{\partial \sigma_y}\frac{\partial \sigma_y}{\partial \bar{\varepsilon}_p} \text{ is defined to be the hardening modulus.} \tag{4.66}$$

Hence $d\lambda$ can be written as:

$$d\lambda = \frac{\{n\}^T [C]\{d\varepsilon\}}{H + \{n\}^T [C]\{n\}} \tag{4.67}$$

$$\text{where } \{\text{n}\} = \left\{\frac{\partial f}{\partial \sigma_{ij}}\right\} \tag{4.68}$$

$\frac{\partial \sigma_y}{\partial \bar{\varepsilon}_p}$ can be calculated from hardening law as shown below.

4.9.8. Isotropic hardening

The yield stress is a function of the amount of plastic strain in the material. A power law [76] was used for hardening, which says that the yield stress is a function of effective plastic strain.

$$\sigma_y(\bar{\varepsilon}^p) = \frac{E\bar{\varepsilon}^p}{\left(1+\left(\frac{E\bar{\varepsilon}^p}{\sigma_0}\right)^n\right)^{\frac{1}{n}}} \tag{4.69}$$

$$\Rightarrow \frac{\partial\sigma_y(\bar{\varepsilon}^p)}{\partial\bar{\varepsilon}^p} = \frac{E}{\left(1+\left(\frac{E\bar{\varepsilon}^p}{\sigma_0}\right)^n\right)^{\frac{1+n}{n}}} \tag{4.70}$$

The Eqn. (4.69) is also called the master curve [76] equation and was used to define the hardening behavior. The E, n and σ_0 (called *master curve parameters* herein) are constants, which were used to fit the yield stress versus effective plastic strain data.

4.10. Summary

The theory of the analysis and equations involved were discussed in this chapter. The necessary equations for any boundary value problem involve equations of equilibrium, kinematics (strain-displacement relations), constitutive relations and boundary conditions. In additions to these relations, constitutive equations for damage initiation and progression as well as for plasticity were discussed.

5. LINEAR ELASTIC ANALYSES OF STRESS CONCENTRATIONS IN 2X2 BRAIDED COMPOSITES

The stress distribution in braided composites is complex even for simple uni-axial loading. The interlacing of the tows creates a complex load path that results in full 3D stress distributions. Various parameters like type of loading, material properties, braid angle (BA) and waviness ratio (WR) affect the stress distributions in braids. The sensitivity of peaks to braid angle and waviness ratio is studied here. Detailed three dimensional (3D) finite element models are analyzed to determine the effect of these parameters on stress distributions in braids. The stress concentrations in braid are compared with an equivalent tape laminate model to find out the severity of the stress peaks in braids as compared to those in an equivalent tape laminate.

Various techniques are used to process the stress distribution data. Stress contours give some surface information about stress distributions. Of course, much of the information is not seen in the contour plots. Stress volume distribution plot is used to characterize the extent of high stress regions. It will be shown that even for simple uni-axial loading, the stress state in braids is fully three-dimensional. The location and magnitude of peak stresses in the tow will be shown. Braid angle changes the magnitude of stress concentrations considerably. It will be shown that this is primarily because of the orientation effect which can be predicted by the laminate theory. By matching the loading that a tow of different braids experiences, this orientation effect is eliminated and the effect of braid angle due to phase shift on stress distribution will be compared. Finally, the variation of stress peaks with waviness ratio is studied.

In summary, the goal of this linear elastic analysis is to predict the stress distribution in the tow of a braid, analyze the sensitivity of predicted stress concentrations to various design parameters (braid angle, waviness ratio) and compare the stress distribution with an equivalent tape laminate.

5.1. Configurations

Figure 5.1 shows an idealized microstructure of a dry mat of a 2x2 braid. The effect of various parameters on the stress distributions in a symmetrically stacked braid was studied. The braid configurations were chosen for studying linear elastic stress distribution because due to phase shift, the architecture of braids is more complex and relatively fewer studies have been conducted for the braids as compared to weaves. The overall fiber volume fraction in the model was assumed to be 50%. The braid angle (BA) is the angle between the axis of the tow and the longitudinal direction of the braid and is shown in Fig. 5.1.

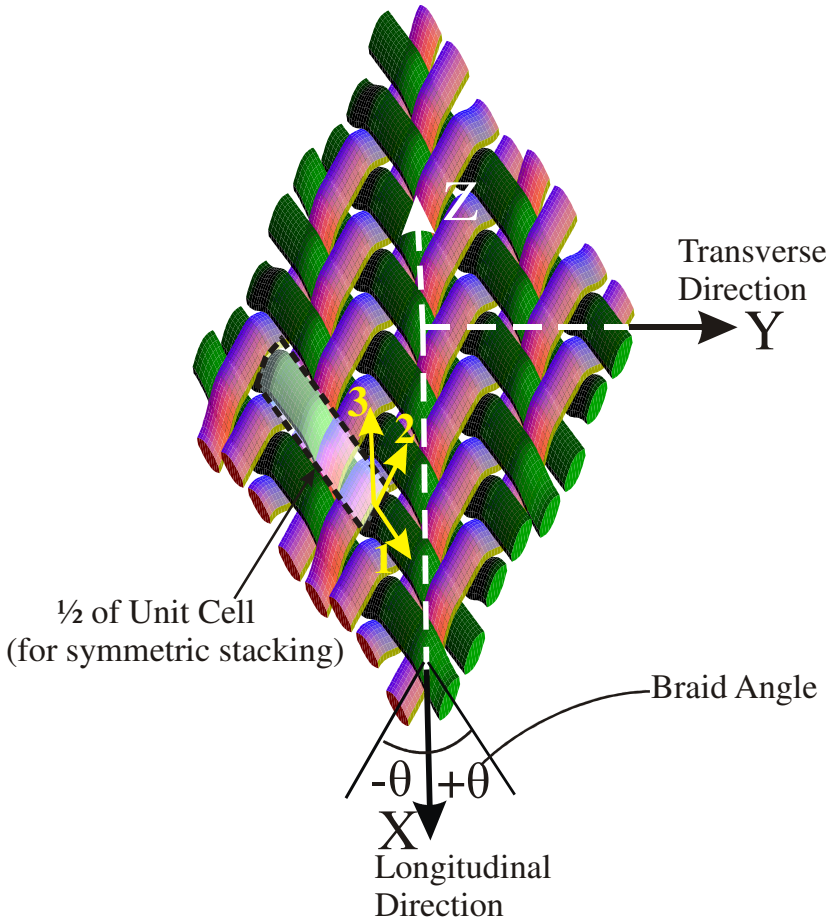

Figure 5.1. Microstructure of a 2x2 braid.

The range of braid angle considered in these studies was ±15˚ to ±65˚. The waviness ratio (WR) is a measure of undulation or crimp in the tows. It is defined as the ratio of the height h to the wavelength λ (Fig. 5.2). Very low (1/20, 1/9), moderate (1/6) and very high (1/3) waviness ratios were considered. Uni-axial loading was applied along the longitudinal direction (see Fig. 5.1). Note that in the following text, XYZ are the global directions and *123* are the material coordinates directions, such that *"1"* is along the fiber. The material coordinate and global directions are shown in Fig. 5.1.

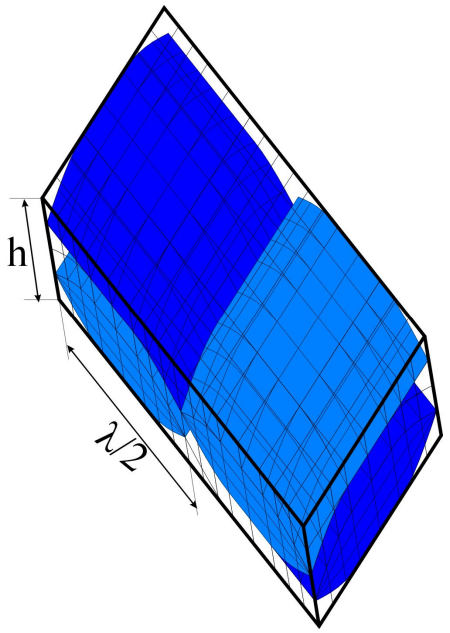

Figure 5.2. Typical finite element model (matrix transparent to reveal architecture), quarter of unit cell (see Fig. 5.1).

The material system used consists of AS4 carbon fibers and EPON epoxy resin. The material properties were taken from refs. [1, 45, 77]. The resin is isotropic with

E=2.96 GPa and υ=0.38. The fiber is transversely isotropic with the following properties: E_{11}=227.53 GPa, $E_{22}=E_{33}$=16.55 GPa, $G_{12}=G_{13}$=24.82 GPa, G_{23}=6.89 GPa, $\upsilon_{12}=\upsilon_{13}$=0.2, and υ_{23}=0.25, where the "1" direction is along the longitudinal axis of the fiber. The symbols E, G and υ refer to extensional modulus, shear modulus and Poisson's ratio respectively. The fibers were assumed to be arranged in a hexagonal array in the tow and the properties of the tow were calculated using finite element based micromechanics. The fiber fraction in the tow was assumed to be 0.69. The properties of the tow were determined to be: E_{11}=157.9 GPa, $E_{22}=E_{33}$=9.088 GPa, $G_{12}=G_{13}$=4.839 GPa, G_{23}=3.276 GPa, $\upsilon_{12}=\upsilon_{13}$=0.251, υ_{23}=0.4117.

A typical finite element model used for the studies consists of 20-node brick elements and is shown in Fig. 5.2. This model is one-fourth of the unit cell and sufficed for analysis because periodicity of the microstructure and mirroring and rotational symmetries within the unit cell were exploited [35-36]. The boundary conditions consist of numerous multipoint constraint relations and are given in ref. [32]. A typical finite element model used in these studies consists of 1152 elements and 5008 nodes.

An equivalent tape laminate model corresponding to each ±θ braid configuration was also used to compare with a braid. The stacking sequence for the laminate model is $[+\theta_{tow}/-\theta_{tow}/0^{\circ}_{resin}]_S$ as shown in Fig. 3.1. In this laminate, four layers [two in +θ direction and two in –θ direction] have properties of the tow and the rest have properties of the matrix to account for matrix pockets in the braid model. The layer thicknesses were consistent with the tow and matrix volume fractions in the braid model. The laminate model was used to quantify the severity of the stresses in the braid as compared to stresses in a corresponding tape laminate. The same amount of load was applied to both the laminate and the braid.

Numerous finite element analyses were performed to study the effect of braid angle and waviness ratio on the stress distribution in braids. The distribution in braids was compared with those in equivalent laminates also. The results are discussed below using various techniques.

5.2 Analysis of Stress Contours in the Tows of Different Braids

Figure 5.3 shows the locations of peak stresses in the tow when unit uni-axial load ($<\sigma_{xx}> = 1$) along the longitudinal direction is applied to a ±25˚ braid with WR of 1/3. Even for simple loading like this, a three dimensional stress state exists in the tow and any stress component could be critical, depending upon the allowables [79]. Figure 5.3 shows the contours for all the six stress components with their respective ranges. The value of each stress component for an equivalent lamina is also given. For a lamina of an equivalent tape laminate, only in-plane stresses are non-zero and value of each stress component lies within the braid stress range. The out of planes stress values are zero because there are no free edge effects. Moreover, the in-plane stresses in the lamina of a tape laminate are constant, but the value of each stress component varies significantly in the braid tow.

Three dimensional stress distributions exist for ±45˚ and ±65˚ braid tows (not shown in Fig. 5.3) also, but there are certain similarities and differences in the stress distributions as one changes the braid angle. The σ_{11} stress peaks in the tow are tensile for all the braid angles. In contrast, the peaks for σ_{22} are compressive for ±25˚ and tensile for ±45˚ and ±65˚, which is consistent with equivalent laminates. Figure 5.3 shows that σ_{13} is the only component whose peak extends through the thickness of the tow, as shown in Fig. 5.3. For the rest of the stress components the peaks are only on the surface of the tow. For all the braid configurations, there were significant tensile and compressive σ_{33} concentrations. However, for a ±65˚ braid, tensile peaks were much larger than the compressive peaks. Figure 5.4 shows the effect of braid angle on the σ_{33} stress distribution. Braids with different braid angles were stressed at the same stress level ($<\sigma_{xx}> = 1$). It can be seen that the stress distribution differs considerably with braid angle. With increase in braid angle to ±65˚, the peak stresses changes from tension to compression in nature in the center portion of the tow. Also, the location of peak stresses changes from center portion of the tow to the edge of the tow. The magnitude of tensile peaks also changes from 0.22 to 0.367 when the braid angle is increased from

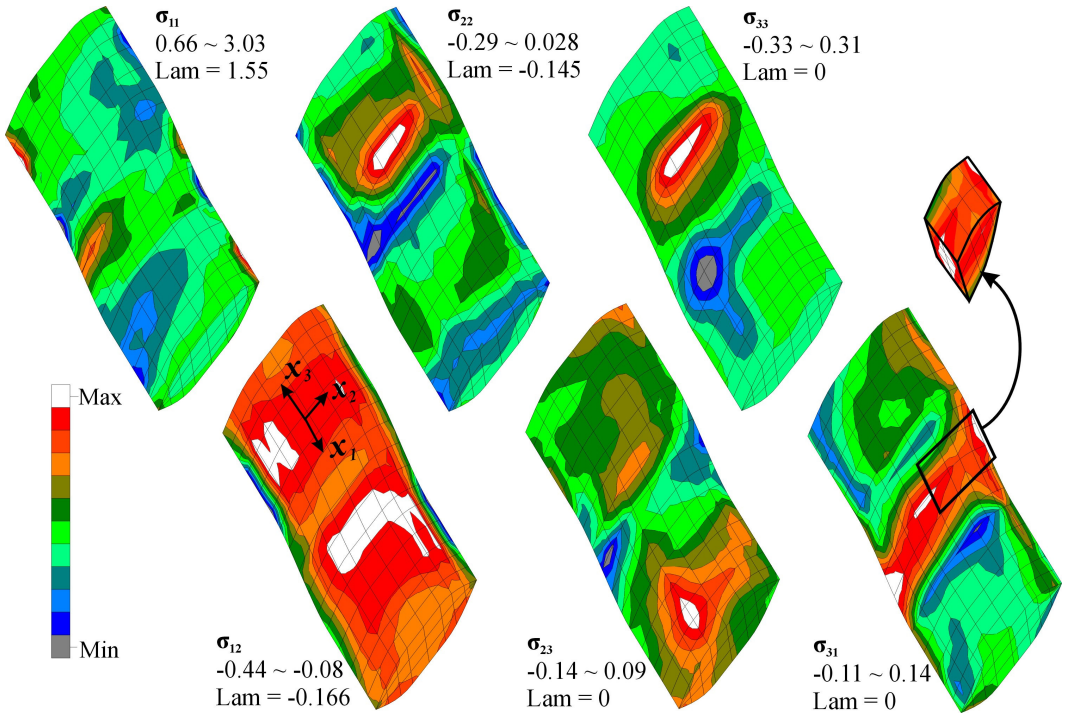

Figure 5.3. Three-dimensional stress state in the +θ tow for ±25˚ braid with WR =1/3 ($<\sigma_{xx}>$ =1).

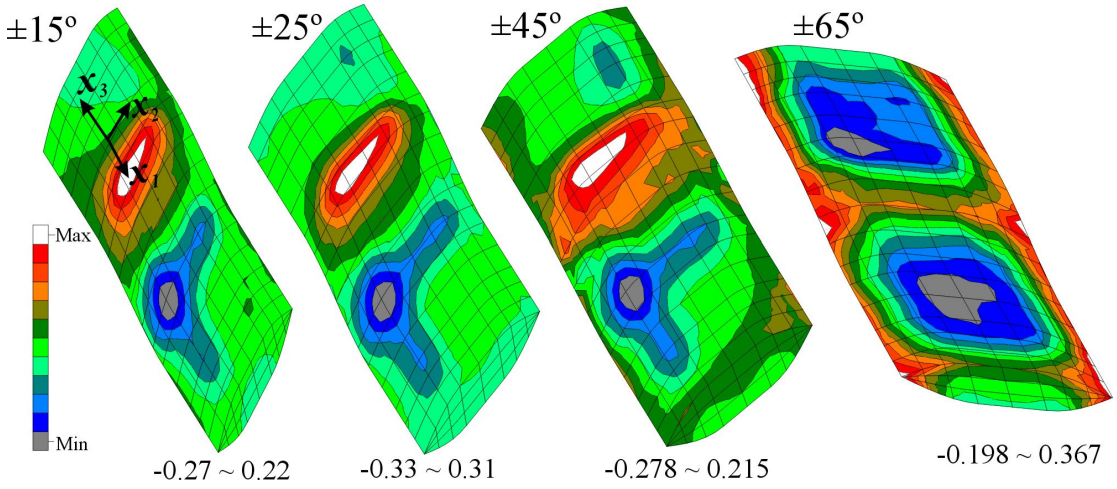

Figure 5.4. Effect of braid angle on σ_{33} stress concentration in the +θ tow (Uni-axial loading ($<\sigma_{xx}>$ = 1), WR=1/3).

±15˚ to ±65˚. The ±65˚ braid tow has a smaller tensile area, which is near its edges, but a larger tensile value than the others. In summary, the location and magnitude of peak stresses vary considerably with braid angle.

5.3 Comparison of Severity of Stresses in Braids and Tape Laminates

Stress contour plots shown in Figs. 5.3 and 5.4 give stress information only on the surface of the tow. To obtain internal information, one has to cut the tow and show more and more plots. The percentage of the tow having peak stress can be small enough not to be noticeable in the stress contours. Also, it is possible that peak stresses are hidden in the interior of the tow. One needs to determine what percentage of the tow exceeds a certain stress level. A volume distribution plot quantifies the percentage volume of the material that is stressed more than a particular value. Figure 5.5 shows a typical volume distribution plot of σ_{33} in the +θ tow of a ±30˚ braid with waviness ratio

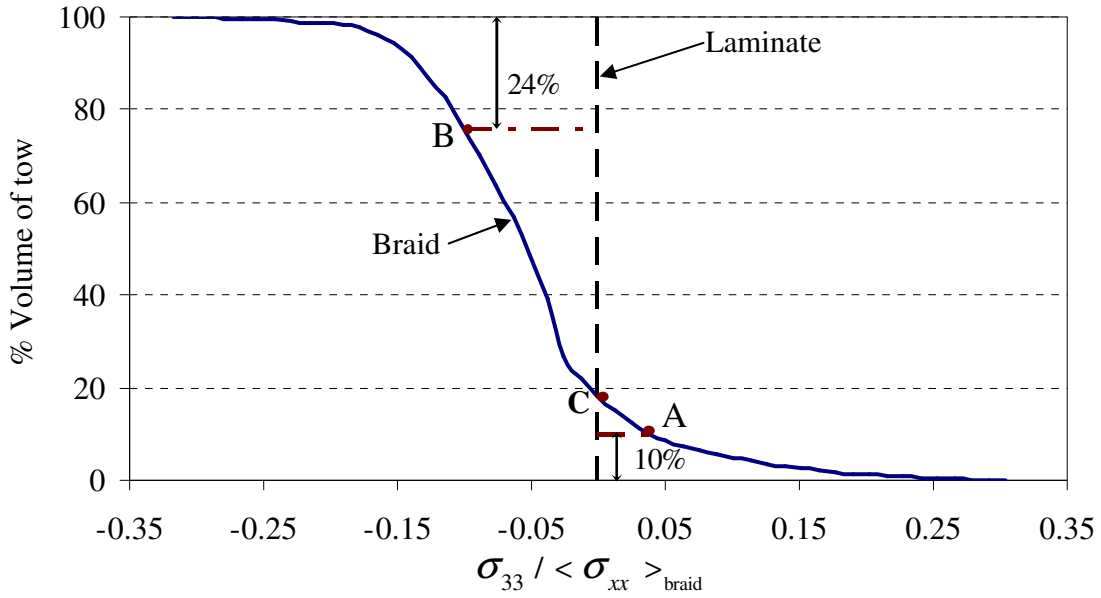

Figure 5.5. Volume distribution of σ_{33} in ±30˚ braid tow (Applied $< \sigma_{xx} > = 1$).

=1/3 when uni-axial load is applied. The σ_{33} in an equivalent lamina is also plotted. For the lamina, σ_{33} is zero. The σ_{33} in the braid was normalized by the applied stress. The figure shows that 18% (point C) of the volume of the tow has a tensile σ_{33}. Point A, which is in the tensile region, indicates that 10% of the volume has a σ_{33} that is larger than 0.037 times the applied stress. Point B, which is in the compressive region, indicates that 24% of the volume has a compressive stress larger than 0.1 times the magnitude of the applied stress. One can use the information provided by a volume distribution plot in several ways. The percentage of the tow having larger stress than that in an equivalent lamina can be found. One can also find the percentage of the tow having tensile or compressive stress. The amount of the tow having stress larger than a particular value can also be found. For example, questions like, what percentage of the tow has a larger σ_{33} than 0.25 times the applied stress, can be answered.

Tape laminates and braids have their own advantages and disadvantages in terms of ease and cost of manufacturing, engineering properties and ease of analysis. Analysis of tape laminates is easily understood by designers and engineers but tapes have the disadvantage of hand lay-up and high manufacturing cost. In contrast, analysis of braids is complicated but they have an edge in terms of manufacturing cost. Here the severity of stresses in braids as compared to those in equivalent tape laminates is discussed. Figure 5.6 shows the volume distribution of in-plane normal local stresses in the $+\theta$ tow of $\pm 45^{\circ}$ braid when unit uni-axial load along the longitudinal direction was applied ($<\sigma_{xx}> = 1$). The in-plane stresses were plotted, because out of plane stresses are zero for tape laminate. In both plots, the volume distribution curves correspond to five waviness ratios: 1/3, 1/4, 1/6, 1/9 and 1/20. The vertical straight line corresponds to the constant stress value in the $+\theta$ lamina of an equivalent tape laminate. The stresses shown in the figure are normalized with the corresponding absolute $+\theta$ lamina values. That is, the plots show $\sigma_{11\_tow} / |\sigma_{11\_lamina}|$ and $\sigma_{22\_tow} / |\sigma_{22\_lamina}|$. There are several differences between the stress distribution in a braid tow and a lamina. Figure 5.3 showed that braid tows have a wide variation in in-plane stresses. In contrast, in-plane stresses in an

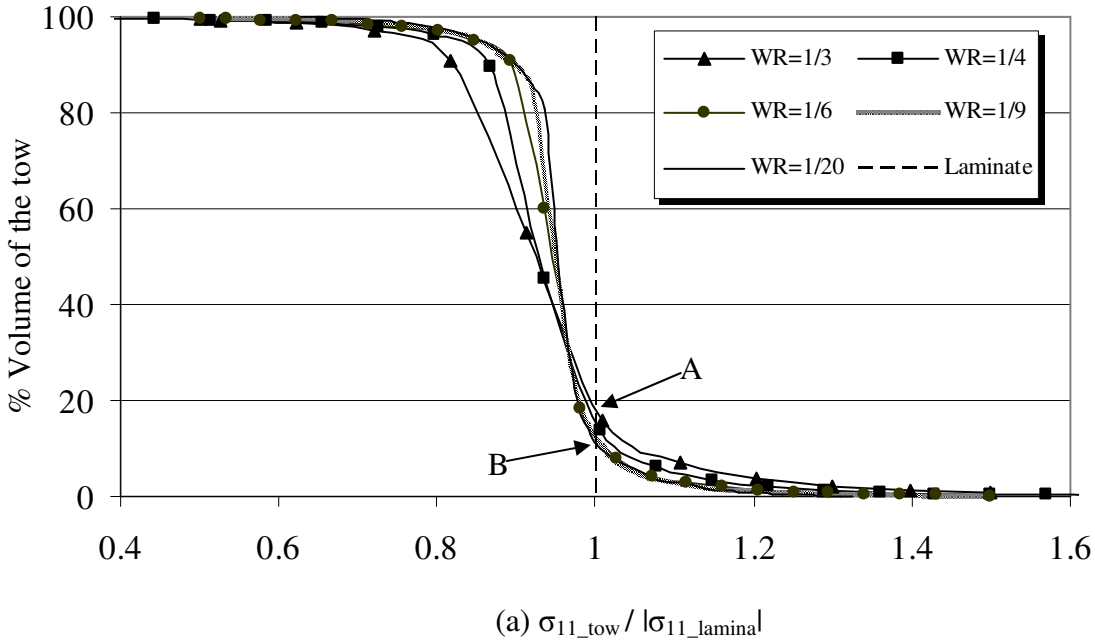

(a) $\sigma_{11\_tow} / |\sigma_{11\_lamina}|$

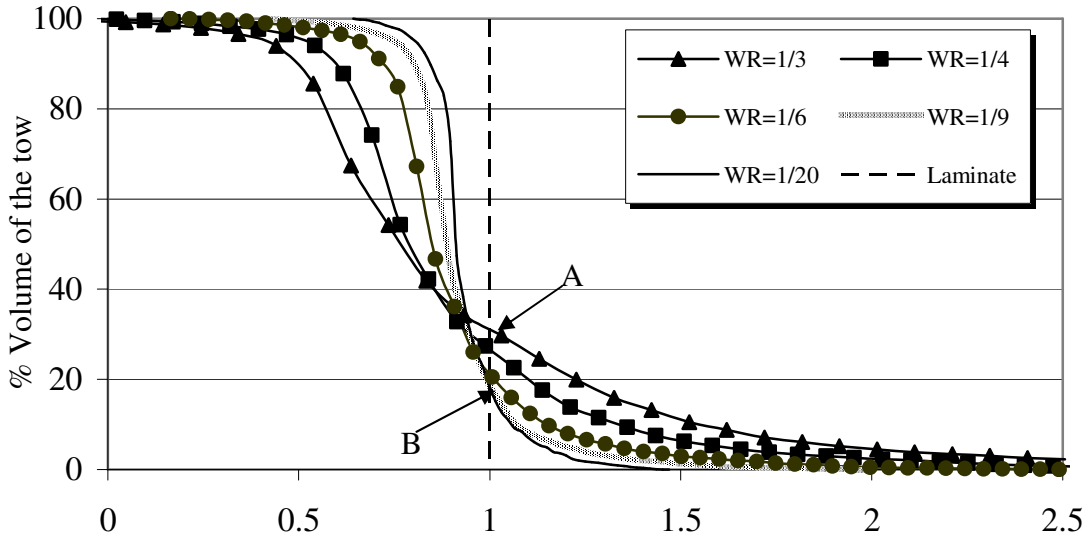

(b) $\sigma_{22\_tow} / |\sigma_{22\_lamina}|$

Figure 5.6. Comparison of stress volume distribution in a ±45˚ braid with that in an equivalent tape laminate. Normalized stress $(\sigma_{tow} / |\sigma_{lamina}|)$ in the tow versus percentage volume of the tow exceeding a particular value is plotted.

equivalent lamina are constant. The volume of the tow that exceeds the value of stresses in a tape lamina is defined to the "*severity"* of stresses in a tow as compared to those in lamina. Figure 5.6(a) shows the volume distribution of σ_{11} for a ±45˚ braid tow for several waviness ratios. The figure shows that 19% of the tow (marked by arrow A) has larger σ_{11} than an equivalent lamina for WR =1/3 and the severity is maximum for this WR. When the waviness ratio is reduced to 1/20, the severity reduces to 11.5% (marked by arrow B). The σ_{11} severity is smallest for the smallest WR (1/20) in the considered range of WR (1/20 - 1/3). Figure 5.6(b) shows the volume distribution of σ_{22}. The figure shows that 31% of the tow (marked by arrow A) has larger σ_{22} than an equivalent lamina for WR =1/3. When the waviness ratio is reduced to 1/20, the severity reduces to 19% (marked by arrow B). For all other waviness ratios considered, the severity lies in between the highest WR (1/3) and lowest WR (1/20) for both the in-plane stresses shown in Fig. 5.6.

Figure 5.6 showed the stress distribution for ±45˚ braid only. The severity of stresses in ±25˚ and ±65˚ braids was also investigated. The results are tabulated in Table 5.1. Table 5.1 shows the severity of stresses for the considered range of BA (±25˚- ±65˚) and WR (1/20-1/3).

Table 5.1. Severity of stresses in braid as compared to an equivalent tape laminate (the "*severity*" of stresses in a tow is defined herein to be the volume of the tow that exceeds the value of stresses in a tape lamina).

Range of Braid Angle = ±25˚ - ±65˚, Range of Waviness Ratio = 1/20 – 1/3												
	% volume of tow having more severe stress than those in an equivalent lamina											
	WR =1/3			WR =1/6			WR =1/9			WR =1/20		
BA	±25˚	±45˚	±65˚	±25˚	±45˚	±65˚	±25˚	±45˚	±65˚	±25˚	±45˚	±65˚
σ_{11}	40	18.5	24.6	19.5	12.3	27.5	16	12.1	28.8	15	11.2	30
σ_{22}	45	31	27.3	38.5	21	31	36	18.5	30	36	18.2	29.5
σ_{12}	24.5	33	9.5	24.5	33	26.5	27.5	33.7	29.5	28	34	30

The severity decreases with a decrease in WR for ±25˚ and ±45˚ braids for both in-plane normal stresses. For ±65˚ braid, the severity increases with a decrease in WR for σ_{11}, and remains almost constant for σ_{22}. For σ_{12}, the severity increases with a decrease in WR for all the braid angles. Overall, in this range of parameters, the maximum volume of the tow that could have more stresses than an equivalent lamina is 40% for σ_{11}, 45% for σ_{22} and 34% for σ_{12}.

5.4 Effect of Braid Angle on Stress Peaks

Figure 5.7 shows the effect of braid angle on the σ_{22} and σ_{13} stress volume distributions. Braid angle affects other stress components too, but σ_{22} and σ_{13} are plotted in Fig. 5.7 because in the case of σ_{22}, the difference between stress volume curves of different braids is large and in the case of σ_{13}, the difference is small. The waviness ratio = 1/3 and a unit volume averaged stress of $<\sigma_{xx}>$ was applied. Also shown are the values of equivalent tape laminates corresponding to each braid. Dotted lines are lamina stress values and are constant. There is wide variation in the stresses in the tow of all the braids. Figure 5.7(a) shows that as the braid angle changes, the σ_{22} stress distribution changes considerably. The ±15˚ braid tow has compressive stresses in more than 95% of its volume, whereas ±45˚and ±65˚ braid tows have only tensile stresses in their entire volume. The peak values of σ_{22} for ±15˚, ±45˚ and ±65˚ tows are -0.14, 0.4 and 1.5 respectively. Figure 5.7(b) shows the variation for σ_{13}. The laminate value is zero for all equivalent laminates in this case, but braids have wide variation. The wide variation in σ_{22} is mostly due to *orientation effect* and is expected based on the behavior of an equivalent laminate. The orientation effect is due to the fact that the braid tows are oriented at angles of ±θ to the longitudinal direction. This effect of orientation can easily be eliminated by normalizing with laminate theory results. The other effect is due to the fact that, the material architecture of braids with different braid angles is different, because the tow shape of different braids is different due to phase shift in the undulation. The orientation affects the volume distribution for all the stress components. Hence, a technique was used to eliminate the effect of orientation. By matching the loading that a tow of different braids experiences, the orientation effect is eliminated and the effect of

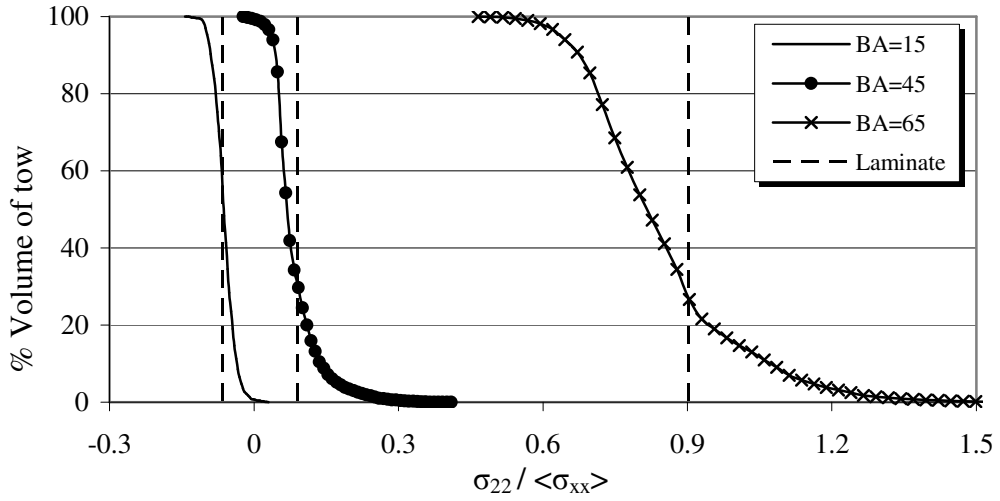

(a) σ_{22} volume distribution

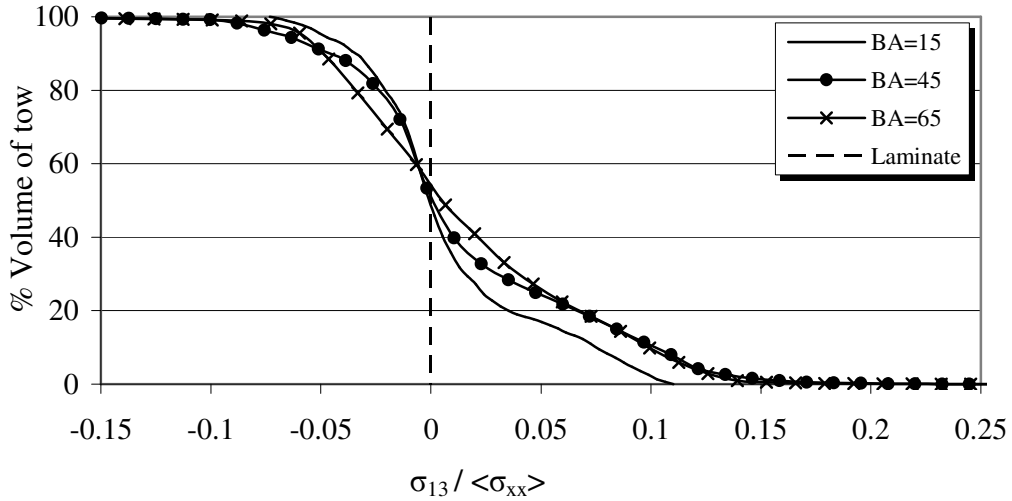

(b) σ_{13} volume distribution

Figure 5.7. Effect of braid angle on σ_{22} and σ_{13} volume distribution ($<\sigma_{xx}> = 1$, WR = 1/3).

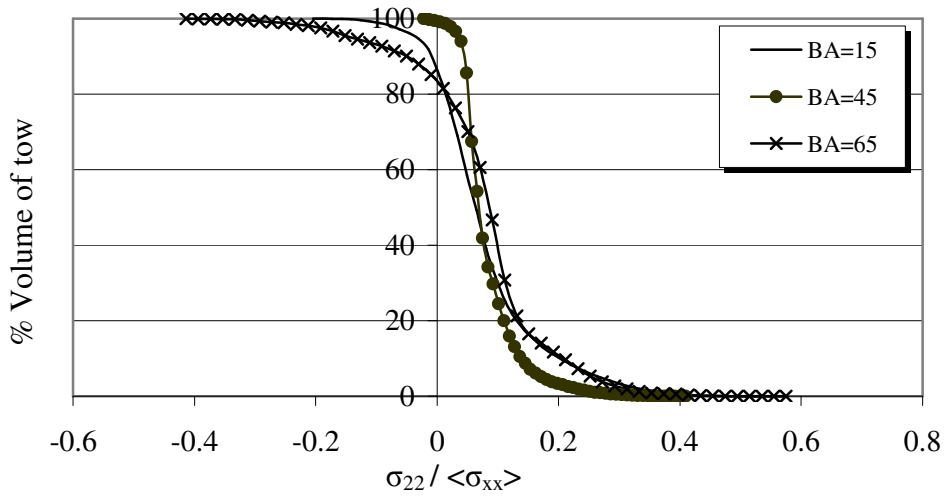

(a) σ_{22} volume distribution

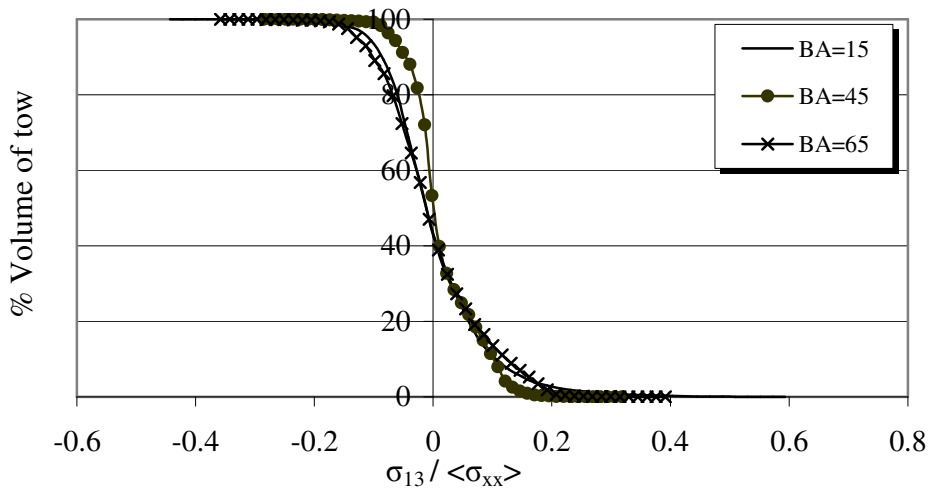

(b) σ_{13} volume distribution

Figure 5.8. Effect of braid angle on σ_{22} and σ_{13} volume distribution when $\langle\sigma_{ij}\rangle$ in the tow are matched (WR=1/3).

phase shift on stress distribution is investigated here. A volume averaged stress $<\sigma_{xx}>$ = 1 was applied on ±45˚ braid. The +45˚ braid tow experienced a certain amount of loading because of this. In particular, the tow was subjected to the following volume averaged stresses: $<\sigma_{11}>$ = 1.203, $<\sigma_{22}>$ = 0.087, $<\sigma_{33}>$ = -0.0026, $<\sigma_{12}>$ = -0.593, $<\sigma_{23}>$=0 and $<\sigma_{13}>$=0, where the "*1*" direction is along the axis of the braid tow. The same amount of multi-axial loading was applied on a +25˚ braid tow. This was made possible by applying multi-axial loading on the ±25˚ braid model. The same thing was done for other braid angles. Now the stress volume distribution in the different braids was compared. The stress volume distribution after matching the loading on tows of different braids is shown in Fig. 5.8. It is interesting to see that now the stress volume distribution curves lie very close to each other as compared to when the loading on tow was not matched (Fig. 5.7). The σ_{22} ranges from tensile to compressive for all the braids as shown in Fig. 5.8(a). The peak values of all the braids are also very close to each other for all the braids now. Similarly, volume distribution curves came closer for σ_{13} stress also as shown in Fig. 5.8(b). The orientation effect could be similarly eliminated for other stress components also (figure not shown). The difference that still remains is attributed to the fact that the tow shape of different braids is different due to phase shift in the undulation. This phase shift is shown in Fig. 5.9. In this figure, $x_1x_2x_3$ is the local coordinate system. Different fibers across the width of the tow start to undulate at different x distance, which means that they have different phase angle. The phase shift is given by $\Phi = x_2*\tan(2\theta - 90°)$, where θ is the braid angle. Due to this, different fibers of the tow do not undulate and straighten at the same x coordinate. One fiber may have started undulating and another may not have yet started to undulate. The overall effect of this phase shift is different material architecture for different braids, which results in different stress distribution even if the loading on the tow of different braids was matched.

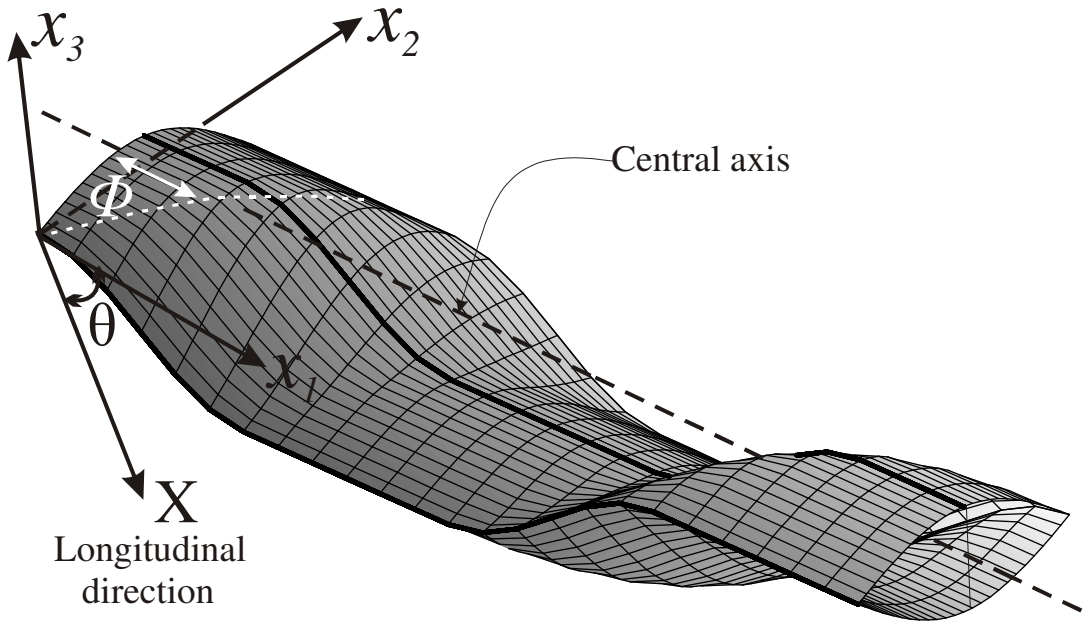

Figure 5.9. Phase shift in the tow of a braid.

5.5. Effect of Waviness Ratio on Stress Peaks

Figure 5.10 shows the effect of waviness ratio on the stress volume distribution for a ±45˚ braid. A unit uni-axial load ($<\sigma_{xx}> = 1$) was applied. Three different waviness ratios (1/3, 1/6 and 1/9) were used. The figure shows the stress volume distribution for all the stress components. It can be seen that for all the stress components, with an increase in waviness ratio the volume distribution curve tends to broaden in the horizontal direction. In other words, the severity of the peaks increases with an increase in waviness ratio for all the stress components. The effect of waviness ratio is more pronounced for out of plane stresses (σ_{33}, σ_{23} and σ_{13}) than for in-plane stresses (σ_{11}, σ_{22} and σ_{12}).

Figure 5.11 summarizes the effect of waviness ratio on the stress peaks. The figure shows the variation of normalized stress peak values with waviness ratio for all the six stress components. The peak values correspond to a particular percentage of the tow volume. For example, in Fig. 5.11(a), 5% of the tow volume had more severe

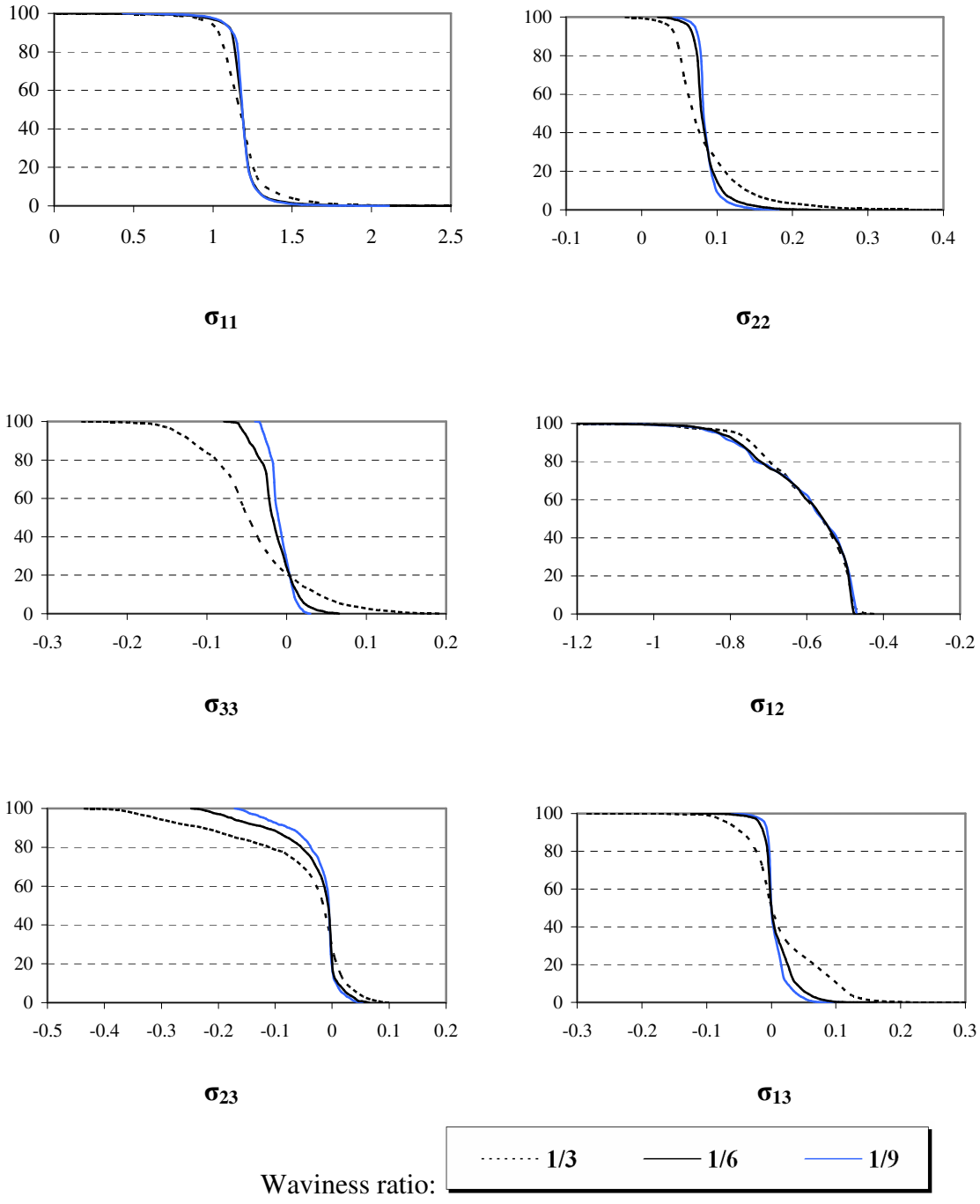

Figure 5.10. Effect of waviness ratio on stress volume distribution (BA = ±45˚). For all the cases, stress component is plotted along the horizontal and % volume of the tow is plotted along the vertical. Applied stress is $\langle\sigma_{xx}\rangle = 1$.

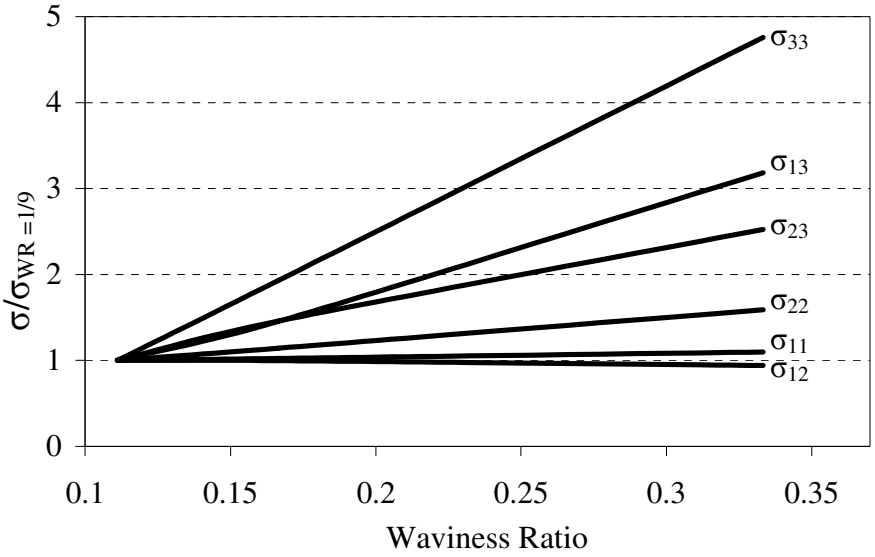

(a) Peak stresses correspond to 5% of the tow volume

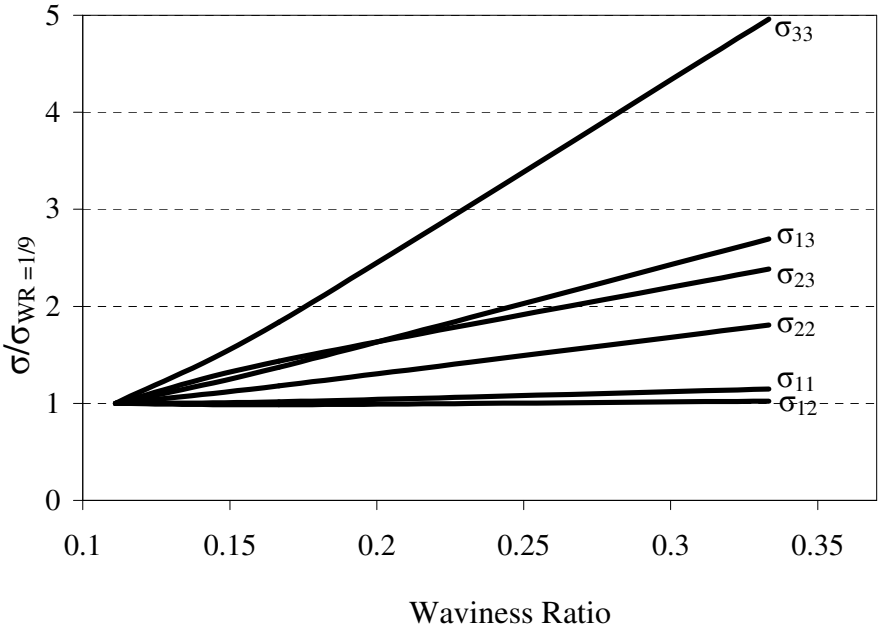

(b) Peak stresses correspond to 2% of the tow volume

Figure 5.11. Variation of peaks with waviness ratio ±45˚ braid under $<\sigma_{xx}> =1$.

stresses than the value plotted for all the stress components. Similarly, in Fig. 5.11(b), 2% of the tow volume was chosen to find the value of peak stresses. The σ_{ij} (where i, j =1, 2, 3) peak values were normalized with the peak values corresponding to a waviness ratio of 1/9. The results are for a ±45˚ braid under unit uni-axial load ($<\sigma_{xx}>=1$). It can be seen that the stress peaks increase linearly with an increase in waviness ratio (except for σ_{12} for which there is little variation). Again, it can be seen that the effect of waviness ratio is more pronounced on out of plane stresses as compared to in-plane stresses. Out of plane normal stress is most severely affected.

5.6 Summary

The tow stress state in 2x2 braids was investigated. The effect of various parameters on the stress state was studied. The following observations were made:

- A complex stress state which is fully three-dimensional exists in the tow even for simple uni-axial loading.
- In the considered range of parameters (WR =1/3 – 1/20, BA = ±25˚ - ±65˚), a considerable volume of the tow has higher magnitude of stresses than an equivalent lamina.
- The wide variation in stress volume distribution with braid angle is due to simple orientation effects and can be eliminated by matching the loading on the tow. Some difference that still remains is attributed to the phase shift.
- The severity of the stress peaks increases linearly with an increase in waviness ratio for all stress components (except for σ_{12}, for which there is little variation).

6. EFFECT OF ASSUMED DAMAGE MODEL ON PREDICTED DAMAGE EVOLUTION IN TEXTILE COMPOSITES

In the previous chapter, linear elastic behavior of braided composites was studied. When excessive load or fatigue cycles are applied, damage initiates and grows in textile composites. To exploit the full potential of these materials, it is necessary to understand the damage initiation and progression. The knowledge of the stress state that exists both in tows and matrix is required to be able to predict potential damage locations. Detailed 3D finite element models with refined meshes are necessary to determine the stress distribution and failure behavior of textiles.

Using the finite element models, the stress distribution can be predicted both in the tows and in the matrix. Although the moduli predictions are simple, prediction of the stress state is difficult as a full three dimensional stress state exists in the matrix as well as in the tows even for simple uni-axial loading. Hence the stress analysis tends to be complex. Prediction of accurate stress states is critical to predict damage initiation and progression and is the first step of the challenge. The next one is utilizing this information to predict the damage evolution. A classical non-linear approach was adopted for predicting damage initiation and progression. A particular load is applied to the finite element model initially. The stresses were computed at each Gauss point within an element. If the stresses at any Gauss point satisfied a pre-selected failure criterion, the elastic properties at that Gauss point were degraded. After degrading the properties, the analysis was conducted again at the same load level to calculate redistributed stresses. This was iterated until no further failure occurred and the model was in equilibrium. The procedure for conducting damage initiation and progression using the finite element method was discussed in detail in the theory chapter earlier. A flow chart of the analysis was shown in Fig. 4.2.

Prediction of failure response is challenging both in terms of computational time and modeling. Various researchers have proposed different damage models. Most of these models are similar in the sense that they degrade the engineering constants of the

tows and matrix after a failure criterion detects the occurrence of a damage mode. These models differ from each other in various ways. The models basically differ in terms of which property and how much of it they degrade under a particular failure mode. Secondly, a damage mode in a specific direction in a tow will affect the deformation in the other direction too, hence the Poisson's ratios will change. Some of the models affect the off-diagonal compliance coefficients and some don't. Another difference between damage models is whether the matrix, which was isotropic to start with, is considered anisotropic or not after damage. Some of the models are based on experimental observations while some have a theoretical basis. A comparison of some of the damage models available in the literature will be provided here.

This part of the research has two goals. One is to present a common framework to allow use of a wide variety of damage initiation and growth models. Some of the damage models available in the literature and their salient features will be discussed. The second goal is to predict the damage initiation and growth in some woven composites using different damage models. The stress strain curves under uni-axial tensile loading will be predicted. Studies conducted include analysis of plain weave and twill weave with different material systems. These configurations were selected because the experimental stress-strain response, geometric parameters and material properties for these configurations were available in the literature [38-39,42]. A comparison of predictions of stress-strain curves using different damage models will be shown. All the predictions are also compared with experimental data.

6.1. Damage Mechanisms in Textile Composites

Different types of damage mechanisms can be present in textile composites under different types of loadings. The matrix and tows can develop transverse cracks. Different damage mechanisms seen in the tows are transverse cracking, inter and intra tow delamination, fiber buckling and fiber breakage etc. The resin rich areas can develop transverse matrix cracks independent of matrix cracks in the tows. Three main damage mechanisms observed experimentally under microscope by Quaresimin et al. [69] in twill weave composites

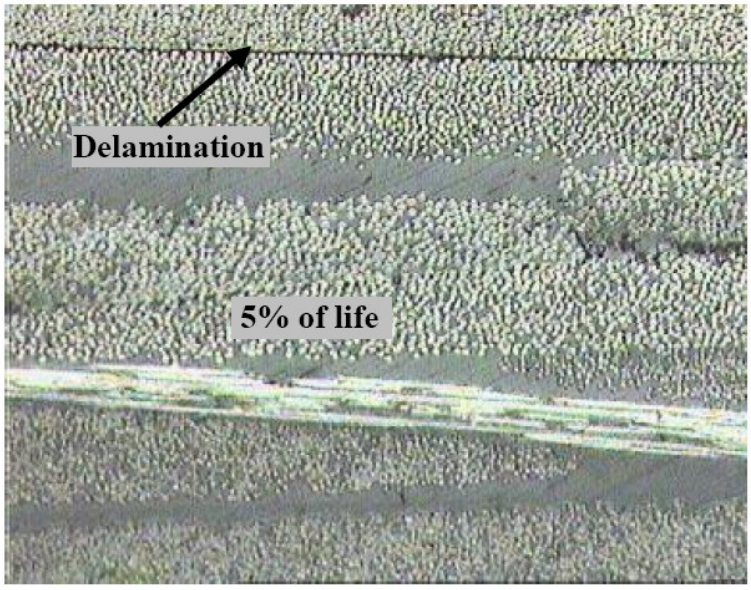

(a) Delamination

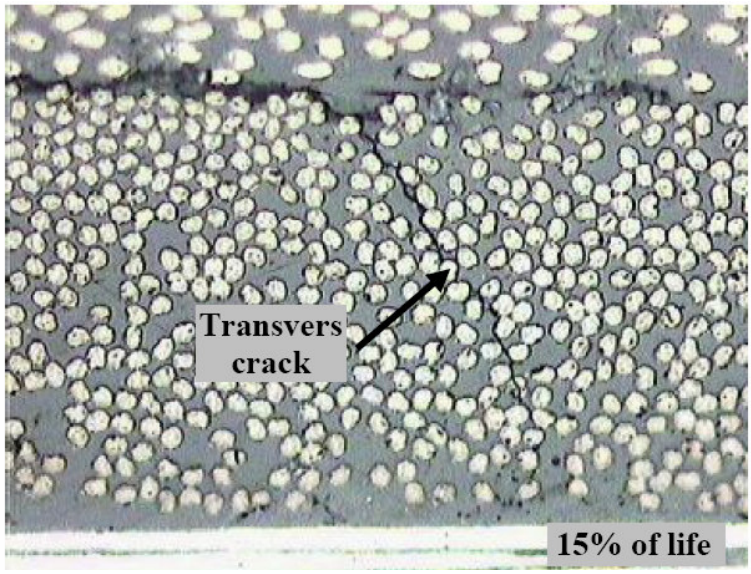

(b) Transverse matrix crack

Figure 6.1. Damage mechanisms in woven composites [69].

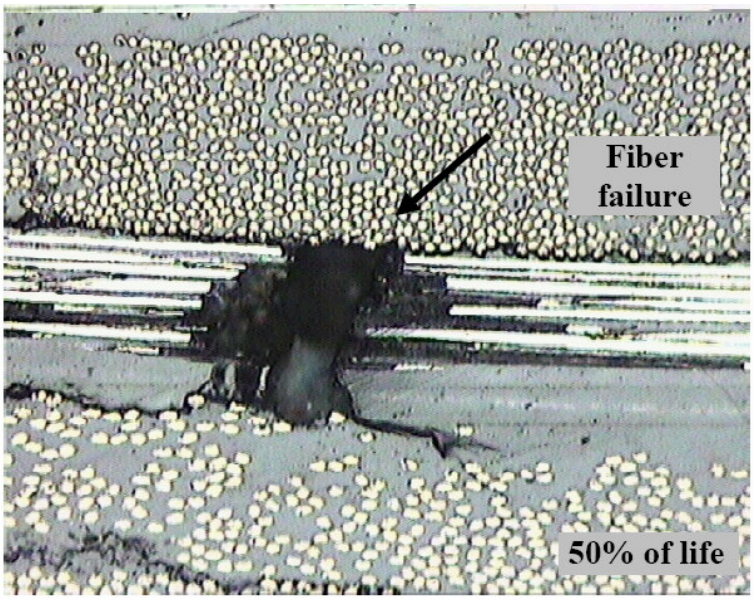

(c) Fiber failure

Figure 6.1. Continued.

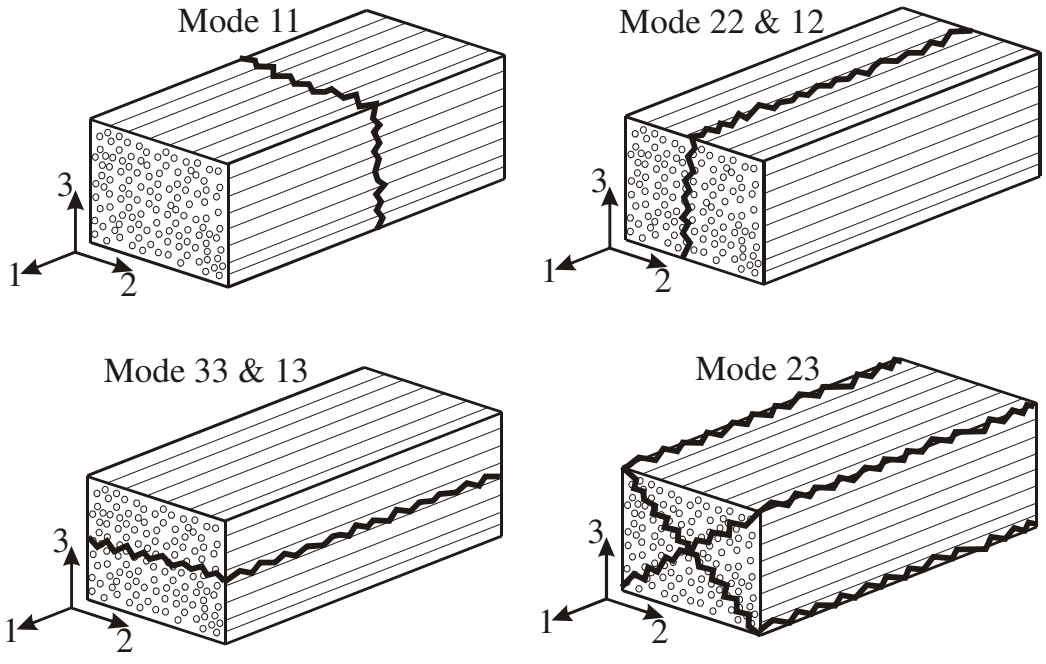

Figure 6.2. Schematic of different damage modes in the tow of textile composites.

under fatigue loading are layer delaminations, transverse matrix cracking and fiber failure. These damage mechanisms are shown by micrographs in Fig. 6.1. It was observed by Quaresimin et al. [69] that all three damage mechanisms were present in various laminate sequences under different types of fatigue loadings, but the sequence of appearance was different [69]. Moreover, the laminate behavior was generally ruled by only one predominant mechanism.

The schematic of different damage modes in the tow is shown in Fig. 6.2. The damage mode that takes place is the one in which a corresponding failure criterion gets satisfied. Failure criteria that were used are discussed later on. The damage modes in the tows can be classified into four types as shown in Fig 6.2. The direction *"1"* is along the fiber direction and *"2"* and *"3"* are in plane and out of plane transverse directions respectively. The *"1", "2"* and *"3"* are the principal coordinate axes of the tow, which is transversely orthotropic. In the finite element model, the material angles are constantly varying for the tow at different locations. Under failure mode 11, the fiber breakage occurs and this damage mode is generally caused by excessive σ_{11} stress in the tow. This failure mode generally is the cause of ultimate failure of the composite. Failure mode 22 and 12 are the cause of transverse matrix cracking in the tows, which is generally one of early damage mechanisms seen in the tows. Failure mode 33 and 13 can be caused by either σ_{33} or σ_{13} stress components and can cause intra or inter laminar delaminations. The damage mode 23 caused by σ_{23} stress is also shown in Fig. 6.2.

6.2. Failure Criteria for Tows and Matrix

To determine which failure mode has occurred, a suitable failure criterion is necessary. The maximum principal stress criterion was used for the matrix. Depending upon the damage model, the matrix was considered to be isotropic or anisotropic at a material point where failure has occurred. For tows, maximum stress criterion for anisotropic materials was used, which says that the failure occurs when any of the stress components in the material coordinates exceeds its corresponding strength. If σ_{ij} are the

stress components in the material coordinates of the tow and S_{ij} are the corresponding strength values, then the failure criteria used in this work can be summarized as below:

For isotropic matrix:

Max principal stress criterion

For transversely isotropic tow: Max stress criterion: (6.1)

$\sigma_{ij} / S_{ij} > 1$ Failure mode *ij* has occured

$\sigma_{ij} / S_{ij} \leq 1$ Material point did not fail

The values of failure strengths for the matrix can be determined experimentally. It is relatively difficult to determine all of the six strength values for the tow. Experimental tests can be conducted for unidirectional lamina to determine different strength values for the tow. Chamis's micromechanics strength formulae [80] can also be used to determine the strength properties of the tow. For the damage studies conducted here, the strength properties were taken from refs. [38-39,42].

6.3. Framework for Implementation of Different Damage Models

In the current damage initiation and progression scheme, the material properties are degraded every time a damage mode is determined to have occurred. The scheme that guides which material property and how much of it needs to be degraded for the failed material point under a particular failure mode is called the *"property degradation model"* herein.

Various researchers have proposed different property degradation models. A review of the state of the art in damage initiation and progression for textile composites was done in the literature review chapter earlier. In this chapter, the attention is on four different property degradation models given by Whitcomb et al. [40], Blackketter et al. [28], Tamma et al. [43] and Zako et al. [42]. These models have certain similarities and differences from each other. All the property degradation models are similar in the sense that they guide the amount of degradation under different failure modes for the tow and the matrix.

These models differ from each other in various ways. First of all, the damage models differ in their formulation. For example, some damage models increase

compliance coefficients and some decrease stiffness coefficients. Some follow a damage tensor approach. The models also differ in terms of which property and how much of it they degrade under a particular failure mode. Some damage models affect the off diagonal terms of compliance matrix and some do not. Another difference between damage models is whether a material point in the matrix, which was isotropic to start with, is considered anisotropic or not after damage. Below some formulations of damage models available in literature are discussed and then a convenient framework to allow implementation of wide variety of damage models in a common way is proposed. Using that framework, a comparison of different property degradation models is presented.

6.3.1. Existing property degradation schemes

Four different damage models considered are given by Whitcomb et al. [40], Blackketer et al. [28], Tamma et al. [43] and Zako et al. [42]. In the following text, property degradation schemes of different models for tows as well as for matrix are discussed. The damage model given in ref. [28] has been widely used to predict initiation and growth of damage by many researchers [37-40]. This uses the following scheme for the tows.

$$\varepsilon_i = \overline{S_{ij}}\sigma_j$$

$$\overline{S_{ij}} = \begin{bmatrix} \frac{1}{\alpha_1 E_{11}} & \frac{-\upsilon_{12}}{E_{11}} & \frac{-\upsilon_{13}}{E_{11}} & 0 & 0 & 0 \\ \frac{-\upsilon_{21}}{E_{22}} & \frac{1}{\alpha_2 E_{22}} & \frac{-\upsilon_{23}}{E_{22}} & 0 & 0 & 0 \\ \frac{-\upsilon_{31}}{E_{33}} & \frac{-\upsilon_{32}}{E_{33}} & \frac{1}{\alpha_3 E_{33}} & 0 & 0 & 0 \\ 0 & 0 & 0 & \frac{1}{\alpha_4 G_{12}} & 0 & 0 \\ 0 & 0 & 0 & 0 & \frac{1}{\alpha_5 G_{23}} & 0 \\ 0 & 0 & 0 & 0 & 0 & \frac{1}{\alpha_6 G_{31}} \end{bmatrix} \tag{6.2}$$

where $\overline{S_{ij}}$ is the compliance tensor for the damage material point. In this scheme, the values of α_i (i =1 to 6) is either 0.01 or 0.2 which means that the moduli are degraded to almost 1% or original or 20% of original value. Note that the values of parameters α_i are different under different damage modes. The only reason behind choosing some of the values of α_i to be 0.01 and not absolute 0 was to avoid numerical difficulties [28]. Shear moduli were not reduced more than 80% due to the assumption that some shear stiffness remained due to frictional resistance still present on the failure plane [28]. For the matrix, a maximum normal stress criteria was used and property reduction was the same under all the failure modes. Hence the matrix remains isotropic after failure, which is a questionable assumption. The tensile modulus was reduced to 1% of its original value and shear modulus was reduced to 20% of its original value.

Whitcomb and Chapman [40] proposed a property degradation model based on the Blackketter et al's [28] model. This was a combination of the method used by Blackketter et al. [28], Stanton and Kipp [41] and Whitcomb and Srirengan [37]. The model involved increasing the compliance matrix entries in the following manner when a certain failure mode was detected

$$\overline{S_{ij}} = \begin{Bmatrix} b_i S_{ii}, & i = j \\ S_{ij}, & i \neq j \end{Bmatrix}, \text{ no sum on i, } 1 \leq i, j \leq 6 \tag{6.3}$$

Of course the factors b_i were different under different failure modes. Also a matrix material point, if isotropic before failure, was treated as anisotropic after damage. Whitcomb et al.'s model is similar to the model given by Blackketter el al. in ref. [28] except that the degradation factors are different in the two models and treatment for the matrix's degradation is different. These two models reduce only diagonal entries in the compliance matrix. Whether this changes the Poisson's ratios or not, is not obvious at this point, but will become obvious later on when we discuss the common implementation scheme for different property degradation models.

Tamma et al. [43] proposed a damage model in which they attempted to provide a physical explanation of what properties should be degraded under particular failure modes. They considered the degradation of Poisson's ratio also. Anisotropic damage models were proposed both for the tows and for the matrix. The degradation equation can be defined as $E_D = (1-D)E$, where E is modulus of the undamaged material, E_D is the modulus of the damaged material and D is the degradation factor.

Zako et al. [42] developed a theoretical anisotropic damage constitutive equation based on damage mechanics. Different damage modes were considered in the tows. The degradation factors were calculated from a damage tensor. This model considers the degradation of Poisson's ratios too such that the off-diagonal entries in the compliance matrix also get affected. An anisotropic damage model was considered for tows, and an isotropic damage model was considered for matrix. Some questions arise about the selection of an isotropic damage model for the matrix because the matrix can become anisotropic after damage. Their formulation has the following form:

$$D = F\begin{bmatrix} D_L & 0 & 0 \\ 0 & D_T & 0 \\ 0 & 0 & D_Z \end{bmatrix} \tag{6.4}$$

F can vary from 0 to 1 to allow different amount of degradation

The parameters d_L, d_T and d_Z are defined as follows [42]:

$$d_L = 1 - D_L,\ d_T = 1 - D_T,\ d_Z = 1 - D_Z$$
$$d_{TZ} = \left(\frac{2d_T d_Z}{d_T + d_Z}\right)^2,\ d_{ZL} = \left(\frac{2d_Z d_L}{d_Z + d_L}\right)^2,\ d_{LT} = \left(\frac{2d_L d_T}{d_L + d_T}\right)^2 \tag{6.5}$$

The damaged stiffness tensor then looks like below:

$$\begin{Bmatrix} \sigma_L \\ \sigma_T \\ \sigma_Z \\ \sigma_{TZ} \\ \sigma_{ZL} \\ \sigma_{LT} \end{Bmatrix} = \begin{bmatrix} d_L^2 Q_{11} & d_L d_T Q_{12} & d_Z d_T Q_{13} & 0 & 0 & 0 \\ & d_T^2 Q_{22} & d_T d_Z Q_{23} & 0 & 0 & 0 \\ & & d_Z^2 Q_{33} & 0 & 0 & 0 \\ & & & d_{TZ} Q_{44} & 0 & 0 \\ & SYM & & & d_{ZL} Q_{55} & 0 \\ & & & & & d_{LT} Q_{66} \end{bmatrix} \begin{Bmatrix} \varepsilon_L \\ \varepsilon_T \\ \varepsilon_Z \\ \gamma_{TZ} \\ \gamma_{ZL} \\ \gamma_{LT} \end{Bmatrix} \tag{6.6}$$

Hence, in this case the stiffness coefficients are being decreased to take into account the effect of a failed material point. Moreover, the off-diagonal coefficients in stiffness matrix are also being affected. A change in off-diagonal coefficients of stiffness matrix causes a change in off-diagonal coefficients of compliance matrix too. This in contrast to Whitcomb et al. or Blackkketer et al.'s models, where compliance coefficients were increased and only diagonal entries were affected. Using these current schemes, it is not possible to compare the amount of degradation being done by different property degradation models under various failure models. Hence a common implementation of different property degradation models in terms of degradation in engineering elastic properties is proposed below.

6.3.2. Framework for common implementation of different property degradation schemes

The compliance increase of Whitcomb and Blackketter and the stiffness decrease scheme of Zako ultimately affect the engineering elastic properties of the material. Hence in the common implementation scheme, the drop in *engineering elastic properties* under different failure modes and under different property degradation models was found out.

We know that the elements in compliance and stiffness tensors are functions of engineering moduli and can be written as:

$$\begin{aligned} &\overline{C_{ij}} = d_{ij} C_{ij}, \text{ no sum on i, j, } 1 \le \text{i, j} \le 6 \\ &\overline{C_{ij}} = \overline{C_{ij}}(\overline{E_{ii}}, \overline{G_{ij}}, \overline{\upsilon_{ij}}), \rightarrow \text{set of 9 equations} \end{aligned} \tag{6.7}$$

where $\overline{C_{ij}}$ is the damaged compliance tensor and is equal to $d_{ij} C_{ij}$ (no sum on i,j) , where C_{ij} is the original compliance tensor and d_{ij} are the degradation factors. The 6x6 compliance tensor has nine independent coefficients. There are 9 independent engineering elastic properties for an orthotropic material. The above set of 9 equations can be solved to find the degradation parameters for effective engineering moduli and Poisson's ratios. The degradation factor (a_i) for any engineering elastic property is defined as the original modulus (or Poisson's ratio) divided by the damaged modulus (or Poisson's ratio) and can be written as:

$$\begin{aligned} &a_1 = E_{11} / \overline{E_{11}}, \quad a_2 = E_{22} / \overline{E_{22}}, \quad a_3 = E_{33} / \overline{E_{33}} \\ &a_4 = G_{12} / \overline{G_{12}}, \quad a_5 = G_{23} / \overline{G_{23}}, \quad a_6 = G_{13} / \overline{G_{13}} \\ &a_7 = \upsilon_{12} / \overline{\upsilon_{12}}, \quad a_8 = \upsilon_{23} / \overline{\upsilon_{23}}, \quad a_9 = \upsilon_{13} / \overline{\upsilon_{13}} \end{aligned} \tag{6.8}$$

Similar methodology was applied also in the case of Zako's stiffness increase scheme to find the degradation parameters for engineering properties.

For the common implementation scheme, the degradations parameters for engineering properties were found for different models and implemented in a common framework. The degradation factors were found for the tows as well as for matrix and are given in Tables 6.1 and 6.2. The "*1*" is the local fiber direction of the tow and "*2*" and "*3*" are the local transverse directions of the tow. As suggested by Zako et al. [42], a value of 0.99 was used for F for Zako's model while calculating damage factors in Tables 6.1 and 6.2.

Table 6.1. Degradation factors for engineering elastic properties of the tow.

	Mode σ_{11}				Mode σ_{22}				Mode σ_{33}			
	Whit	**Black**	**Zako**	**Tamma**	**Whit**	**Black**	**Zako**	**Tamma**	**Whit**	**Black**	**Zako**	**Tamma**
E_{11}	100	100	10,000	100	1*	1	1	1	1*	1	1	1
E_{22}	8	100	1	1	8	100	10,000	100	1	1	1	1
E_{33}	8	100	1	1	1	1	1	1	8	100	10,000	100
G_{12}	8/3	100	2,550	100	8/3	5	2,550	100	1	1	1	1
G_{23}	8/3	100	1	1	8/3	5	2,550	100	8/3	5	2,550	100
G_{13}	8/3	100	2,550	100	1	1	1	1	8/3	5	2,550	100
υ_{12}	100	100	100	100	1*	1	0.01	1	1*	1	1	1
υ_{23}	8	100	1	1	8	100	100	100	1	1	0.01	1
υ_{13}	100	100	100	100	1*	1	1	1	1*	1	0.01	1
					*100 if $\sigma_{22} < 0$				*100 if $\sigma_{33} < 0$			

	Mode σ_{12}				Mode σ_{23}				Mode σ_{13}			
	Whit	**Black**	**Zako**	**Tamma**	**Whit**	**Black**	**Zako**	**Tamma**	**Whit**	**Black**	**Zako**	**Tamma**
E_{11}	1*	1	1	2	1	1	1	1	1*	1	1	2
E_{22}	8	100	10,000	100	8	100	10,000	100	1	1	1	1
E_{33}	1	1	1	1	8	100	10,000	100	8	100	10,000	100
G_{12}	8/3	100	2,550	100	8/3	100	2550	100	1	1	1	100
G_{23}	1	1	2,550	100	8/3	100	10,000	100	1	1	2,550	100
G_{13}	1	1	1	100	8/3	100	2,550	100	8/3	100	2,550	100
υ_{12}	1*	1	0.01	2	1	1	0.01	1	1*	1	1	2
υ_{23}	8	100	100	100	8	100	1	100	1	1	0.01	1
υ_{13}	1*	1	1	2	1	1	0.01	1	1*	1	0.01	2
	*100 if $\sigma_{11}/S_{11} > 0.5$								*100 if $\sigma_{11}/S_{11} > 0.5$			

Table 6.2. Degradation factors for engineering elastic properties of the matrix.

	Mode σ_{11}		Mode σ_{22}		Mode σ_{33}	
	Whit	Tamma	Whit	Tamma	Whit	Tamma
E_{11}	8	100	1	1	1	1
E_{22}	1	1	8	100	1	1
E_{33}	1	1	1	1	8	100
G_{12}	8/3	100	8/3	100	1	1
G_{23}	1	1	8/3	100	8/3	100
G_{13}	8/3	100	1	1	8/3	100
υ_{12}	8	100	1	1	1	1
υ_{23}	1	1	8	100	1	1
υ_{13}	8	100	1	1	1	1

	All Modes	
	Zako	Black
E_{11}	10,000	100
E_{22}	10,000	100
E_{33}	10,000	100
G_{12}	10,000	5
G_{23}	10,000	5
G_{13}	10,000	5
υ_{12}	1	100
υ_{23}	1	100
υ_{13}	1	100

	Mode σ_{12}		Mode σ_{23}		Mode σ_{13}	
	Whit	Tamma	Whit	Tamma	Whit	Tamma
E_{11}	8	100	1	1	8	100
E_{22}	8	100	8	100	1	1
E_{33}	1	1	8	100	8	100
G_{12}	8	100	1	100	1	100
G_{23}	1	100	8	100	1	100
G_{13}	1	100	1	100	8	100
υ_{12}	8	100	1	1	8	100
υ_{23}	8	100	8	100	1	1
υ_{13}	8	100	1	1	8	100

6.3.3. Comparison of different property degradation models using common framework

Tables 6.1 and 6.2 can now be conveniently used to compare the amount of degradation under different property degradation models. The tables facilitate a comparison of the degradation factors for the tows as well as for the matrix under any failure mode.

The models differ from each other based on various things. First of all, different property degradation models sometimes degrade different engineering properties even under the same failure mode. For example, under failure mode σ_{11}, Whitcomb and Blackketter's models degrade all the 9 elastic properties, whereas Zako and Tamma's models do not degrade E_{22}, E_{33}, G_{23} and υ_{23}. The amount of degradation under one particular mode could also be different under different property degradation models. For example, under σ_{22} failure mode, G_{12} is degraded by 62.5%, 80%, 99.9% and 99% under Whitcomb, Blackketter, Zako and Tamma's models respectively.

It must be noted that under most of the damage modes, the Poisson's ratios υ_{12}, υ_{13} and υ_{23} are also degraded. But a careful examination of Table 6.1 shows that degradation factors for υ_{12} & υ_{13} are the same as the degradation factors for E_{11}, and the degradation factors for υ_{23} are the same as the degradation factors for E_{22} under all property degradation models but Zako's. The equality between degradation factors for υ_{12} & υ_{13} and E_{11}, and the equality between degradation factors for υ_{23} and E_{22} cause the off-diagonal coefficients of the compliance matrix to remain unchanged after damage. In the case of Zako's model, the off-diagonal coefficients of the compliance matrix also get affected.

Whitcomb's model is different from other's in one more regard. Whitcomb's model also degrades E_{11} modulus of the tow by 99% if the tow has failed under transverse compression. Whitcomb's model also treats degradation of E_{11}, υ_{12} and υ_{13} differently if under σ_{12} or σ_{13} failure mode, σ_{11} stress has exceeded at least half the S_{11} strength.

Last but a very important difference between different damage models is how

they handle the degradation of matrix elastic properties. Table 6.2 shows the degradation factors for the matrix. The table shows that Whitcomb and Tamma's model degrade the properties differently under different failure modes, whereas Zako and Blackketter's models degrade the properties by the same amount. An important consequence of this is that under Whitcomb and Tamma's models a material point that was isotropic to start with, can become anisotropic, whereas in Zako and Blackketter's models, all the matrix material points always remain isotropic. For the matrix failure, the maximum amount of degradation allowed by Whitcomb's model is 87.5%, both Tamma & Blackketter's model is 99% and by Zako's model is 99.99%.

6.4. Configurations

Three textile configurations were considered. The studied configurations and geometric parameters were based on experimental data available in the literature [38-39, 42]. One is plain weave consisting of E-glass and Vinyl ester. The other two are plain and twill weaves, both consisting of Graphite and Epoxy. Tows were assumed to be transversely isotropic and matrix to be initially isotropic. The elastic constants and ultimate strengths for these material systems were taken from ref. [38-39, 42] and are summarized in Table 6.3. The geometric parameters and fiber volume fractions for all the configurations are given in Table 6.4. V_{ft} is fiber volume fraction in the tow. It should be noted that the overall fiber volume fraction of plain weave configuration with E-glass/Vinyl ester material system is just 22%, which is quite low.

Table 6.3. Elastic and strength properties of tows and matrices [38-39, 42].

	Plain Weave		Twill Weave		Plain Weave	
	Tow Graphite/ Epoxy	**Matrix Epoxy**	**Tow Graphite/ Epoxy**	**Matrix Epoxy**	**Tow E-Glass/ Vinyl Ester**	**Matrix Vinyl Ester**
E_{11}	165	4.4	150	4.8	42.8	3.33
$E_{22} = E_{33}$	9.95	4.4	10	4.8	12.22	3.33
$G_{12} = G_{13}$	7.26	1.64	5.7	1.79	4.77	1.28
G_{23}	3.9	1.64	3.4	1.79	4.87	1.28
$\upsilon_{12} = \upsilon_{13}$	0.24	0.34	0.3	0.34	0.23	0.3
υ_{23}	0.5	0.34	0.5	0.34	0.25	0.3
	Ref: Riva et al. 1999		Ref: Zako et al. 2003		Ref: Riva et al. 2004	

All Moduli in GPa

	Plain Weave		Twill Weave		Plain Weave	
	Tow Graphite/ Epoxy	**Matrix Epoxy**	**Tow Graphite/ Epoxy**	**Matrix Epoxy**	**Tow E-Glass/ Vinyl Ester**	**Matrix Vinyl Ester**
S_{11}	2550	36	2550	36	2042	88.26
$S_{22} = S_{33}$	152	36	152	36	108.2	88.26
$S_{12} = S_{13}$	97	36	97	36	121.6	88.26
S_{23}	55	36	55	36	121.6	88.26
S_{11}^{C}	2550	36	2550	36	2982	117.7
$S_{22}^{C} = S_{33}^{C}$	152	36	152	36	242.3	117.7
	Ref: Blacketter et al. 1993		Ref: Zako et al. 2003		Ref: Blacketter et al. 1993	

All Strengths in MPa

Table 6.4. Geometric parameters of the analyzed configurations [38-39, 42].

Configuration	Material system	WR	V_{ft}	V_{fo}
1. Plain weave	Glass-Vinyl Ester	0.15	57%	22%
2. Twill weave	Graphite-Epoxy	0.08	70%	42%
3. Plain weave	Graphite-Epoxy	0.07	75%	48%

The finite element models of the three configurations are shown in Figs. 6.3-6.5. All the meshes have 20 node solid brick elements. Each element contains 27 Gauss quadrature points. Figure 6.3 shows the finite element meshes for plain weave with E-glass/Vinyl ester material system. This configuration has considerable gap between adjacent warp and fill tows, hence the overall fiber volume fraction is very low. This mesh is $1/16^{th}$ of a unit cell of plain weave's microstructure. Periodicity and symmetry with in the unit cell allowed the analysis this smaller region of the unit cell. Based on experimental configuration [42], the configuration is infinite in the in-plane directions and the top and bottom surfaces are free. So, essentially a lamina was analyzed. The mesh shown in Fig. 6.3 consists of 588 elements and 2907 nodes. Figure 6.4 shows the finite element mesh for plain weave configuration with Graphite/Epoxy material system. This mesh is 1/32nd region of the unit cell for symmetric stacking and contains 196 elements and 1037 nodes. Figure 6.5 shows the finite element mesh for the twill weave configuration. The mesh is one-fourth of a unit cell for symmetric stacking of mats. It contains 480 elements and 2158 nodes. The meshes shown in Figs 6.4 and 6.5 were periodic in in-plane as well as in out-of-plane directions. A symmetric stacking of mats was considered. The boundary conditions for all the configurations involve multi-point constrain relations and are provided in ref. [35-36]. All the models were applied a uni-axial tensile load along the warp direction. All the damage analyses were run on a dual core personal Pentium IV computer with 3.4 GHz processor. The runtime for the E-glass plain weave configuration was 6 hrs to go up 3% strain, the runtime for the Graphite plain weave configuration was 30 minutes to go up to 1.5% strain and it was 3 hours to go up to 2% strain for the twill weave configuration. The maximum strain level was selected based on the experimental data.

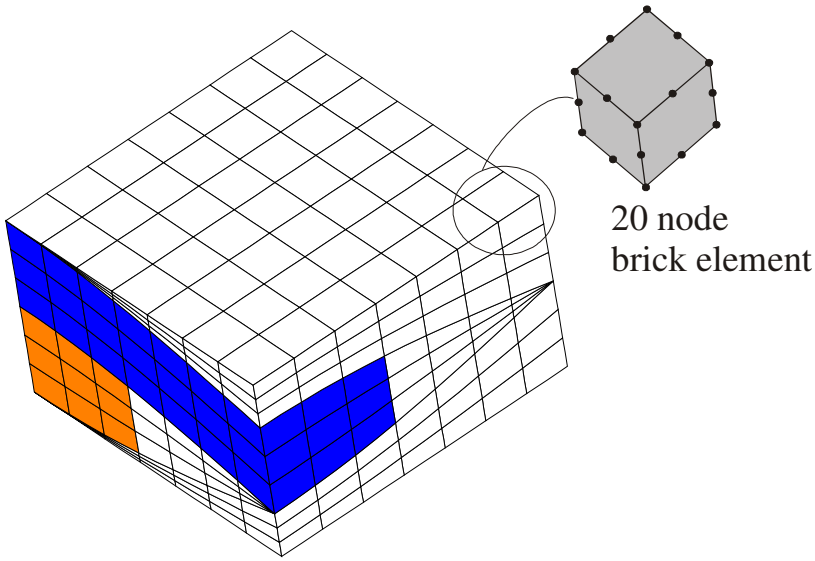

Figure 6.3. Finite element model of plain weave (E-glass/Vinyl ester configuration).

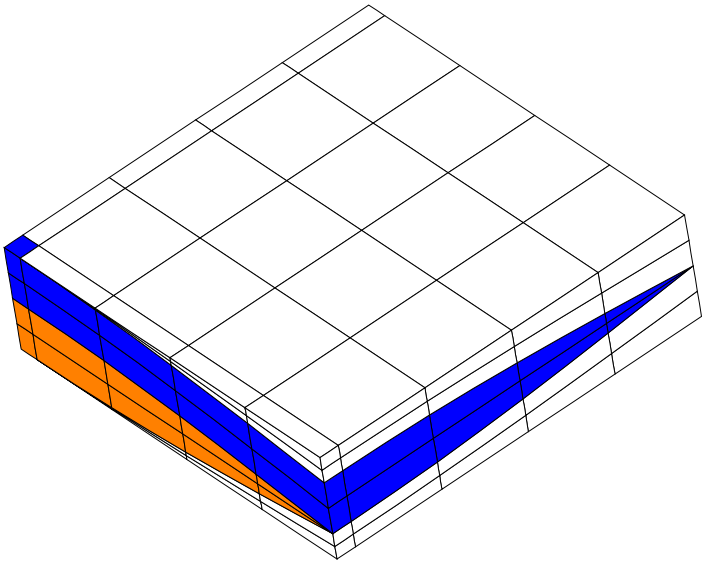

Figure 6.4. Finite element model of plain weave (Graphite/Epoxy configuration).

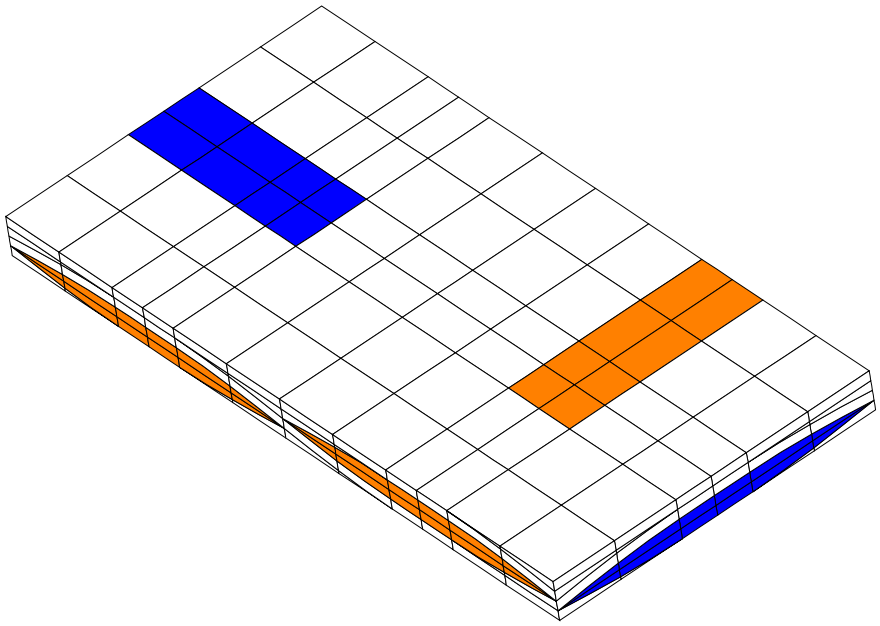

Figure 6.5. Finite element model of twill weave.

6.5. Results and Discussion

The effect of assumed damage model on macroscopic stress-strain behavior of different woven composites was investigated. The effect of making the property degradation models similar to each other is also investigated. Finally, a detailed examination of the damage initiation and progression in a Graphite/Epoxy plain weave composite is performed. This is presented in terms of percentage damaged volume of different components versus applied strain and stress volume distribution plots.

6.5.1. Effect of assumed damage model

In this work, a uni-axial tensile loading was applied on all the three configurations. Although Zako et al. proposed a different failure criterion in their work [42], it must be pointed out here that all the property degradations models used the same failure criterion so that the difference in predictions of different property degradation models can be reasonably compared.

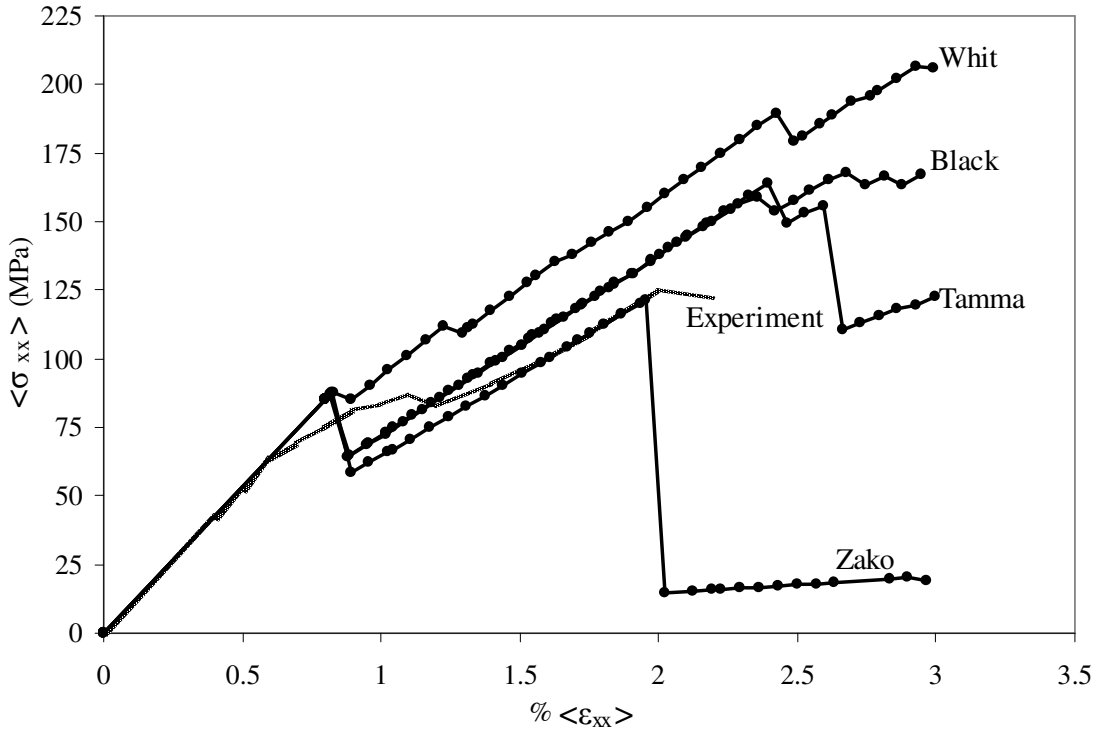

Figure 6.6. Predicted and experimental stress-strain behavior of E-glass/Vinyl ester plain weave configuration. Predictions using different property degradation models are shown.

Figure 6.6 shows the stress-strain predictions for the first configuration i.e. plain weave with E-glass/Vinyl ester material system. The predictions using different property degradation models are shown and compared with the experimental data [42]. The experimental data shows a gradual drop in the modulus from 0.5% to 1.2% strain levels. Zako, Blackketter and Tamma's model also accurately show failure initiation around 0.8% strain whereas Whitcomb's model shows a very small drop in modulus near that strain level. After the initial drop, the test shows that the stress in the material keeps on increasing with final failure at 2.2% strain. Zako's model predicts final failure accurately around 2% strain. But Whitcomb, Blackketter and Tamma's model do not predict final failure accurately. Tamma's model predicts considerable modulus drop around 2.6%

strain level, but Blackketter and Whitcomb's model are not able to capture the final failure at all in this case. In summary, Zako's model's predictions compares well with experimental data whereas the other three models do not.

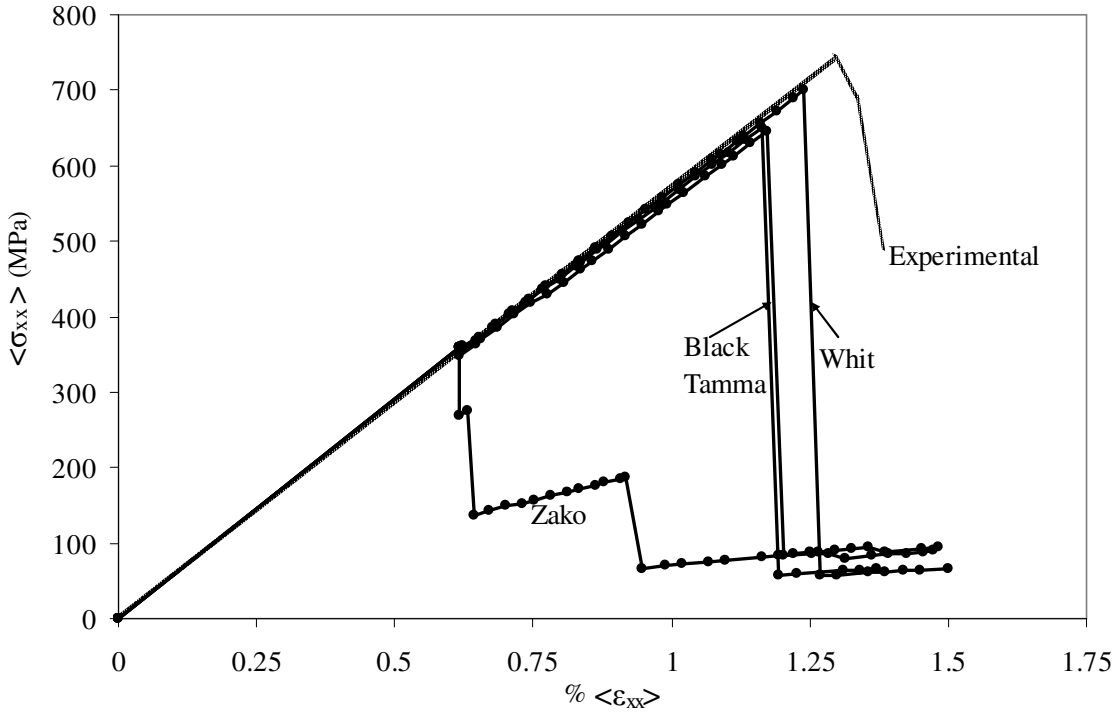

Figure 6.7. Predicted and experimental stress-strain behavior of Graphite/Epoxy plain weave configuration. Predictions using different property degradation models are shown.

The second configuration is a plain weave with a Graphite/Epoxy material system. The experimental stress-strain data [39] and predictions using different property degradations are shown in Fig. 6.7. It can be seen that experiments predict the failure strain to be 1.29% and the strength to be 743 MPa. In this weave, there is not any significant loss of stiffness and the final failure is due to sudden breakage of fibers in the warp tow. The finite element predictions match well with test data for initial modulus. Whitcomb, Tamma and Blackketter's models do not show any significant drop in

modulus till the final failure. Predictions of Whitcomb's model match the best with the experimental data. The final failure predicted by Whitcomb's model is around 1.25% strain and at a stress level of 700 MPa. Blackketter's and Tamma's model underpredict the failure stress and strain slightly. Both have very similar predictions with each other. These models predict the failure strain to be approximately 1.23% and failure stress to be around 650 MPa. Unlike for the previous configuration, Zako's model gives the worst predictions for this configuration. Zako's model predicts a considerable drop in stress level at very low strain levels of around 0.6%, and 0.9%. In summary, predictions of Whitcomb's model match very well with the test data, predictions of Blackketter and Tamma's models are very similar to each other and match reasonably well with the test data. Predicted stress strain curve with Zako's property degradation model is very different from the test data.

Lastly, a twill weave with Graphite/Epoxy material system was considered. Figure 6.8 shows the stress-strain predictions for this weave. The figure shows experimental data, predictions of four property degradation models and two curves for Riva et al.'s [38] finite element predictions. One is their FE predictions with constant load step and the other using variable load step. Riva et al. used Blackketer's property degradation model. The experimental data for this material system shows that there is not much loss of stiffness as the load increases. The final failure is a brittle failure with fiber breakage being the main event leading to the collapse of the composite. The experimental data shows that the failure strain of the composite is 1.35% and the strength is 810 MPa. Using four property degradation models, the predicted stress-strain curves lie on top of experimental data to start with. Predictions using Whitcomb, Blackketter and Tamma's models show small reduction in stiffness from around 0.5% strain to 1.35% strain. At approximately 1.35% strain, all these three models predict a large drop in stress indicating final failure of the composite. All three models also predict a failure stress that matches very well with the experimental data. Zako's property degradation model

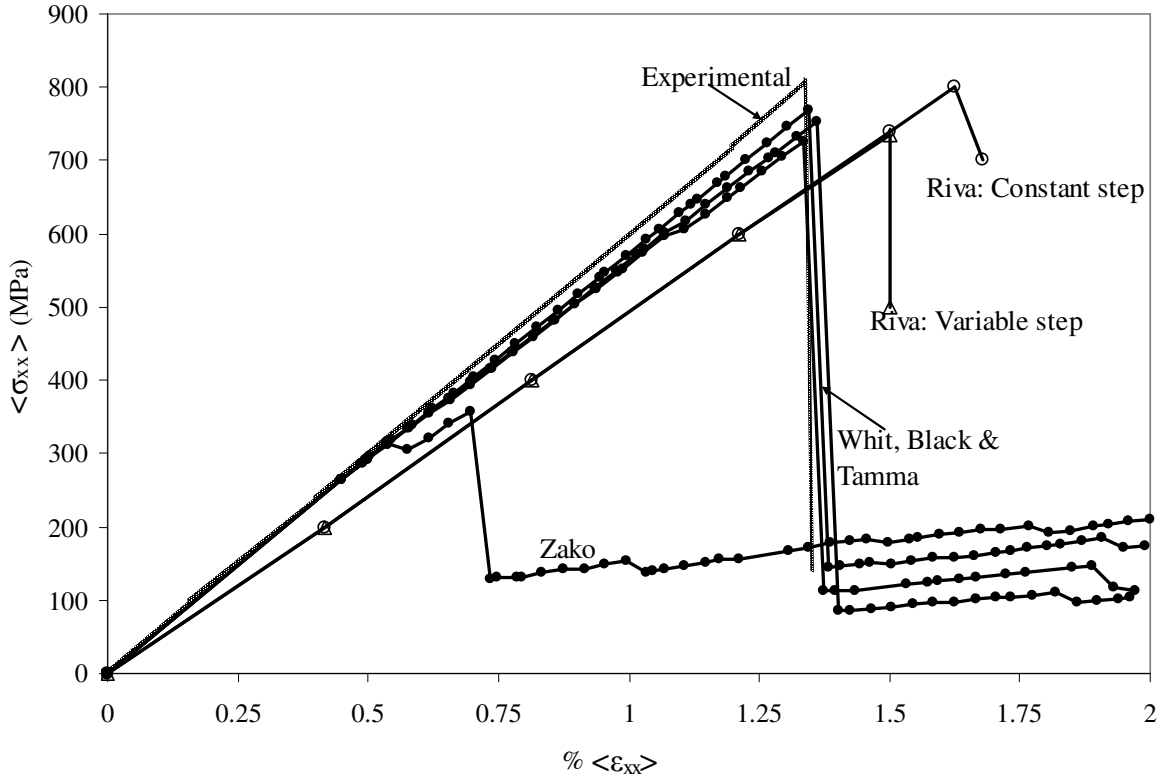

Figure 6.8. Predicted and experimental stress-strain behavior of Graphite/Epoxy twill weave configuration. Predictions using different property degradation models and FE predictions by Riva et al. [38] are also shown.

predicts a stress-strain response that shows large differences from the test data. This model predicts small drop in modulus around 0.6% strain and predicts the failure strain and stress to be 0.7% and 350 MPa respectively. Both failure strain and stress values show large differences from experimental data. Riva et al.'s [38] finite element model also predicts failure stress which is close to the test data but over predicts the failure strain, which could be due to the fact that the modulus is under predicted by their model to begin with. In short, Whitcomb, Blackketer and Tamma's property degradation models predict the failure stress and strains that match well with the test data, where as Zako's property degradation model considerably under predict failure stress and strain.

In summary, predictions of property degradation models of Whitcomb, Blackketter and Tamma match well with the test data for woven composite configurations with Graphite/Epoxy material system and Zako's model has poor predictions for this material system. In contrast, Zako's model's predictions match very well for S-glass/Vinyl ester material system configuration whereas other three models over predict failure stress and strain considerably for that material system.

To investigate the reasons for having different predictions with different property degradation models, below we investigate the effect of making some degradation parameters similar to each other.

6.5.2. Effect of tweaking the property degradation models

In the previous section, it was seen that some property degradation models predict the damage initiation and progression behavior better for one material system and others predict better for the other material system. Below, some of the parameters in different property degradation models were tweaked so that the models are similar to each other. It must be noted that that the degradation parameters were made similar but not exactly the same.

Tables 6.5 and 6.6 show the tweaked property degradation models. Whitcomb's model was chosen as reference property degradation models and the degradation parameters for others were made similar to Whitcomb's model. The key features of the other property degradation models were not changed at all. For example, the particular elastic constants that a particular damage model degrades under a particular failure model were not altered, only the amounts of degradations were altered.

In Tables 6.5 and 6.6, the degradation parameters that are highlighted are exactly the same as the reference, which is Whitcomb's model, whereas the degradations parameters that are not highlighted are not similar to the reference. Blackketter's degradation parameters for the tow are very similar to the reference, except for the cases where the reference gives special allowance for the tow failure under transverse

Table 6.5. Degradation factors, when made similar, for engineering elastic properties of the tow.

	Mode σ_{11}				Mode σ_{22}				Mode σ_{33}			
	Whit	**Black**	**Zako**	**Tamma**	**Whit**	**Black**	**Zako**	**Tamma**	**Whit**	**Black**	**Zako**	**Tamma**
E_{11}	100	100	8	100	1*	1	1	1	1*	1	1	1
E_{22}	8	8	1	1	8	8	8	8	1	1	1	1
E_{33}	8	8	1	1	1	1	1	1	8	8	8	8
G_{12}	8/3	8/3	3.66	8/3	8/3	8/3	3.66	8/3	1	1	1	1
G_{23}	8/3	8/3	1	1	8/3	8/3	3.66	8/3	8/3	8/3	3.66	8/3
G_{13}	8/3	8/3	3.66	8/3	1	1	1	1	8/3	8/3	3.66	8/3
υ_{12}	100	100	2.83	100	1*	1	0.35	1	1*	1	1	1
υ_{23}	8	8	1	1	8	8	2.83	8	1	1	0.35	1
υ_{13}	100	100	2.83	100	1*	1	1	1	1*	1	0.35	1
					*100 if $\sigma_{22} < 0$				*100 if $\sigma_{33} < 0$			

	Mode σ_{12}				Mode σ_{23}				Mode σ_{13}			
	Whit	**Black**	**Zako**	**Tamma**	**Whit**	**Black**	**Zako**	**Tamma**	**Whit**	**Black**	**Zako**	**Tamma**
E_{11}	1*	1	1	2	1	1	1	1	1*	1	1	2
E_{22}	8	8	8	8	8	8	8	8	1	1	1	1
E_{33}	1	1	1	1	8	8	8	8	8	8	8	8
G_{12}	8/3	8/3	3.66	8/3	8/3	8/3	3.66	8/3	1	1	1	8/3
G_{23}	1	1	3.66	8/3	8/3	8/3	8.00	8/3	1	1	3.66	8/3
G_{13}	1	1	1	8/3	8/3	8/3	3.66	8/3	8/3	8/3	3.66	8/3
υ_{12}	1*	1	0.35	2	1	1	0.35	1	1*	1	1	2
υ_{23}	8	8	2.83	8	8	8	1	8	1	1	0.35	1
υ_{13}	1*	1	1	2	1	1	0.35	1	1*	1	0.35	2
	*100 if $\sigma_{11}/S_{11} > 0.5$								*100 if $\sigma_{11}/S_{11} > 0.5$			

Table 6.6. Degradation factors, when made similar, for engineering elastic properties of the matrix.

	Mode σ_{11}		Mode σ_{22}		Mode σ_{33}	
	Whit	Tamma	Whit	Tamma	Whit	Tamma
E_{11}	8	8	1	1	1	1
E_{22}	1	1	8	8	1	1
E_{33}	1	1	1	1	8	8
G_{12}	8/3	8/3	8/3	8/3	1	1
G_{23}	1	1	8/3	8/3	8/3	8/3
G_{13}	8/3	8/3	1	1	8/3	8/3
υ_{12}	8	8	1	1	1	1
υ_{23}	1	1	8	8	1	1
υ_{13}	8	8	1	1	1	1

	All Modes	
	Zako	Black
E_{11}	8	8
E_{22}	8	8
E_{33}	8	8
G_{12}	8	8/3
G_{23}	8	8/3
G_{13}	8	8/3
υ_{12}	1	8
υ_{23}	1	8
υ_{13}	1	8

	Mode σ_{12}		Mode σ_{23}		Mode σ_{13}	
	Whit	Tamma	Whit	Tamma	Whit	Tamma
E_{11}	8	8	1	1	8	8
E_{22}	8	8	8	8	1	1
E_{33}	1	1	8	8	8	8
G_{12}	8	8/3	1	8/3	1	8/3
G_{23}	1	8/3	8	8/3	1	8/3
G_{13}	1	8/3	1	8/3	8	8/3
υ_{12}	8	8	1	1	8	8
υ_{23}	8	8	8	8	1	1
υ_{13}	8	8	1	1	8	8

compression, and considerably large tow tensile stress in conjunction with σ_{12} or σ_{13} failure modes. As far as degradation parameters for matrix are concerned, Blackketter's degradation parameters were reduced from 100 to 8 for the tensile moduli and from 5 to 8/3 for shear moduli (see Table 6.6). For the matrix, Blackketter's degradation parameters are still very different from the reference because Blackketter's model changes the properties in a similar manner for all the failure modes for matrix.

As discussed in section 6.3.1, Zako's formulation is basically different, hence Zako's parameter's were tweaked in a unique way. The value of F in Eqn. (6.4) was changed to be 0.6466, which gave E_{22} under σ_{22} failure mode as 8, which was a match. Using this technique, some other parameters like degradation for E_{33} under σ_{33} failure mode, degradation for E_{22} and E_{33} under σ_{23} failure mode etc also matched. Like Blackketter's model, Zako's model also considers the same amount of degradation of elastic properties under different failure modes for the matrix. For the matrix, Zako's model was tweaked from a factor of 10,000 to a factor of 8 for all the tensile and shear moduli. Hence, whenever any failure mode occurred in the matrix, all the tensile and shear moduli of the matrix were degraded by 87.5% as compared to 99.99% earlier.

Lastly, Tamma's factors were changed to match with the reference. In Tamma's model, whenever a property is degraded, it is degraded by 99% of the original value. Tamma's degradation parameters were tweaked to allow for smaller degradation to match with the reference. The amount of degradation was reduced from 99% to 87.5% (factors changed from 100 to 8) for the tensile moduli (except for E_{11} under σ_{11} failure mode, which was already a match) and from 99% to 62.5% (factors changed from 100 to 8/3) for the shear moduli. This was done both for tows as well as for the matrix. The matched degradation parameters are shown in Tables 6.5 and 6.6 using highlighted areas.

Now we discuss how the predictions changed after the parameters in different property degradations models were tweaked to match with the reference.

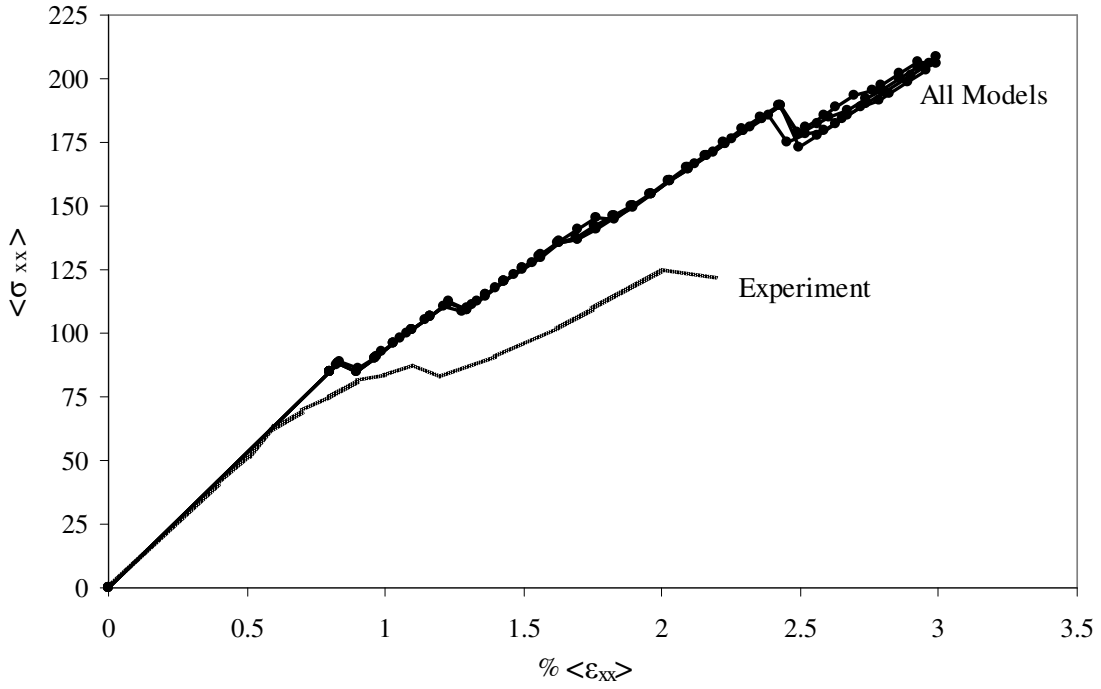

Figure 6.9. Predicted and experimental stress-strain behavior of E-glass/Vinyl ester plain weave configuration. Predictions using different property degradation models, when damage factors were made similar, are shown.

Figure 6.9 shows the stress-strain behavior of plain weave consisting of E-glass/Vinyl ester material system after the degradation factors were tweaked. The predictions of different damage models are very similar to each other now. If we compare the predictions with the experiments, none of the predictions match well with the experimental data. Zako's model, whose predictions matched well with the experimental data earlier (see Fig. 6.6), is not matching well anymore.

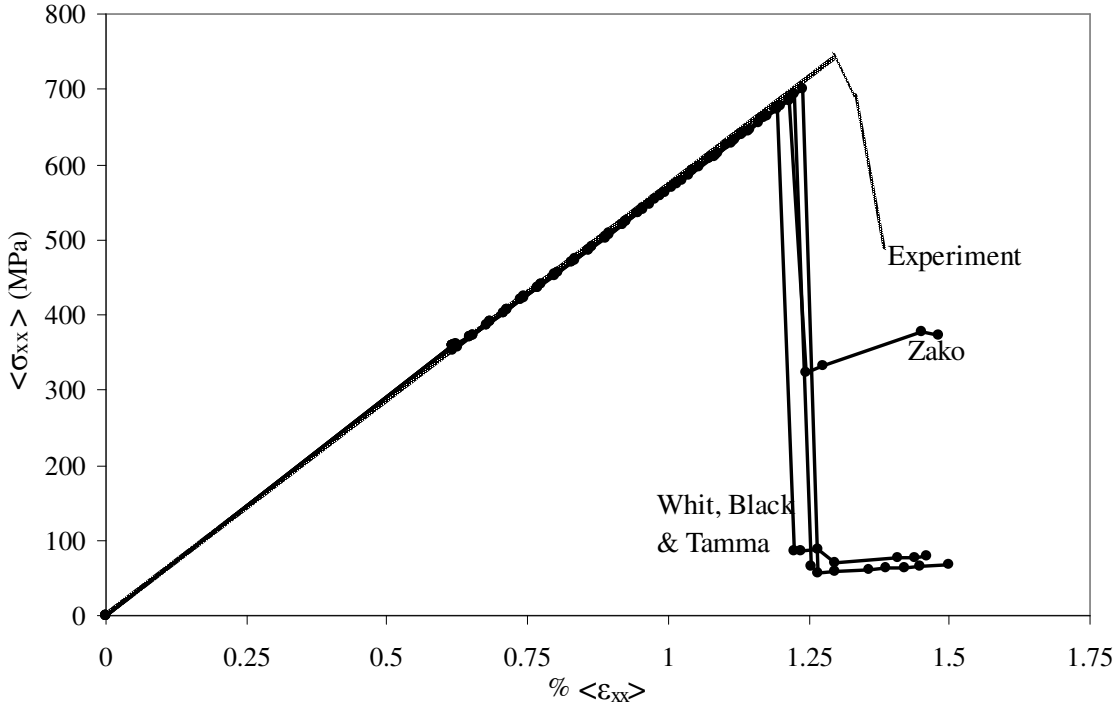

Figure 6.10. Predicted and experimental stress-strain behavior of Graphite/Epoxy plain weave configuration. Predictions using different property degradation models, when damage factors were made similar, are shown.

Figure 6.10 shows the stress-strain predictions of all the models for Graphite/Epoxy plain weave composite when damage factors were made similar. In this case also, the predicted response with different property degradation models is very similar to each other. All the models predict the failure stress and strain very reasonably. The experimental data shows the failure strain to be 1.29% and strength to be 743 MPa. All four models predict the failure strain to be around 1.25% and the failure stress to be around 700 MPa. Unlike earlier (see Fig. 6.7), there is tremendous improvement in predictions with Zako's damage model. Earlier Zako's model predicted a considerable drop in stress level at very low strain level (around 0.6% strain) and final failure strain to be around 0.9%. After tweaking the damage factors, Zako's model also predicted the final failure strain and stress very well. Though the Zako's model still does not predict

the final failure as well as the other three models because predictions using the tweaked Zako's model show that some load bearing capacity of the composite is still in tact (see the corresponding stress-strain curve around 325 MPa stress level in Fig. 6.10).

In summary, when the degradation factors of different models were tweaked, we saw that the predictions of different damage models were very similar to each other and did not necessarily match well with the experimental data. The main conclusion from this exercise is that although different property degradation models may degrade different elastic properties under particular failure modes, failure initiation, progression and final failure predictions are quite sensitive to the amounts of degradation parameters. If the amounts of degradations are similar, predicted response is similar even when properties to be degraded are not exactly the same.

6.5.3. Detailed damage analysis

In the previous section, we discussed the macroscopic stress-strain behavior of the woven composites. In this section, a detailed examination of the damage initiation and progression in a Graphite/Epoxy plain weave composite is discussed. Whitcomb's property degradation model is considered since that model yielded the most reasonable predictions for this particular composite. Below, a detailed examination is done in terms of % damaged volume at various strain levels, plots showing the failed locations and stress volume distribution plots.

6.5.3.1. Percentage damaged volume of different components versus applied strain

Figure 6.11 shows the macroscopic stress strain predictions for the configuration. The damage initiates at a strain level of around 0.62%. There is very little drop in E_{xx} modulus of the composite till a strain level of 1.24%. After that, the composite suddenly fails and a large stiffness loss is observed. Below, we examine what failure modes are active and how the damage initiates and progresses.

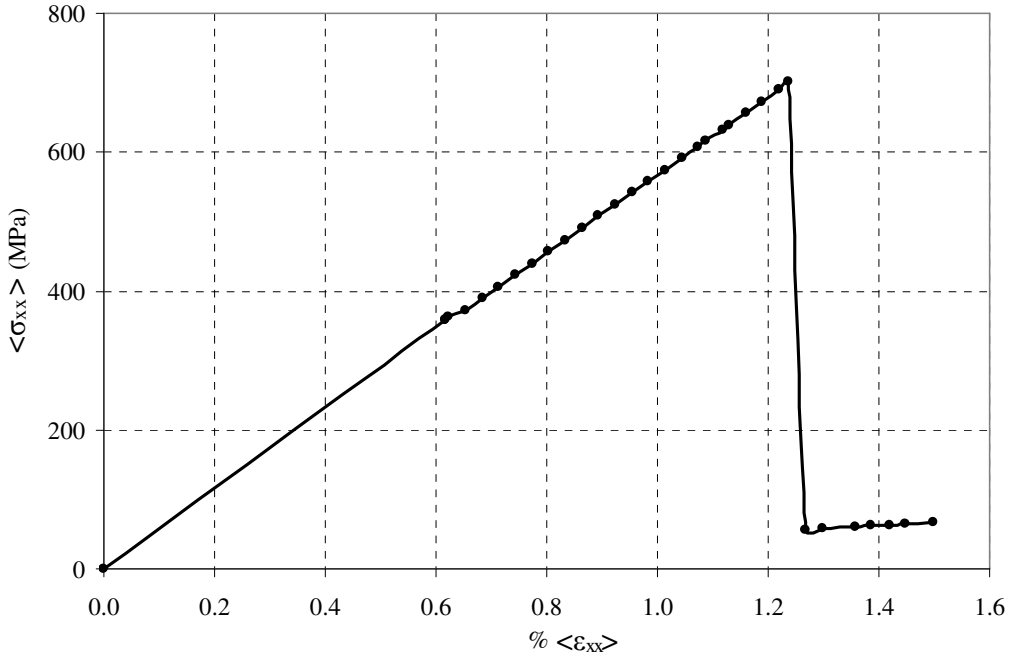

Figure 6.11. Predicted stress-strain response of Graphite/Epoxy plain weave composite using Whitcomb's property degradation.

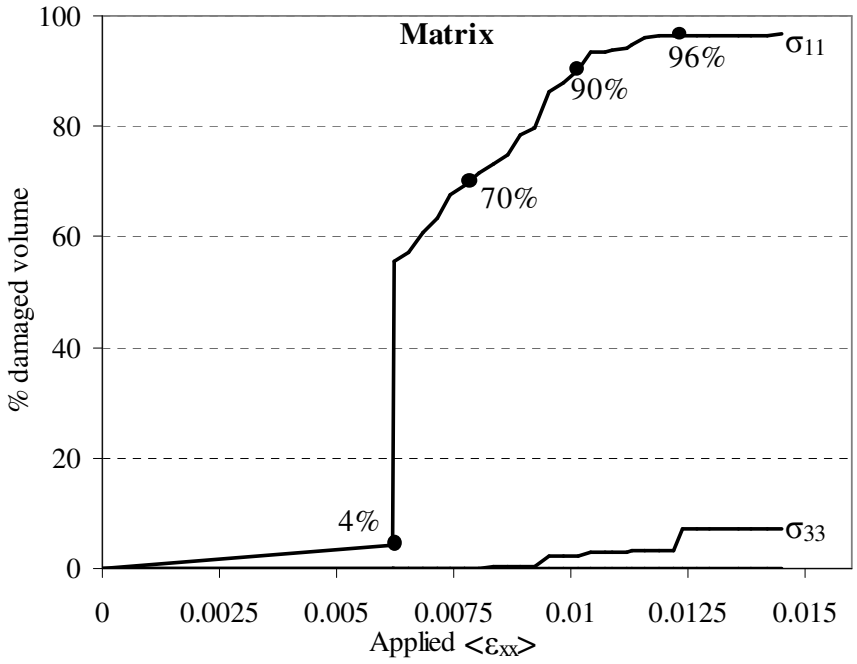

(a) Damaged volume versus strain in the matrix

Figure 6.12. Variation of damaged volume at different strain levels in the Graphite/Epoxy plain weave composite.

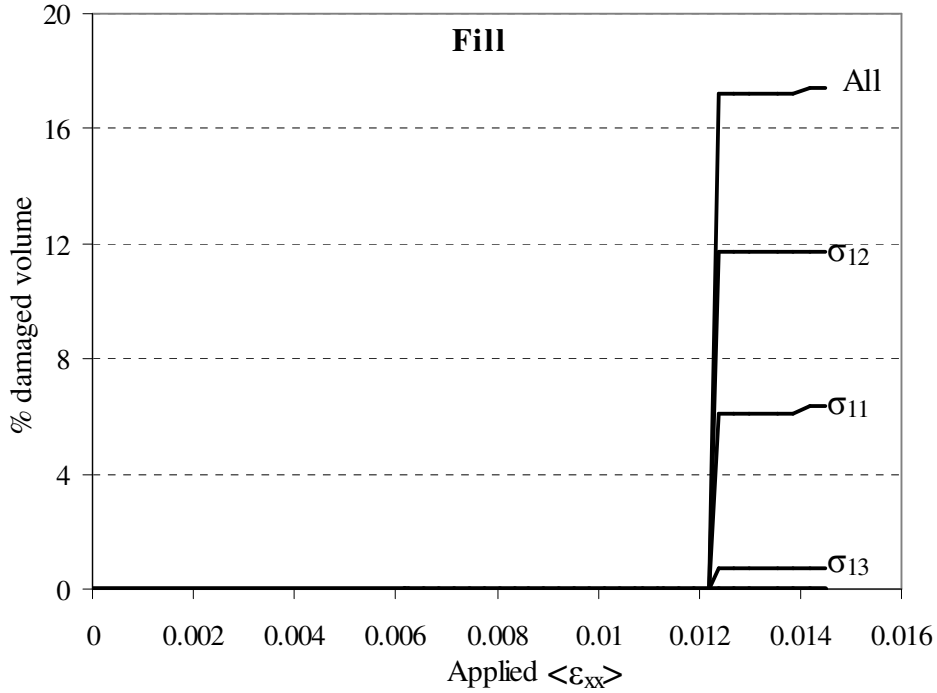

(b) Damaged volume versus strain in the fill tow

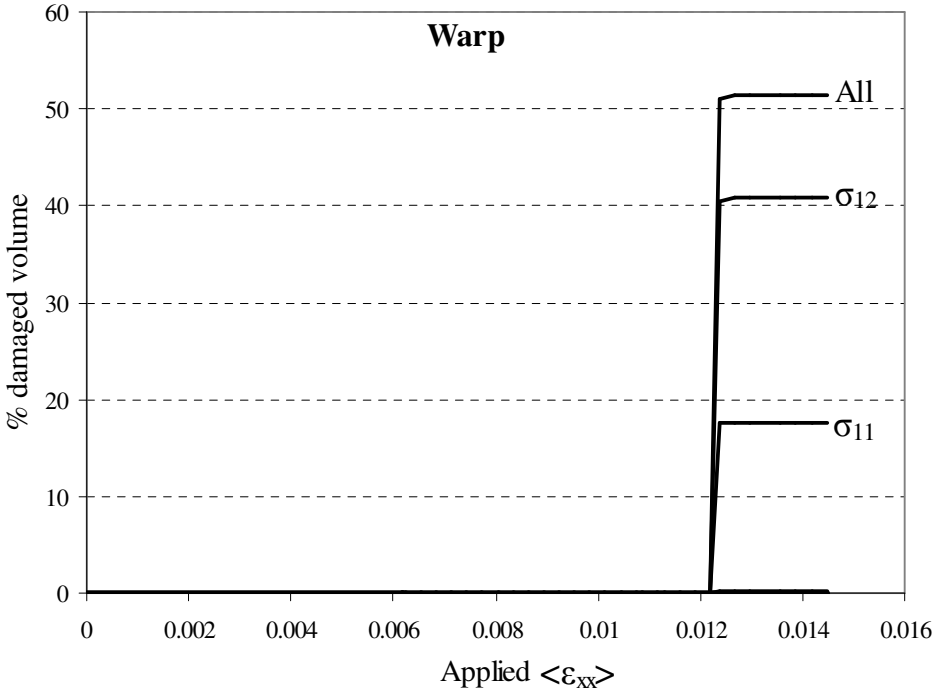

(c) Damaged volume versus strain in the warp tow

Figure 6.12. Continued.

Figure 6.12 shows the variation of damaged volume versus the macroscopic strain level in different components of the composite. The damaged volume for the warp tow, fill tow and the matrix is shown separately in Figs. 6.12 (a), (b) and (c) respectively. Figure 6.12 (a) shows the variation of % damaged volume of the matrix versus applied macroscopic strain to the model. Failure mode σ_{33} causes some damage, but it can be seen that majority of the failure in matrix occurs due to σ_{11} failure mode. This implies the occurrence of transverse matrix cracks in the matrix pockets.

Table 6.7. Percentage damaged volume of different components at different strain levels.

Warp	No damage until 1.24% strain	
Fill	No damage until 1.24% strain	
Matrix	**% strain level**	**% of matrix damaged**
	0.62	4
	0.77	70
	1	90
	1.24	96

Table 6.7 shows that at 0.62% strain, 4% of the matrix volume is damaged under σ_{11} stress. This increases to 70% and 90% at 0.77% and 1% strain levels respectively. At about 1.24% strain, 96% volume of the matrix is damaged. This means almost whole of the matrix is saturated with transverse matrix cracks and would have stopped supporting any load along the applied (longitudinal) direction. Figure 6.13 shows the damage locations in the matrix at different strain levels. The figure shows that the damage starts near thin matrix pockets and moves towards thicker material.

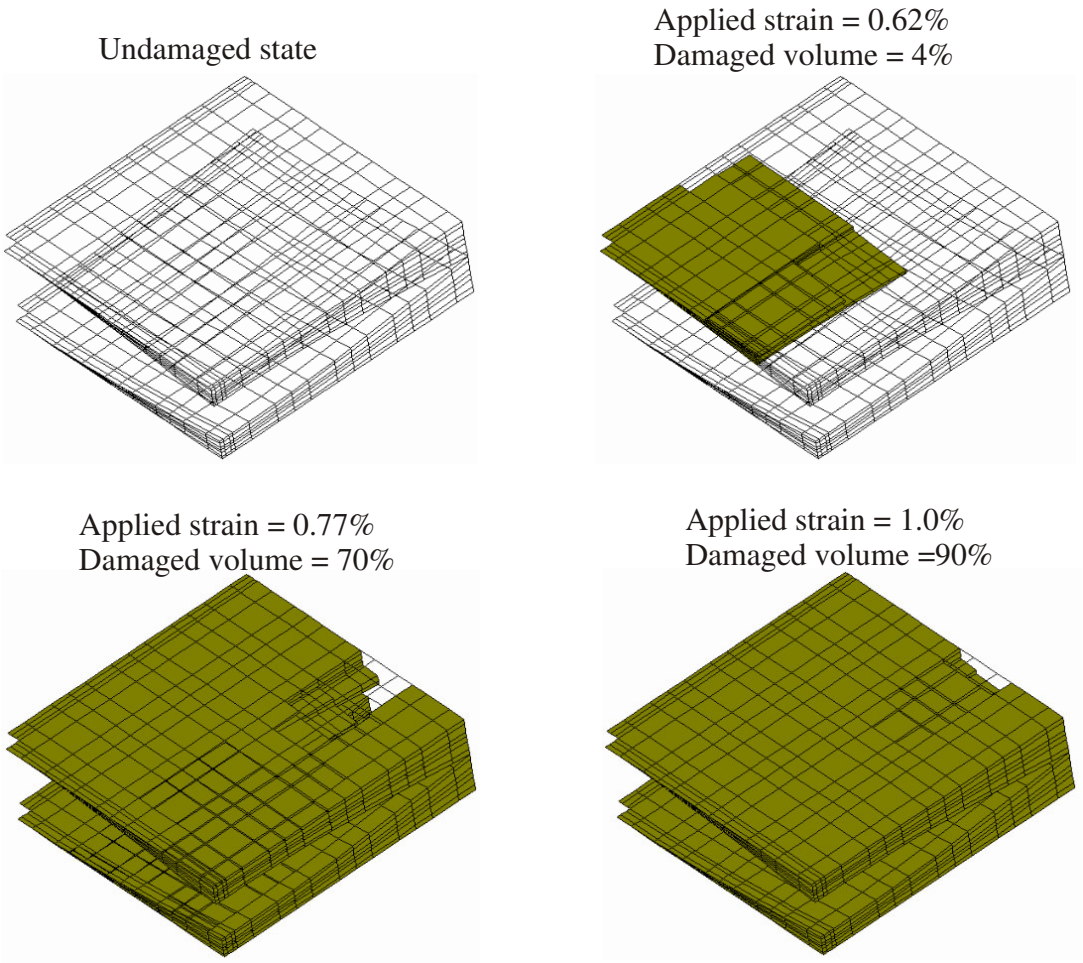

Figure 6.13. Damage evolution in matrix.

For fill and warp tows, no damage starts until 1.24% strain. Figure 6.12(b) shows damaged volume under different failure modes as well as total damaged volume in the fill tow. Fig. 6.12 (b) shows that until 1.24% strain, the whole of the fill tow is intact and no damage has occurred. At a strain level of 1.24%, σ_{13}, σ_{11} and σ_{12} failure modes come into play and damage the fill tow. The σ_{13} failure mode causes little damage (around 1% of the fill tow) whereas σ_{12} failure mode causes maximum damage (around 12%) of the fill tow. Almost 16% of the fill tow is damaged at 1.24% strain level. It should be noted that the % damaged volume caused by different damage modes might not add up to the total % damaged volume because multiple damage modes are sometimes active at the

same time (i.e. at a particular strain level). Figure 6.12(c) shows that for warp tow, only σ_{11} and σ_{12} failure modes cause considerable damage. Like fill tow, no damage is seen till 1.24% strain and after that σ_{11} damages 18% of the warp tow and σ_{12} damages more than 40% of the warp tow. Around 52% of the warp tow is damaged at 1.24% leading to the collapse of the composite.

6.5.3.2. Stress volume distribution plots

Figure 6.14 shows the σ_{xx} stress volume distribution in the warp tow at different strain levels. Figure 6.14(a) is for the absolute σ_{xx} stress distribution and shows that as the strain level increase from 0.62% to 1.24% strain, the average stress in the warp tow is also increasing. The stress volume distribution lines are also almost vertical meaning that a large volume of the tow has uniform stress state. As soon as the load level exceeds 1.24% strain, global failure takes place, average stress in the warp tow drops considerably, and a wide variation in σ_{xx} distribution in the warp tow takes place. Figure 6.14(a) shows that, at 1.27% and 1.5% strain levels, σ_{xx} stress range in the warp tow expands. In Fig. 6.14(b), the σ_{xx} stress is normalized by applied volume averaged stress to the model. From 0.62% to 1.24% strain levels, the stress distribution curves lie almost on top of each other suggesting almost a linear variation in the σ_{xx} stress. But as soon as the strain exceeds the failure strain of 1.24%, the curves flatten and vary considerably from the lower strain level curves.

Figure 6.15 shows the σ_{xx} stress volume distribution in the fill tow throughout the load history. The σ_{xx} distribution in the fill tow is very similar to that in the warp in the sense that the most of the volume of the fill has uniform stress state. Also, the average stress keeps on increasing linearly until final failure has occurred. Before failure, the normalized stress magnitude is much less in the fill tow as compared to the warp tow. The normalized σ_{xx} in the warp is around 17 times that in fill tow and the warp modulus along the x direction (which is loading direction) is also around 17 times the fill tow modulus along that direction. Whether this observation is coincidental or not requires further study.

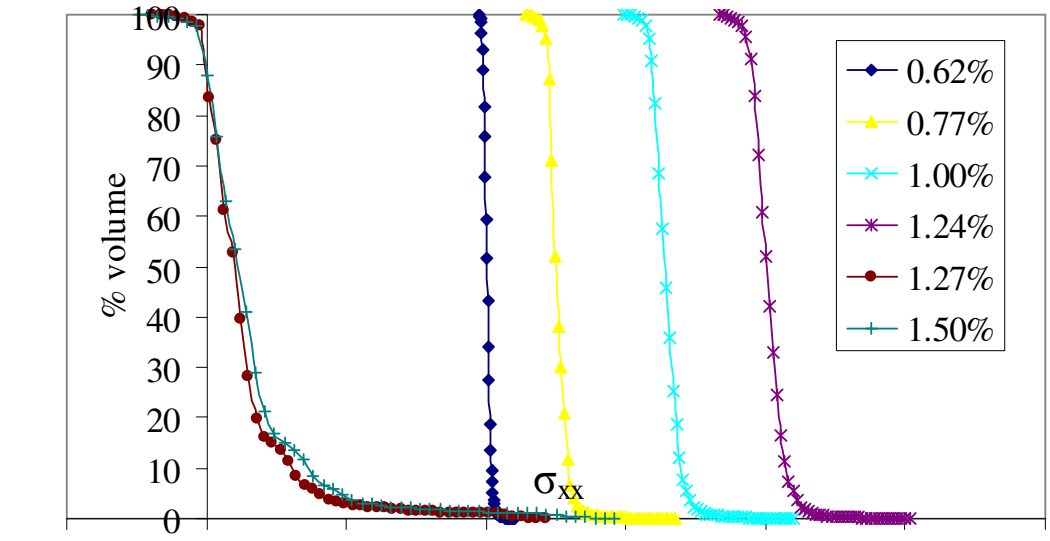

(a) Absolute stress is plotted

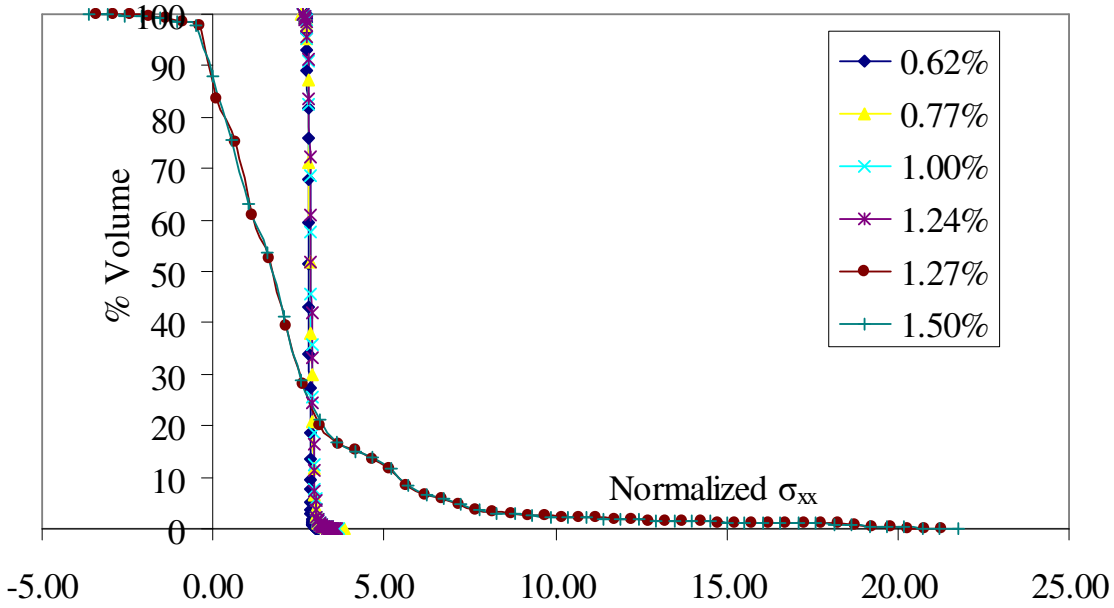

(b) Normalized (by volume averaged stress applied to the model) stress is plotted

Figure 6.14. σ_{xx} stress volume distribution in the warp tow at various strain levels.

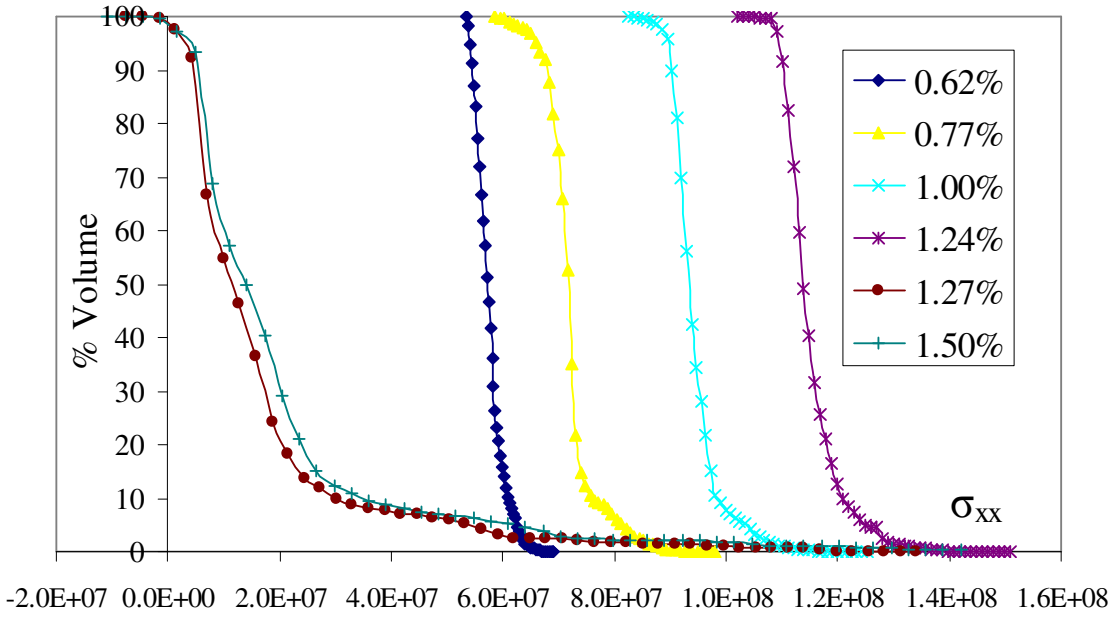

(a) Absolute stress is plotted

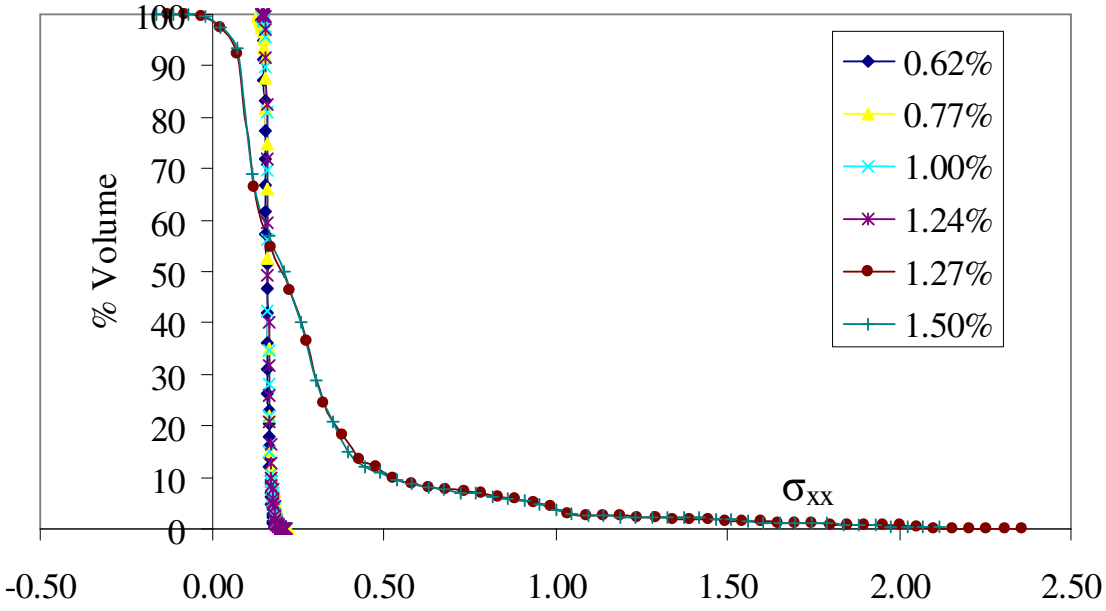

(b) Normalized (by applied volume averaged stress to the model) stress is plotted

Figure 6.15. σ_{xx} stress volume distribution in the fill tow at various strain levels.

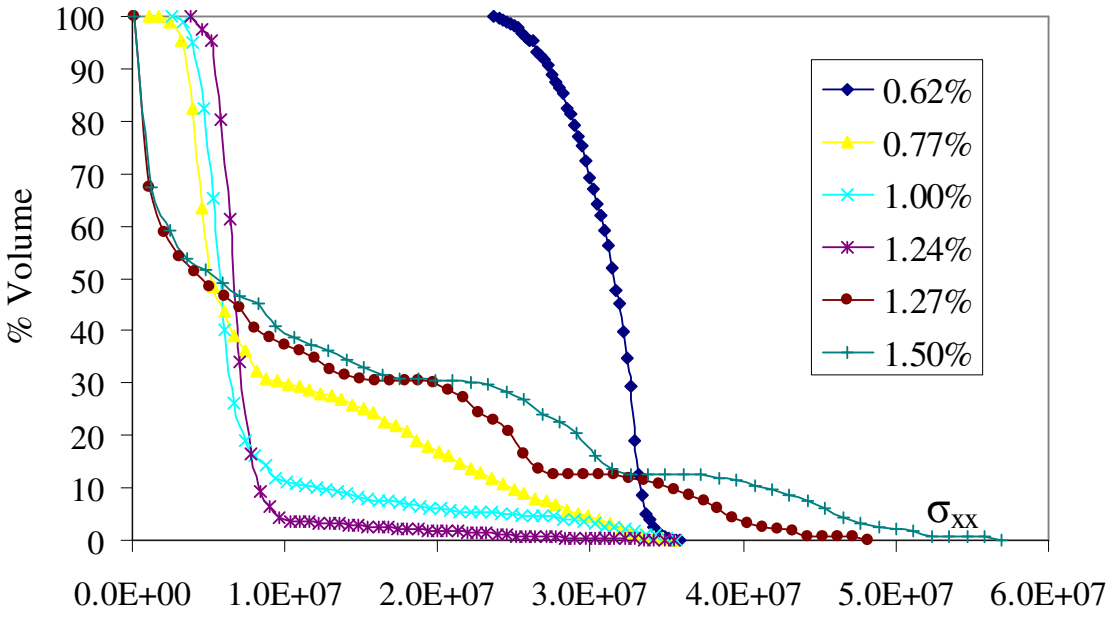

(a) Absolute stress is plotted

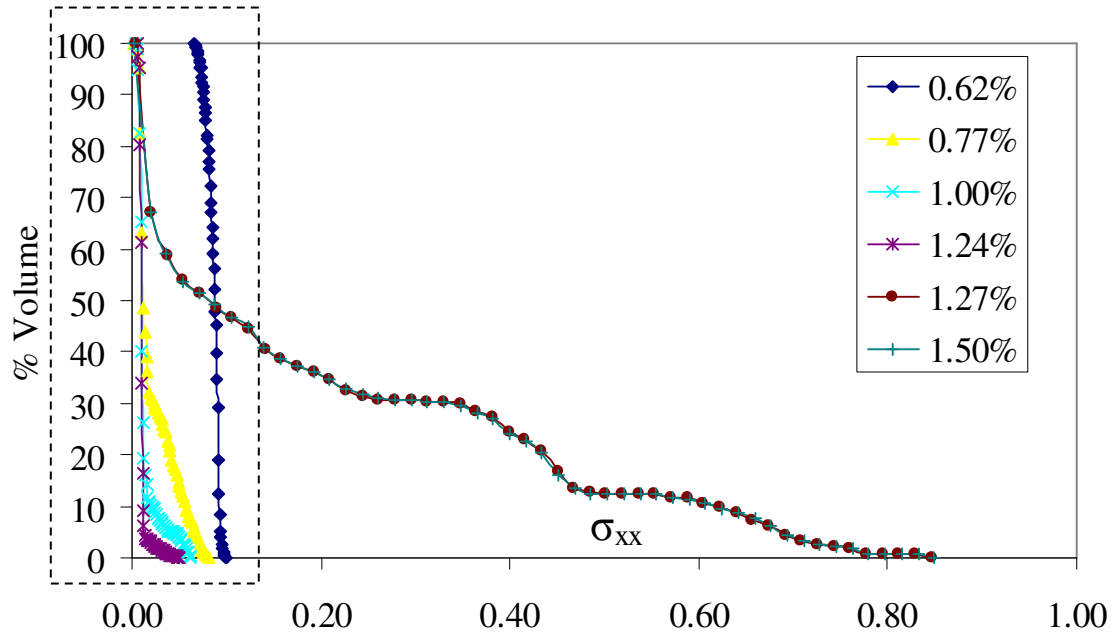

(b) Normalized (by volume averaged stress applied to the model) stress is plotted

Figure 6.16. σ_{xx} stress volume distribution in the matrix at various strain levels.

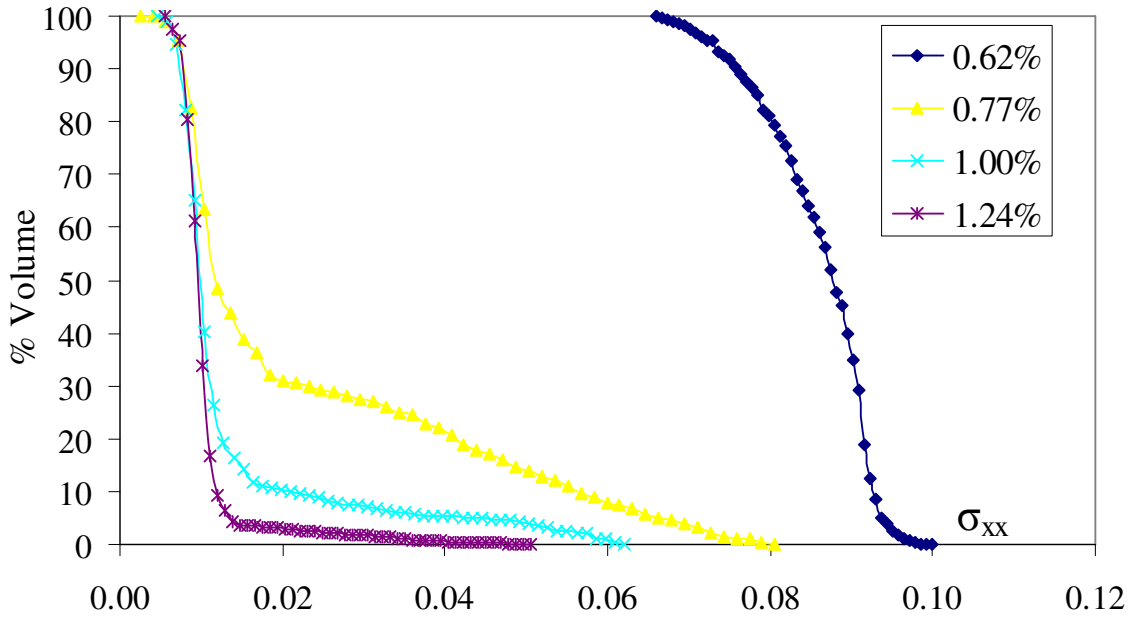

(c) Narrower range (inset of (b) above) of normalized stress (only up to 0.1% strain) is plotted

Figure 6.16. Continued.

Figure 6.16 shows the σ_{xx} volume distribution in the matrix. At 0.62% strain, very little (only 4%, see Fig. 6.13) of the matrix volume has damaged and the variation in the σ_{xx} stress is not much. After 0.77% strain when 70% of the matrix has damaged, the stress volume distribution curves show large variations in the stress state. Figure 6.16(b) shows the variation of normalized σ_{xx}. Unlike warp and fill tows, the variation of σ_{xx} is not linear, so as strain increases from 0.62% to 1.24%, the curves do not lie on top of each other. This happens because of damage progressions in matrix from 0.62% to 1.24% strain. Figure 6.16(c) shows that as the damage in matrix progresses, the load redistribution takes place and average stress is decreasing in the matrix. Also, the peak stress values in the matrix decrease as the strain increases from 0.62% to 1.24% strain due to damage progression in the matrix only. As soon as damage initiates in the warp and fill tows after 1.24% strain, the matrix again picks up load and normalized stress increases in the matrix as shown by Fig. 6.16(b).

6.6. Summary

A framework to allow use of a wide variety of damage initiation and growth models was presented. Four different damage models in terms of degradation of engineering elastic properties were implemented. The models differ in terms of amount of degradation as well as the properties to be degraded under a particular failure mode. All the models degrade only diagonal terms in compliance matrix except for Zako's model, which degrades off-diagonal terms also. Zako's model gave fairly good predictions for Glass/Epoxy plain weave composite whereas other models predicted well for Graphite/Epoxy plain and twill weave composites. All the models predicted similar response when damage factors were made similar, which shows that the magnitude of damage factors are very important even when all the models do not degrade the same engineering properties under particular failure modes. Stress volume distribution plots for the warp, fill and matrix show that before the damage initiates, the average stress is uniform in most of the volume of the component. Damage initiation in any component increases the range of stress in that component considerably.

7. PLASTICITY INDUCED NON-LINEARITY IN 2x2 BRAIDED COMPOSITES

Braided composites show considerable non-linear stress-strain behavior, which could be due to geometric (caused by tow waviness) or material non-linearity (due to plasticity or progressive damage). The effect of material damage was studied in the previous chapter. In this chapter, plasticity-induced nonlinearity in braided composites is investigated. There are several reasons for this effort. Firstly, conventional matrix materials used to make textile composites exhibit significant inelastic response. Secondly, due to fiber tow interlacing and undulation, the local stress concentrations are significant [74] and could cause material yielding at low overall stress level. Although such plastic deformation may be contained by the surrounding elastic material, it could be significant in cyclic loading situations

Figure 2.4 shows the experimental stress–strain data for ±45˚ and ±25˚ VARTM manufactured Carbon/Epoxy braids subjected to uni-axial tension in the longitudinal direction [45]. The figure shows the response is highly non-linear. At 1% strain, ±45˚ braided composite has lost 54% of its initial tangent tensile modulus and ±25˚ braid has lost 36% of its initial tangent modulus. At 2% strain, the ±45˚ braided composite has lost 76% of its initial tangent tensile modulus and ±25˚ braid has lost 78% of its initial tangent modulus.

The effect of plastic deformation on the stress-strain behavior of braided composites is analyzed using finite element modeling. As illustrated in Fig. 2.1, a two scale modeling approach [47] was used. The first scale, which is called the *fiber/matrix scale* herein, predicts the effective elastic and plastic properties of the tow from the properties of the constituent fiber and resin. The second scale, which is called the *tow architecture scale* herein, models the composite unit cell and utilizes the properties predicted by the first scale for the tow. The details of the two scale modeling approach will be given later. This modeling approach was used to predict the behavior of 2x2 braided AS4, E-glass, and S-glass composites. The resin was EPON 9504 epoxy for all

the cases. The predicted stress-strain response for ±25˚, ±30˚ and ±45˚ carbon braids, ±25˚ E-glass braid and ±45˚ S-glass braid will be compared with the experimental data to validate the analysis. These braid configurations were analyzed based on the available experimental data in literature [45, 81-82].

If one is only interested in the macroscopic stress-strain response, it might be worthwhile to analyze an equivalent tape laminate also, which requires only 3 elements and much less computational time. An equivalent tape laminate configuration, as shown in Fig. 3.1, consists of two unidirectional laminas (with properties of the tow) in the +θ and –θ directions and a third lamina of matrix to account for matrix pockets in the braid. The predictions of equivalent tape laminates will be compared with the full 3D finite element models and experimental data as well. The tape analysis will also be helpful in comparing the performance of braided composites with tape laminates containing the same fiber volume fraction.

The effect of fiber type on the plasticity induced non-linearity in ±25˚ 2x2 braids was also investigated. Two ±25˚ biaxial braided composites that used the same resin (EPON 9504) but different fibers (AS4 carbon and E-glass) were analyzed under uniaxial tensile loading. The resin was chosen to be the same so that the effect of fiber type on the degree of plasticity induced non-linearity could be characterized. First, the effect of fiber properties on the macroscopic stress-strain response will be investigated. The macroscopic stress-strain response only gives a quantitative measure of averaged behavior. To obtain insights about the potential damage spots, the effect of plastic deformation on local stress distributions will also be explored. Development of the plastic zone at different load levels will be analyzed. The difference in stress distribution and plastic zone size due to change in fiber properties will also be discussed. In summary, the effect of fiber type on the plasticity induced non-linearity in ±25˚ 2x2 braids will be investigated using (a) macroscopic stress-strain behavior (b) stress distribution plots and (c) plastic zone plots. This chapter focuses on the following:

1. Predicting the elasto-plastic behavior of biaxial braided composite using a two scale finite element modeling scheme.

2. Validation of the analysis by comparing the finite element predictions with experimental data.
3. Comparison of the performance of equivalent tape laminates and braided composites of same fiber volume fraction.
4. Effect of fiber type on the plasticity induced non-linearity in ±25˚ 2x2 braids

7.1. Modeling Approach for Plasticity Induced Non-Linearity in 2x2 Braided Composites

The following sections describe the plasticity model used in the analyses, the two scale modeling approach, the equivalent tape laminate and the full 3D finite element models at both the scales, geometric parameters, constituent material properties and homogenized material properties of the tow.

7.1.1. Two scale modeling approach

The finite element models were developed at two scales. The first scale is the fiber/matrix unit cell and the second scale is the tow architecture scale. This section describes the two scale modeling approach, geometric parameters, material properties, and the output at each scale.

7.1.1.1 .First scale: Fiber/Matrix unit cell

a. Theory

The top row in Fig. 2.1 is the first scale, which is the fiber/matrix unit cell. This scale is used to predict the properties of the tow. Typically, in braided composites, each tow consists of resin reinforced by thousands of fibers. In reality, the fibers are distributed irregularly throughout the resin. But here, a hexagonal arrangement of the fibers in the resin was assumed so that a representative volume element (RVE) can be chosen. The input data for the fiber-matrix scale are the fiber volume fraction and material properties of the fiber and the resin.

The RVE for the fiber/matrix scale is the full unit cell and is shown in Fig. 2.1. Periodic boundary conditions were used on all the faces of the unit cell [32, 35-36]. As

discussed earlier, the analysis region was the full unit cell and was not further reduced because combined loadings were considered at this scale. At this scale, a two step procedure was used. The first step was to impose a series of volume averaged strains on the fiber/matrix unit cell. Following the coordinate system for the fiber/matrix unit cell in Fig. 3, the various load cases that were considered are listed here.

$$
\begin{aligned}
&1.\ \langle \varepsilon_{22} \rangle = 0.02 \\
&2.\ \langle \varepsilon_{12} \rangle = 0.02 \\
&3.\ \langle \varepsilon_{23} \rangle = 0.02 \\
&4.\ \langle \varepsilon_{22} \rangle = 0.02 \ \text{ and } \ \langle \varepsilon_{12} \rangle = 0.02 \\
&5.\ \langle \varepsilon_{22} \rangle = 0.02 \ \text{ and } \ \langle \varepsilon_{23} \rangle = 0.02 \\
&6.\ \langle \varepsilon_{22} \rangle = 0.02 \ \text{ and } \ \langle \varepsilon_{33} \rangle = -0.02
\end{aligned}
\tag{7.1}
$$

In each of these load cases, the load is applied incrementally and at each load step, the boundary value problem is solved to calculate the microscopic stress and strain fields. The microscopic fields are volume averaged to obtain macroscopic stresses, total strains, and plastic strains. Using Eqns. (4.52) and (4.50), the volume averaged effective stress and incremental effective plastic strains for the tow are related to the volume averaged stresses and incremental plastic strains as follows:

$$
\langle \bar{\sigma} \rangle = \sqrt{3\langle f \rangle} \ \text{ and } \ \langle d\bar{\varepsilon}^{\,p} \rangle = \frac{\langle \sigma_{ij} \rangle \langle d\varepsilon_{ij}^{p} \rangle}{\sqrt{3\langle f \rangle}} \tag{7.2}
$$

$$
\text{where } \langle f \rangle = \frac{1}{2}\left[\begin{aligned} &F\left(\langle \sigma_{22} \rangle - \langle \sigma_{33} \rangle\right)^2 + G\left(\langle \sigma_{33} \rangle - \langle \sigma_{11} \rangle\right)^2 + H\left(\langle \sigma_{11} \rangle - \langle \sigma_{22} \rangle\right)^2 \\ &\qquad L\langle \sigma_{23} \rangle^2 + 2M\langle \sigma_{31} \rangle^2 + 2N\langle \sigma_{12} \rangle^2 \end{aligned} \right]
$$

After solving the boundary value problem for all the load steps, $\langle \sigma_{ij} \rangle$ and $\langle d\varepsilon_{ij}^{p} \rangle$ are known values but F, G, H, L, M and N are unknown parameters for the tow. If the correct orthotropic parameters F, G, H, L, M and N were known, the effective stress versus effective plastic strain for the different load cases would collapse into a

single curve. Hence the second step involves attempting to find the orthotropic parameters of the tow such that all these effective stress versus effective plastic strain curves collapse into a narrow band around a single curve. A Matlab® v6.5 [75] optimization utility was used to determine the orthotropic parameters of the tow. This involved solving a non linear least square problem using the *lsqnonlin* function.

b. Configurations

Three different material systems were considered. The resin is the same for all the systems, but the fibers are different. The fibers are AS4 carbon, E-glass and S-glass. The dry fiber braid mats were manufactured by A & P Technology, Inc. [1]. The glass fibers are isotropic and the carbon fiber is transversely isotropic. All the fibers are

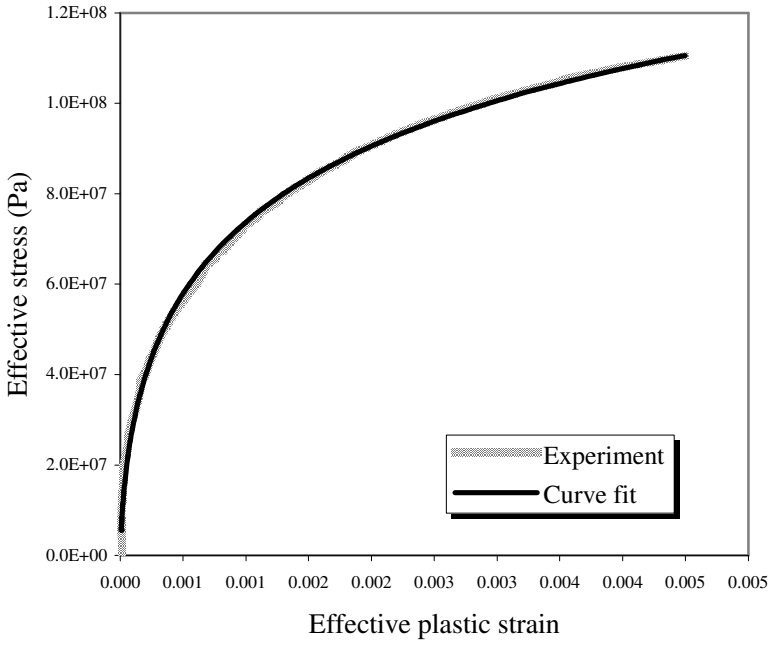

Figure 7.1. Effective stress versus effective plastic strain for the EPON 9504 resin.

Table 7.1. Constituent and tow properties.

		Constituent material properties				Predicted homogenized properties of the tow		
		EPON Resin	Carbon Fiber	E-Glass Fiber	S-Glass Fiber	Carbon/EPON Tow, Vft = 78%	E-Glass/EPON Tow, Vft = 78%	S-Glass/EPON Tow, Vft = 60%
	E_{11} (GPa)	3.21	227.53	68.94	85.5	178.17	54.5	52.6
	E_{22} (GPa)	3.21	16.55	68.94	85.5	11.01	21.84	12.2
Elastic	υ_{12}	0.38	0.2	0.22	0.2	0.236	0.249	0.264
Properties	υ_{23}	0.38	0.25	0.22	0.2	0.37	0.362	0.456
	G_{12} (GPa)	1.16	24.82	28.25	35.6	7.15	7.41	4.16
	G_{23} (GPa)	1.16	6.89	28.25	35.6	4.11	8.00	4.19
Master	E (GPa)	2200	na	na	na	3000	4000	200
Curve	σ_0 (MPa)	235	na	na	na	258.45	300	140
Parameters	n	0.3343	na	na	na	0.3262	0.3	0.57
Orthotropic	F	1	na	na	na	0.48	0.48	0.45
Parameters	G = H	1	na	na	na	1.0E-05	1.0E-05	1.0E-04
	L	3	na	na	na	1	1	1
	M = N	3	na	na	na	1.5	1.8	1

na = Not Applicable as fibers were assumed to be linear elastic

assumed to be linearly elastic. The resin is EPON 9504 epoxy manufactured by Resolution Performance Products, Inc. [77] and utilized the curing agent EPICURE 9551, which was 26% by weight [45]. The EPON 9504 resin is isotropic and elasto-plastic. The initial modulus of the resin is 3.21 GPa and the Poisson's ratio is 0.38 [45]. The effective stress versus effective plastic strain response of the EPON 9504 resin is shown in Fig. 7.1. This was curve fitted very closely using the master curve (Eq. (4.68)). The constituent material properties and master curve parameters are given in Table 7.1. For E-glass and carbon material systems, the fiber volume fraction in the tow was taken to be 78% and for S-glass material system the fiber volume fraction in the tow was taken to be 60%.

Figure 7.2 shows the effective stress versus effective plastic strain curves after they *nearly* collapsed into one single curve. It's not possible to collapse these curves into a single curve because the constitutive model is only an approximation. Figure 7.2 shows effective stress-effective plastic strain curves for the tows consisting of different material systems. It can be seen that at 1.2% effective plastic strain level, the effective stress for the S-glass braid tow is considerably less than for the other two systems because the fiber volume fraction is much lower (60%) in the S-glass braid tow as compared to other two braid tows, which have higher (78%) fiber volume fraction. The collapsed data is fitted using the master curve. Figure 7.2 also shows the curve fits. This completes the analysis at the fiber/matrix scale. The constituent material properties, homogenized properties of the tow and master curve parameters for all the material systems are summarized in Table 7.1.

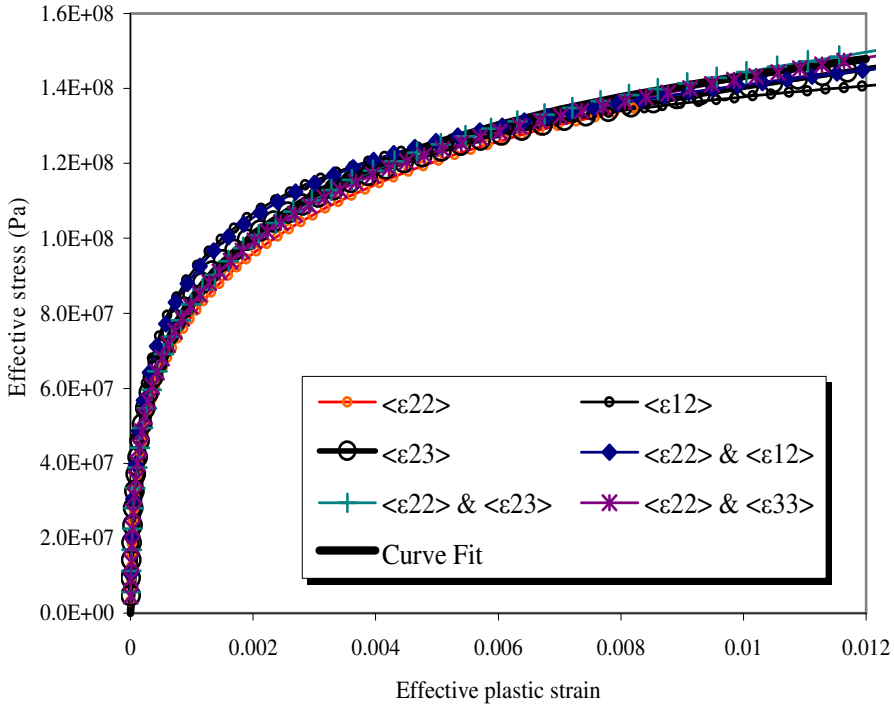

(a) Carbon/EPON 9504

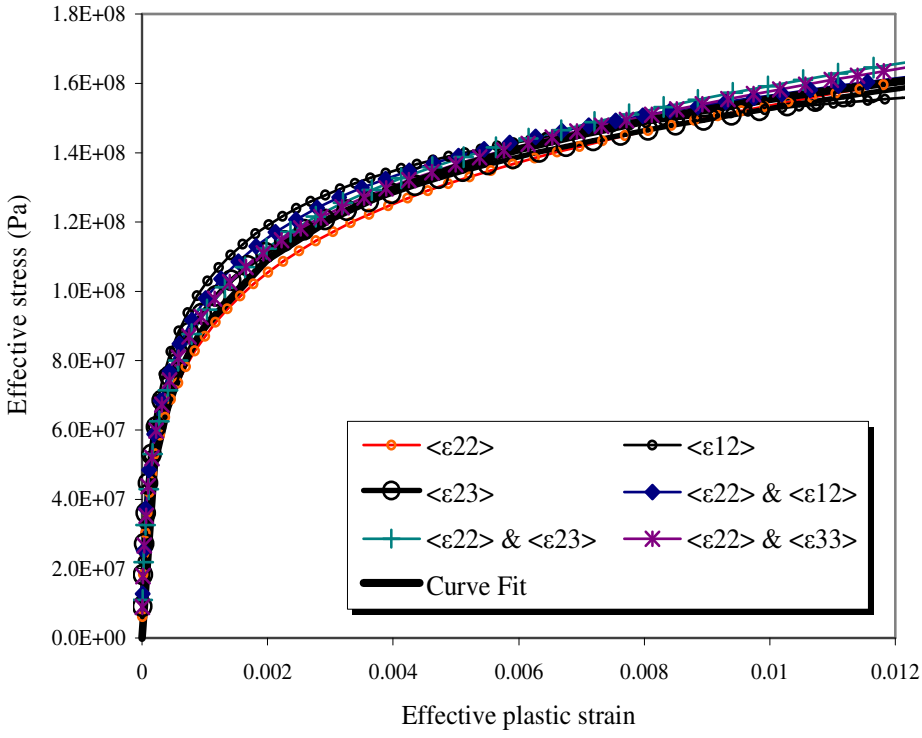

(b) E-Glass/EPON 9504

Figure 7.2. Effective stress versus effective plastic strain curves for the tow.

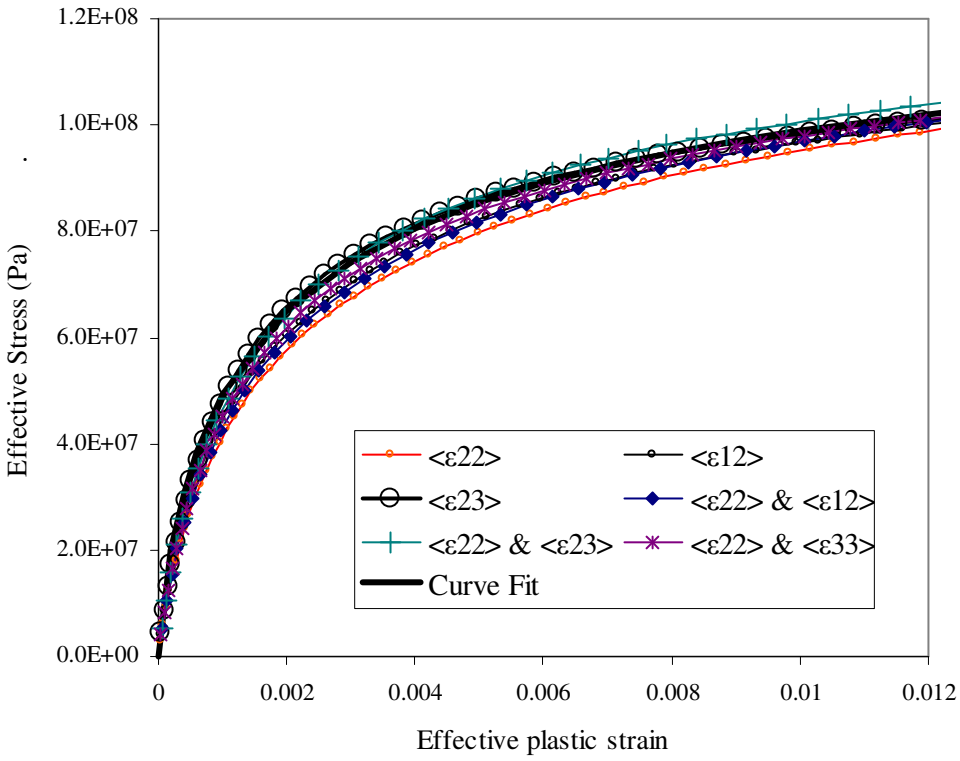

(c) S-Glass/EPON 9504

Figure 7.2. Continued.

7.1.1.2. Second scale: Tow architecture scale

a) Theory

Figure 2.1 also shows the second scale, which is the tow architecture scale. The materials involved at this scale are homogenized tows and the neat resin. The output at the tow architecture scale is the stress-strain behavior of the braid, microscopic stress distributions and microscopic plastic strain distributions in the tow. The homogenized tow is transversely isotropic and the resin is typically isotropic. Both the tow and the resin are elasto-plastic. The output of the first scale (i.e. the tow elasto-plastic properties) is input at the tow architecture scale. The other inputs at the tow architecture scale are stacking sequence of mats, braid geometric parameters like braid angle, waviness ratio,

tow cross-section shape and tow volume fraction in the model. Based on experiments, a simple stacking was analyzed for the E-glass and carbon braids and a symmetric stacking was analyzed for the S-glass braid in this work. One half of the unit cell was taken to be the RVE for simple stacking and one-fourth of the unit cell was taken to be the RVE for symmetric stacking. A typical finite element model at the tow architecture scale is shown in Fig. 2.1. The boundary conditions for this finite element model are in terms of numerous multi-point constraint relationships and are given in ref. [32].

b) Configurations

Seven configurations (see Table 7.2) were analyzed at this scale. First five configurations were analyzed to validate the analysis and the last two configurations were analyzed to study the effect of fiber modulus on plastic behavior of 2x2 braids.

The material systems, braid angles, waviness ratios and fiber volume fractions for the first five configurations were chosen based on the experimental data [45, 81-82]. Three configurations that were used to validate the analysis are AS4 carbon/EPON 9504 braids with braid angles ±25˚, ±30˚ and ±45˚ and waviness ratio of 1/6. The fourth configuration is an E-glass/EPON 9505 ±25˚ braid with waviness ratio 1/3.11. And the fifth configuration is an S-glass/EPON 9504 ±45˚ braid with waviness ratio of 1/9 (i.e. this braid was quite flat). All the geometric parameters including the tow fractions, fiber volume fraction in the tow and overall fiber volume fraction for these configurations are shown in Table 7.2.

Two additional configurations were used to analyze the effect of fiber type on plastic behavior of 2x2 braids. These are configuration #6 and #7. Configuration #6 consists of AS4 carbon/EPON braid and the configuration #7 consists of E-glass/EPON braid. Both configurations have a braid angle of ±25˚, waviness ratio of 1/6, tow fraction of 63.6% and an overall fiber volume fraction of 50%. It should be noticed that both configurations have exactly the same geometric and material parameters except for the fiber properties, because one of the goals of plasticity analyses was to study the effect of elastic properties of the fiber on the elasto-plastic response of the braided composites.

Table 7.2. Geometric parameters for various configurations.

Config. #	Material System	Braid Angle	Waviness ratio	% Fiber volume fraction in tow	% Tow fraction	% Overall fiber volume fraction
1	AS4/EPON	±25º	1/6	78	65.3	51
2		±30º	1/6	78	68	53
3		±45º	1/6	78	66.8	52
4	E-glass/EPON	±25º	1/3.11	78	63.7	50
5	S-glass/EPON	±45º	1/9	60	80	48
6	AS4/EPON	±25º	1/6	78	63.7	50
7	E-glass/EPON	±25º	1/6	78	63.7	50

The finite element model for a ±25˚ E-glass braid configuration is shown in Fig. 2.1. The mesh used 20 node solid elements. Each element contains 27 Gauss quadrature points. The mesh has 256 elements and 1154 nodes. Uniaxial tensile loading along the longitudinal direction of the braid was considered by applying a non-zero volume averaged strain in the longitudinal direction ($\langle \varepsilon_{xx} \rangle = 0.02$) in small increments. The other volume averaged strains were allowed to vary such that the macroscopic loading was uniaxial….i.e. the only non zero volume averaged stress was $\langle \sigma_{xx} \rangle$. The output at the tow architecture scale is discussed in the results and discussion section.

7.1.2. Equivalent tape laminates

Equivalent tape laminate models (see Fig. 3.1) corresponding to each braid configuration were also analyzed. The stacking sequence for the tape laminate model is $[+\theta_{tow}/-\theta_{tow}/0_{resin}]$ with periodicity imposed on all the faces of the unit cell. In this laminate, two layers have properties of the tow and the third have properties of the

matrix to account for matrix pockets in the braid model. The layer thicknesses were determined by the tow/matrix volume fraction in the braid model. Note that the equivalent tape laminates do not consider any tow undulation.

7.2. Results and Discussion

The results of the plasticity analysis at the tow architecture scale are discussed in the following sub-sections. First the analysis is validated by comparing the predicted macroscopic response of different carbon and glass braids with the experimental data. Then the predictions of equivalent tape laminates are compared with the experimental data and full 3D finite element predictions. Lastly, the effect of fiber properties on braid response is discussed in terms of macroscopic stress-strain response, stress distribution and plastic zone

It should be noted that in the macroscopic stress-strain predictions, the initial modulus of the braid and tape laminate configurations differed slightly from the experimental data. There can be various reasons for this. For example, damaged fibers during the braid manufacturing, variation in braid angle and waviness ratio throughout the microstructure etc. are potential causes for some degradation of properties and hence a lower initial modulus. In the results involving comparisons with the experimental data, predicted macroscopic stress-strain curves were normalized to match the initial modulus with the experimental data. Hence, those results show the relative changes in the moduli.

7.2.1. Validation of the full 3D and equivalent tape analysis

The variation of volume averaged stress with volume averaged strain in the longitudinal direction for different braid configurations will be discussed in this section. To validate the analysis, the predicted plastic response is compared with experimental data.

First, carbon braid predictions are compared with the experimental data. Figure 7.3 shows the predicted and experimentally measured [45] stress-strain response of different carbon braids subjected to uni-axial tensile loading along the longitudinal direction. Figure 7.3 also shows the linear elastic extrapolation for comparison purposes.

Experimental data shows that the behavior of all the braids is quite non-linear. Even before 0.5% applied strain, the linear elastic extrapolations differ considerably from the corresponding experimental values. Hence, linear elastic analysis can not be relied upon for predicting the behavior of these braids. Below, first the predictions of full 3D models and then the predictions of laminate models are compared with experimental data for carbon braids.

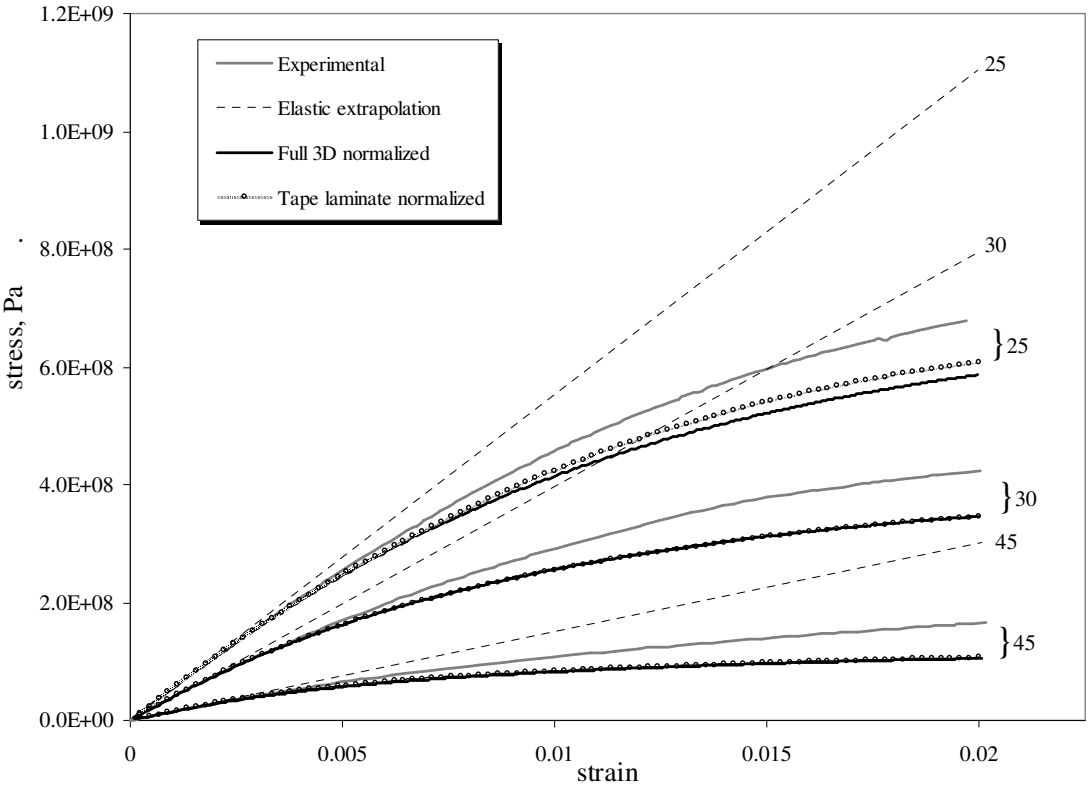

Figure 7.3. Predicted versus measured response [45] for various carbon/EPON 9504 braids subjected to uni-axial tension in longitudinal direction. The predicted stress strain curves were normalized to match initial experimental moduli.

For a ±25˚ braid, the measured secant modulus of the braid in the longitudinal direction is initially 55.3 GPa and it drops to 34 GPa at 2% strain. There was small error in the initial modulus predicted by the full 3D model, which was 54.86 GPa and hence the predicted stress-strain curve was normalized to match the initial modulus. Figure 7.3 shows that the normalized full 3D predictions are reasonably close to the experimental data. The errors in the predicted volume averaged longitudinal stress at 1% and 2% strains are 10.2% and 13.5% respectively. Figure 7.3 also shows the experimental data for ±30˚ and ±45˚ carbon braids. For ±30˚ braid, the measured value for the secant modulus is 21 GPa at 2% strain, which is almost half the initial modulus. The experimental data shows that the initial modulus for ±45˚ braid (15.1 GPa) is quite low as compared to ±25˚ and ±30˚ braids. This is expected as the fibers are more off-axis. Like ±30˚ braid, at 2% strain level, this braid has also lost almost half of its initial modulus. Figure 7.3 compares the normalized full 3D finite element predictions with experimental data for ±30˚ and ±45˚ carbon braids also. For ±30˚ braid, the measured and predicted initial moduli were 39.8 GPa and 43.98 GPa respectively. And for ±45˚ braid, the measured and measured initial moduli were 15.1 GPa and 16.59 GPa respectively. Hence the predicted stress strain curves were normalized to match initial moduli. For the ±30˚ braid, the errors in the predicted stress levels are 12.2% and 18.1% at 1% and 2% strain, respectively. For the ±45˚ braid, the difference between predictions and experimental data is higher as compared to the other two braids. At 1% and 2% strain levels, the errors in predicted stress are 24% and 36% respectively. In all the carbon braid configurations, the stress level is under predicted.

Figure 7.3 also compares predictions of equivalent tape laminates against experimental data and full 3D finite element predictions. The initial modulus of tape laminates equivalent to ±25˚, ±30˚ and ±45˚ braids were 59.13 GPa, 45.26 GPa and 17.48 GPa respectively. The equivalent tape laminates had around 7-15% higher initial modulus than experimental data. This is expected because tape laminates have straight fibers and do not consider any tow undulation [32]. The tape laminate results were also normalized to match the initial experimental moduli and are shown in Fig. 7.3. At 1%

strain, the error in predicted stress level by equivalent tape laminates and experimental data is 8.4%, 12.8% and 22.3% for tapes equivalent to ±25˚, ±30˚ and ±45˚ braids. This error increases to 10.3%, 18.3% and 35.2% respectively at 2% strain. These errors in equivalent tape laminate predictions are not much different from the full 3D plasticity solution (At 2% strain, errors were 13.5%, 18.1% and 36% for ±25˚, ±30˚ and ±45˚ braids respectively). As a matter of fact, the equivalent tape laminate has less error as compared to full 3D plasticity solution for a ±25˚ braid.

Next , a ±25˚ E-glass braid was used to validate the analysis. Figure 7.4 shows the predicted and measured response [82] of the configuration. It can be seen that this braid is also quite non-linear. The experimentally measured initial secant modulus is 20

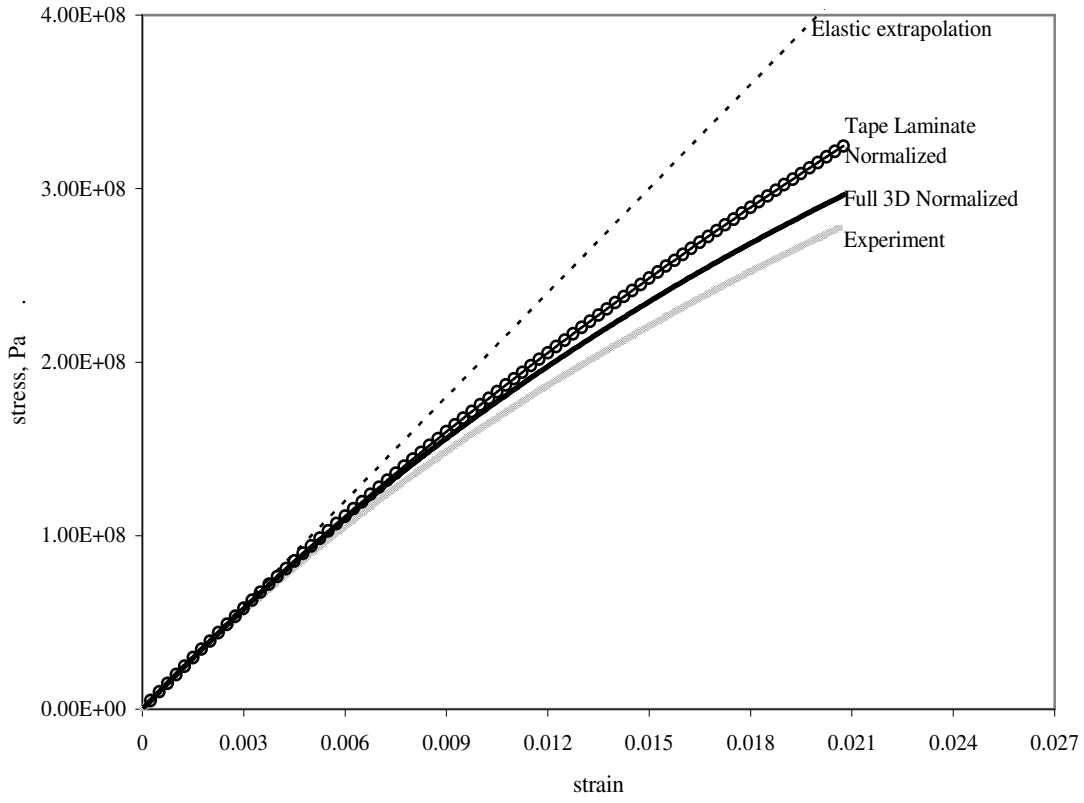

Figure 7.4. Predicted versus measured response [82] for E-glass/EPON 9504 ±25˚ braid subjected to uni-axial tension in longitudinal direction. The predicted stress strain curves were normalized to match initial experimental moduli.

GPa and it drops to 16.15 GPa at 1% strain and 13.57 GPa at 2% strain. In this case also, the predicted response was normalized to match the initial modulus and is shown in Fig. 7.4. The experimentally measured initial secant modulus is 20 GPa whereas the predicted initial elastic modulus using full 3D model was 22.7 GPa. The normalized predictions of full 3D analysis matched very well with the experimental data. The error in predicted stress level at 1% and 2% strain was just 5.5% and 6.4% respectively. Unlike carbon braids, the stress level is over-predicted in this case. Again, the linear elastic extrapolation differs considerably from the corresponding experimental values. There is 24% and 48% difference in the predicted stress level at 1% and 2% strain respectively by linear elastic extrapolation.

Figure 7.4 also compares the predictions of an equivalent tape laminate with experimental data and full 3D analysis. The initial modulus of equivalent tape is 25.77GPa. The equivalent tape has 29% higher initial modulus than the experiments. Hence the stress-strain predictions of the tape laminate were normalized to match the initial modulus. Like full 3D plasticity solution predictions, the equivalent tape also over predicts stress level at various strains. At 1% and 2% strain levels, the equivalent tape has 8% and 16% higher stress level than the experimental data. Recall that the full 3D plasticity solution over predict the stress level by 5.5% and 6.4% at 1% and 2% strain respectively. Hence in this case, the tape laminate prediction has higher errors than the full 3D solution.

The final configuration used to validate the analysis was a ±45˚ S-glass braid. This response of this configuration is extremely non-linear as shown by Fig 7.5. At 3% strain, the secant modulus drops to almost one fourth of its initial modulus of 10.2 GPa. Figure 7.6 shows the predicted and experimentally measured stress-strain response of this braid. Different experimental stress-strain curves correspond to eight tested specimens [81]. The response was predicted only up to 3% strain, since the analysis involves the assumption of small strains. In this case, the initial tensile modulus of finite element predictions matches well with the experimental data, so no normalization was

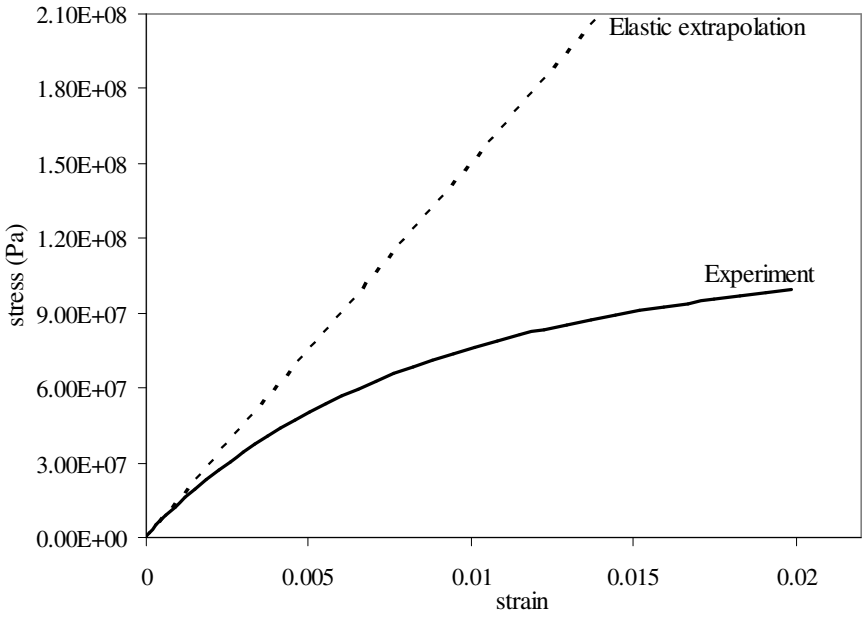

Figure 7.5. Comparison of elastic extrapolation with one of the test data [81] for a ±45˚ S-glass/EPON 9504 braid subjected to uni-axial tension in longitudinal direction.

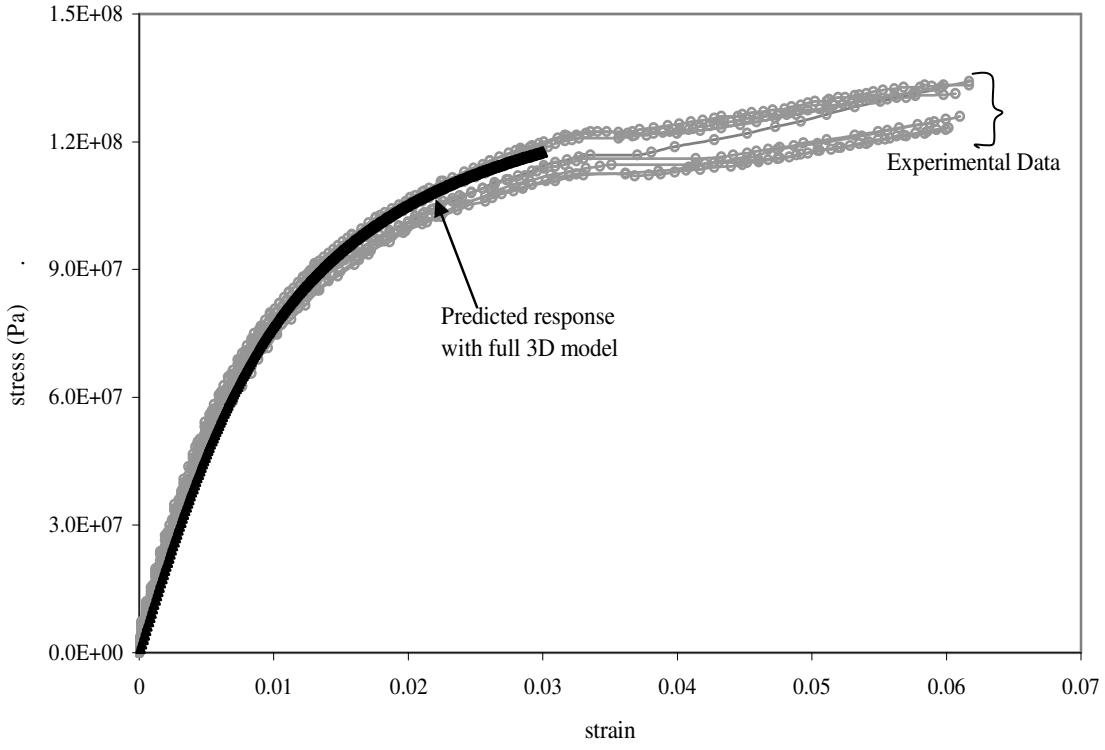

Figure 7.6. Predicted versus measured response [81] for ±45˚ S-glass/EPON 9504 braid subjected to uni-axial tension in longitudinal direction.

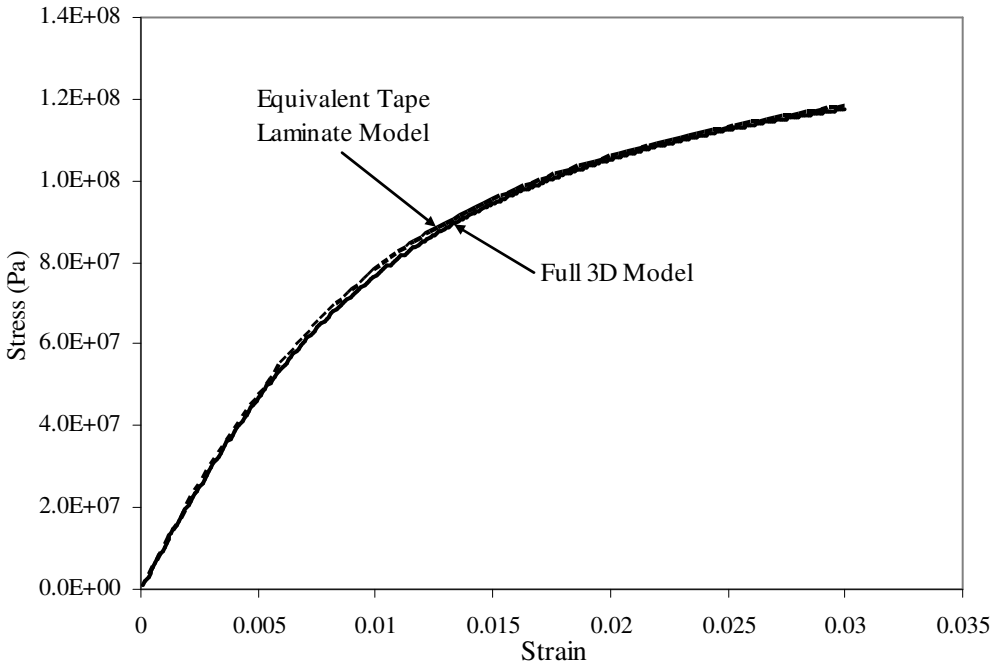

Figure 7.7. Comparison of predicted response by equivalent tape laminate versus full 3D model for ±45˚ S-Glass/EPON braid under uni-axial tension in longitudinal direction.

required. The predictions lie within the range of experimental data. This is an excellent agreement between predicted and measured response.

Figure 7.7 shows a comparison of predictions of the equivalent tape laminate with the full 3D model predictions for the ±45˚ S-glass. Generally speaking, the equivalent tape laminates have higher initial modulus than their braid counterparts because braids have undulating tows which causes them to lose some in-plane stiffness [32]. Since this braid is very flat, the initial modulus of tape laminate is very similar to that predicted by full 3D model. More importantly, not just the initial modulus but the macroscopic response at higher stress levels is also very similar. For example at 2% and 3% strain, the difference in predicted stress levels by equivalent tape laminate model from full 3D model is less than 1%, which is exceptionally good from the standpoint of computational savings a simple tape laminate model offers. For example, the analysis of

full 3D braid model took 8 and a half hours on a supercomputer, whereas the equivalent tape laminate model took less than 2 minutes. Both full 3D and equivalent tape laminate predictions match very well with the experiments in this case and the tape laminate is extremely computationally efficient.

This completes the validation of the plasticity analysis for different braids. In summary, all the considered braids show quite non-linear response and a linear elastic extrapolation does not suffice. The plastic solution predictions agree reasonably well with the experiments for ±25˚ and ±30˚ carbon braids even at strains as high as 2% strain. For a ±45˚ carbon braid, the plastic solutions predictions show more deviation from the measured response. There is an excellent agreement between predicted and measured response both for a ±25˚ E-glass braid and a ±45˚ S-glass braid even at as high as 2% strain. Errors predicted by tape laminates are not very much different from those of full 3D models, but the tape laminate models are extremely computationally efficient

7.2.2. Comparison of the performance of braids with equivalent tape laminates of same fiber volume fraction

In this section we compare the performance of braids with equivalent tape laminates. The performance is compared in terms of initial modulus and degradation of modulus due to plastic deformation. Unlike the previous section, the original i.e. un-normalized stress-stress response is compared here because that is the actual predicted response for these composites.

First the carbon braid configurations are discussed. Figure 7.8 shows the comparison of predicted performance of braids versus tape laminates. The tapes have around 2-7% higher initial moduli because there is no undulation in the fiber tows. Figure 7.8 shows that equivalent tape laminates have higher secant modulus throughout the load history which shows that they have a better performance in terms of longitudinal modulus. A ±25˚ equivalent tape has around 11% higher secant modulus than the ±25˚ braid both at 1% and 2% strains. Both ±30˚ and ±45˚ equivalent tape laminates have around 2.5% higher secant moduli than their braid counterparts at both

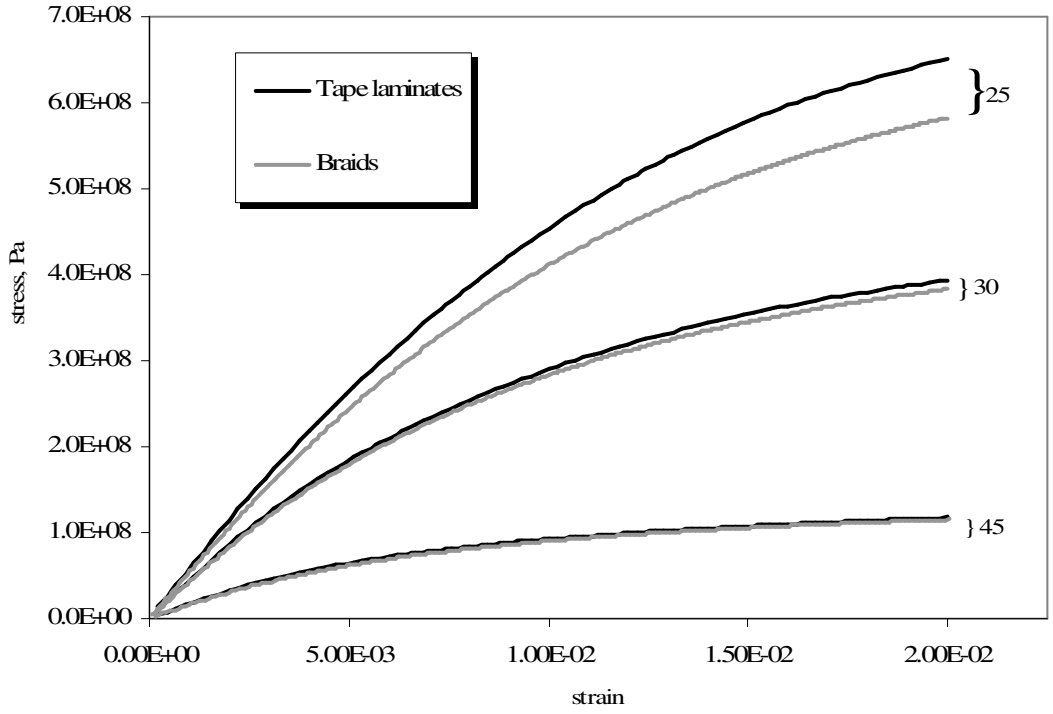

Figure 7.8. Comparison of predicted performance of different braids with equivalent tape laminates for carbon/EPON 9504 material system.

1% and 2% strain levels. At 2% strain, the secant modulus drop from initial modulus for equivalent tapes and their braid counterparts is 47% versus 45% for a ±25˚ configuration, 56.4% versus 56.5% for a ±30˚ configuration and 65.4% versus 66.4% for a ±45˚ configuration respectively. This shows that both braids and tapes have similar performance in terms of moduli degradation due to plasticity.

Next, we compare the performance of equivalent tape laminate with the braid for ±25˚ E-glass configuration. Figure 7.9 shows the un-normalized stress-strain response for the braid and the tape laminate, which has 12% higher initial modulus than its braid counterpart. Like carbon braids, throughout the load history, the equivalent tape laminate has higher secant modulus than its braid counterpart. The tape has 17% and 24% higher

secant modulus than the braid at 1% and 2% strain respectively. Also, in terms of drop in secant modulus from initial modulus, tape laminate performs better than the braid. The braid has 15% and 28% drop in secant modulus from its initial modulus at 1% and 2% strain levels as compared to 12% and 21% drop in secant modulus from its initial modulus for the tape laminate. Hence both in terms of secant modulus as well as degradation of secant modulus due to plastic deformation, the tape laminate performs better in this case. In contrast, in the case of an S-glass ±45˚ configuration, both tape and braid behave very similarly as shown by Fig. 7.7.

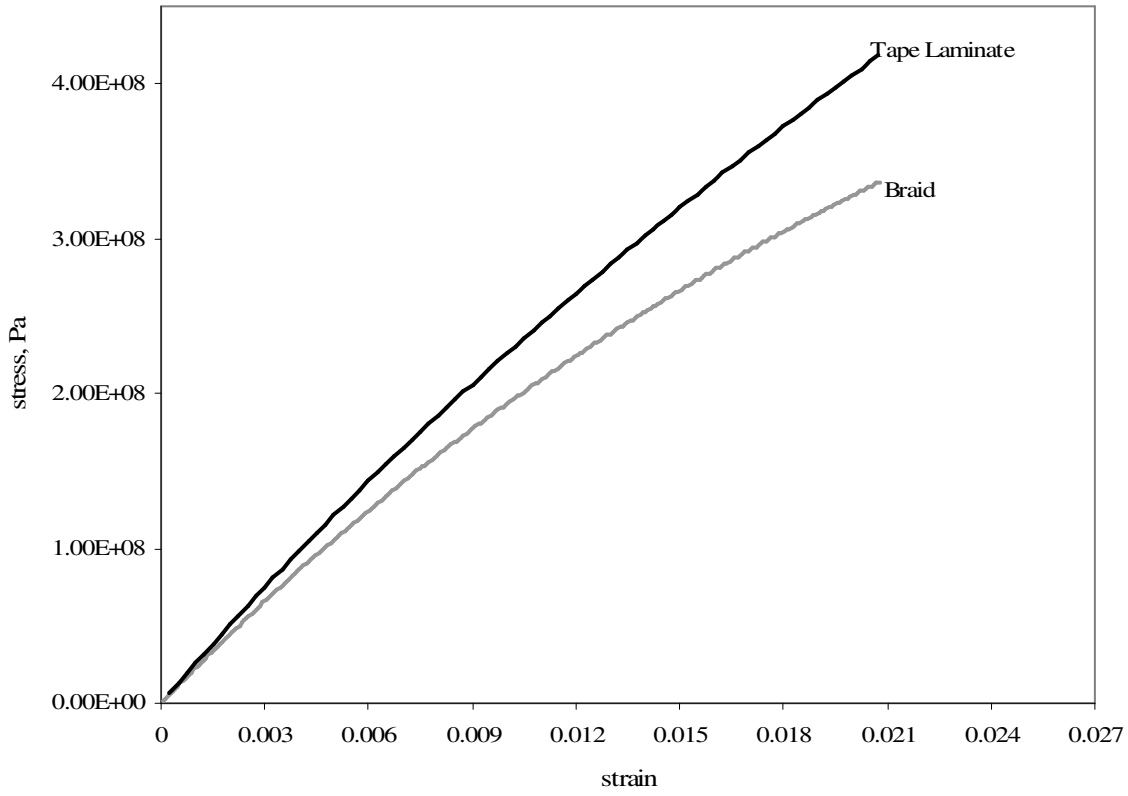

Figure 7.9. Comparison of predicted performance of ±25˚ braid with an equivalent tape laminates for E-glass/EPON 9504 material system.

In summary, the tape laminates have better performance in terms of secant modulus at various stress levels. But as far as moduli degradation due to plasticity is concerned, the braids have comparable performance as compared to their tape laminate counterparts.

7.2.3. Effect of fiber properties on plastic behavior of 2x2 biaxial braided composites

Two configurations (#6 which is ±25° carbon/EPON braid and the #7 which is ±25° E-glass/EPON braid in Table 7.2) were used to study the effect of fiber properties on plastic behavior of ±25° braids. The effect of fiber properties on braid response is discussed in terms of macroscopic stress-strain response, stress distribution and plastic zone below.

7.2.3.1. Effect of fiber properties on macroscopic non-linear behavior

In this section, the effect of fiber properties on the macroscopic response of the two braids is discussed. Macroscopic response is measured in terms of volume averaged variables. The non-linear behavior at the macroscopic scale was quantified using the following measures [83]:

- Loss in secant modulus
- Loss in tangent modulus
- Amount of plastic strain
- Energy dissipated during plastic deformation per unit energy supplied.

Let $\left\langle \sigma_{xx} \right\rangle, \left\langle \varepsilon_{xx} \right\rangle$, $\left\langle \Delta\sigma_{xx} \right\rangle$ and $\left\langle \Delta\varepsilon_{xx} \right\rangle$ be volume averaged stress, volume averaged strain, change in volume averaged stress, and change in volume averaged strain respectively in the longitudinal direction and let E^e_{xx} be the elastic tensile modulus. Loss in secant modulus can be calculated by the expression $\left(\left\langle \sigma_{xx} \right\rangle / \left\langle \varepsilon_{xx} \right\rangle - E^e_{xx} \right) / E^e_{xx}$. Loss in tangent modulus can be calculated by the

expression $\left(\left\langle \Delta\sigma_{xx} \right\rangle \Big/ \left\langle \Delta\varepsilon_{xx} \right\rangle - E^{e}_{xx}\right) \Big/ E^{e}_{xx}$. The plastic strain in the longitudinal direction can be calculated as $\left\langle \varepsilon^{p}_{xx} \right\rangle = \left\langle \varepsilon_{xx} \right\rangle - \left\langle \sigma_{xx} \right\rangle \Big/ E^{e}_{xx}$. Relative energy dissipated during plastic deformation can be calculated by dividing the energy dissipated (the area between the loading-unloading curve) with the energy supplied (the area under the loading curve).

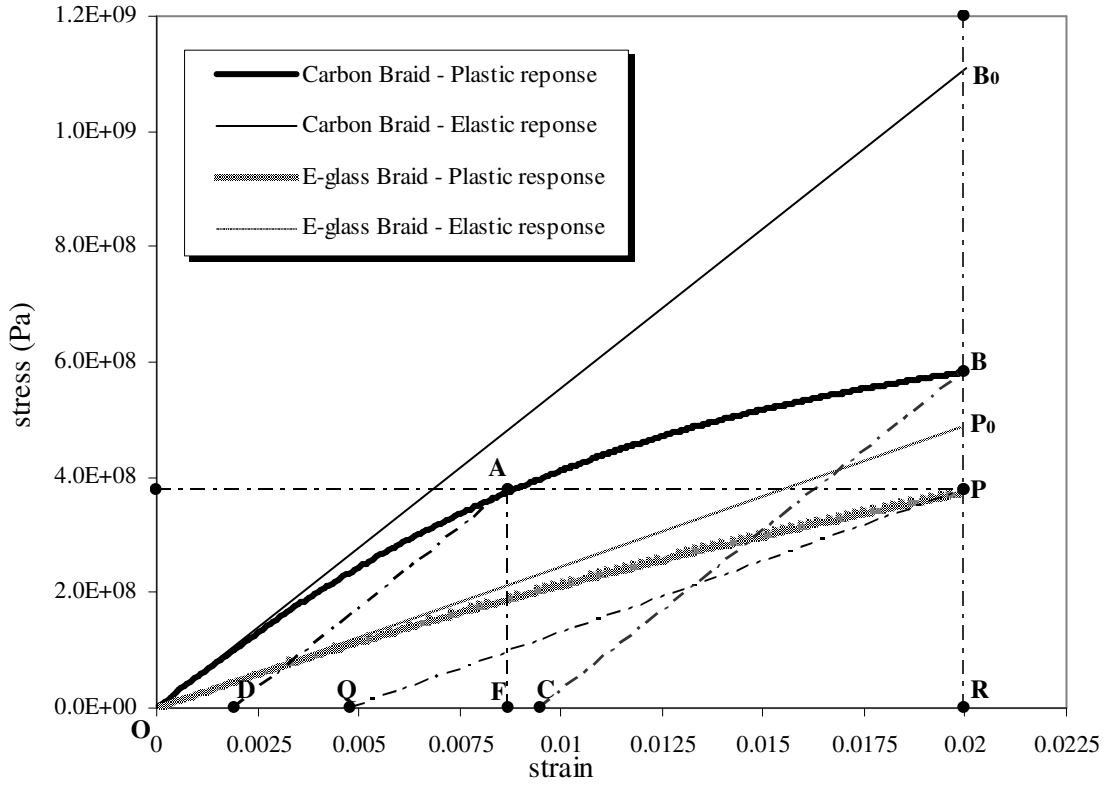

Figure 7.10. Predicted effect of fiber properties on plasticity induced non-linearity in a ±25˚ braid subjected to uni-axial tension in longitudinal direction.

Figure 7.10 shows the predicted stress-strain behavior for ±25˚ carbon/EPON 9504 and ±25˚ E-glass/EPON 9504 braids with waviness ratio of 1/6. Both the elastic and plastic solution predictions are shown.

Let us first compare the drop in secant modulus for the carbon and glass braid at the same overall strain level using Fig. 7.10. At 2% strain, the carbon braid's secant modulus drops from an initial value of 55.3GPa to 29Gpa (47% drop) whereas the E-glass braid's secant modulus drops from an initial value of 24.6 GPa to 18.7 GPa (24% drop). The drop in secant modulus for carbon braid is far more than for glass braid. Looking at these values, one is tempted to conclude that in terms of drop in modulus, the carbon braid has a greater degree of non-linearity than the glass-braid. But, this might not hold true if the behavior is compared at the same stress level. For these high performance materials, the structure is generally designed for load carrying capacity. Hence, below, we compare the braid behavior at the same stress level.

The data in Fig. 7.10 is now used to compare different measures of non-linearity at a stress level of 374 MPa, which is the overall stress in the glass braid at 2% applied strain. At this stress level, the carbon braid's secant modulus drops by 22% from an initial value of 55.3 GPa and the E-glass braid's secant modulus drops by 24% from an initial value of 24.6 GPa. The drop in tangent modulus is 46% and 43% for carbon braid and E-glass braid respectively. This implies that when the braids are compared at same stress level in terms of loss in moduli, the difference in behavior is very little.

Figure 7.11 shows the variation of normalized secant and tangent moduli with applied load level. Both moduli are normalized with respect to the initial moduli. The drop in secant modulus is greater for the glass braid than for the carbon braid. The difference in drop in secant modulus of two braids increases up to an applied stress level of approximately 200 MPa and then it starts to decrease. The glass braid also has a greater drop in tangent modulus than the carbon braid up to a stress level of 300 MPa, but after that the drop in modulus becomes greater for the carbon braid. The maximum difference between the drop in moduli of two material systems is approximately 38% for both secant and tangent measures in Fig. 7.11.

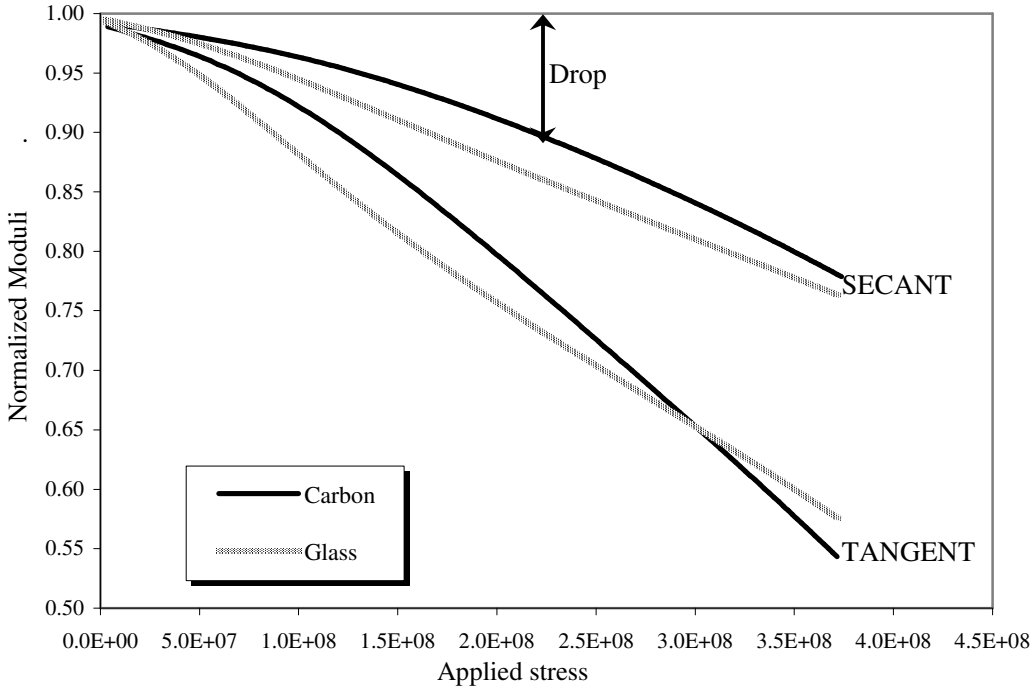

Figure 7.11. Variation of secant and tangent moduli with applied load.

The area under the loading-unloading curve in Fig. 7.10 is now used to calculate the energy dissipated per unit energy supplied when a stress level of 374 MPa is applied to both the material systems. It should be noted that the unloading lines are not actual simulations, but assumed lines drawn parallel to the elastic response lines. In reality, because of the complex stress distribution in the tows and matrix, the unloading response might not be exactly linear, but for these calculations a linear unloading response was assumed. For the carbon braid, the energy dissipated (area OADO) is 29% of energy supplied (area OAFO). For the glass braid, the energy dissipated (area OPQO) is 34% of energy supplied (area OPRO). By modulus drop and energy measures, the degree of non-linearity is not much different in the two braids. However, considerably more plastic strain is occurring in the glass braid (0.48% volume averaged effective plastic strain) as

compared to the carbon braid (0.19% volume averaged effective plastic strain) when loaded at the same stress level (=374 MPa). This shows that a glass braid might be more susceptible to fatigue damage than a carbon braid.

In summary, the conclusions about the effect of fiber type on the degree of plasticity induced non-linearity in a ±25˚ braid are not that easily drawn if we compare the behavior at the same stress level. They depend on the measure of non-linearity.

7.2.3.2. Effect of fiber properties on elastic and plastic stress distributions

Figures 7.12 and 7.13 show the σ_{11}, σ_{33} and σ_{13} stress distributions in the tow obtained by elastic and plastic solutions respectively for the carbon and glass braids. The stresses in both the figures are in the material coordinate system and correspond to 2% volume averaged strain $<\varepsilon_{xx}>$. The stresses are normalized by the volume averaged $<\sigma_{xx}>$ stress at 2% strain level in each configuration. These results will be examined three ways. First, the effect of analysis type (elastic versus plastic) on the stress distributions in the tow is considered. In this comparison, the material system is kept the same (carbon or glass braid). Second, the effect of fiber type on stress distributions is discussed for the elastic analysis. And third, the effect of fiber type on stress distributions is discussed for the plastic analysis and is contrasted with the elastic analysis. In the later two comparisons, the analysis type is kept the same whereas the material systems are different.

First, the effect of analysis type (elastic versus plastic) on the stress distributions in the tow is considered. The goal is to determine how plastic deformation affects the stress distributions. The largest σ_{11} value increases by 40% for the carbon tow (compare Fig. 7.12(a) with 7.13(a)) and 19% for the glass tow (compare Fig. 7.12(b) with 7.13(b)) due to plastic deformation. Similar trends with much higher intensity can also be seen for σ_{33}, in which plastic deformation increases the largest value by 140% for carbon and 118% for the glass braid tow from their respective elastic solutions. In contrast, plastic deformation reduces the σ_{13} peak value by 46% and 49% for the carbon and glass braid tows, respectively. Similar trends were seen by Whitcomb et al. [46] for a plain weave consisting of S2-glass/SC15 material system. A possible explanation is that the

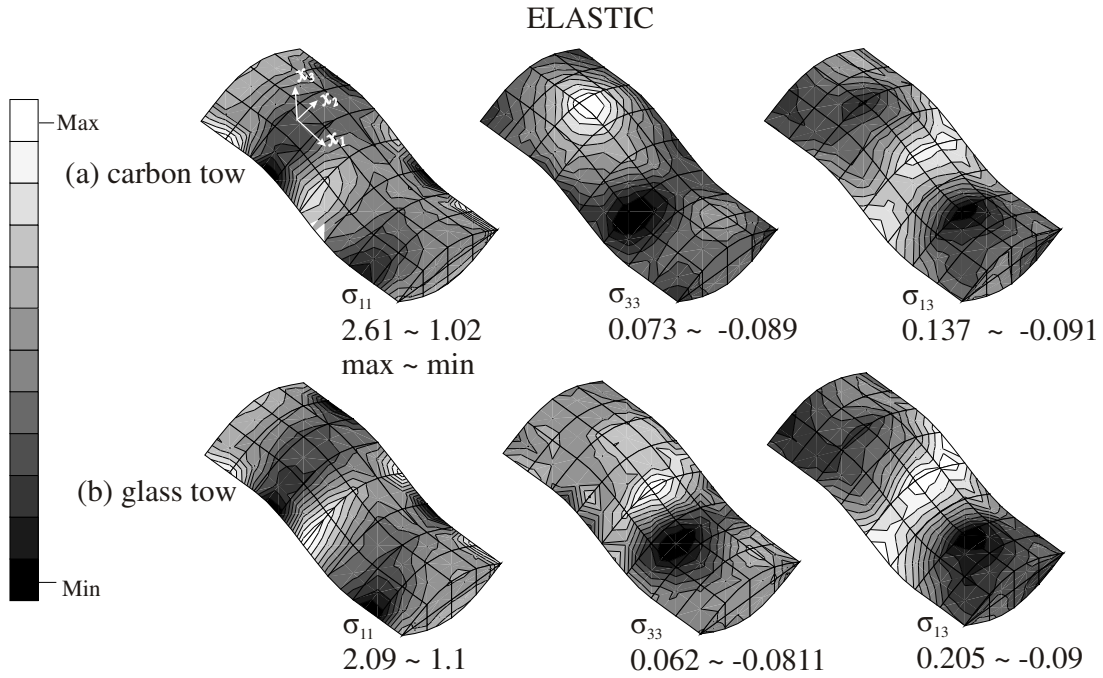

Figure 7.12. Effect of fiber type on elastic stress distributions (applied strain $<\varepsilon_{xx}>=2\%$, and stresses are normalized by $<\sigma_{xx}>$ at 2% strain in each configuration).

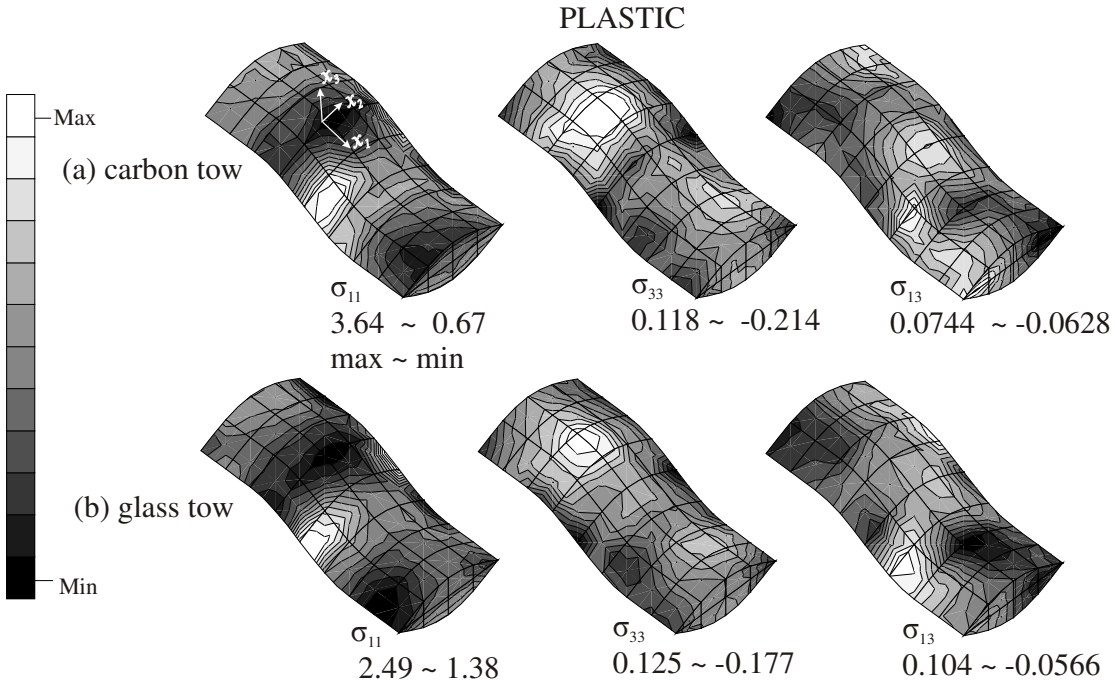

Figure 7.13. Effect of fiber type on plastic stress distributions (applied strain $<\varepsilon_{xx}>=2\%$, and stresses are normalized by $<\sigma_{xx}>$ at 2% strain in each configuration).

plasticity is driven by the σ_{13} stress component. When yielding occurs, the local concentration of σ_{13} is reduced, but the resulting load redistribution increases other stress concentrations. Evaluation of this hypothesis will require further study.

The effect of fiber type on elastic stress distributions is investigated by comparing location and magnitudes of the largest stresses in carbon braid tow versus those in glass braid tow (See Fig. 7.12). The largest stress values are positive for σ_{11} and σ_{13} stress components and are negative for σ_{33} for both the materials. The locations of the largest stresses do not differ much for the two material systems, but the magnitudes are different. The carbon braid tow has 25% larger σ_{11} and 10% larger σ_{33} than the glass braid. In contrast, the carbon braid tow has a 33% lower σ_{13} than the glass tow.

Figure 7.13 shows the plastic stress distributions for carbon braid tow and E-glass braid tows. Similar to the elastic case, the locations of largest stress values in the carbon braid tow and the glass braid tow are very similar to each other but the values are different. The carbon braid tow has 46% larger σ_{11} and 21% larger σ_{33} than the glass braid tow. For σ_{13}, carbon braid tow has a 28% lower value than the glass braid tow. This shows that plastic deformation worsens the stress state in a carbon braid more than it does in a glass braid.

7.2.3.3. Effect of fiber properties on plastic zone sizes and locations

The effect of fiber type on the development of the plastic zone in the tow as the load increases is discussed here. In this study, the plastic zone is defined to be the region of the tow that has exceeded 0.2% effective plastic strain. Figure 7.14 compares the development of the plastic zone in carbon braid tow with glass braid tow. The maximum load level $\left\langle \sigma_{xx}^{\max} \right\rangle$ is 374 MPa, which corresponds to the applied stress at 2% strain for the glass braid. The plastic zone sizes for the two material systems are compared at five load levels: $0.3\left\langle \sigma_{xx}^{\max} \right\rangle$, $0.4\left\langle \sigma_{xx}^{\max} \right\rangle$, $0.5\left\langle \sigma_{xx}^{\max} \right\rangle$, $0.6\left\langle \sigma_{xx}^{\max} \right\rangle$, and $0.7\left\langle \sigma_{xx}^{\max} \right\rangle$.

Figure 7.14 shows that fiber type significantly affects the development of plastic zone in the braid tow. At an applied stress of $0.3\left\langle \sigma_{xx}^{\max} \right\rangle$, no plastic deformation has

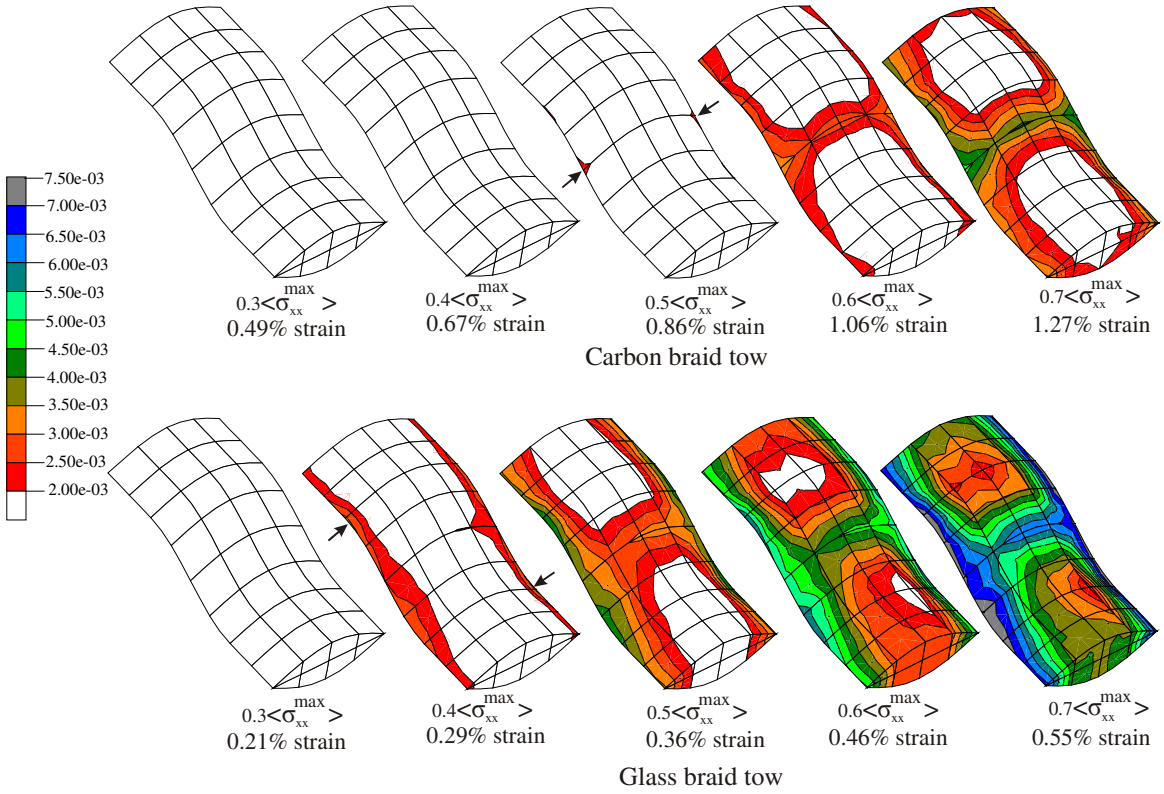

Figure 7.14. Development of plastic zone size ($\langle \sigma_{xx}^{max} \rangle$ = 374 MPa).

occurred in either carbon or glass tow. The plastic zone gradually develops for the glass tow as load increases from $0.3\langle \sigma_{xx}^{max} \rangle$ to $0.7\langle \sigma_{xx}^{max} \rangle$. At $0.7\langle \sigma_{xx}^{max} \rangle$, the glass tow is completely saturated with plastic deformation. The carbon tow starts developing a plastic zone at an applied load level of $0.5\langle \sigma_{xx}^{max} \rangle$. The plastic zone at any load level is considerably higher for the glass tow than for the carbon tow. Thus, the overall plastic strain $\langle \varepsilon_{xx}^{p} \rangle$ in the glass braid is also expected to be more than in carbon braid. This is consistent with the observation of macroscopic stress-strain response in section 7.2.3.1 above. The initiation locations of the plastic zone are slightly different for the two braids. For carbon tow, it is the edges of the region of the maximum undulation, marked by arrows in Fig. 7.14. For the glass tow, the initiation locations are at the beginning of

the undulation region (see arrows in figure). After the initiation, the plastic zone develops along both the edges of the tow, eventually growing into the center portion of the undulation region for both material systems. Since the plastic zone size is considerably larger for the glass tow than for the carbon tow, it is probable that the glass tow might be at a higher risk of initiating damage. The validation of this hypothesis requires further study.

7.3. Summary

A two scale modeling approach was used to analyze plasticity induced non-linearity in 2x2 braided composites. The analysis was validated by comparing the predicted response using elastic and plastic solutions with experimental data for carbon, E-glass and S-glass braids. Both experimental and analytical results showed that the braid is quite non-linear. The following conclusions can be drawn from the analysis:

- Full 3D as well as tape laminate models predictions agree reasonably well with the experiments for ±25˚ and ±30˚ carbon braids even at 2% strain. For a ±45˚ carbon braid, predictions show more deviation from the measured response. An excellent match between measured and predicted response using a full 3D model was seen for a ±25˚ E-glass braid even at as high as 2% strain level. Full 3D as well as equivalent tape laminate predictions lie within the range of experimental data for the ±45˚ S-glass braid even at as high as 3% strain
- Predictions based on equivalent tape laminates are almost as accurate as the full 3D braid model predictions in terms of percentage modulus reductions, which shows that one can use much simpler equivalent tape laminate model to reasonably predict some aspects of the braid behavior and have significant computational time savings.
- Equivalent tape laminates have higher secant modulus throughout the load history which shows that they have a better performance in terms of longitudinal modulus, but in terms of percentage moduli degradation due to plasticity, both braids and tapes have similar performance.
- Conclusions about the effect of fiber type on the degree of plasticity induced non-linearity in a ±25˚ braid depend on the measure of non-linearity. At same applied

stress, the degree of non-linearity is not much different in the two braids by modulus drop and energy measures. However, considerably more plastic strain occurs in the glass braid as compared to the carbon braid when loaded at the same stress level.

- Plastic deformation increases the largest σ_{11} and σ_{33} values and reduces the largest σ_{13} values in the tow.
- Since the plastic zone size is considerably larger for the glass tow than for the carbon tow of a geometrically similar braid, the glass tow might be at a higher risk of initiating damage.

8. MECHANICS OF LOAD FLOW IN TEXTILE COMPOSITES

The increase in computational power that is readily available is making detailed three-dimensional finite element analyses of textile composites practical. One of the weak links in developing these models has been the difficulty in creating a finite element model. For this reason, initial efforts focused on the plain weave composite [21-22, 24]. However, tools and techniques have improved and now 3D models have been developed for a variety of textiles (see Fig. 1.2). The current 3D models of textile composites make very fewer assumptions about the geometry and modes of deformation than the simple laminate theory models were developed as part of the early efforts [13-16]. The wealth of raw numerical information provided by the typical finite element analysis provides less basis for developing an intuitive understanding than the simpler models. The simple models represent the behavior in terms of a small number of basic modes of deformation and load transfer. Intuition is required to develop the models and the result is a framework for understanding the response. Since the finite elements models are based on very few assumptions and the results are also unbiased. For example, the stress contours in a 5 harness satin weave shown in Fig. 2.2 give many details, but no framework for interpretation.

The thesis of this part of the research is to understand the mechanics of load flow in textile composites using special techniques. Optimal use of rapidly improving 3D finite element models requires non-standard techniques to interpret the data. In particular, techniques must be developed that not only highlight the important details, but also transform the massive amount of output data into comprehensible modes of behavior. We will discuss two techniques. The first technique is calculation of stress resultants that give forces and moments at any cross-section of the tow. The second technique converts the 3D variation of a stress component into a stress versus volume distribution plot. Both of the techniques will be described in detail.

These techniques were applied in various ways to investigate textile behavior. First, the behavior of a plain weave was analyzed. How the load flows along the various

cross-sections of a plain weave and load distribution among warp, fill and matrix was investigated. It will be shown that in the warp tow, maximum axial and out of plane transverse stress resultants occur at the maximum undulation region. The reason for this will be discussed. The existence of out of plane transverse stress resultant will be explained by simple stress transformation. The location of stress concentrations will be correlated with stress resultants. Different architectures that were analyzed are Plain weave (PW), Twill weave, 4 Harness Satin weave (4HS), 5 Harness Satin weave (5HS) and 8 Harness Satin weave (8HS). Similar regions in these weaves were identified. The effect of tow architecture on the load flow in comparable regions of different weaves will be shown. The volume distribution plot will be used to show which stress components of a plain weave tow could initiate failure. Finally, the effect of material damage and plasticity on load flow in a plain weave will be investigated.

It should be noted that these postprocessing techniques are not meant to eliminate the details. Instead a hierarchical strategy is proposed that allows interpretation of the predictions at different levels of detail. Also, by providing the "coarse level" interpretation of the results, a better basis is provided for evaluating and refining simpler models.

8.1. Configurations

Five different weave architectures that were analyzed are PW, Twill weave, 4HS, 5HS and 8HS weaves. Their solid models and corresponding finite element models are shown in Fig. 1.2 and Fig. 8.1 respectively. Because the mats are symmetrically stacked, only one-half unit cells were modeled. By exploiting symmetries within these half unit cells, one could model smaller regions, but one half unit cells were typically employed here so that load flow and stress volume calculations could be conducted conveniently. Periodic boundary conditions were imposed on all the faces of the unit cell. The boundary conditions for different weave architectures are provided in detail in refs. [35-36]. Some of the analyses for plain composites were also conducted for $1/32^{nd}$ of the unit cell. This smaller unit cell was especially helpful to keep the runtimes low for plasticity and damage studies.

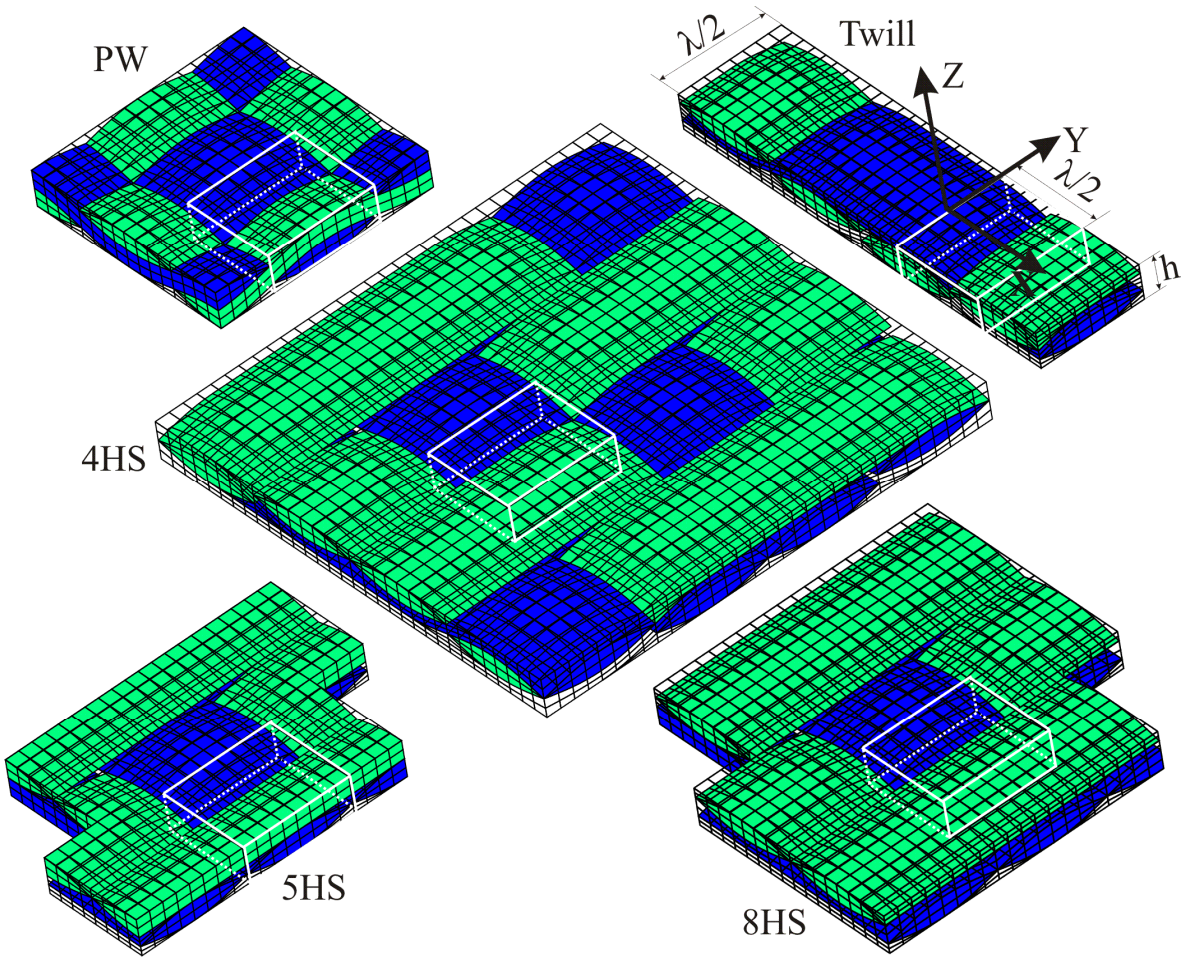

(a) Finite element meshes for half unit cells
(comparable regions are marked by white boxes)

Figure 8.1. FE meshes and comparable regions for different weave architectures
(The matrix is shown transparent to reveal the architecture clearly).

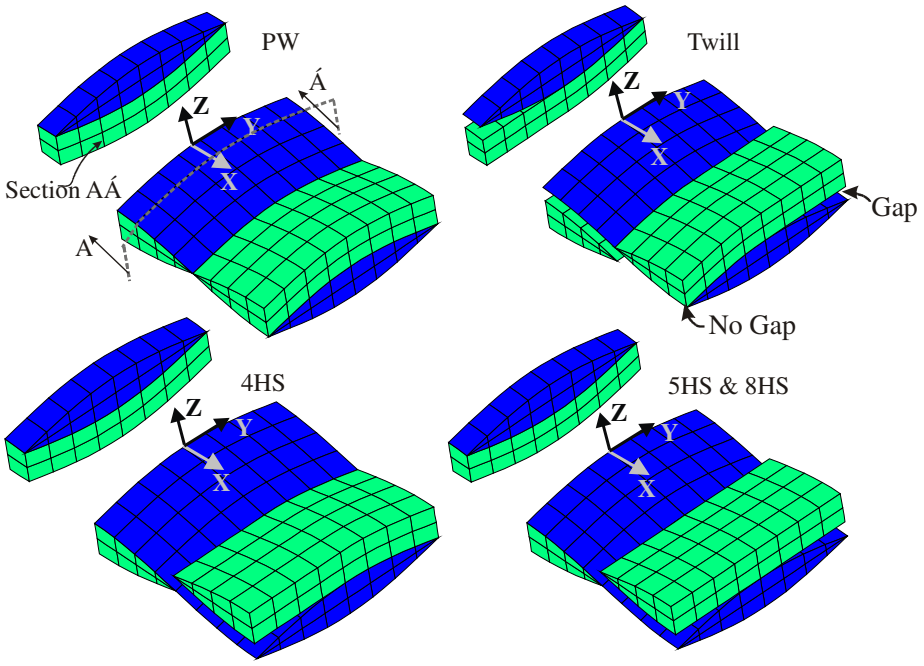

(b) Comparable regions (without the matrix pockets)
The layer of elements at x=0 is also shown detached to show gap between the tows

Figure 8.1. Continued.

The global coordinate system xyz (see Fig. 8.1) is shown for the twill weave and lies at a similar location on the white boxes for other weaves too. Notice that except for PW, all the weaves have wavy (undulating) as well straight regions. The geometric parameter h is the model thickness, and λ is the wavelength of the wavy region and was generally = 6 herein. Hence waviness ratio was 1/6. Limited analyses were also performed for plain weave configurations with higher waviness ratio. In those cases, the wavelength of the wavy region λ was 3. Comparable regions in different weaves were identified and are also shown in Fig. 8.1. Comparable regions contain only undulating portion of the warp tow and fill tows plus the matrix pockets. The comparable regions in different weaves are marked by white boxes. They contain the whole thickness (h) of the model and vary from x=0 to x= λ/2 and y= -λ/4 to y=λ/4 (see Fig. 8.1) in each weave. The comparable regions without the matrix pockets are shown in Fig. 8.1(b). The

weaves consisted of S2 glass and SC-15 resin. To validate certain hypotheses, a limited number of studies were also conducted for Carbon/EPON 9504 material system. The material properties are given in Table 8.1. The fiber volume fraction in the tow was 78%. The tow fraction in the model was 63.6%, hence the overall fiber volume fraction in each model was 50%. The strength values for the tow were obtained based on the analytical formulas given by Chamis [80]. A volume averaged stress $<\sigma_{xx}>=1$ was applied to each model, unless specified otherwise.

Table 8.1. Material properties.

Moduli (GPa) & Poisson's ratios	Tow* S2 Glass/ SC-15	Matrix SC-15	Tow* Carbon/ EPON	Matrix EPON
$\mathbf{E_{11}}$	75.92	2.82	178	3.21
$\mathbf{E_{22} = E_{33}}$	22.98	2.82	11	3.21
$\mathbf{G_{12} = G_{13}}$	7.16	1.01	7.1	1.16
$\mathbf{G_{23}}$	8.26	1.01	4.18	1.16
$\mathbf{\upsilon_{12} = \upsilon_{13}}$	0.26	0.395	0.23	0.38
$\mathbf{\upsilon_{23}}$	0.39	0.395	0.37	0.38
*Fiber volume fraction in tow = 78%				

Strengths (MPa)	Tow* S2 Glass/ SC-15
$\mathbf{S_{11}}$	2861
$\mathbf{S_{22} = S_{33}}$	53
$\mathbf{S_{12} = S_{13}}$	48.3
$\mathbf{S_{23}}$	31.2
$\mathbf{S_{11}^{C}}$	2861
$\mathbf{S_{22}^{C} = S_{33}^{C}}$	53
^{C} = compressive	

		Tow* S2 Glass/ SC-15	Matrix SC-15
Master Curve Parameters	**E** (GPa)	4819	2200
	$\mathbf{\sigma_0}$ (MPa)	155	146
	n	0.38	0.42
Orthotropic Parameters	**F**	0.48	1
	G = H	1.0E-05	1
	L	1	3
	M = N	1.67	3

8.2. Description of Postprocessing Techniques

In this section, two post processing techniques that are used to interpret the FE analysis data are discussed. The first technique converts the 3D variation of a stress component into a stress versus volume distribution plot. This kind of plot reveals how much volume of the material has a stress magnitude larger than a particular value. The plot gives a measure of the non-uniformity of the stress distribution. This is especially useful for assessing whether a local stress concentration is so localized that slight yielding will eliminate the high stress. This technique is used to obtain some valuable insights, which will be discussed in the results section.

The other technique is the calculation of stress resultants. In approximate models, the components of the textile are treated as simple structural elements like rods or beams and stress resultants are used to describe the load flow. The fully three-dimensional finite element results can be post- processed to obtain stress resultants, such as the

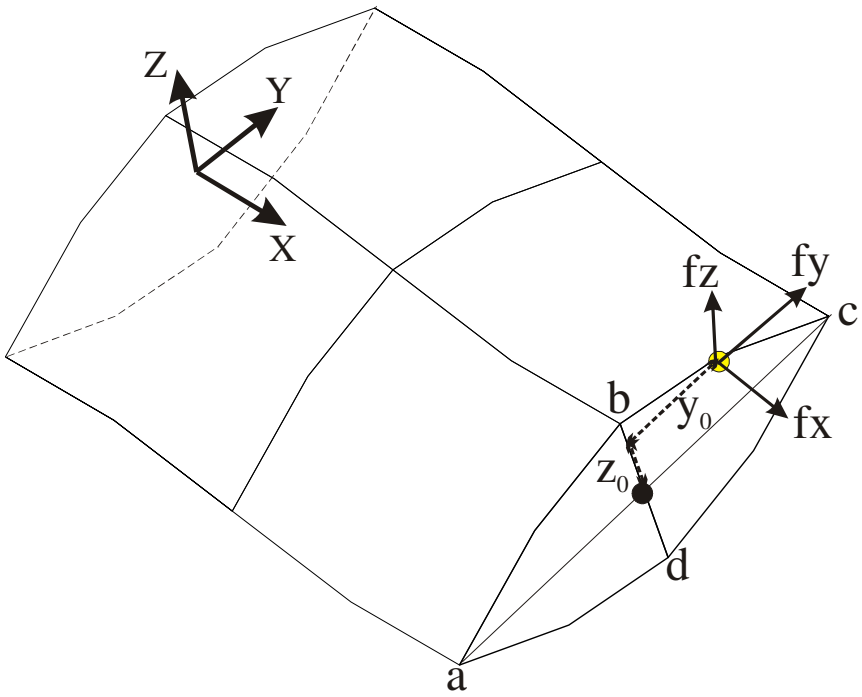

Figure 8.2. Stress resultants at cross-section abcd.

axial force or moment acting at any cross-section of the tow or matrix. The concept is illustrated for a cross-section *abcd* of the warp tow in Fig. 8.2. The nodal forces on the nodes lying on cross-section *abcd* can be calculated during the finite element analysis. We used 20 node brick elements, therefore each element has 60 forces, 3 at each node in x, y and z direction. These are labeled as fx, fy and fz respectively and are shown in Fig.8.2 for one node.

The forces Fx, Fy and Fz on a particular cross-section are simply the summation of all the nodal forces on that cross-section in the x, y and z directions respectively. At each cross-section, the moments about the cross-section centroid due to the nodal forces were calculated. The moments about the x, y, and z-axes are defined to be Rx, Ry, and Rz, respectively. Since stress resultants are obtained from full 3D models, the results are much more reliable than one could obtain by using a simplified model. Use of this technique to post process the finite element data will be shown in the results sections. It should be noted that cross-section *abcd* is the interface between two layers of elements. The magnitude of forces and moments acting on cross-section *abcd* calculated from the left layer of elements will not be equal to that calculated from the right layer because due to tow undulation, the stress state is different in the two layers of elements. But if the layer thickness is reduced, the difference between the forces on the left and right should decrease. The hypothesis was found to be true by considering meshes with different refinement. Figure 8.3 shows smaller regions of different meshes of a PW with 4, 12, 24 and 48 cross-sections. The number of degrees of freedom for meshes with 4, 12, 24 and 48 cross-sections are 2169, 16569, 63369 and 247689 respectively. The number of degrees of freedom is very small for 4 section meshes and is more than 100 times larger for the 48 section mesh. The maximum difference between Fx calculated from the left layer of elements and right layer of elements for the warp tow was 2.65, 1.38, 0.81 and 0.46% for meshes with 4, 12, 24 and 48 cross-sections respectively. Hence, as the number of cross-sections increased, the difference between the magnitudes of forces calculated from the left and right layers of elements decreased. In the results that follow,

4 section meshes were used to keep the runtimes low. The average forces or stress resultants were used in the analyses and were calculated by averaging the magnitudes of forces from the left and right layers of elements. The maximum difference between the average forces calculated using 4 sections meshes and those calculated using 48 section meshes was less than 3%.

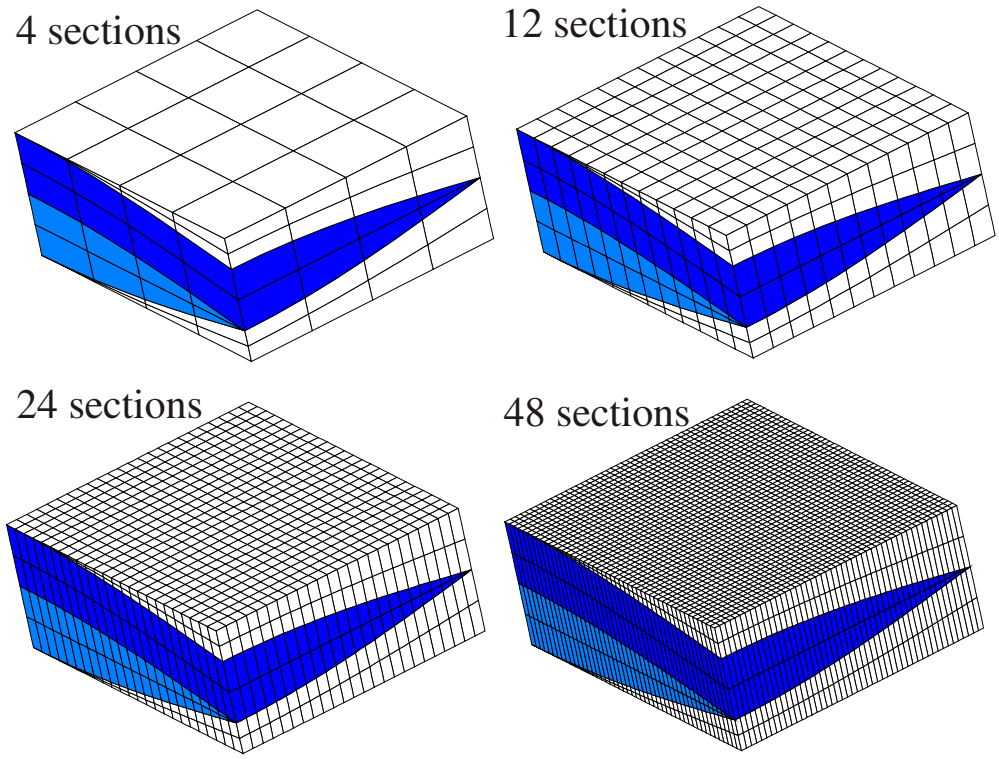

Figure 8.3. Meshes used for convergence study.

8.3. Results and Discussion

Special post processing techniques were applied to investigate the mechanics of load flow in textile composites. Load flow and stress volume distribution plots were employed to understand the behavior of a plain weave. The effect of tow architecture on the load flow in comparable regions of different weaves was also investigated. Finally, the effect of damage and plasticity on load flow in a plain weave was investigated. The results are discussed below.

8.3.1. Analysis of a plain weave

First, a plain weave was analyzed for the load flow in the warp tow, fill tow and matrix pockets. The potential correlation between the stress concentrations and magnitudes of stress resultants in the warp tow was investigated. The behavior of plain weave under in-plane shear stress was also analyzed. Typical stress volume distributions in the tow of a plain weave were also examined. The results are discussed below.

8.3.1.1. Fx load flow in a plain weave

Uniaxial tensile load was applied to a PW along the x direction as indicated by the arrows in Fig. 8.4. Since the area of the cross-section is 3 and the applied volume averaged $<\sigma_{xx}>$ was 1, the total Fx force at any cross sections of the model along the load direction (For e.g. sections $A\bar{A}$ and $B\bar{B}$ in Fig. 8.4) was 3. This causes considerable Fx and Fz stress resultants, but the Fy stress resultants were negligibly small. Figure 8.5 shows the Fx distribution in the warp tow, fill tow, matrix pockets and the total. The warp, fill and matrix do not have a uniform load flow, but the total load is always constant. Both the warp tow and matrix have a load peak where the crimp angle for the warp tow is maximum. The region where the crimp angle for the warp tow is maximum (section B in Fig. 8.4) is also called the *maximum undulation region* herein. The Fx in the warp tow increases by 23% from its value at x=0 and the corresponding peak in the matrix is around 8 times its value at x=0. In contrast, the fill tow has a dip and the load reduces by 86% at the maximum undulation of the warp tow.

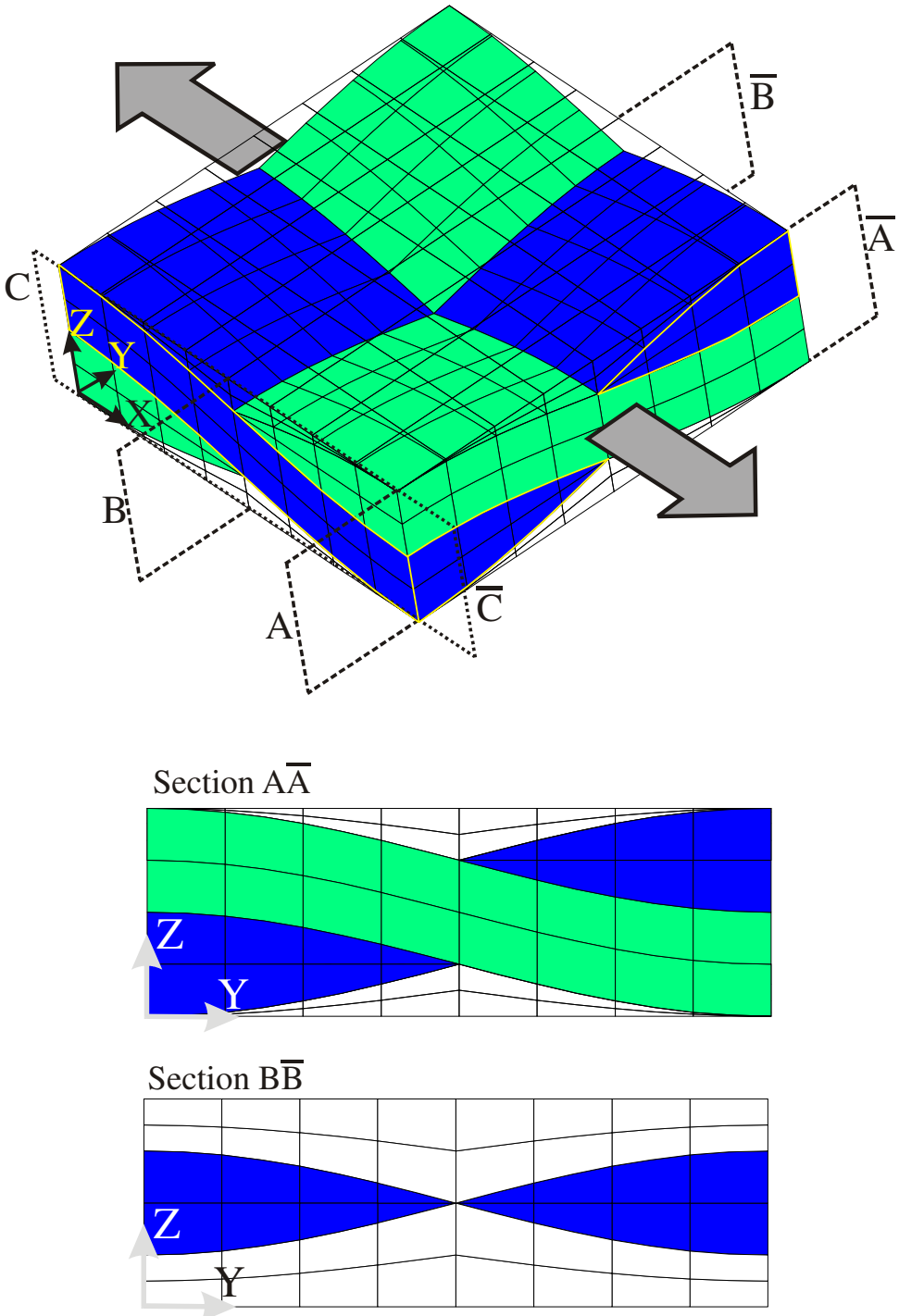

Figure 8.4. Variation in relative material areas of fill tow and matrix pockets at different cross-sections along the applied load direction (warp tow area is constant).

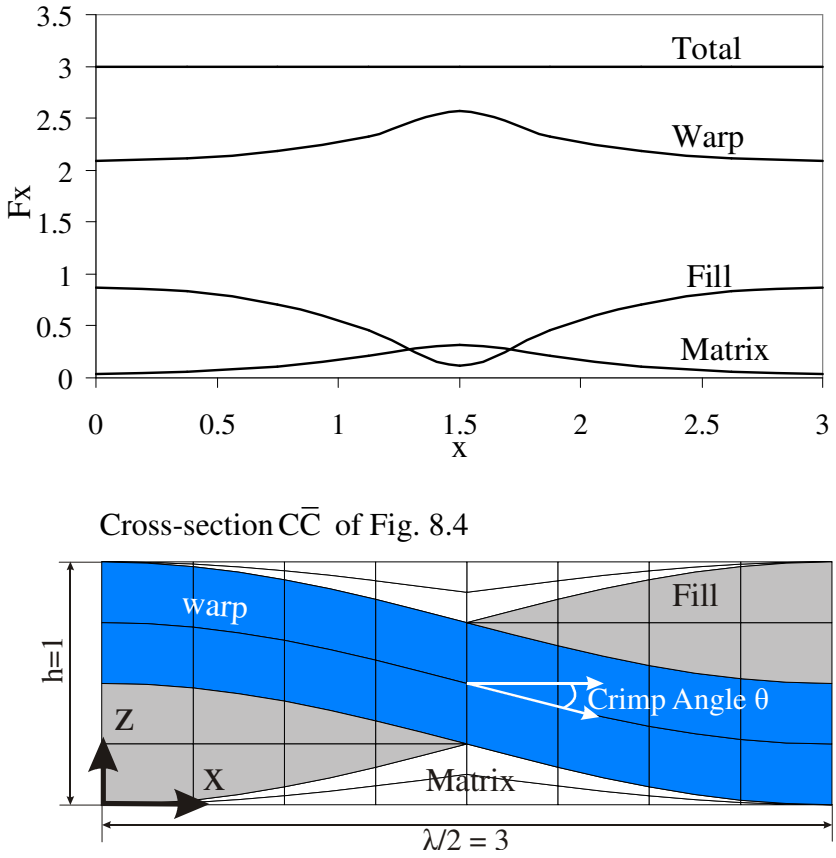

Figure 8.5. Fx load distribution in warp/fill & matrix.

The load redistribution occurs because at different cross sections of the model along the x-direction, the relative material areas of fill tow and matrix pockets vary (see Fig 8.4). At x=3 (i.e. cross-section $A\bar{A}$), there is very little matrix pocket as compared to at x=1.5 (i.e. cross-section $B\bar{B}$), where there is no fill tow material. The matrix has much less stiffness as compared to the transverse stiffness of the fill (E=3GPa for matrix versus E_{yy}=22GPa for fill tow). Depending upon the relative areas of matrix and fill tow at any cross-section, load will redistribute between warp, fill and matrix pockets. Hence the warp tow and matrix pick up the load at the maximum undulation region.

This reasoning was validated by investigating a "*stiffened matrix configuration*" in which the matrix shown in Fig. 8.5 has the same properties as the transverse

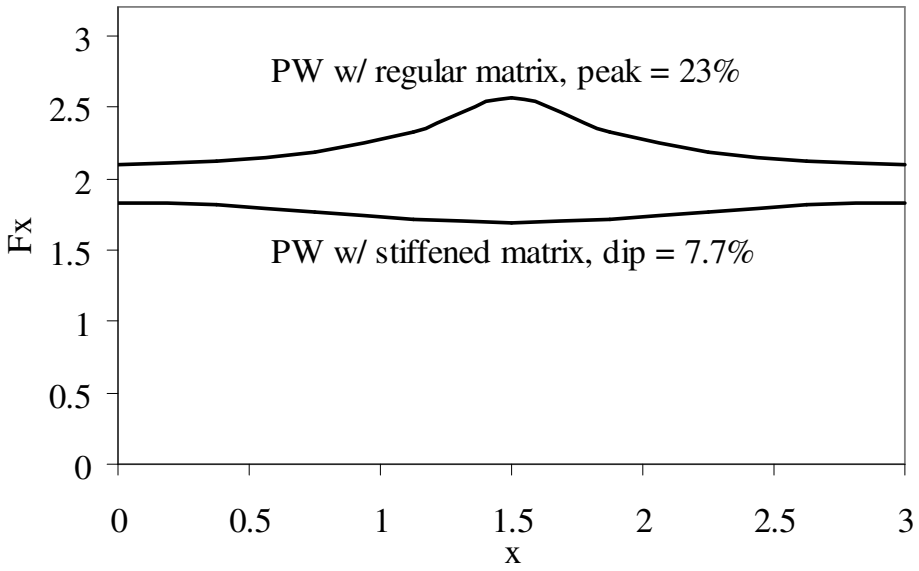

(a) Variation of Fx

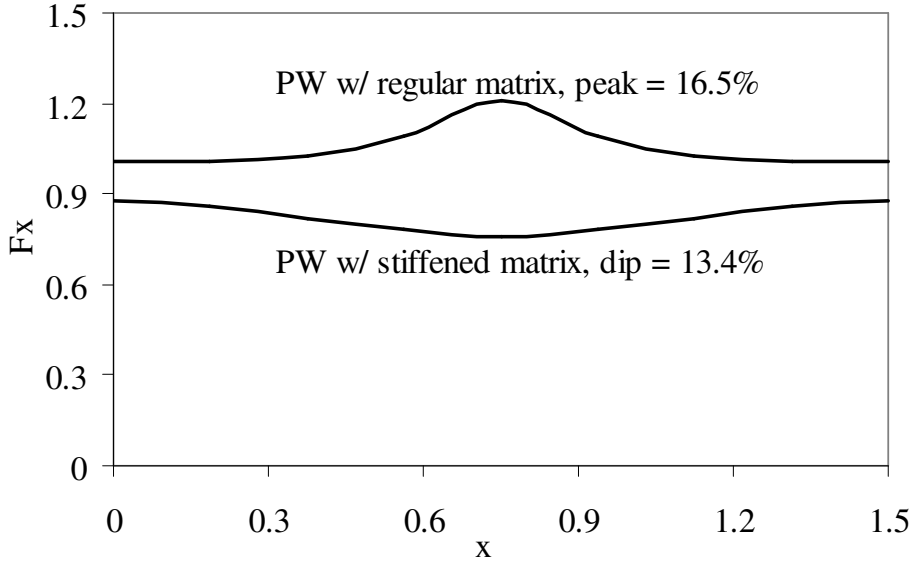

(b) Variation of Fx in configurations with higher undulation (wavelength λ=3)

Figure 8.6. Comparison of Fx load flow in different configurations.

properties of the tow. When the matrix is stiffened, the Fx in the warp tow decreases by 7.7% (see Fig. 8.6 (a)) at the point of maximum undulation….in sharp contrast to the 23% increase for the warp tow of regular matrix configuration. In Fig. 8.5, there are apparently two competing mechanisms. First is the load redistribution into the warp tow as fill tow is replaced by softer matrix. The second is load redistribution out of the warp tow because an inclined tow is not as stiff as a horizontal tow. In Fig. 8.5, the first is the dominant mechanism. When the matrix is stiffened, the first mechanism is virtually non-existent and the second mechanism results in a reduction in Fx at x=1.5. If we increase the undulation angle (i.e. waviness) by decreasing the wavelength (λ), the load shedding mechanism should become more pronounced. Fig. 8.6(b) shows the variation of Fx for the PW with the smaller wavelength λ=3. In the case of warp tow of a PW with regular matrix, the load peak at the maximum undulation region dropped to 16.5% (as compared to 23% in the case of less wavy configuration) and in the case of stiffened matrix configuration, the load dip increased to 13.4% (as compared to 7.7% in the case of less wavy configuration). These observations are consistent with the proposed mechanisms.

Next the effect of material system was studied to investigate if the above proposed hypotheses hold true in general or not. A plain weave configuration with Carbon/EPON material system was considered, since the carbon tow has considerably higher E_{11} moduli as compared to a glass tow. Table 8.1 shows that the E_{11} modulus for carbon tow was around 2.3 times the E_{11} modulus of glass tow, whereas the E_{22} modulus of the carbon tow was half that for the glass tow. The wavelength was kept the same (λ=6) as the original glass weave.

Figure 8.7 shows the variation of Fx load for the carbon/EPON plain weave configuration. In this case, the percentage increase in Fx in warp tow at x=1.5 is just 2.5% as compared to 23% in glass tow (see Fig. 8.5). The increase in Fx in the warp tow is little for the carbon weave, because the fill tow of the carbon weave carries only 7.2% of the total load as compared to fill tow of the glass weave, which carries 29% of the total load at x=0. So, the fill tow of the carbon weave has very little load to dump to the

warp or the matrix when the fill's cross-sectional area decreases at maximum undulation region. The fill tow carries a considerably smaller share of the total load in carbon weave, which is due to a much larger difference in the warp and fill tow moduli along the load direction for that weave. The modulus ratio of warp tow and fill tow for the carbon weave along the load direction (E_{11_warp}/E_{22_fill}) is around 16, which is much higher than for the glass weave (the ratio is ~3.3 in that case). The matrix modulus is approximately the same in both the configurations. Due to this, the warp tow in glass weave carries 70% of the total load at x=0, whereas for carbon weave, the warp tow carries the majority (91%) of the load at x=0. Load carried by matrix at x=0, in both the configuration is very little (around 1% of the total).

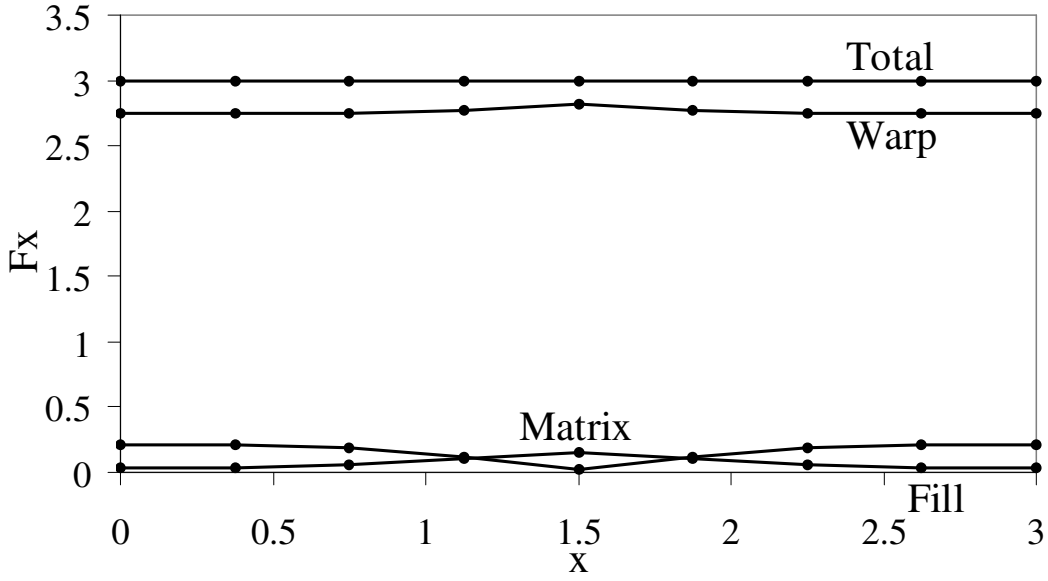

Figure 8.7. Variation of Fx for the Carbon/EPON plain weave configuration.

8.3.1.2. Fz load flow in a plain weave

Now the variation of Fz load at various cross-sections long the load direction is discussed. Figure 8.8 shows the distribution of the out of plane stress resultant Fz along the x direction both for Glass/SC-15 and for Carbon/EPON plain weaves. The existence and variation of Fz in plain weave can be approximately explained by a simple stress transformation. Let us assume that the only non-zero stress in the warp tow is σ_{11}, which is the normal stress along the axis of the fibers (see Fig. 8.9). It is also assumed that σ_{11} is constant throughout the warp tow. The average σ_{11} was approximated by dividing the Fx stress resultant at x=0 with the cross-sectional area of the warp tow.

This simplified stress state was transformed to the global coordinate system xz. The transformed transverse shear stress is given by:

$$\sigma_{xz} = -\sigma_{11}\cos(\theta)\sin(\theta)$$

$$\text{where } \theta = \tan^{-1}\left(\frac{\partial z}{\partial x}\right) \text{ and } z = \frac{h}{4}\cos\left(\frac{2\pi x}{\lambda}\right)$$

The transverse force Fz is simply $A\sigma_{xz}$ .The Fz stress resultant obtained by this simple transformation is also plotted in Fig. 8.8 as a function of x. It can be seen that the simple formula predicts the trend reasonably well. The maximum difference between the finite element predictions and the simple stress transformation is around 18.5% (see Fig. 8.8(a)) for the glass weave and very little (3.2% in Fig 8.8 (b)) for the carbon weave. A much better prediction for the carbon weave as compared to that for the glass weave by the simple formula is again due to the fact that in the carbon weave, the warp tow is the main load carrying component. Unlike Fx, whose variation is mainly governed by relative fill and matrix properties, the existence and variation of Fz is due to the warp tow undulation. Hence, the dip at maximum undulation should not disappear even in the case of a stiffened matrix configuration. Figure 8.8(a) shows that, in fact, is the case.

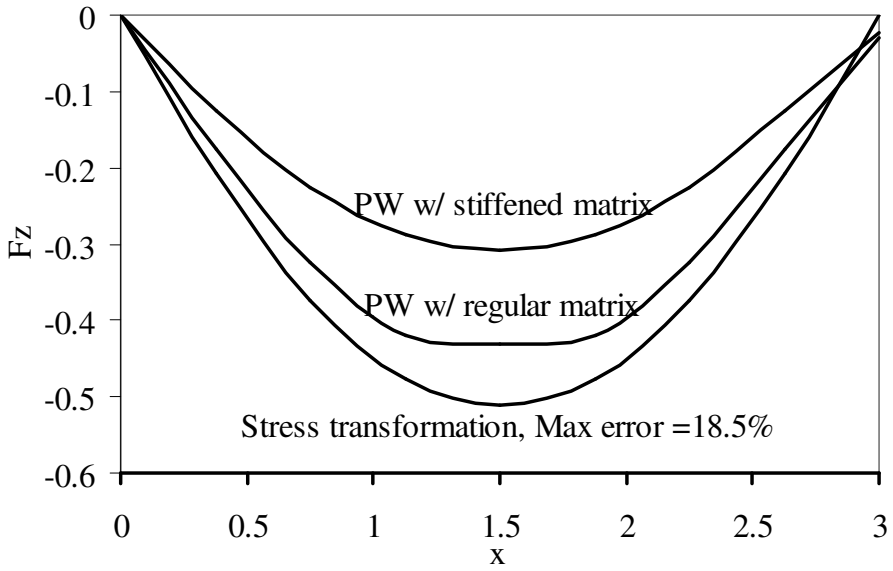

(a) S2-glass/SC15 configuration

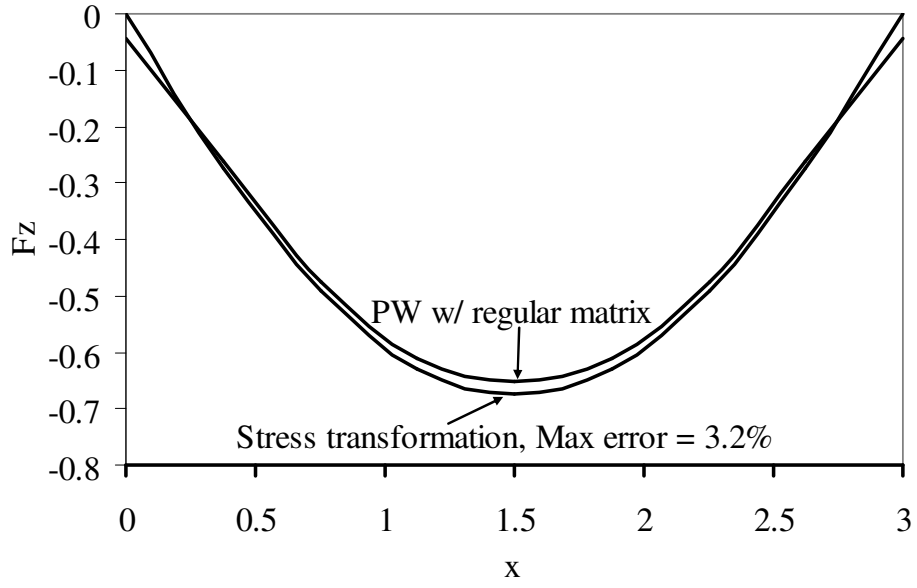

(b) Carbon/EPON configuration

Figure 8.8. Variation of Fz in plain weave configurations with different material systems.

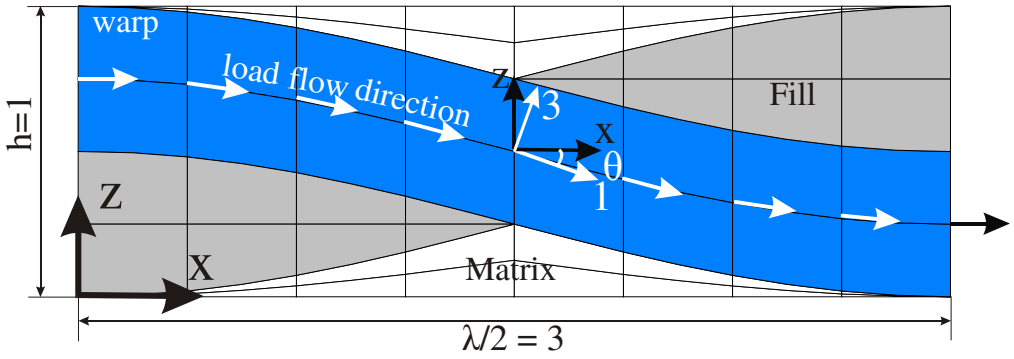

Figure 8.9. Load flow direction in warp tow with the coordinate system for stress transformation.

8.3.1.3. Variation of σ_{xx} average stress in a plain weave

Earlier we saw the variation of Fx stress resultant in the plain weave along the applied load direction. It must be noted that the relative areas of fill tow and matrix pockets do not stay constant at different cross-sections, hence the variation of average stress would be different from the variation of the Fx stress resultant. Here, this difference is investigated. Figure 8.10 shows fill areas for different cross-section locations along the applied load direction. The warp area at any cross-section is constant and is equal to 31.8% of the total. The sum of fill and matrix area is also constant (=62.8% of the total), but the relative areas of fill and matrix changes. It can be seen that maximum fill area is 50.8% of the total area of the cross-section and it deceases to 0% as we move to the maximum undulation region of the warp tow. To obtain a measure of average stress at different cross-sections, the Fx force shown in Fig. 8.5 was divided by the respective areas to obtain the variation of average stress along the x direction. It must be pointed out here that average stresses were calculated for the 24 section mesh (see Fig. 8.11) because there was a singularity in average stress in the fill tow at maximum undulation region of the warp. Figure 8.12 shows the variation of normalized average

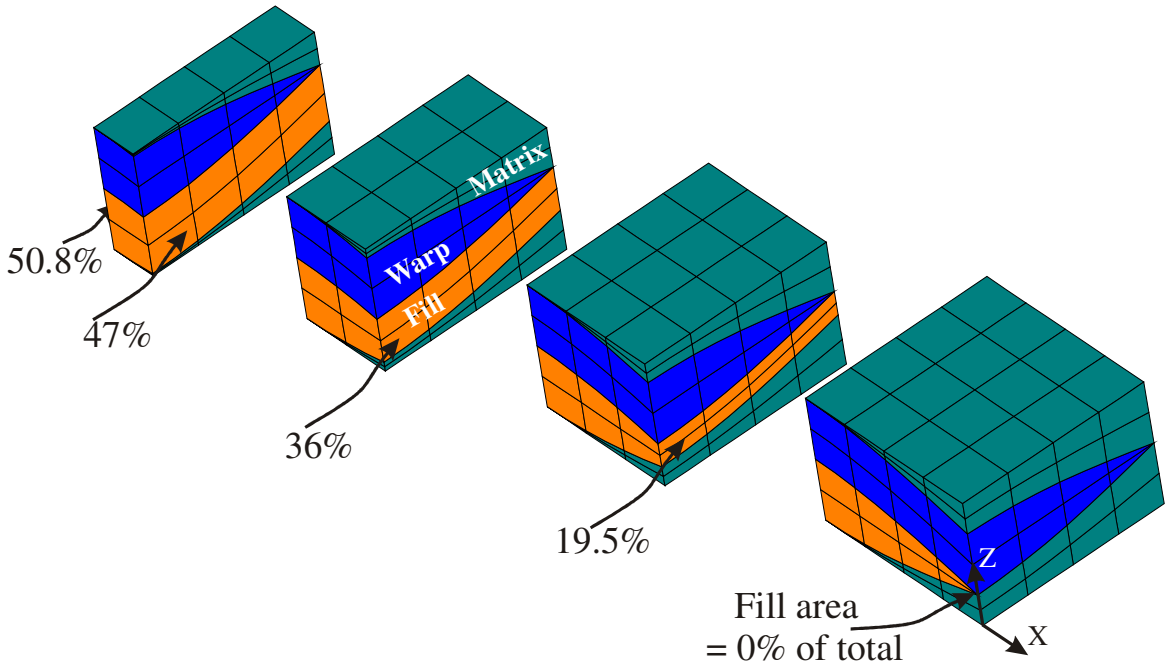

Figure 8.10. Variation of area of fill tow along the applied load directions.

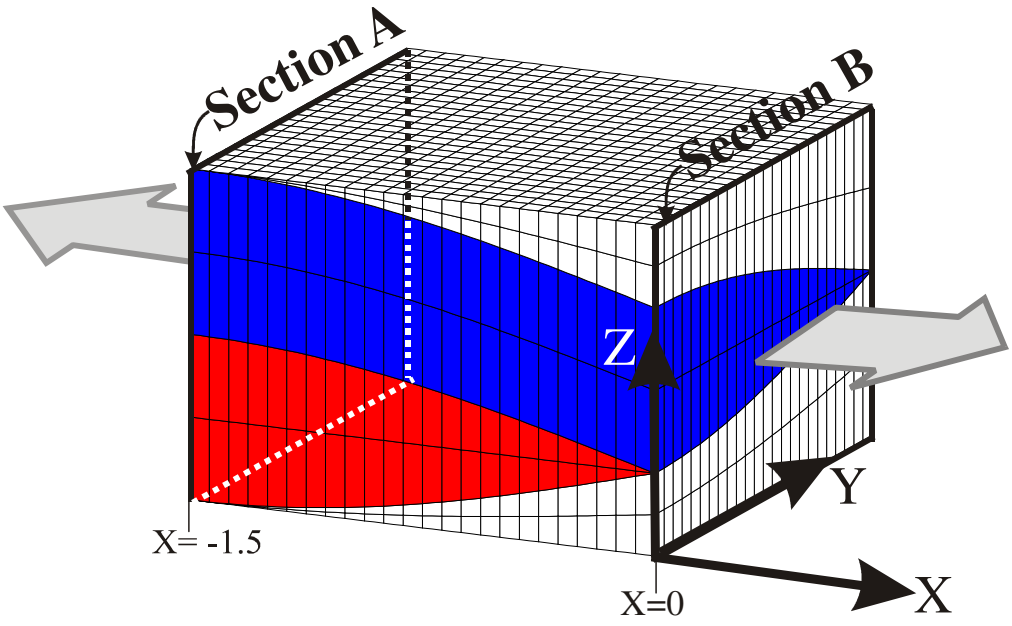

Figure 8.11. Refined mesh that was used to calculate the variation of average stress.

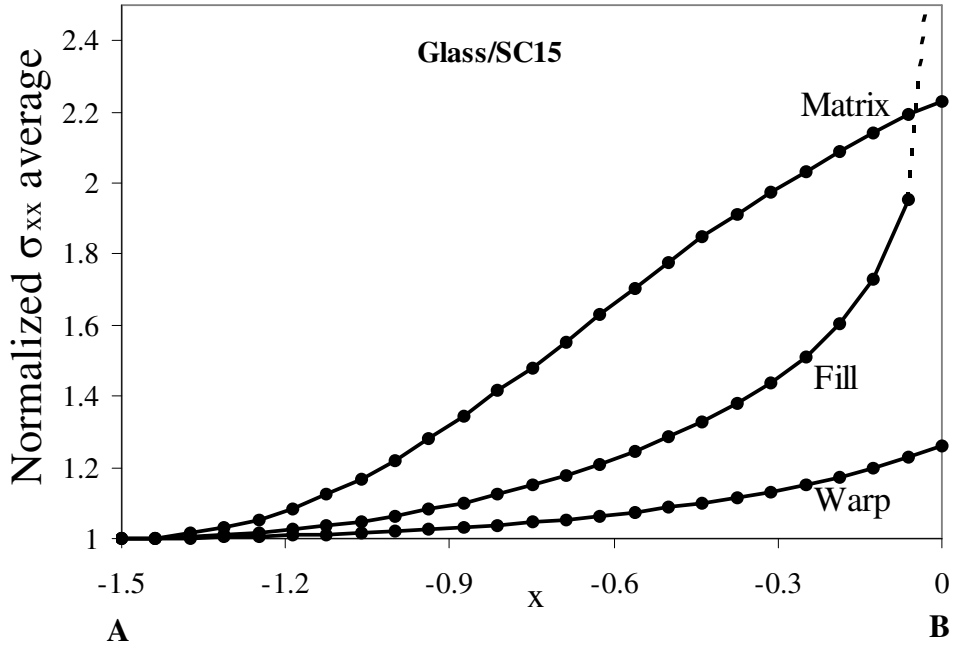

(a) S2-glass/SC15 configuration

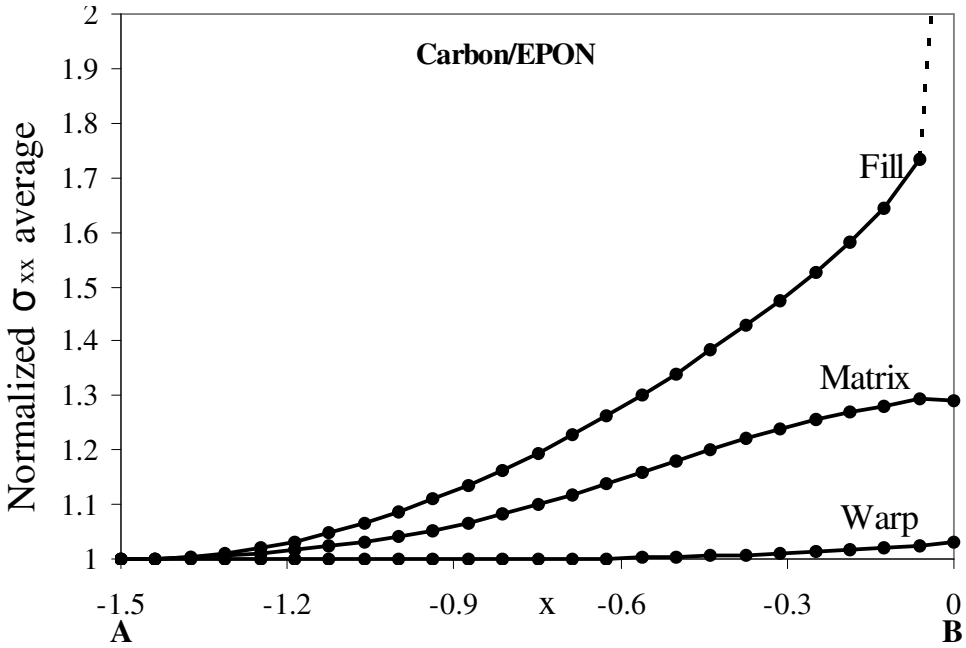

(b) Carbon/EPON configuration

Figure 8.12. Variation of average stress in plain weave configurations with different material systems ($\sigma_{xx\_avg} = F_x/A$ and Normalized $\sigma_{xx\_avg} = \sigma_{xx\_avg} \big/ \sigma_{xx\_avg\_@\ x = -1.5}$).

σ_{xx} stress at different cross-sections. The σ_{xx} stress is normalized by the respective value at x = -1.5. The locations x = -1.5 and x=0 Fig. 8.12 correspond to cross-section A and B (in Fig. 8.11) respectively. Unlike the force Fx, the average stress is maximum at maximum undulation region (section B) for fill tow also. Since the fill area reduces to zero at section B, there is a sharp rise in average σ_{xx} at that section. Although the matrix area at section B is maximum, the average σ_{xx} for matrix still increases at that section, because the percentage increase in Fx at section B is greater than percentage increase in area of the matrix. The increase in average stress at maximum undulation region can potentially make that region very susceptible to damage. Figure 8.12 shows that these observations are valid for plain weaves with both the considered material systems.

8.3.1.4. Correlation between stress resultants & stress concentrations

A correlation exists between the variation of the stress resultants and the location of stress concentrations in the warp tow. Note that since the area of cross-section of the warp tow is constant along the length of the warp tow, the variation of stress resultants is the same as the variation of average forces in the warp tow. Therefore the stress concentrations have the same correlation with the average stresses too. The regions where stress is concentrated are the potential damage initiation spots. Figure 8.13 shows σ_{xx} and σ_{xz} stress contours for the warp tow of a plain weave and curved beam. The *"curved beam configuration"* has only the warp tow in space and was used to obtain insights about the behavior of the warp tow of a PW. In Fig. 8.13, the location of peak stresses is marked by arrows for both of the configurations.

Figure 8.13(a) shows that for the warp tow, there is a large variation in σ_{xx} stress. The peak σ_{xx} occurs at the maximum undulation region, which is also the region of peak in Fx in the warp tow. The σ_{xz} stress is also non-uniform throughout the warp tow with a maximum at the maximum undulation region. This is also the region of the maximum Fz, as discussed earlier (Fig. 8.8). Hence, a correlation between the magnitudes of stress resultants and location of stress concentrations exists. The correlation between peak stress resultants and peak stresses was also observed for the stiffened matrix configuration. An investigation of plain weave configurations with truncated cross-

section showed that these correlations are not due to peculiarities of the lenticular cross-section shape.

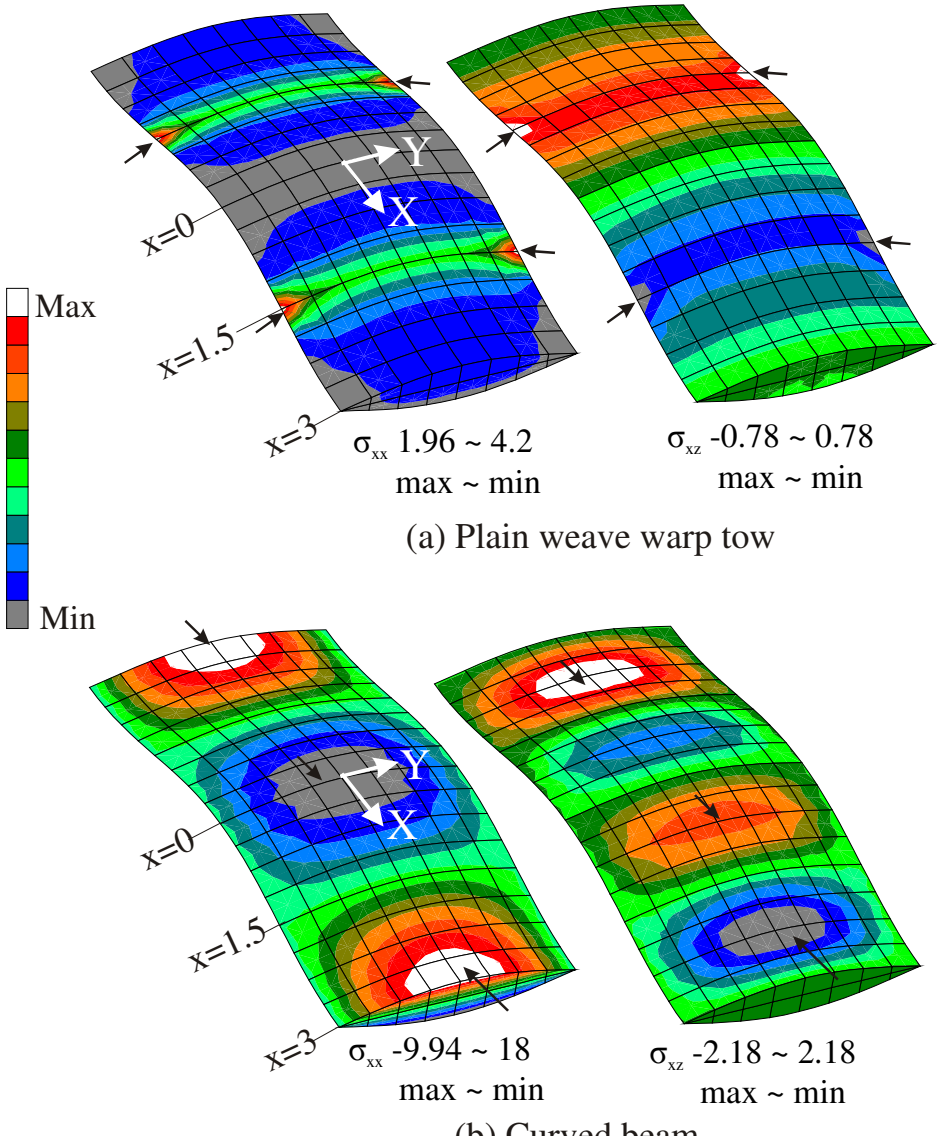

Figure 8.13. Stress contours for σ_{xx} and σ_{xz}.

In the case of a curved beam, though Fx is constant, there is a wide variation in the σ_{xx} stress distribution. In a curved beam, the maximum stress exists in the region of zero crimp because that is the region of maximum bending moment. Variation of the Ry bending moment along the length of warp tow and curved beam is shown in Fig. 8.14. The warp tow has almost zero bending moment, whereas for the curved beam, the moment varies considerably as we move along different cross-sections of the beam. The bending moment is maximum at the zero crimp angle region (i.e. at x=0 and x=3) and zero at the maximum undulation (i.e. at x=1.5), which is expected.

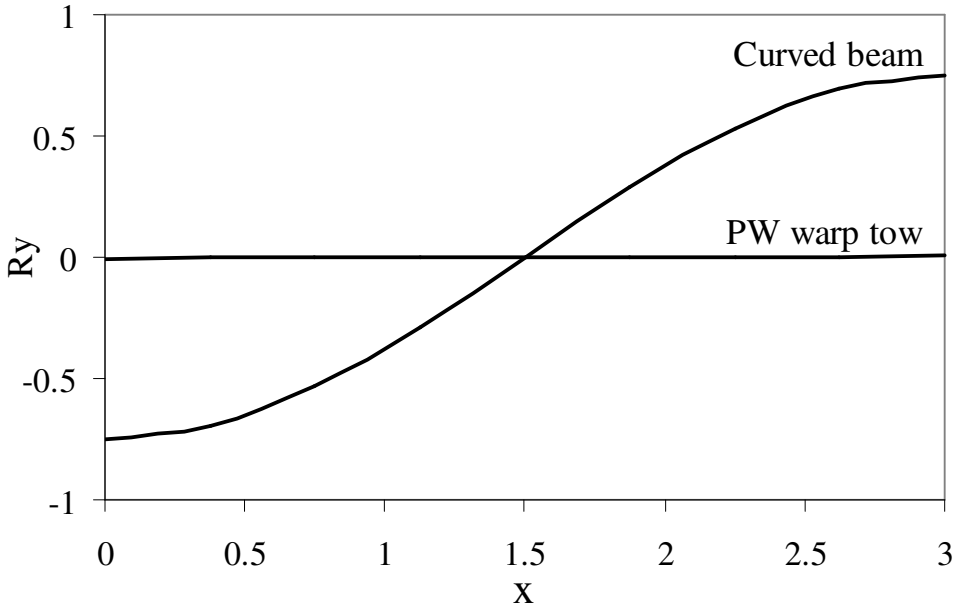

Figure 8.14. Comparison of bending moment in PW warp tow and in curved beam.

Non-zero bending moment in a curved beam causes almost a linear variation of the σ_{xx} stress whereas in the warp tow, the variation is not linear. The peak stress locations, magnitudes, stress resultants and bending moment are distinctly different in the warp tow of a plain weave as compared to in a curved beam. These results suggest

that one should be careful about approximating the tows as curved beams in approximate models.

8.3.1.5. Load flow in a plain weave under the application of in-plane shear stress

The behavior of a plain weave was also analyzed under the application of in-plane shear load. A unit volume averaged in-plane shear stress was applied to a plain weave with S2-glass/SC15 material system. The mesh used for this study is shown in Fig. 8.11. The variation of different stress resultants Fx, Fy and Fz in the warp tow is shown in Fig 8.15. It can be seen that the only significant non-zero stress resultant is Fy and the other two resultants are relatively small. Unlike the uniaxial tensile loading, the Fz is almost zero in this case.

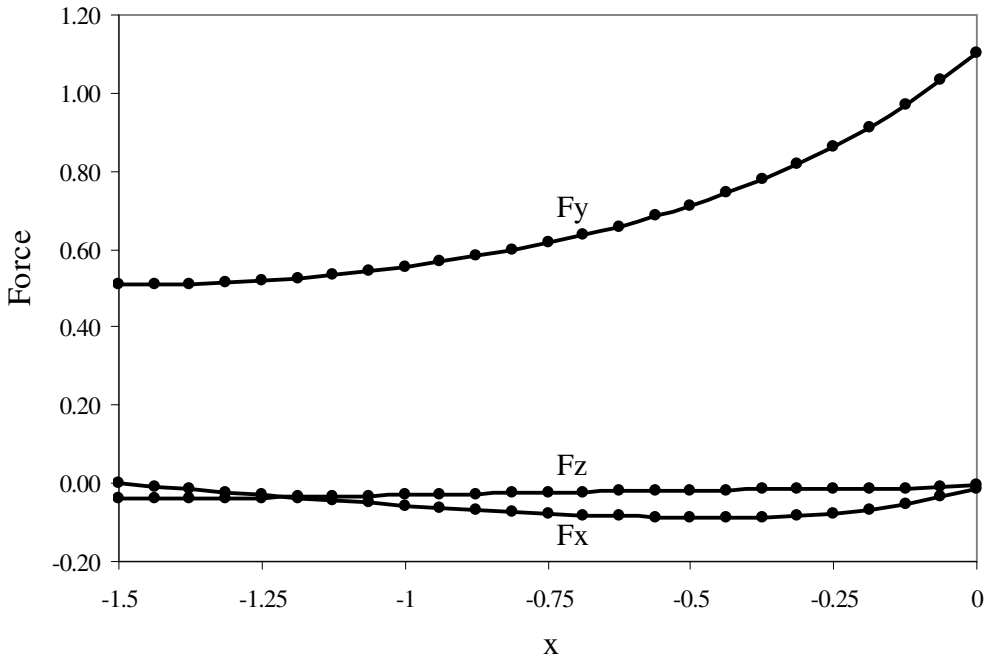

Figure 8.15. Variation of load flow in warp tow of a plain weave (applied stress is $\langle\sigma_{xy}\rangle = 1$).

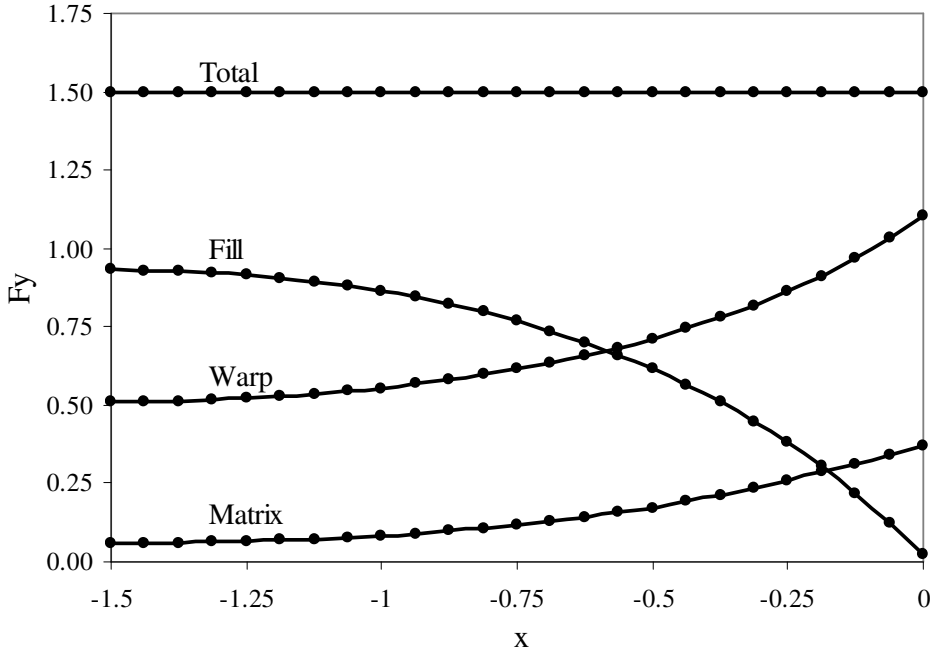

Figure 8.16. Variation of Fy in a plain weave (applied stress is $<\sigma_{xy}> = 1$).

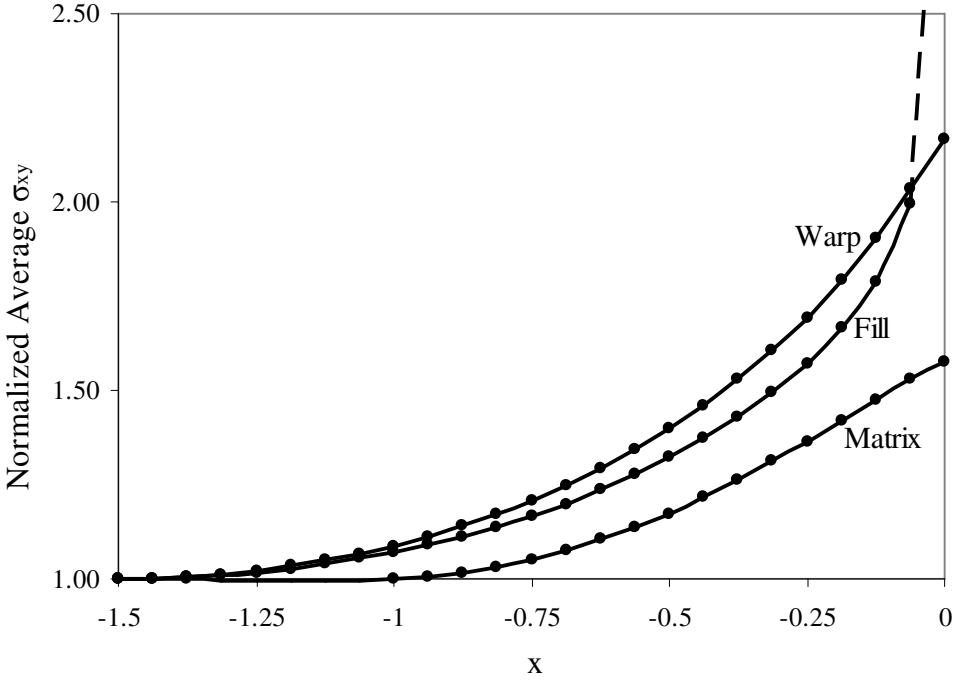

Figure 8.17. Variation of normalized average σ_{xy} in a plain weave ($\sigma_{xy\_avg} = \text{Fy/A}$ and $\text{Normalized}\,\sigma_{xy\_avg} = \sigma_{xy\_avg} \big/ \sigma_{xy\_avg\_@\ x = -1.5}$).

Since Fy is the significant stress resultant in this case, Fig. 8.16 shows the variation of Fy in the warp, fill tow and matrix. Like, the uni-axial tensile loading, in this case also, there is considerable variation in the load flow at different cross-sections of the weave along the x-direction. The plane x=0 is the maximum undulation region for the warp tow and the load reaches maximum value at this location for the warp tow as well as for the matrix. In contrast, the load drops in the fill tow at maximum undulation region. These variations in the load flow are similar to the load flow in the case of uni-axial tensile loading and are again due to the difference in moduli of warp, fill tows and matrix and changing material areas of the matrix and fill tow at different cross-sections.

Figure 8.17 shows the variation of normalized average σ_{xy} stress in matrix, warp and the fill tow. The stress was normalized by its respective value at x = -1.5 for different components. The average σ_{xy} in any component at a particular cross-section was obtained by dividing the stress resultant Fy with the area of the component at that cross-section. The normalized average σ_{xy} increases as we move toward the maximum undulation region (section B in Fig. 8.11). In this case also, there is a singularity in average σ_{xy} for the fill tow at x=0, because the fill area is almost zero at that location. Due to the presence of peak average stress at maximum undulation region, that region is prone to having high localized stresses also. Figure 8.18 shows that is actually the case. The figure shows the σ_{12} stress contours in the warp and fill tows weave. Figure 8.18 shows that unlike uniaxial tensile loading, the stress distribution is the same in the warp and fill tows. Peak local stresses exist at the maximum undulation regions, the same place where maximum average stress exists in the warp and fill tows. This makes the maximum undulation region very susceptible to damage initiation under in-plane shear load too.

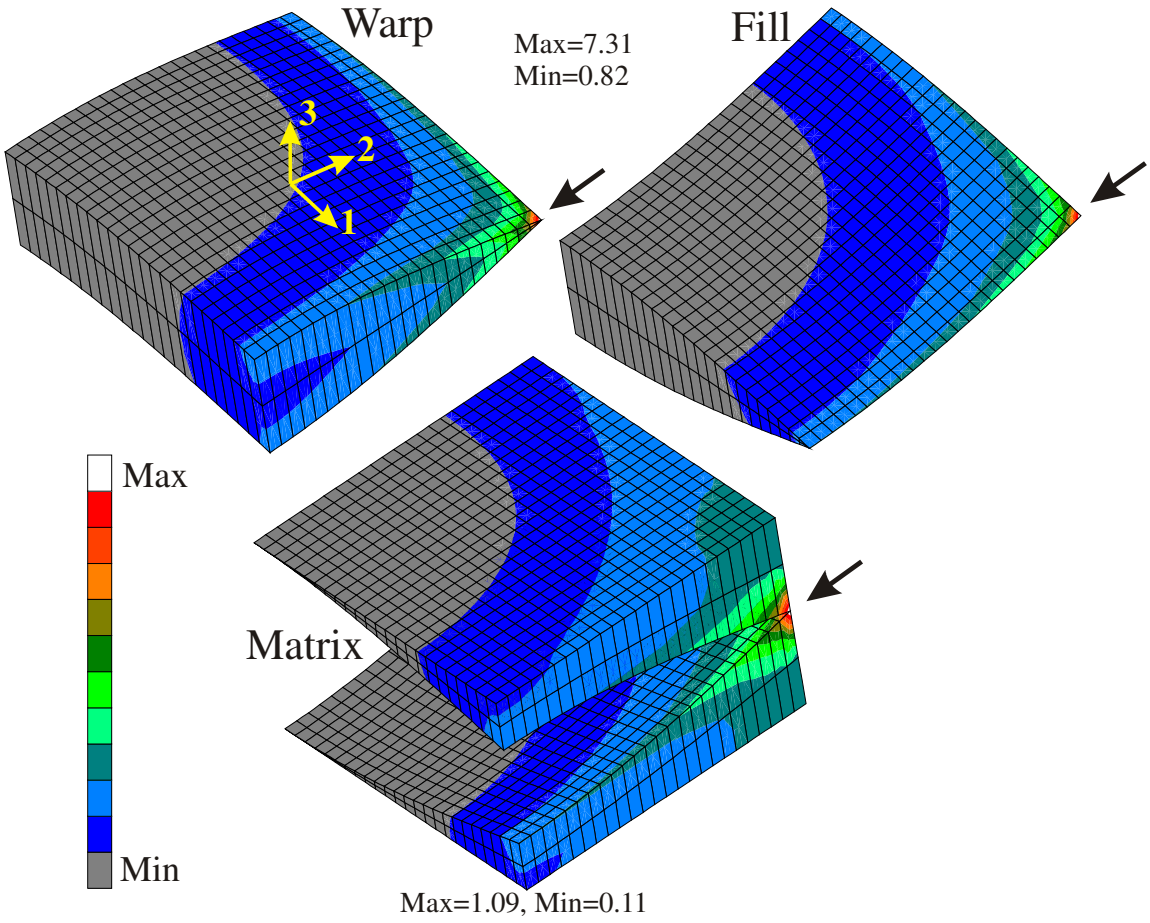

Figure 8.18. σ_{12} stress contours in a plain weave under the application of unit in-plane shear stress (peaks are marked by arrows).

8.3.1.6. Typical stress volume distribution in the warp tow of a plain weave

Here the stress distributions are analyzed using a stress volume distribution plot for the warp tow of a plain weave. A volume averaged stress $<\sigma_{xx}>$=304 MPa was applied to the plain weave model with S2-glass/SC15 material system. It caused a volume averaged strain of $<\varepsilon_{xx}>$=1%. Figure 8.19 shows the stress contours for different components in the warp tow of the plain weave. All the shown stresses are normalized by the respective strength values. Analysis of stress contours in the warp tow shows that

the peak σ_{11}, σ_{22}, σ_{33} and σ_{13} stress magnitudes are 0.46, 1.84, 1.27 and 1.7 times their corresponding strengths, respectively. This suggests that σ_{22} is the most critical component for failure initiation. Below we examine a stress volume distribution plot to obtain another perspective.

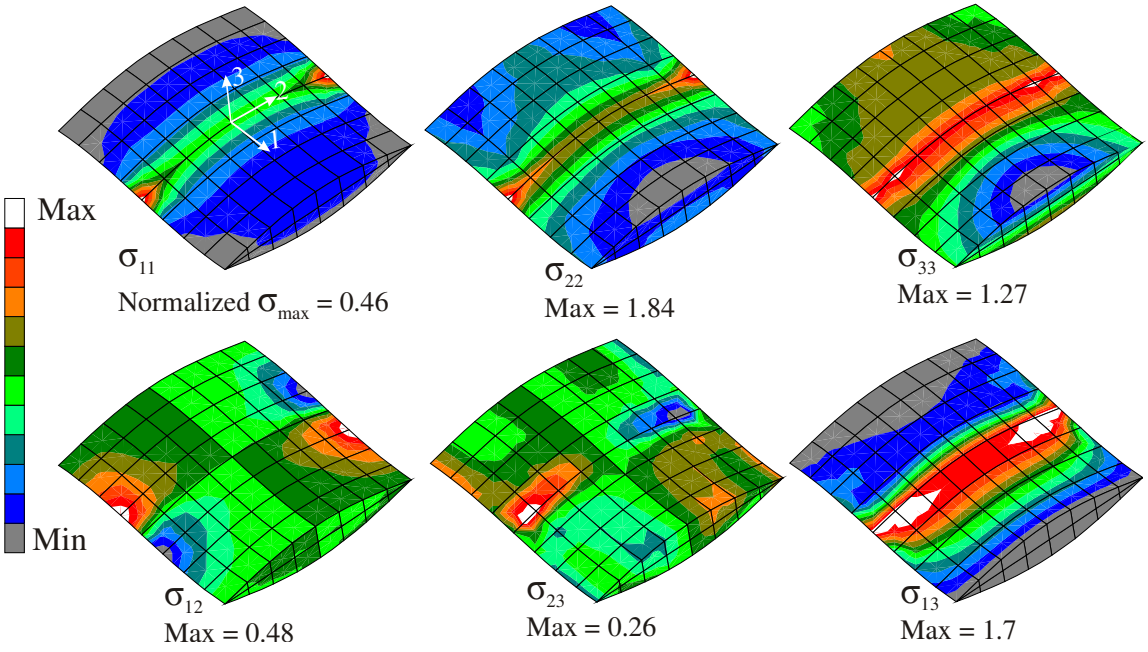

Figure 8.19. Normalized stress contours in the warp tow of a plain weave. Applied load is $<\sigma_{xx}>$=304 MPa and stresses are normalized by their corresponding strengths.

Figure 8.20 shows the stress volume distribution in the warp tow. The distribution is shown for all six stress components. The stresses (σ_{ij}) are normalized with their respective strengths (S_{ij}). This plot reveals how much volume of the material has a stress magnitude larger than a particular value. Assuming a maximum stress failure criterion, one could also find how much volume exceeds a critical stress.

Figure 8.20 shows that only 1.2% of the volume has σ_{33} stress greater than S_{33}. The σ_{22} peak value is $1.84S_{22}$, but less than 5% of the tow has σ_{22} greater than $1.03S_{22}$. Hence, these stress concentrations are so localized that slight yielding might eliminate the stress concentrations. In contrast, a considerable volume of the tow (about 19%) has σ_{13} greater than S_{13}. This means that a considerable volume of the tow is highly stressed and might cause failure initiation under this mode. Thus, σ_{13} might be the most critical stress component unlike that which was initially suggested by analysis of stress contours.

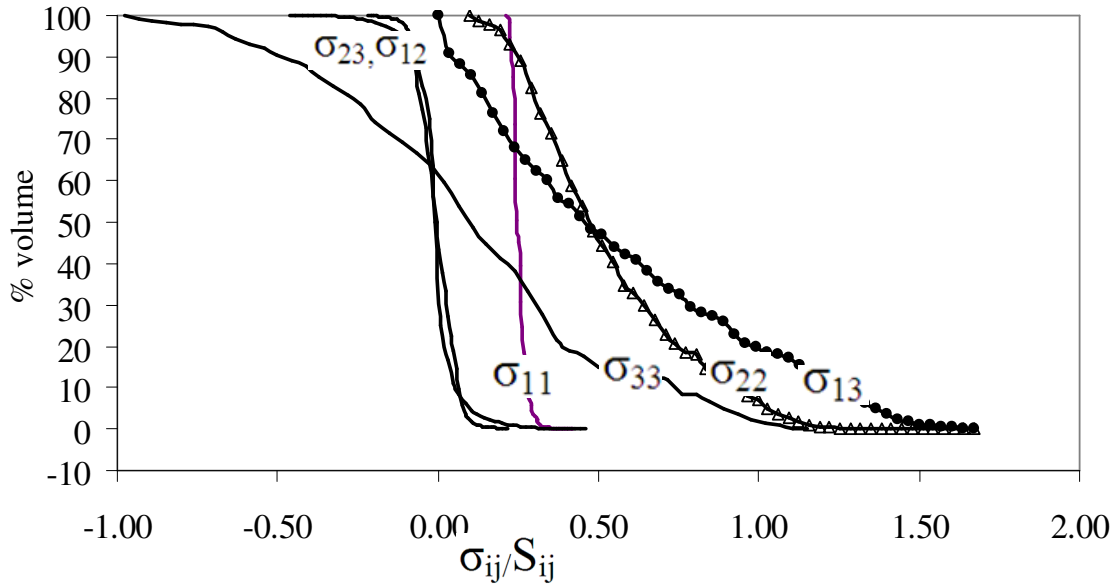

Figure 8.20. Stress volume distribution in warp tow (Applied volume averaged $<\sigma_{xx}>$=304 MPa & the stress components are normalized by their corresponding strengths).

8.3.2. Effect of Textile Architecture on Stress Resultants

Here the effect of weave architecture on the variation of stress resultants along the length of a warp tow was considered. To have meaningful comparisons, comparable regions were identified and analyzed. The comparable regions are shown in Fig. 8.1. Mesh refinement was the same for the different weave architectures. In this section, the variation of stress resultants is compared for the warp tow present in comparable regions. Meshes for different weave architectures are shown in Fig. 8.1. Figures 8.21, 8.22 and 8.23 show the effect of weave architecture on the variation of stress resultants in the warp tow.

In the comparable regions, all the weaves show a similar peak in Fx at the maximum undulation region (see Fig. 8.21). The distribution for PW and Twill is symmetric while for satin weaves, it is not. This is due to the fact that PW is symmetric and Twill weave is anti-symmetric whereas others are not (see Fig. 8.1(b)). The Fz distributions (see Fig. 8.22) are also very similar to each other for different weaves. Hence, in terms of Fx and Fz stress resultants, the global architecture has little effect on the warp tow in the local comparable regions.

The observations are different in the case of moment distribution, which is shown in Fig. 8.23. If non-zero stress resultants Fx or Fz do not act through the center of the cross-section of the tow, then it will result in non-zero moment at that cross- section of the tow. All the architectures have non-zero out of plane bending moment Ry. But this out of plane bending is very small for all the cases as shown in Fig. 8.23. Twill and 4HS have significant non-zero in plane bending Rz and out of plane bending Rx. Although nodal forces in the y- and z directions contribute to the Rx moment, the nodal forces in the y-direction were negligibly small, hence their contribution to the Rx moment was also negligibly small.

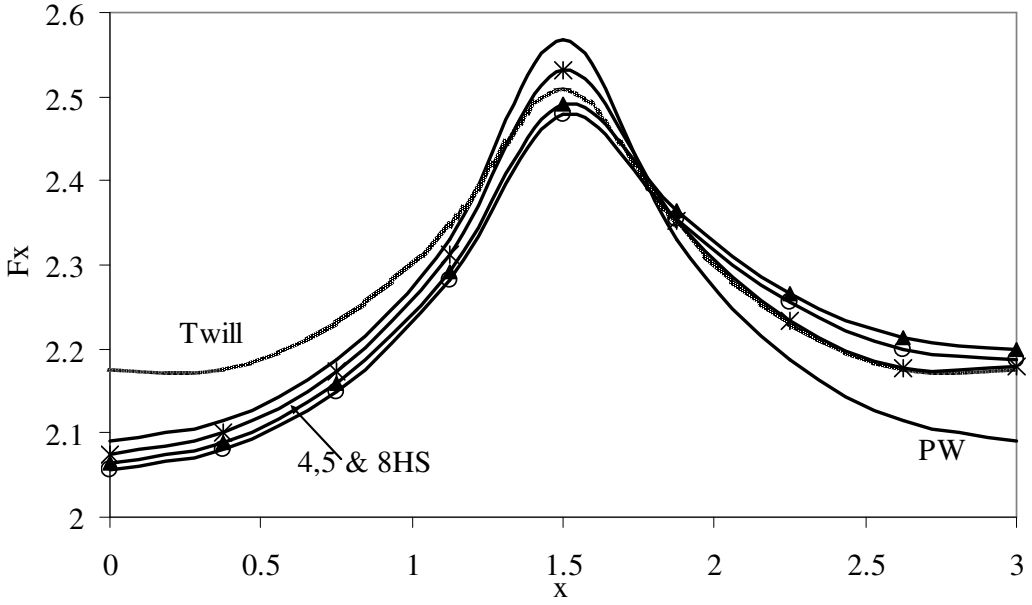

Figure 8.21. Effect of weave architecture on Fx distribution in the warp tow.

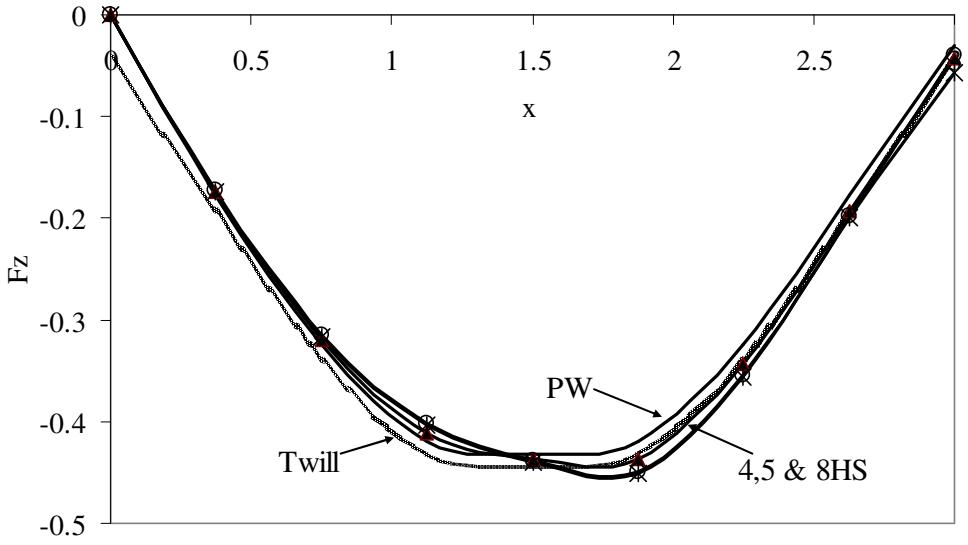

Figure 8.22. Effect of weave architecture on Fz distribution in the warp tow.

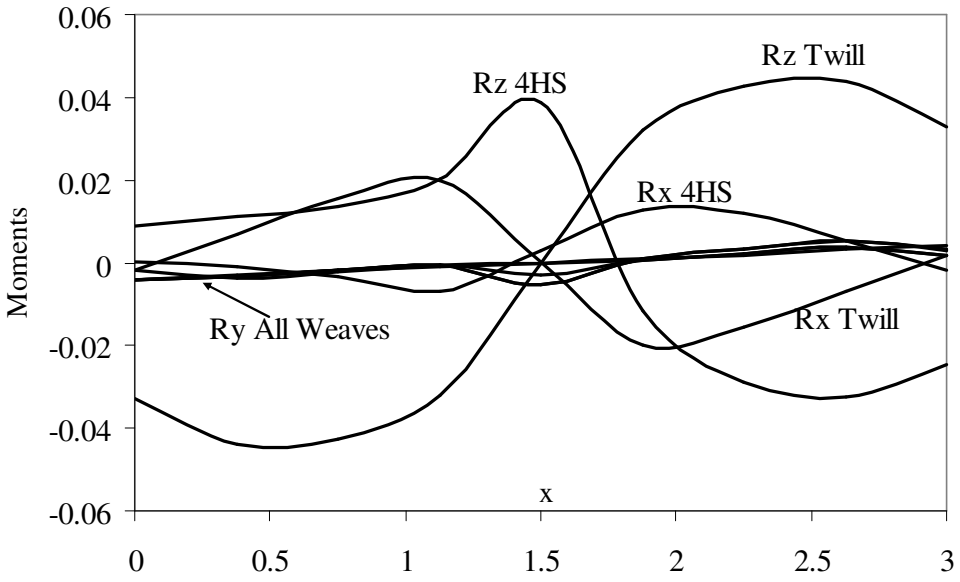

Figure 8.23. Effect of weave architecture on variation of moments in the warp tow.

The y offsets between the lines of action of stress resultants Fx and Fz and the xz plane are referred to as y_{Fx}^{off} and y_{Fz}^{off} respectively herein. It must be noted that the moment is a combined measure of offsets and magnitude of the force stress resultants. The moment at any cross-section will be zero if either of those is zero. Both y_{Fx}^{off} and y_{Fz}^{off} are non-zero at most of the warp tow cross-sections of the Twill and 4HS weaves. The existence of y_{Fx}^{off} only for Twill and 4HS weaves and not for others, can be explained by carefully examining the architecture of different weaves. Figure 8.1(b) shows the weave architectures in the comparable regions. For Plain, 5HS and 8HS weaves, y=0 is a plane of symmetry. For Twill weave, there is no symmetry about y=0. For 4HS, there is no symmetry about y=0 for half of the comparable region from x=1.5 to x=3. For the rest of the comparable region, the 4HS weave is symmetric about y=0.

Now if we examine the cross-section of the twill model at x=3 (refer Fig. 8.1(b)), we can see that the left half has fill tow woven around the warp tow whereas the right

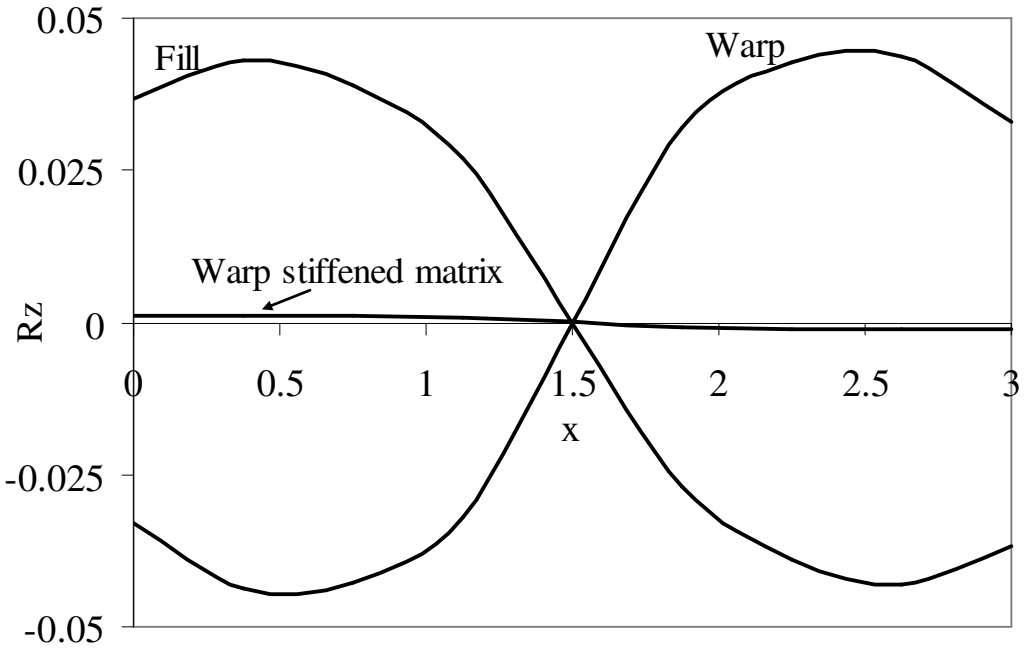

Figure 8.24. Variation of R_x^y for warp, fill and matrix.

half has a gap (filled by matrix) between the fill and warp. This causes better reinforcement of the warp on the left half than on the right half. Hence, the right half of the warp tow has to take more Fx load than the left half. This causes Fx to shift to the right (positive y direction) for the warp tow cross-section at x=3. If this hypothesis is true, then the following should also be true for the Twill weave:

- Warp tow should have negative y offset in Fx at cross-section x=0.
- Fill tow should have opposite offsets in Fx as compared to warp tow offsets at each cross-section.
- Offset in Fx for warp/fill tow should disappear for stiffened matrix configuration.

Figure 8.24 shows that this is the case. In Fig. 8.24, the bending moment Rz for warp and fill tows of the Twill weave is shown. From x=0 to x=1.5, the warp tow has negative Rz due to the presence of gaps in warp and fill in the negative y direction. Also,

the variation of Rz is anti-symmetric about x=1.5 since the architecture of the twill weave is anti-symmetric. The fill tow has an opposite moment distribution as compared to the warp tow. Figure 8.24 also shows that Rz for the warp tow of a stiffened matrix configuration is very small. Since Fx for each cross-section is considerably large, y_{Fx}^{off} for the warp tow was calculated to be negligible for the stiffened matrix configuration.

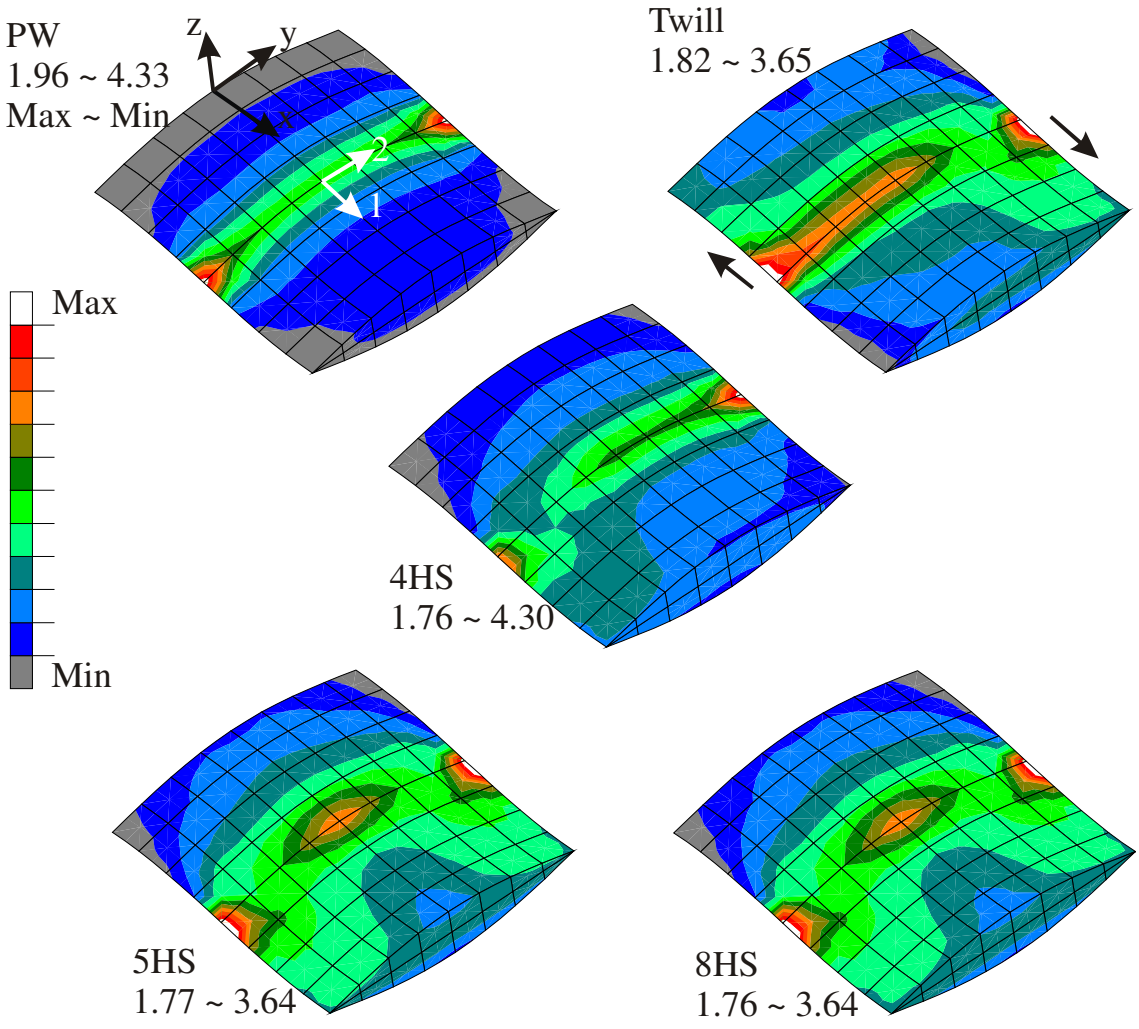

Figure 8.25. The σ_{11} contours in comparable regions of the warp tow for different architectures.

The effect of offset of Fx on the location of σ_{11} stress concentrations was also examined. Figure 8.25 shows the σ_{11} contours in comparable regions of the warp tow for different architectures. For PW, 5HS and 8HS weaves the stress contours are symmetric about the plane y=0. The stress concentrations are located at the maximum undulation regions and near both edges of the tow. For the case of Twill and 4HS weaves, the stress contours are not symmetric. For Twill weave, the stress concentrations are shifted slightly, as indicated by arrows in Fig. 8.25. This shift in locations of stress concentrations might be caused by the Fx offset. Since there is negligible Fx offset for a stiffened matrix twill weave configuration, the σ_{11} stress contours are almost symmetric about y=0 plane as shown by Fig. 8.26.

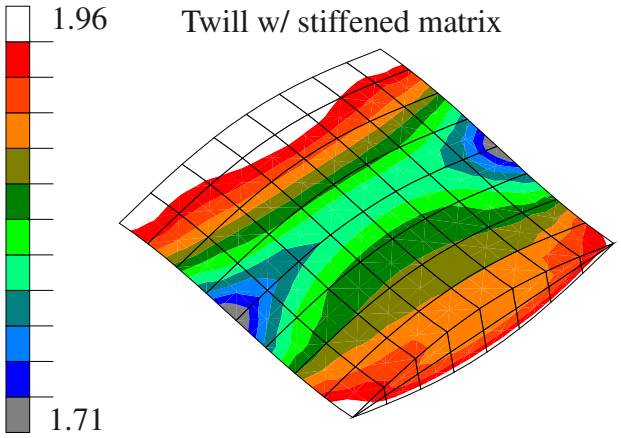

Figure 8.26. The σ11 contours in the warp tow of the stiffened matrix twill weave configuration.

8.3.3. Effect of Damage on Load Flow in a Plain Weave

So far we have investigated only the load flow if the composite is behaving linear elastically, but the textile composites show considerable non-linear response due to plasticity and material damage when static or fatigue load is applied. Here we investigate the effect of damage on the mechanics of load flow in a plain weave composite. The material system is kept to be S2-glass/SC15. The mesh used is shown in Fig. 8.27. The strength properties for the tow were obtained using Chamis' micromechanics formulas [80] and are given in Table 8.1. Whitcomb et al.'s [40] property degradation model was used for this study. The details of property degradation model and failure criteria were given in chapter VI earlier and are not repeated here. A uniaxial tensile load along the x direction was applied until the woven composite failed.

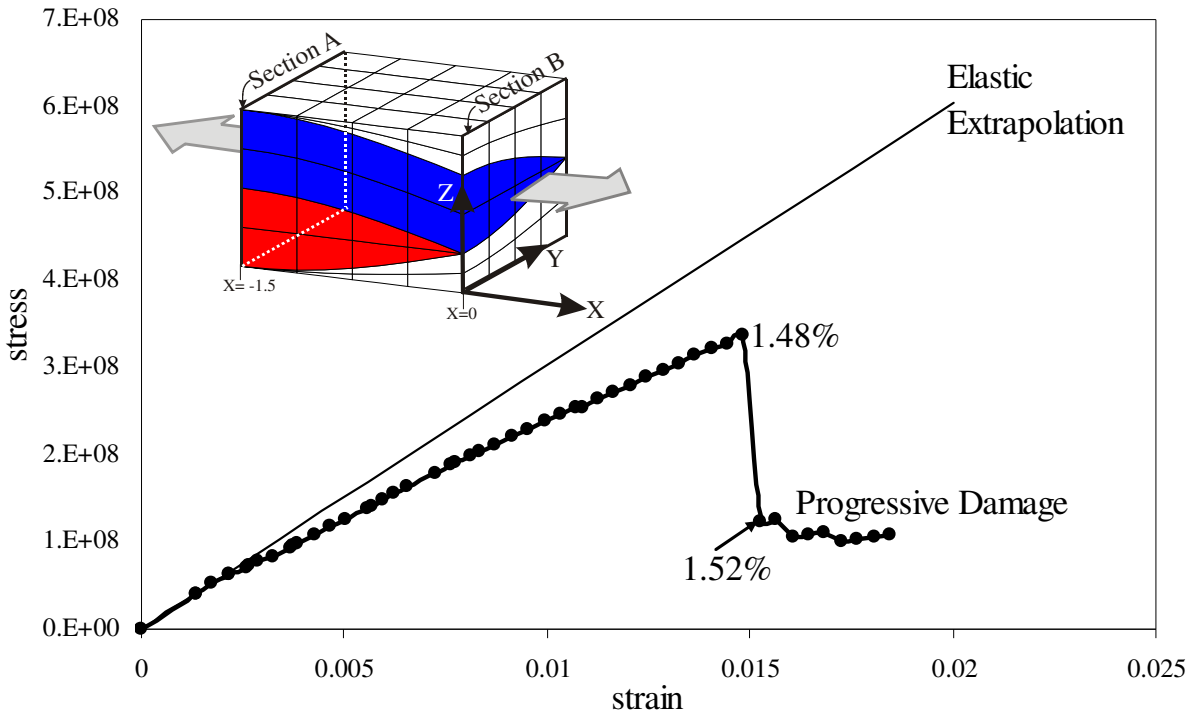

Figure 8.27. Stress-strain response of S2-glass/SC15 plain weave under uni-axial tensile load.

Figure 8.27 shows macroscopic stress strain behavior of the weave along the applied load direction. A linear elastic extrapolation is also shown in the figure for comparison purposes. The secant modulus of the composite decreases gradually until 1.48% strain. At that strain, the stress level drops by 24% from a linear elastic extrapolation. At 1.52% strain, the composite looses its load bearing capacity and the stress drops suddenly.

Figure 8.28 shows the effect of damage on load flow in the warp, fill tow and the matrix. The Fx load is shown at different strain levels and the load is normalized by the applied volume averaged stress at any strain level. At 0.135%, the Fx load in the warp, fill and the matrix is same as the elastic solution predictions, because no damage has occurred in any of the components at that strain level. At 0.135% strain, load at x=0 (section B in Fig. 8.27) increases in the warp tow and matrix pockets whereas it decreases in the fill tow due to reasons discussed earlier. As the load increases to 0.32% strain, a considerable drop in the load occurs in the fill tow. There is slight increase in the load in the matrix, and the majority of the load dropped by the fill is taken by the warp tow. Also, at this strain level, there is not as much variation in the load in the fill and warp tows (going from section A to section B of the mesh shown in Fig. 8.27). A considerable increase in the load in the warp and drop in the fill tow suggest occurrence of considerable damage in the fill tow. Figure 8.29 shows that in fact is the case. Figure 8.29 shows damage initiation and progression in the fill tow, matrix and the warp tow at different strain levels. If the material point failed under any of the six failure modes, then it is shaded, otherwise not. Damage initiation takes place at 0.175% strain in the fill tow and all of the fill tow is damaged at 0.32% strain level. It must be pointed out here that the location of damage initiation is consistent with our earlier observations and discussion of peak average σ_{xx} stress in the fill tow. It was noted in Fig. 8.12 earlier that there is a singularity in average σ_{xx} in the fill tow at maximum undulation region, which makes that region very susceptible to damage. Figure 8.29 validates that hypothesis and shows that the damage, in fact, does initiate in the fill tow in that region.

The damage has not initiated in either matrix or the warp tow at 0.32% strain level. Note that even though, a considerable damage has taken place in the fill tow, it is still able to withstand some load along the x-direction, because in Fig. 8.29, the material point is shaded if any failure mode took place. For example, if some damage occurred along out of plane direction in the fill tow, it might still be able to withstand load along applied load direction. Hence the load in the fill does not completely drop down to zero in Fig. 8.28 at 0.32% strain. At this strain level, the load in the matrix increases from section A to B, as the area of the matrix increases from section A to B and no damage has occurred in the matrix at this strain level. Damage initiates at a strain level of 0.465% and 0.81% in the matrix and warp tow respectively as shown by Fig. 8.29. At a strain level of 1.48%, a considerable damage has occurred in the matrix also. Hence, there is drop in the average load in the matrix. Although, there is considerable damage in the warp, its load bearing capacity is still in tact and load in the warp increases. But as soon as the strain level increases to 1.52%, the damage saturates in the warp tow as shown by Fig. 8.29. This causes a considerable load drop and load becomes quite non-uniform in the warp, fill as well as matrix as seen in Fig. 8.28. An excellent agreement between the load flow variation and the occurrence of damage in the warp, fill and matrix shows that based on load flow calculations, an intuitive understanding can be developed about where and how damage could be progressing even without looking at detailed microscopic damage simulation data.

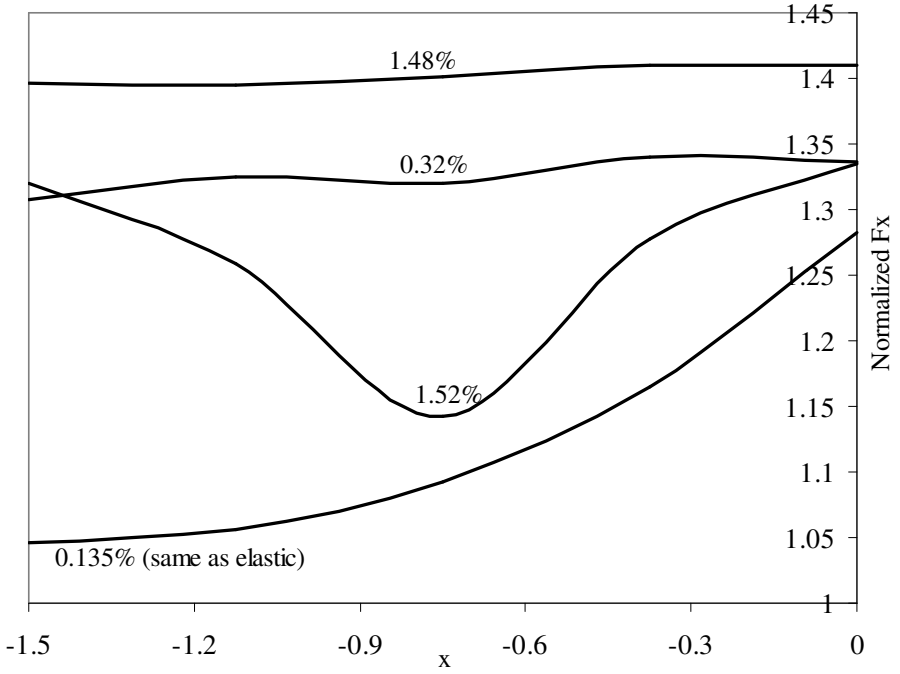

(a) Fx variation in the warp tow

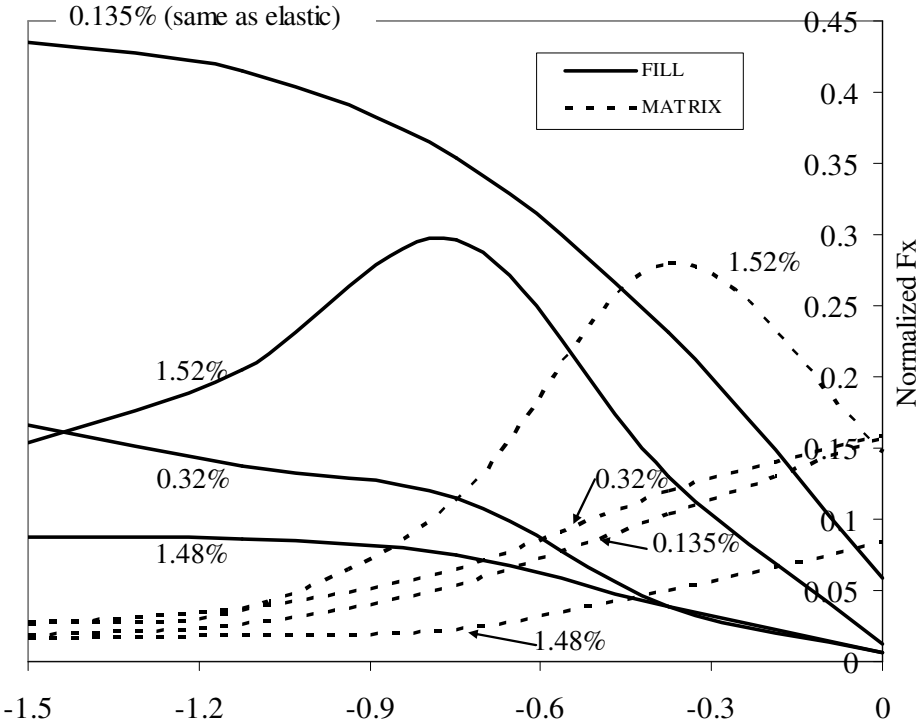

(b) Fx variation in the fill tow and matrix

Figure 8.28. Effect of damage on variation of Fx in the plain weave ($\text{Normalized } F_x = F_x \big/ \langle \sigma_{xx} \rangle_{\text{model}}$).

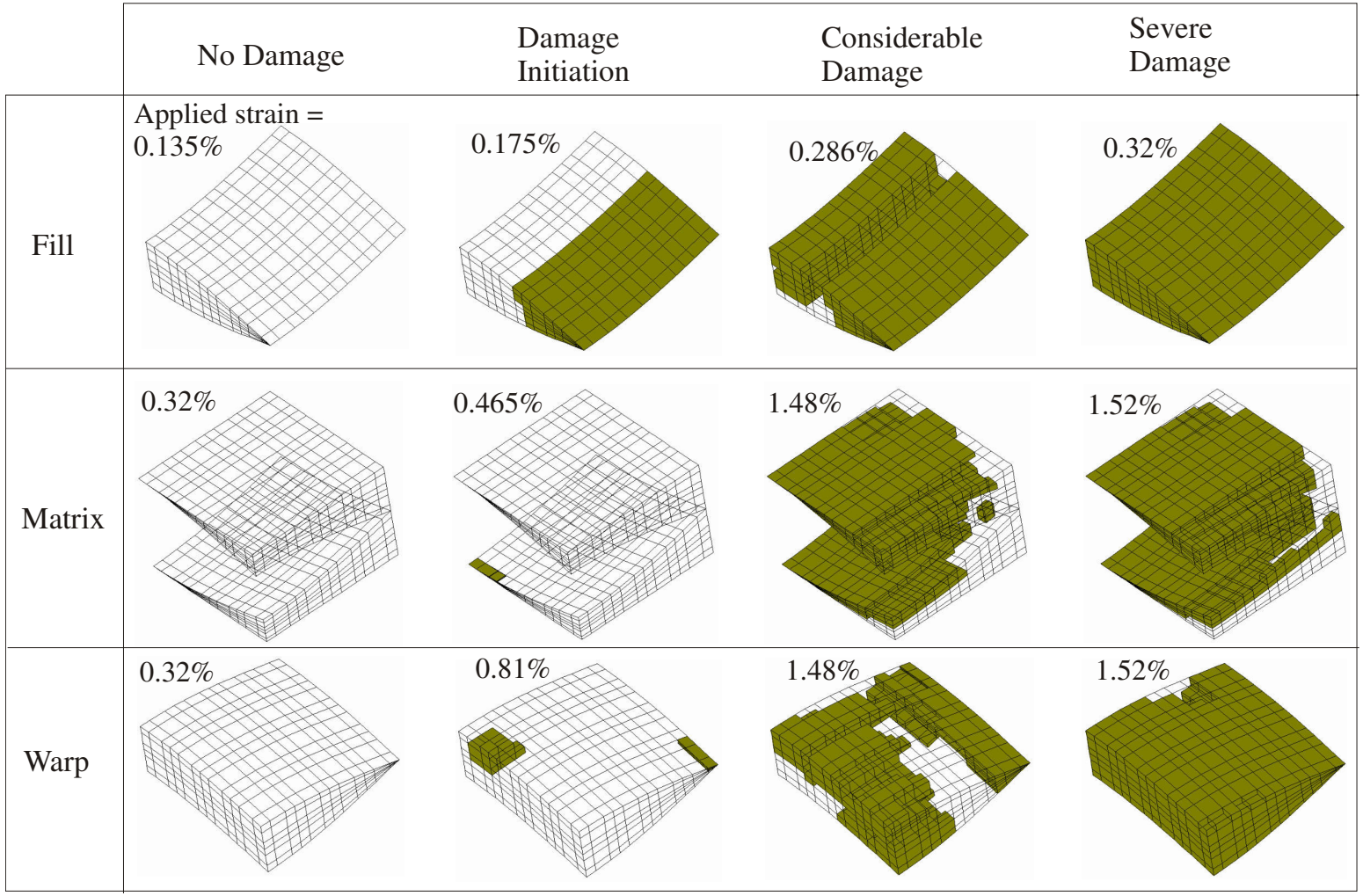

Figure 8.29. Damage initiation and progression in the plain weave.

Figure 8.30 shows the effect of damage on variation of normalized Fz in the warp tow. The variation is similar to the elastic case and exactly the same as linear elastic solution at 0.135% strain level because no damage has taken place in the weave. As the strain level increases, the maximum normalized Fz in the warp tow also increases because the average σ_{xx} stress also keeps increasing in the warp tow. Before the final failure, the variation in Fz is related to the amount of average stress in the warp tow in the fiber direction.

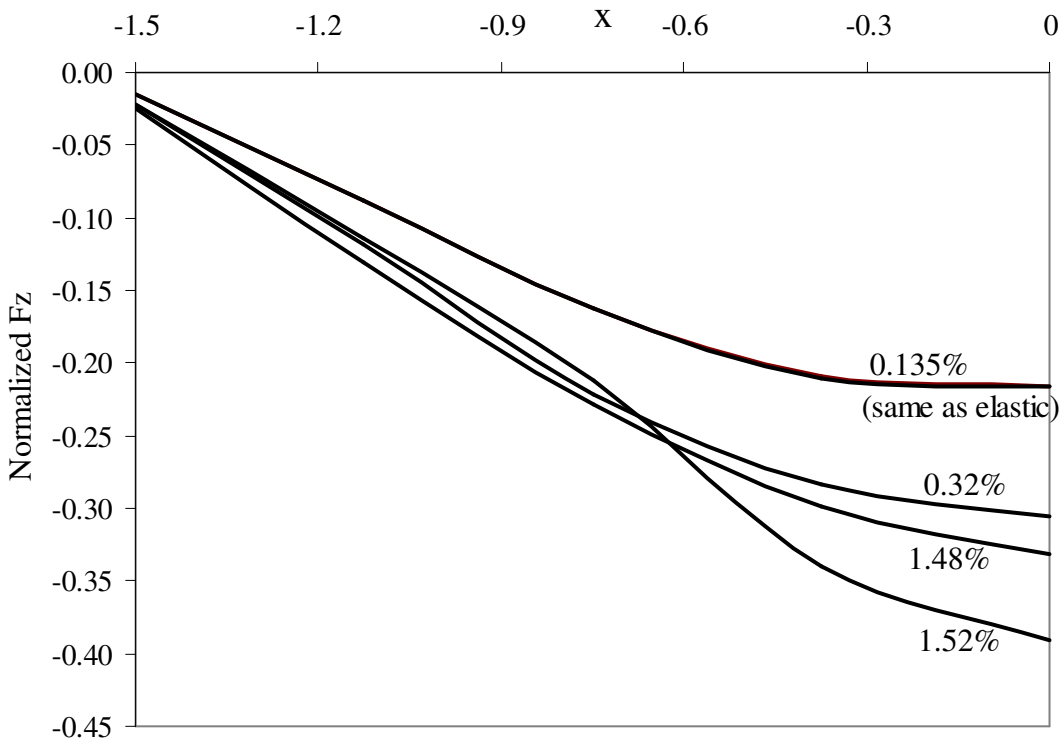

Figure 8.30. Effect of damage on variation of normalized Fz in the warp tow (Normalized $F_z = F_z / \langle \sigma_{xx} \rangle_{model}$).

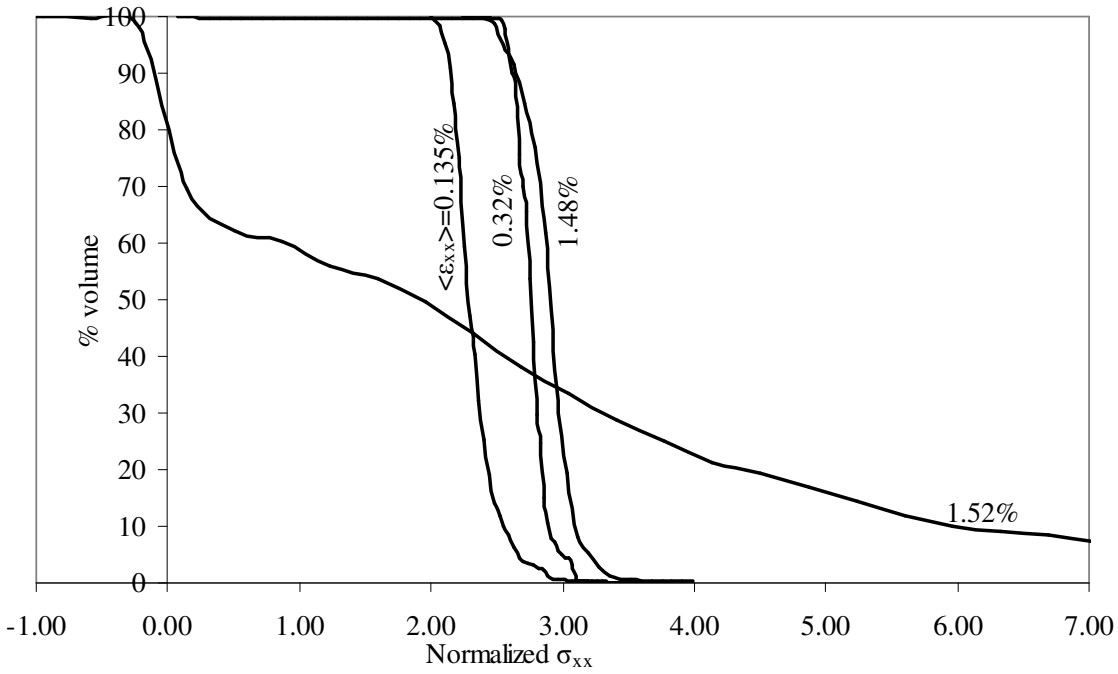

Figure 8.31. Effect of damage on σ_{xx} volume distribution in the warp tow (Normalized $\sigma_{xx} = \sigma_{xx} \big/ \langle \sigma_{xx} \rangle_{model}$).

Now the effect of damage on the σ_{xx} stress contours and σ_{xx} stress volume distribution in the warp tow is discussed. Figure 8.31 shows the normalized σ_{xx} volume distribution in the warp tow. The stress is normalized with applied volume average stress $<\sigma_{xx}>$ at different strain levels. At 0.135% strain, the stress volume distribution is the same as the linear elastic predictions. The σ_{xx} stress contours in the warp tow are shown in Fig. 8.32 and at 0.135% strain, the σ_{xx} stress contours are same as elastic solution. Stress peaks occur at the maximum undulation region and are marked by an arrow in the figure. As the strain increases to 0.32% and 1.48%, the average stress increases as shown in the stress volume distribution plot in Fig. 8.31. Since the load variation in the warp tow at these strain levels was little (see Fig. 8.28(a)), there is not much variation in the stress range too at these strain levels. However, as soon as the strain increases to 1.52%,

the warp tow has considerable damage, and the stress volume curve spreads out in horizontal direction (see Fig. 8.31), which indicates a wide variation in stress range. The σ_{xx} contours in Fig. 8.32 at 1.52% strain also show a wide variation in the stress and the stress range (-18.7 to 18.0) at that strain level is much larger as compared to the stress range at lower strain levels.

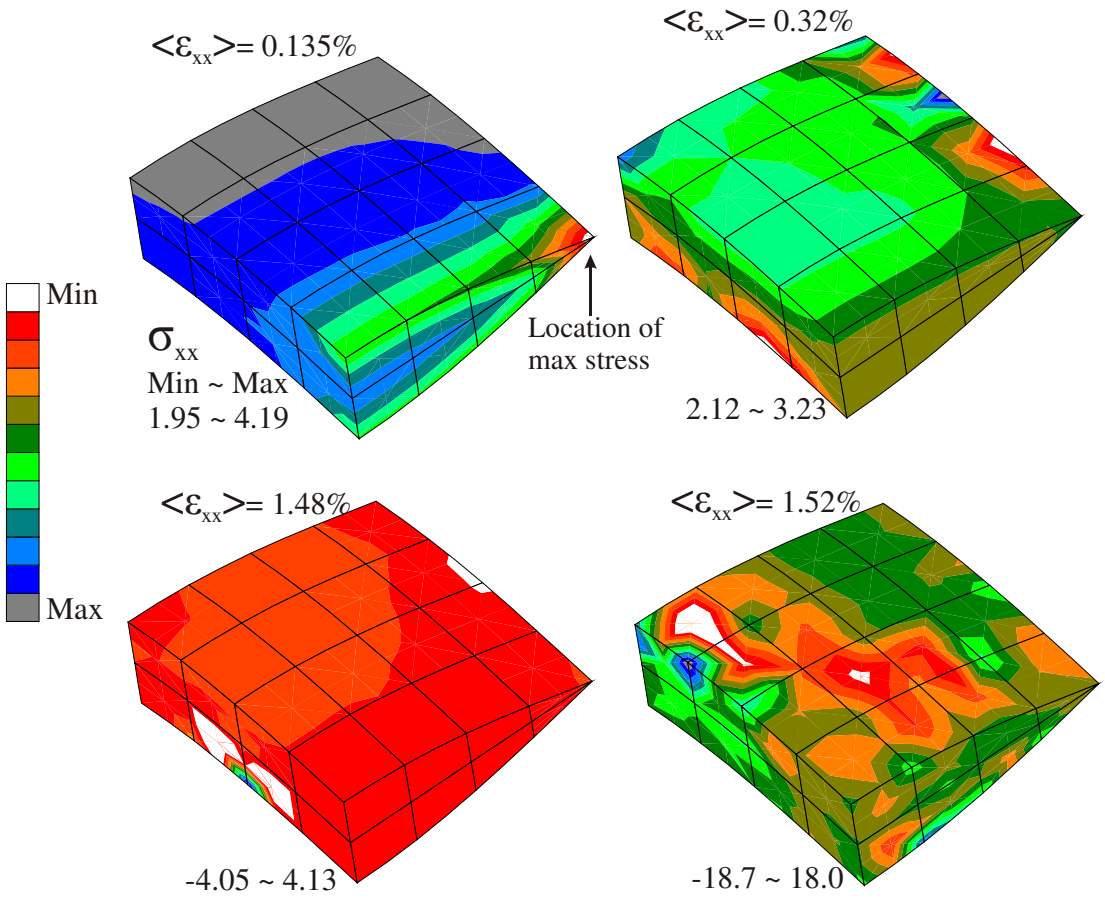

Figure 8.32. Effect of damage on σ_{xx} contours in warp tow.

8.3.4. Effect of Plasticity on Load Flow in a Plain Weave

In this section, we investigate how plastic deformation affects the load flow in a plain weave when a uniaxial tensile load along the warp direction is applied. The effect of plasticity is investigated on variation of Fx, Fz, average σ_{xx} and stress volume distribution in a plain weave. For this study also, a plain weave with S2-glass/SC15 configuration was chosen, the same configuration as used in the damage study earlier. The mesh is shown in Fig. 8.33. The plasticity analysis was based on a two scale modeling approach based on Hill's yield criterion for orthotropic materials. The details of plasticity modeling were provided in chapter VII earlier. The elasto-plastic material properties for the SC15 resin and S2-glass/SC15 tow are given in Table 8.1.

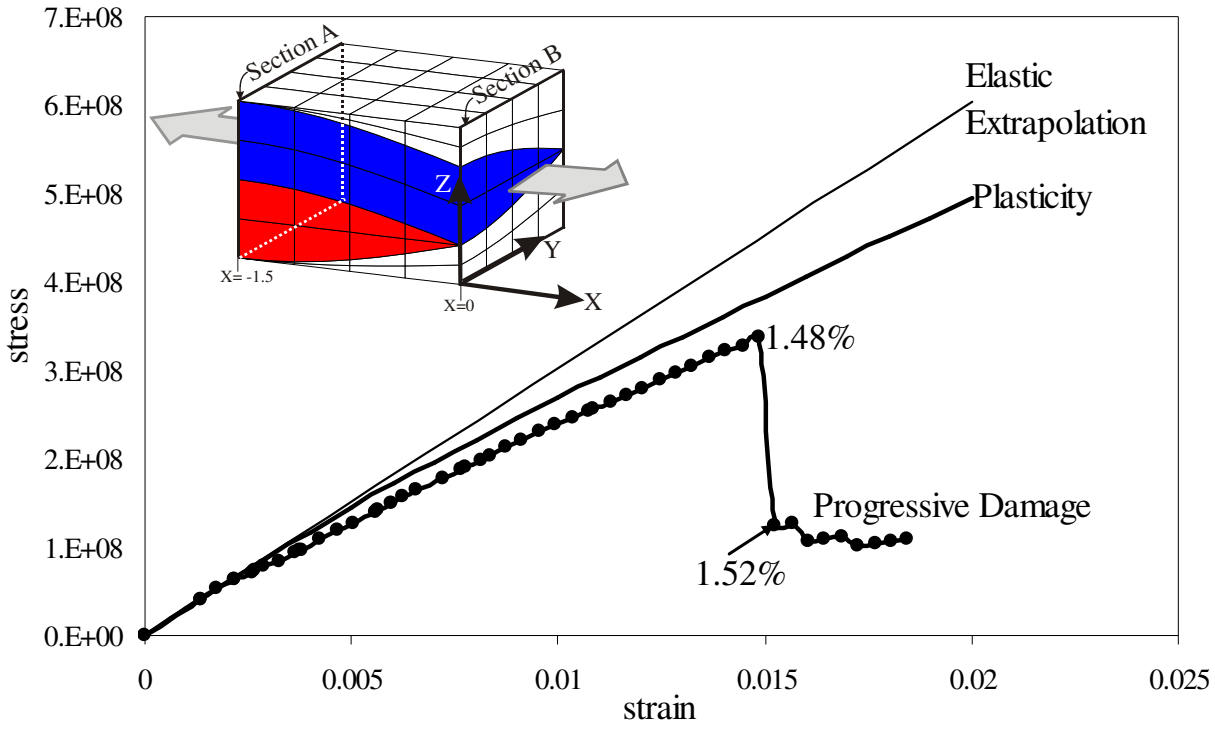

Figure 8.33. Plasticity induced non-linear stress-strain response of S2-glass/SC15 plain weave under uni-axial tensile load.

Figure 8.33 shows the plasticity induced non-linear macroscopic stress-strain response of the plain weave. A linear elastic extrapolation and progressive damage simulations are also shown for comparison purposes. The figure shows that due to plastic deformation the E_{xx} modulus of the weave starts decreasing from the very beginning and keeps decreasing gradually till 2% strain. The simulations were stopped at that strain level because infinitesimal strains were assumed in the analysis. The stress-strain curve predicted by the plastic analysis lies above the damage simulation, which shows that the degradation of modulus predicted by plastic analysis is less than that predicted by damage analysis. At 1.48% strain level, the percentage loss in the stress level due to damage is 24% as compared to 14% due to plasticity. Damage simulation predicts that at a strain level of 1.52%, the woven composite collapses, whereas plasticity simulation does not predict failure.

Figure 8.34 shows the effect of plasticity on the normalized Fx load flow in the warp tow, fill tow and the matrix at different strain levels. The Fx is normalized by applied volume averaged stress $<\sigma_{xx}>$ to the model at various strain levels. The variation of Fx as predicted by a linear elastic analysis is also shown for comparison purposes. Unlike damage analysis predictions, at a low strain level of 0.1%, the plastic and elastic solution predictions for variation of normalized Fx are similar but not exactly the same. This is due to the fact that the matrix and tows are elasto-plastic in nature starting from very low strain levels, which causes yielding at as low as 0.1% strain. Elastic as well as plastic solution at 0.1% strain predict that as we go from x = -1.5 to x = 0, the Fx increases in the warp tow and matrix and it decreases in the fill. As discussed previously, this is due to changing relative material areas of the fill and matrix at different cross-sections and relative difference in moduli of different components in the applied load direction. But when the load increases from 0.1% to 2% strain, the average load in the warp tow increases and in the fill tow decreases, suggesting occurrence of considerable yielding in the fill tow. Different load flow curves in Fig. 8.34 show that as the strain level increases to 2%, the variation in Fx along the x-direction has decreased considerably in the warp as well as the fill tow and the load flow is more uniform. The

figure also shows that the load flow in matrix is affected very little, suggesting little effect of plasticity on the load flow in the matrix. It should be noted that the total load in the plain weave is always constant at different strain levels, which is expected.

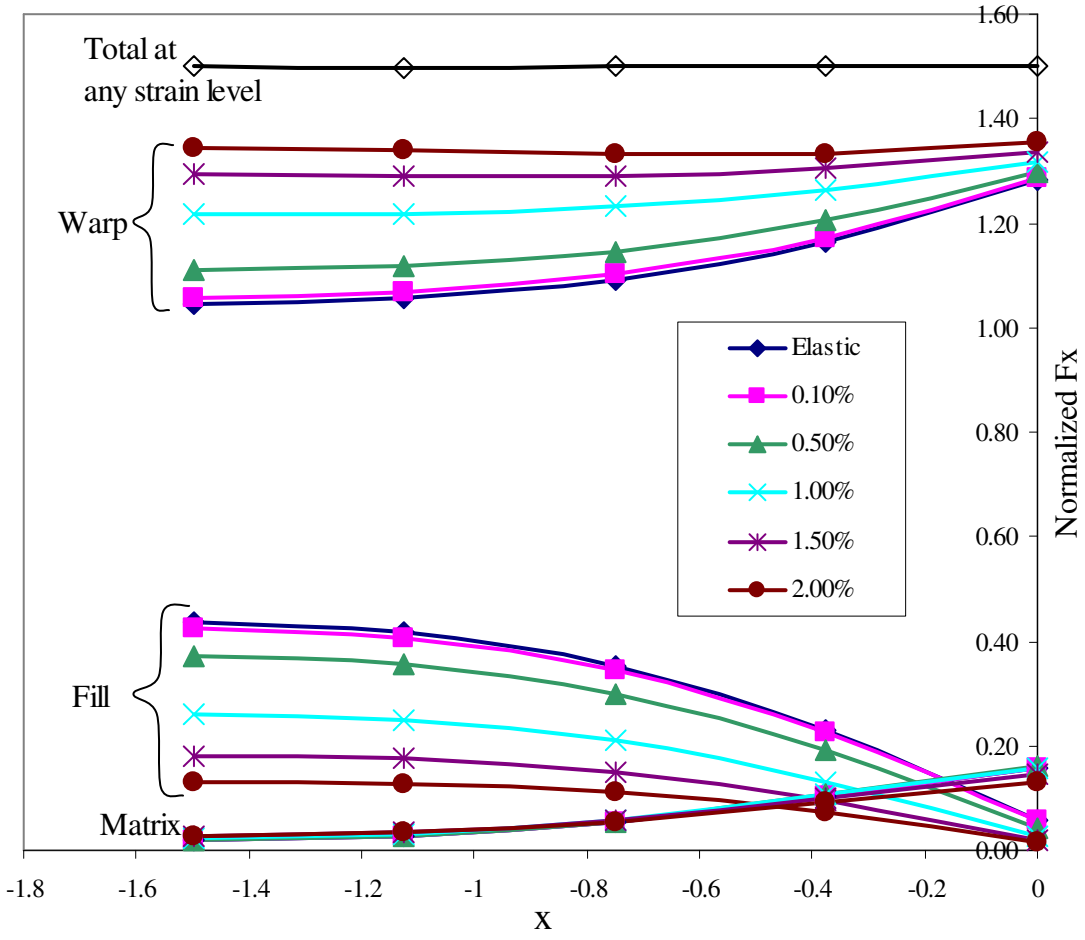

Figure 8.34. Effect of plasticity on the variation of Fx in the plain weave (Normalized $F_x = F_x / \langle \sigma_{xx} \rangle_{model}$).

The variation of average σ_{xx} in the tows and matrix along the x-direction was also investigated. The average σ_{xx} stress in any component at a particular cross-section was obtained by dividing the normalized Fx with the area of the component at that cross-section. It can be seen in Fig. 8.35 that the variation of σ_{xx} in the warp tow is exactly the same as the variation of Fx as the area of cross-section of of warp tow does not change

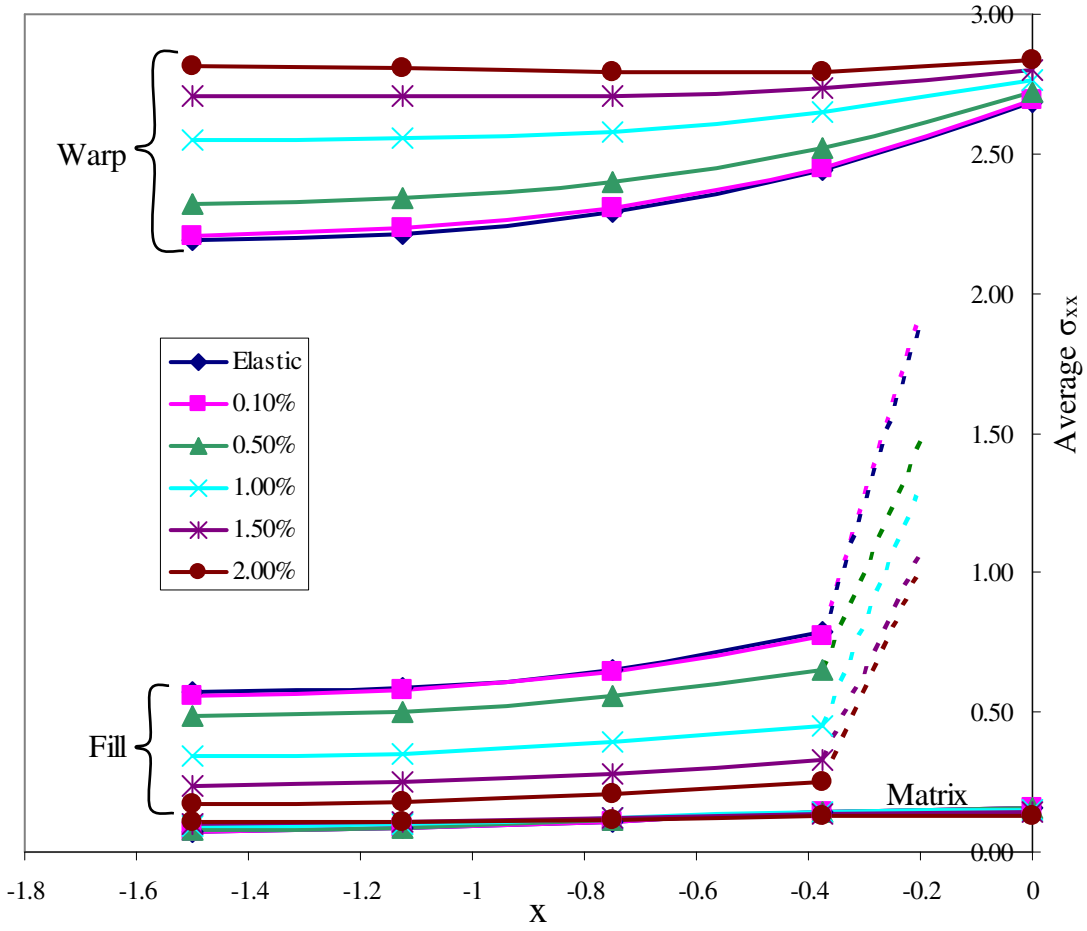

Figure 8.35. Effect of plasticity on the variation of average σ_{xx} in the plain weave ($\sigma_{xx\_avg} = F_x / \langle \sigma_{xx} \rangle_{model} A$).

along x-direction. But the variation of σ_{xx} in the fill tow has considerably changed. The area of the fill tow at different cross-section decreases considerably as we move from x = -1.5 to x = 0 (see Fig. 8.10), reaching zero at x = 0. Hence, the stress in the fill tow increases sharply as we approach the cross-section at x = 0. Nevertheless, the plasticity does decrease the average stress level in the fill tow as the strain increases. The average stress in the matrix is almost unaffected and almost the same at different strain levels as well as at different cross-sections along the x-direction.

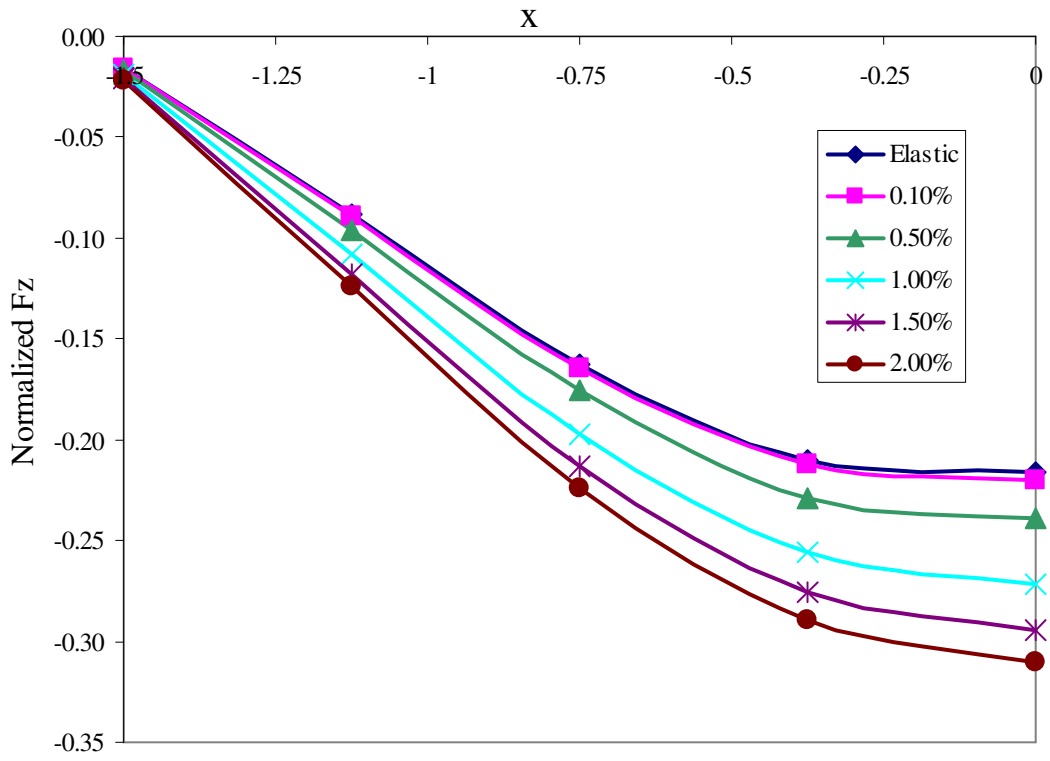

Figure 8.36. Effect of plasticity on the variation of Fz in the warp tow (Normalized $F_z = F_z / \langle \sigma_{xx} \rangle_{model}$) .

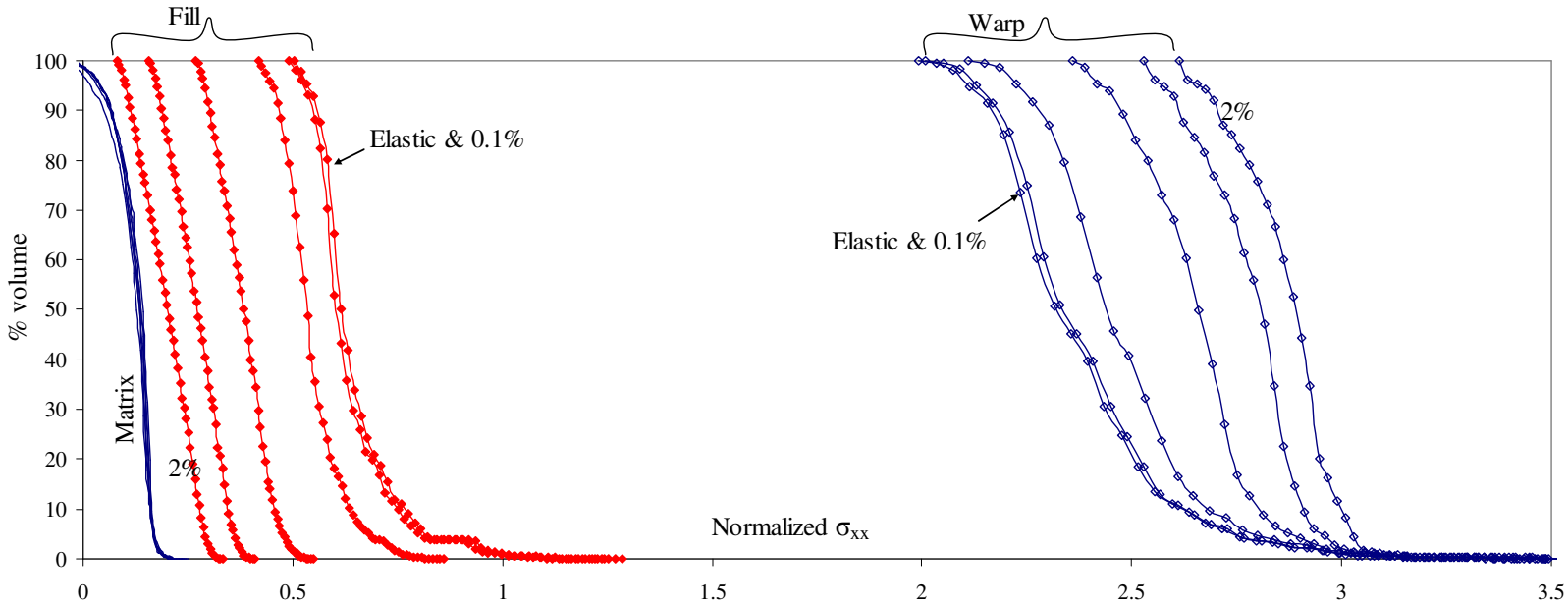

Figure 8.37. Effect of plasticity on σ_{xx} volume distribution in the plain weave
(Normalized $\sigma_{xx} = \sigma_{xx} / \langle \sigma_{xx} \rangle_{model}$) .

Figure 8.36 shows the variation of normalized Fz at different cross-sections of the warp tow along the applied load direction. At the low strain level of 0.1%, the variation is almost the same as the elastic solution. As the strain level increases, the maximum Fz in the warp tow also increases, which is due to the fact that the average σ_{xx} in the warp tow increases with an increase in strain level. As in the elastic case, the variation of Fz along different cross-sections is related to the amount of average stress in the warp tow in the fiber direction.

Figure 8.37 shows normalized σ_{xx} stress volume distribution plot for the warp tow, fill tow and the matrix. The σ_{xx} was normalized by the applied volume averaged stress $<\sigma_{xx}>$ at different strain levels. The distribution is consistent with the Fx load flow observations in Fig 8.34 in the sense that average σ_{xx} stress in the warp tow keeps on increasing as the strain level increases and the average σ_{xx} in the fill tow keeps on decreasing at different strain levels. The stress distribution in the matrix is pretty much unaffected.

8.4. Summary

Increase in computational power has made detailed three-dimensional finite element analyses practical, but special post-processing techniques are required to interpret the massive amount of output data. Use of non-standard post processing techniques brought new insights about the mechanics of load flow in textile composites. The main observations of this chapter are summarized as follows:

- In the warp tow of a plain weave, maximum axial load occurs at the maximum undulation region. Two competing load redistribution mechanisms decide the relative amount of load flowing in warp, fill and matrix. Relative load flow also depends on the material system. Load redistribution in warp, fill and matrix occurs because the distribution of fill and matrix material around the warp tow varies along the warp tow path.
- The existence and variation in transverse load can be explained by using a simple stress transformation.

- There is a correlation between the locations of stress concentrations and locations of peak stress resultants.
- The increase in average stress at maximum undulation region can potentially make that region very susceptible to damage. This is especially true for the fill, which has a singularity in average stress in that region.
- In the case of applied in-plane shear stress too, the load flow in the warp, fill and matrix is not uniform. The average shear stress is maximum for the warp, fill and the matrix in the maximum undulation region which potentially makes that region very susceptible to damage initiation under in-plane shear load too.
- The stress state in the warp tow is non-uniform and fully three dimensional. Some stress concentrations might be so localized that slight yielding might significantly reduce those stress concentrations. Stress-volume distribution plot provided insights that stress contour plots could not, which changed some conclusions about the potential failure modes.
- In comparable regions, all the weaves show a similar peak in the axial and transverse stress resultants at the maximum undulation region.
- In contrast, significant differences in bending moments exist. The lack of symmetry in Twill and 4HS weaves causes offset of the stress resultants from the centroid of the tow cross-section.
- An investigation of effect of damage on load flow in plain weave showed that the damage in fact does initiate in the fill tow in the maximum undulation region. Damage reduces the non-uniformity in the load flow in the warp and fill tows considerably, but the final failure causes a large variation in the load flow and stress distribution.
- Plastic deformation also decreases the variation in load flow in the warp and fill tows. With an increase in applied load, the warp tow picks up the load shed by the fill tow, which suggests that considerable plastic deformation occurs in the fill tow.

9. CONCLUSIONS AND FUTURE WORK

9.1. Conclusions

Various linear elastic, plastic and damage behaviors of textile composites were studied. The following conclusions can be drawn from the studies conducted.

9.1.1. Linear elastic analyses of stress concentrations in braided composites

First the linear elastic behavior of 2x2 biaxial braided composites was analyzed. An investigation of the stress state in the tow of 2x2 braided composites showed that a complex stress state which is fully three-dimensional exists in the tow even for simple uni-axial loading. A comparison of the stress state in the tow with a lamina of an equivalent tape laminate showed that a considerable volume of the tow has more stresses than an equivalent lamina in the considered range of parameters (WR =1/3 – 1/20, BA = ±25˚ - ±65˚). It was also observed that the wide variation in stress volume distribution with braid angle is due to simple orientation effects and can be eliminated by matching the loading on the tow. Some difference that still remains can be attributed to the phase shift of the braid tows. Finally, it was interesting to observe that the severity of the peak stresses increases linearly with an increase in waviness ratio for all stress components (except for σ_{12} for which there is little variation).

9.1.2. Damage initiation and progression in textile composites

Damage initiation and progression in woven composites was studied by using a framework that allowed use of a wide variety of damage initiation and growth models in a common way. Four different damage models in terms of degradation of engineering elastic properties were implemented. The models differ in terms of the amount of degradation as well as the properties to be degraded under a particular failure mode. All the models degrade only diagonal terms in the compliance matrix except for Zako's model, which degrades off-diagonal terms also. Zako's model gave fairly good predictions for Glass/Epoxy plain weave composite whereas other models predicted well for Graphite/Epoxy plain and twill weave composites. All the models predicted similar

response when damage factors were made similar, which shows that the magnitude of damage factors are very important even when all the models do not degrade the same engineering properties under particular failure modes. Stress volume distribution plots for the warp, fill and matrix show that before the damage initiates, the average stress is uniform in most of the volume of the component. Damage initiation in any component increases the range of stress considerably in that component.

9.1.3. Plasticity induced non-linearity in braided composites

The plasticity induced non-linearity in 2x2 braided composites was analyzed using a two scale modeling approach. The analysis was validated by comparing the predicted response using elastic and plastic solutions with experimental data for carbon, E-glass and S-glass braids. Both experimental and analytical results showed that the braid is quite non-linear. The non-linear response could be predicted reasonably well for all the braids at as high as 2% strain. Full 3D as well as equivalent tape laminate predictions lie within the range of experimental data for almost all braid configurations with different material systems.

Equivalent tape laminate plastic analyses were performed and it was observed that their predictions are almost as accurate as the full 3D braid model predictions in terms of percentage modulus reductions, which shows that one can use much simpler equivalent tape laminate model to reasonably predict some aspects of the braid behavior and have significant computational time savings. A comparison of the performance of braided composites and equivalent tape laminates showed that tapes have a better performance in terms of longitudinal modulus, but in terms of percentage moduli degradation due to plasticity, both braids and tapes have similar performance.

Plastic deformation increases the largest σ_{11} and σ_{33} values and reduces the largest σ_{13} values in the tow, which suggest that the plastic deformation is probably being driven by the σ_{13} stress component.

The effect of fiber modulus on the plastic behavior of braided composite was analyzed for a ±25˚ braided configuration and it was concluded that the conclusions about the effect of fiber type on the degree of plasticity induced non-linearity in a ±25˚

braid depend on the measure of non-linearity. By modulus drop and energy measures, the degree of non-linearity is not much different in the two braids with different fiber modulus. However, considerably more plastic strain occurs in the glass braid as compared to the carbon braid when loaded at the same stress level, which can potentially put the glass tow at a higher risk of initiating damage.

9.1.4. Mechanics of load flow in textile composites

Use of special post processing techniques brought new understandings about the mechanics of load flow in textile composites. The behavior of plain woven composite was investigated in detail and the reasons for the variation in load flow in the plain weave were explored. It was found that the load increases in the warp and decreases in the fill tow at the maximum undulation region. Load redistribution in warp, fill and matrix occurs because the distribution of fill and matrix material around the warp tow varies along the warp tow path. This hypothesis was validated by studying various other configurations. Relative load flow in the warp, fill and matrix also depends on the relative material properties of different components. The existence and variation in transverse load was explained by using a simple stress transformation.

The reasons for stress concentrations to occur at certain preferable locations were also investigated. It was seen that a correlation between the locations of stress concentrations and locations of peak stress resultants exists. It was seen that under in-plane tensile as well as under in-plane shear loading, the average stress is maximum in the warp, the fill, and the matrix at the maximum undulation region. Due to this, that region is very susceptible to initiating damage, especially in the fill, because the fill tow had a singularity in average stress in that region. It was very interesting to observe that the hypotheses proposed in linear elastic analysis were consistent with the damage initiation and progression study. The damage, in fact, did initiate in the maximum undulation region in the fill tow.

The stress distribution was also analyzed using stress volume distribution plots. It was observed that stress contours plots can sometimes give incorrect information about the most critical stress component. Some stress concentrations might be so

localized that slight yielding might significantly reduce those stress concentrations. The critical stress components are likely those which have the potential to fail a larger volume of the region.

The effect of textile architecture on the load flow was investigated by identifying equivalent regions in different woven architectures. It was observed that in comparable regions, the force variation was very similar, but the moment distribution was not. The difference in bending moments was attributed to the lack of symmetry in Twill and 4HS weaves, which causes offset of the stress resultants from the centroid of the tow cross-section thereby producing a non-zero bending moments only in those architectures.

The effect of plasticity and material damage induced non-linearity was also studied for glass/epoxy plain weave composite. It was seen that both damage as well as plasticity increase the average load in the warp tow and reduce the average load in the fill tow. Also damage and plasticity remove the non-uniformity in the load flow at different cross-sections of the warp and fill tows. It was also observed that damage induced final failure of the composite causes a large variation in the load flow and stress distribution in the warp tow.

9.2. Future Work

A large number of linear elastic analyses have been conducted for the plain woven composites by various researchers. The analyses for the other complex textile architectures and non-linear analyses have been relatively limited in the literature. A variety of linear elastic as well as non-linear analyses of a variety of textile architectures have been performed in this work. Based on the investigations done in this work, the following studies can be performed in the future.

- Analyses of textile composites that have reinforcement in the out of plane z direction have not been considered in this work. The mesh generation for 3D textile composites is quite challenging and has a lot of research potential.
- In this work, though limited studies were conducted with truncated lenticular cross-sections also, most of the modeling involved lenticular and flattened cross-sections for the tows. In reality, the cross-section shape of the tow varies anywhere from

lenticular to elliptical to flattened or to other non-uniform shapes. A thorough study to take into account the varying shape of the cross-section is required. Mesh generation is again a challenging task for this kind of work.

- The next main task in the area of damage initiation and progression that is left to be done is to compare proposed damage models with the microscopic experimental data for damage. That will give researchers the opportunity to refine and validate damage models.
- In this work, non-linearity due to the material elastic damage and plasticity were studied separately. In reality, the simultaneous occurrence of these phenomena is more likely and is recommended for future studies.

REFERENCES

1. A & P Technology, Inc. http://www.braider.com [cited 01 February 2006].
2. Tang X, Whitcomb JD, Kelkar AD, Tate JS. Progressive failure analysis of 2x2 braided composites exhibiting multiscale heterogeneity. Composites Science & Technology 2006;66(14):2580-2590.
3. Koca O, Buchholz F-G. Analytical and computational stress analysis of fiber/matrix composite models. Computational Materials Science 1994;3(2):135-145.
4. Hatta H, Goto K, Ikegaki S, Kawahara I, Mohamed S, Hassan A, Hamada H. Tensile strength and fiber/matrix interfacial properties of 2D- and 3D-carbon/carbon composites. Journal of the European Ceramic Society 2005;25(4):535-542.
5. Zhifei S, Yanhua C, Limin Z. Micromechanical damage modeling of fiber/matrix interface under cyclic loading. Composites Science and Technology 2005;65(7-8):1203-1210.
6. Whitcomb JD, Noh J. Concise Derivation of Formulas for 3D Sublaminate Homogenization. Journal of Composite Materials 2000;34(6):522-535.
7. Jung-Seok K. Development of a user-friendly expert system for composite laminate design. Composite Structures 2007;79(1):76-83.
8. Mayes JS, Hansen AC. Composite laminate failure analysis using multicontinuum theory. Composites Science and Technology 2004;64(3-4):379-394.
9. Lee SJ, Reddy JN, Abadi FR. Nonlinear finite element analysis of laminated composite shells with actuating layers. Finite Elements in Analysis and Design 2006;43(1):1-21.
10. Zhang Y, Zhu P, Lai X. Finite element analysis of low-velocity impact damage in composite laminated plates. Materials & Design 2006;27(6):513-519.
11. Yang QD, Rugg WKL, Cox BN, Marshall DB. Evaluation of macroscopic and local strains in a three-dimensional woven C/SiC composite. Journal of American Ceramic Society 2005;88(3):719–725.
12. Whitcomb JD, Noh J, Chapman C. Evaluation of various approximate analyses for plain weave composites. Journal of Composite Materials 1999;33(21):1958-1981.
13. Ishikawa T, Chou TW. Elastic behavior of woven hybrid composites. Journal of Composite Materials 1982;16:2-19.
14. Ishikawa T, Chou TW. Stiffness and strength behavior of woven fabric composites. Journal of Material Science 1982;17:3211-3220.

15. Ishikawa T, Matsushima M, Hayashi Y. Experimental confirmation of the theory of elastic moduli of fabric composites. Journal of Composite Materials 1985;19:443-458.

16. Naik NK, Shembekar PS. Elastic behavior of woven fabric composites: I - Lamina analysis. Journal of Composite Materials 1992;26:2196-2225.

17. Naik NK, Ganesh VK. Prediction of thermal expansion coefficients of plain weave fabric composites. Composite Structures 1993;26:139-154.

18. Hahn HT, Pandey R. A micromechanics model for thermoelastic properties of plain weave fabric composites. Journal of Engineering Material Technology 1994;116:517-523.

19. Vandeurzen P, Ivens J, Verpoest I. Micro-Stress analysis of woven fabric composites by multilevel decomposition. Journal of Composite Materials 1998;32(7):623-651.

20. Whitcomb JD, Tang X. Effective moduli of woven composite. Journal of Composite Materials 2001;35(23):2127-2144.

21. Paumelle P, Hassim A, Léné F. Composites with woven reinforcements: Calculation and parametric analysis of the properties of homogeneous equivalent. La Recherche Aérospatiale 1990;1:1-12.

22. Paumelle P, Hassim A, Léné F. Microstress analysis in woven composite structures. La Recherche Aérospatiale 1991;6:47-62.

23. Whitcomb JD, Tang X. Effect of tow architecture on stresses in woven composites. In: 40th AIAA/ ASME/ ASCE/ AHS/ASC Structures, Structural Dynamics and Materials Conference, AIAA-99-1479, 1999, p. 1-10.

24. Whitcomb JD. Three dimensional stress analysis of plain weave composites. In: NASA TM 101672, November 1989. Composite Materials: Fatigue and Fracture, 1991, Third Volume, T.K. O'Brien, ed., ASTM STP 1110, p. 417-438.

25. Kuhn JL, Charalambides PG. Modeling of plain weave fabric composite geometry. Journal of Composite Materials 1999;33(3):188-220.

26. Kuhn JL, Haan SI, Charalambides PG. Stress induced matrix microcracking in brittle matrix plain weave fabric composites under uniaxial tension. Journal of Composite Materials 2000;34(19):1640-1664.

27. Ji KH, Kim SJ. Dynamic direct numerical simulation of woven composites for low-velocity impact. Journal of Composite Materials 2007;41(2):175-200.

28. Blackketter DM, Walrath DE, Hansen AC. Modeling damage in a plain weave fabric-reinforced composite material. Journal of Composites Technology & Research 1993;15(2):136-142.

29. Tang X, Whitcomb JD. Progressive failure behaviors of 2D woven composites. Journal of Composite Materials 2003;37(14):1239-1259.

30. Kollegal MG, Sridharan S. Strength prediction of plain woven fabrics. Journal of Composite Materials 2000;34(3):240-257.

31. Guan H, Gibson RF. Micromechanical models for damping in woven fabric-reinforced polymer matrix composites. Journal of Composite Materials 2001;35(16):1417-1434.

32. Goyal D, Tang X, Whitcomb JD, Kelkar AD. Effect of various parameters on effective engineering properties of 2x2 braided composites. Journal for Mechanics of Advanced Materials and Structures 2005;12(2):113-128.

33. D'Amato E. Finite element modeling of textile composites. Composite Structure 2001;54:467-475.

34. Naik RA. Analysis of 2-D triaxial and 3-D multi-interlock braided textile composites. In: 37th AIAA/ASME/ASCE/AHS/ASC Structures, Structural Dynamics, and Materials Conference and Exhibit. Salt Lake City, UT, AIAA-96-1530-CP, Jan. 1996, p. 1804-1811.

35. Whitcomb JD, Chapman C, Tang X. Derivation of boundary conditions for micromechanics analyses of plain and satin weave composites. Journal of Composite Materials 2000;34(9):724-747.

36. Tang X, Whitcomb JD. General techniques for exploiting periodicity and symmetries in micromechanics analysis of textile composites. Journal of Composite Materials 2003;37:1167-1189.

37. Srirengan K, Whitcomb JD. Finite element based degradation model for composites with transverse matrix cracks. Journal of Thermoplastic Composites 1998;11:113-123.

38. Nicoletto G, Riva E. Failure mechanisms in twill-weave laminates: FEM predictions vs. experiments. Composites: Part A 2004;35:787-795.

39. Guagliano M, Riva E. Mechanical behaviour prediction in plain weave composites. Journal of Strain Analysis 2001;36(2):153-162.

40. Chapman CD, Whitcomb JD. Thermally induced damage initiation and growth in plain and satin weave carbon-carbon composites. Mechanics of Composite Materials and Structures 2000;7:177-194.

41. Stanton EL, Kipp TE. Nonlinear mechanics of two-dimensional carbon-carbon composite structures and materials. AIAA Journal 1985;23(8):1278-1284.

42. Zako M, Uetsujib Y, Kurashikia T. Finite element analysis of damaged woven fabric composite materials. Composites Science and Technology 2003;63:507–516.

43. Choiy J, Tamma KK. Woven fabric composites part I: Predictions of homogenized elastic properties and micromechanical damage analysis. International Journal of Numerical Methods in Engineering 2001;50:2285-2298.

44. Karkkainen RL, Sankar BV. A direct micromechanics method for analysis of failure initiation of plain weave textile composites. Composites Science and Technology 2006;66:137-150.

45. Tate JS. Performance evaluation and modeling of braided composites. In: Ph.D. Dissertation, Dept of Mechanical Engineering, North Carolina A&T State Univ, Greensboro, NC, 2004.

46. Tang X, Whitcomb JD, Kelkar AD. Micromechanics analysis of plasticity-induced nonlinear behavior in woven composites. In: Sixteenth Technical Conference of the American Society for Composites, Blacksburg, VA, Sept. 2001.

47. Xie M, Adams DF. A plasticity model for unidirectional composite materials and its applications in modeling composites testing. Composites Science and Technology 1995;54:11-21.

48. Hill R. The Mathematical Theory of Plasticity. Oxford University Press, London, 1st edition, Chapter 12, 1950.

49. Chen JL, Sun CT. A plasticity potential function suitable for anisotropic fiber composites. Journal of Composite Materials 1993;27:379-1390.

50. Griffin Jr OH, Kamat MP, Herokovich CT. Three-dimensional inelastic finite element analysis of laminated composites. Journal of Composite Materials 1981;5:543-560.

51. Schimidt RJ, Wang DQ, Hansen AC. Plasticity model for transversely isotropic materials. Journal of Engineering Mechanics 1993;119:748-766.

52. Ishikawa T, Matsushima M, Hayashi Y. Geometrical and material nonlinear properties of two-dimensional fabric composites. AIAA Journal 1987;25(1):107-113

53. Hahn HT, Tsai SW. Nonlinear elastic behavior of unidirectional composite laminate. Journal of Composite Materials 1973;7(1):102-118.

54. Hansen AC, Blackketter DM, Walrath DE. An invariant-based flow rule for anisotropic plasticity applied to composite materials. Journal of Applied Mechanics 1991;58:881-888.

55. Dasgupta A, Bhandarkar SM. Effective thermalmechanical behavior of plain-weave fabric-reinforced composites using homogenization theory. Journal of Engineering Materials and technology 1994;116:99-105.

56. Aboudi J. Mechanics of composite materials - A unified micromechanical approach. Elsevier, Amsterdam, ISBN 0-444-88452-1, 1991.

57. Whitcomb JD, Srirengan K, Chapman C. Evaluation of homogenization for global/local stress analysis of textile composites. Composite Structures 1995;31(2):137-149.

58. Aggarwal A, Ramakrishna S, Ganesh VK. Predicting the in-plane elastic constants of diamond braided composites. Journal of Composite Materials 2001;35(8):665-688.

59. Lee CS, Chung SW, Shin H, Kim SJ. Virtual material characterization of 3D orthogonal woven composite materials by large-scale computing. Journal of Composite Materials 2005;39(10):851-863.

60. Bednarcyk BA, Pindera M-J. Inelastic response of a woven carbon/copper composite-Part II: micromechanics model. Journal of Composite Materials 2000;34(4):299-331.

61. Dadkah MS, Flintoff JG, Cox BN. Simple models for triaxially braided composites, Composites 1995;26:561-577.

62. Falzon PJ, Herszberg I. Mechanical performance of 2-D braided carbon/epoxy composites. Composites Science and Technology 1998;58:253-265.

63. Hosur MV, Abraham A, Jeelani S, Vaidya UK. Studies on the influence of through-the-thickness reinforcement on low-velocity and high strain rate response of woven S2-glass/vinyl ester composites. Journal of Composite Materials 2001;35(12):1111-1133.

64. Takatoya T, Susuki I. In-plane and out-of-plane characteristics of three-dimensional textile composites. Journal of Composite Materials 2005;39(6):543-556.

65. Abot JL, Daniel IM. Through-thickness mechanical characterization of woven fabric composites. Journal of Composite Materials 2004;38(7):543-553.

66. Fedro MJ, Willden K. Characterization and manufacturing of braided composites for large commercial aircraft structures. In: NASA CP 3154, 1991, p. 387-429.

67. Baucom JN, Zikry MA. Evolution of failure mechanisms in 2D and 3D woven composite systems under quasi-static perforation. Journal of Composite Materials 2003;37(18):1651-1674.

68. Tate JS, Kelkar AD. Stiffness degradation modeling of biaxial braided composites. Composites Part B: Engineering 2007, first published online as doi:10.1016/j.compositesb.2007.03.001.

69. Quaresimin M, Ricotta M. Damage evolution in woven composite laminates under fatigue loading. In: International Conference on Fatigue Crack Paths, Parma, Italy, Sept. 2003.

70. Hansen U. Damage development in woven fabric composites during tension-tension fatigue. Journal of Composite Materials 1999;33(7):614-639.

71. Khan R, Khan Z. Fatigue life estimates in woven carbon fabric/epoxy composites at non-ambient temperatures. Journal of Composite Materials 2002;36(22):2517-2535.

72. Khashaba UA. Fracture behavior of woven composites containing various cracks geometry. Journal of Composite Materials 2003;37(1):5-20.

73. Chiu CH, Tsai KH, Huang WJ. Effects of braiding parameters on energy absorption capability of triaxially braided composite tubes. Journal of Composite Materials 1998;32(21):1964-1983.

74. Whitcomb JD, Tang X, Chapman C. Comparison of stress concentrations in plain and 8-harness satin weave composites. In: ASME International Mechanical Engineering Congress and Exposition (IMECE), Anaheim, CA, 1998.

75. Matlab, Software Package, Ver. 6.5, The MathWorks Inc. Natick, MA.

76. Richard RM, Blacklock JM. Finite element analysis of inelastic structures. AIAA Journal 1969;7:432-438.

77. Resolution Performance Products, Inc. http://www.resins.com/resins/am/pdf/SC2508.pdf [cited 01 February 2006].

78. Dunne F, Petrinic N. Computational plasticity. 1st edition, ISBN: 0198568266, Oxford University Press, USA, 2005, Chapter. 2.

79. Goyal D, Whitcomb JD. Analysis of stress concentrations in 2x2 braided composites, Journal of Composite Materials 2006;40(6):533-546.

80. Chamis CC. Simplified composite micromechanics equations for strength, fracture toughness, impact resistance and environmental effects. In: Technical memo. access number ADA304541, NASA Cleveland OH Lewis Research Center, p. 1-28, 1984.

81. Zac-Williams A. Fatigue behavior of 45° fiber glass braided composites. In: MS Thesis, Computational Science and Engineering, North Carolina A&T State Univ., Greensboro, NC, 2006.

82. Tate J, Kelkar AD, Goyal D, Whitcomb JD, Tang X. Behavior of biaxial braided composites subjected to uni-axial tensile loading. In: Proceedings of American Society for Composites 20th Annual Technical Conference, Drexel University, Philadelphia, PA, Sept. 2005.

83. Goyal D, Whitcomb JD. Effect of fiber properties on plastic behavior of 2x2 biaxial braided composites. Composite Science & Technology 2007, first published online as doi:10.1016/j.compscitech.2007.08.002.

VITA

Deepak Goyal was born in India on November 21, 1977. He obtained his Bachelor of Engineering degree (with honors) in Mechanical Engineering from Punjab Engineering College, Panjab University, Chandigarh, India in May 2000. He got admitted in the Aerospace Engineering program at Texas A&M University in Fall 2001 and received his Master of Science degree in August 2003. Since then, he has been pursuing a Ph.D. degree in Aerospace Engineering and his expected date of graduation is December 2007. He is a recipient of AIAA open topic graduate award in the year 2006. His current research interests include simulation and design of high performance materials and structures for spacecraft, aircraft, defense, biomedical and industrial applications. Upon completion of his Ph.D. work, he plans to join SIMULIA Inc. as an Application Engineer.

Mr. Goyal can be reached at 539 Bielenberg Drive, Suite 110, Woodbury, MN 55125. His email address is anndee108@gmail.com.